Background and sensitivity studies for the LUX-ZEPLIN experiment

Umit Utku

Department of Physics & Astronomy

University College London

Thesis submitted for the degree of
Doctor of Philosophy in the subject of *Physics*

October 2020

Abstract

The existence of dark matter is now supported by a wide range of physical observations, ranging from galactic to cosmological scales. Our best cosmological models predict dark matter to make up 85% of the matter-content of the universe. One of the leading particle candidates that can effectively explain cosmological observations is the Weakly Interacting Massive Particles (WIMPS), the presence of which can be directly searched for by rare-event underground experiments via its scattering off atomic nuclei. By deploying a multi-tonne dual-phase liquid xenon (LXe) detector, the LUX-ZEPLIN (LZ) experiment, currently under construction in the Davis Campus at the Sanford Underground Research Facility (SURF) (South Dakota, USA) is projected to reach unprecedented sensitivities in search for WIMPs.

In probing deeper into the WIMP landscape, an extensive screening and cleanliness campaign was envisioned, selecting some of the most radio-pure material for the construction of LZ. This work highlights some of the cutting-edge techniques used in understanding and modelling a wide range of backgrounds, focusing primarily on measuring and modeling the radon emanation background projections. By using the LZ simulation and statistical inference frameworks, the impact of radon emanation across different background scenarios are examined, where the 90% CL sensitively is determined to vary from 1.34×10^{-48} cm^2 to 1.76×10^{-48} cm^2 at radon activities of 11.0 mBq and 60.4 mBq, respectively—remaining well below LZ requirement of 3.0×10^{-48} cm^2. The projected LZ sensitivity for a WIMP mass of 40 GeV/c^2, at a 90% CL and the 3σ discovery potential was determined to be 1.43×10^{-48} cm^2 and 3.4×10^{-48} cm^2.

The projected limits from second-generation detectors, such as LZ and XENONnT leave a significant amount of the parameter space prior to the cosmic neutrino floor ($\sim 10^{-49}$ cm^2) unexplored. In envisioning what a future third-generation (G3) detector may hold and examine the background necessities of such a detector, a toy G3 experiment is presented. A cryogenic radon facility currently under construction is outlined to pave the way for achieving the background requirements of a G3 dual-phase LXe observatory.

Impact Statement

One of the hot topics of physics in the twenty-first century is the dark matter conundrum; its implications for the structure formation of the universe, and its connection to the standard model of elementary particles. Upon operation, the LUX-ZEPLIN (LZ) experiment will be the largest and most sensitive dark matter detector on earth, looking for weak interactions massive particles (WIMPs)—one of the leading candidates for dark matter. Reaching ever-so-sensitive domains of the WIMP parameter space arises new experimental challenges. These challenges range from engineering to simulating, characterising, and modelling of signal and background events, to optimise detector design, constructional approaches and science reach.

The work presented in this thesis incorporates a broad extent of research, spanning from measurements of radio-contaminants of the LZ experiment to simulating the detector operations and statistical modelling of the WIMP search. The results highlighted in this thesis were especially impactful in understanding the radon emanation background of LZ, the expected emanation rate in operation and the impact of the radon background for the WIMP search. Furthermore, as part of an R&D process, a cold radon emanation facility (CREF) was developed to measure radon backgrounds for low-background experiments across a multitude of materials and temperatures—the outcome of which will be immense for the next-generation experiments beyond LZ. The CREF project has already become a new ground of research for upcoming PhD students and postdoctoral fellows.

Beyond academia, radiation detection is of great importance for humanity and especially for public health. Airbourne radon is reported to be the second leading cause of lung cancer. The technology developed as part of this research may further be developed to measure and characterise radon levels of our surroundings to improve the quality of our environments and life.

Acknowledgements

There are many people that have played a significant role in shaping, guiding and accompanying my journey as I have navigated the terrains of life, started out in a rural hamlet in Turkey, and lead me to this moment of time. I am grateful for all of those, that one way or another, have came across my path and facilitated the completion of my PhD thesis. However, I would like to acknowledge a few of those individuals, without whom, the completion of this thesis wouldn't have been possible.

Firstly, I would like to extend my deepest gratitude to my supervisor and dear friend, Chamkaur Ghag, for convincing and giving me the opportunity to undertake this research. I am eternally grateful for his support, assistance, guidance and wisdom throughout. His supervision and friendship has guided me in ways unimaginable. I further extend this gratitude to Jim Dobson, a phenomenal human being and a colleague. I am extremely grateful to have had the opportunity to work with him closely and thank him for his eternal patience throughout the years.

I'd like to thank all of the members of the LZ collaboration, whose dedication, hard work and togetherness, not only has made this project a success; but has motivated, inspired and facilitated many invaluable experiences. I'd like to extend my gratitude to those I have worked closely over the years, namely, Sally S., Ibles O., Theresa F., Amy C., Alvine, K., Markus H., Tomasz B., Paul S., Xin L., Alfredo T., and Hans Kraus. I would also like to extend my special thanks to Kevin Lesko, Hugh Lippincott, and Henrique Araujo, for their support, guidance, expertise and trust.

The time I have spent at UCL has been phenomenally rewarding in both personal and professional development and I'd like to thank all the dear members of the particle physics family. Throughout the years I have had many discussions whether in person or during the Friday pub visits, which has undoubtedly added colour to my years at UCL. My special thanks go to all of my colleagues in our UCLDM group and friends in D109, and in particular, Ricky N., Sebastian B., Joanna. H., David Y., and Caishan Q. I'd like

to extend my special gratitude's to Ruben Saakyan for all his assistance, especially with regards the radon emanation work.

Finally, I'd like to show my gratitude to my friends, family and loved ones. To Vasilis K., Deshan A., Nellie M., and Nicolas A., whose friendships has helped me countless times; thank you for trusting and loving me and for all the good times. And to my mother, farther, sisters and cousins, all of whom have been a fundamental part of my life.

With infinite Love,
Umit Utku

Declaration

I hereby declare that this dissertation is the result of my own work, except where an explicit reference is made to the work of others in an effort to broaden and offer an in-depth description for the reader. The following will highlight the chapters of this thesis, specifying my contributions to the broader work that makes up the entirety of this thesis.

Chapter (1) is an introductory overview of the modern cosmological paradigm, referring to may publications to detail the theory and experimentation in our search for dark matter.

Chapter (2) introduces the background to dark matter detection with dual-phase liquid xenon technology and the LUX-ZEPLIN experiment. It builds on past and present literature both from the wider community and work done by the LZ collaboration. A significant amount of my PhD was spent constructing parts of the detector, focused primarily on the cleanliness of the LZ inner cryostat vessel, assembly of the bottom skin PMT array and supervision of various other assembly, quality control and assurance procedures. A significant change in the cleanliness protocols of the Surface Underground Laboratory (SAL) were adopted as a direct consequence of my work out at SURF.

Chapter (3) highlights the radiogenic backgrounds in LZ and our approach in screening and selecting appropriate materials for the detector. Furthermore, the chapter details work done on determining the γ-ray background of Davis cavern. My contributions were towards developing some of the cleanliness protocols under which the detector was constructed and co-authoring the screening paper that summarised the efforts of the collaboration [1]. Moreover, I contributed towards the data-taking and pre-processing and analysis of the γ-ray data from Davis cavern measurements; however, there were a group of collaborators involved in this expedition, which resulted in [2].

Chapter (4) details the radon emanation background in LZ and screening efforts in selecting material and modeling this background for the WIMP search. My contributions

were predominantly through operating the UCL radon emanation system and screening materials for LZ. Furthermore, I was held responsible for collating all radon related results by the collaboration to estimate the total radon emanation background, which is the dominant background in LZ. Many of the measurements mentioned in this chapter, especially the large scale backgrounds were conducted by other collaborators in a co-operative manner.

Chapter (5) introduces the LZ simulation and statistical framework. My contributions involved the developmental work for BACCARAT in coding geometrical changes and I also worked alongside a collaborator to write and develop parts of the LZSTATS framework. I then used these tools to study the statistical implications of various backgrounds in LZ, with an emphasis on the radon background and the final LZ sensitivity and discovery potential for the spin-independent WIMP analysis.

Chapter (6) looks into future of dual-phase liquid xenon technology, envisioning the capacity of a G3 dark matter experiment. I used the LZSTATS framework and the background expectations for an LZ-like experiment to calculate the sensitivity of a 70 tonne experiment with a 300 tonne $\cdot$ year exposure.

Chapter (7) introduces the necessity of the Cold Radon Emanation Facility (CREF), currently developed at RAL. My contributions for this chapter are the design, being constructed and procurement of the gas system that will be used for CREF and in leading the CREF team to finalise the laboratory.

Umit Utku

October, 2020

Contents

List of figures

List of tables

"Writing in English is the most ingenious torture ever devised for sins committed in previous lives."

— James Joyce

Chapter 1

Introduction to Dark Matter

Ever since humankind harnessed the capacity for curiosity, the universe, along with everything it holds has become a vast playground in which the game is to look outwards into the depths of the universe and inwards into the depths of the fabric, the fundamental building blocks of the universe. The introduction of general relativity, followed by the observations of Edwin Hubble lead to a picture of the universe that's non-static and ever expanding. Soon after, dynamical studies of galaxies and galaxy clusters by Fritz Zwicky unfolded a discrepancy between the expected luminous mass and inferred mass of such clusters [3]. The presence of *dark* or unseen matter in galaxies was suggested by a variety of different techniques thereafter. Although unseen, the gravitational influence of dark matter is apparent in many facets of cosmology, leading to a universe that's predominantly dark in matter density and undiscovered. This chapter will explore the theoretical and observational motivations for dark matter, delving into the different candidates to explain it's nature and introducing the Weakly Interacting Massive Particles, one of the leading candidates for dark matter.

1.1 Modern Cosmology

Our modern understanding of the universe emerged with key cosmological observations and realisations at the start of the 20th century. The measurement of the first Doppler shift of the Andromeda galaxy in 1913 and the subsequent measurements made by Vesto Slipher, although controversial at the time, showed that almost all galaxies were receding from Earth [4]. In the 1920s, Georges Lemaitre and Alexnder Friedman independently used Einstein's field equations to show that the universe might be expanding. [5]. The *expanding universe* hypothesis gained further attraction when Erwin Hubble showed

that there is a linear correlation between the distance of galaxies and their recession velocities—dubbed as Hubble's Law [6].

1.1.1 The Expanding Universe

The spectral light from distant stars in galaxies outside of our local group appears to be shifted as these galaxies move away from Earth. Interpreted as the Doppler effect in flat spacetime, the velocity v related to the shift in spectral wavelength $\Delta\lambda/\lambda$ is given by the Doppler formula,

$$v/c = \Delta\lambda/\lambda \equiv z, \tag{1.1}$$

for $V \ll c$, where z is the astronomical definition of redshift.

Erwin Hubble showed that for galaxies sufficiently close, where their distance can be measured, the velocity $\vec{v}$ of these galaxies and their distance $\vec{r}$ followed a simple linear relationship, called Hubble's law:

$$\boldsymbol{\vec{v}} = H_0\boldsymbol{\vec{r}}. \tag{1.2}$$

The constant of proportionality, H_0 is called the Hubble constant. The Hubble constant represents the present day expansion rate of the universe and is usually given with a dimensionless parameter h_0, where

$$H_0 = 100h_0 \text{ km s}^{-1} \text{ Mpc}^{-1}, \text{ where } h_0 = 0.674 \pm 0.005 \text{ [7]}. \tag{1.3}$$

Hubble's law is a phenomenological relationship between redshift and distance, implying that the further a galaxy is, the faster it is moving away from us. Hubble's law holds for galaxies that are far enough that any velocity disruptions due to local gravitational effects are subdominant to the expansion rate, while close enough that spacetime curvature effects or the expansion of the universe in the time it takes for the photons to travel are dominant.

The expansion of the universe leads to the concept of the expansion of space. The expansion is often represented in co-moving coordinates $\boldsymbol{\vec{x}}$. The distance associated with the expansion—the co-moving distance—is a time independent measure between two fundamental observers. In a universe that's expanding under isotropy and homogeneity, the physical distance or proper distance $\boldsymbol{\vec{r}}$ is related to the co-moving coordinates moving

along with the expansion of space by

$$\vec{\boldsymbol{r}} = a(t)\vec{\boldsymbol{x}}, \tag{1.4}$$

where $a(t)$ is the time-dependent cosmological scale factor, representing the change in distance between two fundamental observers due to the expansion.

Differentiating $\vec{\boldsymbol{r}}$ with respect to time leads to the recession velocity $\vec{\boldsymbol{v}}$ of an observer or a galaxy in the same direction as its displacement away from earth, where

$$\vec{\boldsymbol{v}} = \frac{\mathrm{d}\vec{\boldsymbol{r}}}{\mathrm{d}t} \equiv \dot{a(t)}\vec{\boldsymbol{x}}, \tag{1.5}$$

leading to the relationship,

$$H(t) = \frac{\dot{a(t)}}{a(t)}. \tag{1.6}$$

The equation above gives the connection of the Hubble constant to the geometry of spacetime, where $H(t)$ is the time-dependent Hubble parameter, defining the relative expansion of space. The Hubble constant H_0 we measure is $H(t)$ at the present time of the universe.

The expansion of space requires a time-dependent geometry in which a particle's energy moving through this geometry will change similar to it moving through a time-dependent potential. A photon whose energy is proportional to its frequency and therefore its wavelength will experience the expansion as a stretch in its wavelength. This cosmological redshift is defined in terms of the scale factor as

$$z \equiv \frac{\lambda(t_0) - \lambda(t)}{\lambda(t)} = \frac{\lambda(t_0)}{\lambda(t)} - 1 = \frac{a(t_0)}{a(t)} - 1, \tag{1.7}$$

where t represents cosmic time and t_0 present time.

The Hubble constant has the dimensions of an inverse time. The inversion is called the Hubble time t_H. In a version of the universe in which $\ddot{a(t)} \leq 0$, the Hubble time becomes an upper bound and a rough estimate of the age of the universe, placing the age at $\sim$ 14 billion years. With the cosmological observations of this era, the picture of the universe moved towards one in which the universe had a beginning and from that start came the expansion. But the Hubble expansion alone does not provide sufficient evidence and description for what is generally refer to as the hot Big Bang model of cosmology. The

description comes from the application of the cosmological principle to Einstein's theory of General Relativity.

1.1.2 Cosmological Principle

The dynamics of the universe are governed by the Einstein field equation, relating the curvature of spacetime to density of mass-energy [8]

$$R_{\mu\nu} - \frac{1}{2}g_{\mu\nu}R + g_{\mu\nu}\Lambda = \frac{8\pi G}{c^4}T_{\mu\nu}, \tag{1.8}$$

where $R_{\mu\nu}$ is the Ricci curvature tensor, R is the scalar curvature, $g_{\mu\nu}$ is the metric tensor, Λ is the cosmological constant, G is gravitational coupling constant and $T_{\mu\nu}$ is the stress–energy tensor. The left hand side of this equation describes the geometrical structure of spacetime and the right describes the measure of matter and energy density of the Universe. The cosmological constant, Λ, was originally introduced by Einstein as a tuning mechanism for a static cosmology with non-zero matter content but later interpreted as the energy density of the vacuum, a source of energy and momentum that may be present in the absence of matter fields [9].

Modern cosmology for some time has relied upon the premise offered by the cosmological principle. This principle states that the Universe on large scales is homogeneous and isotropic, where local variations in density are averaged over. A homogeneous, isotropic spacetime is one for which the geometry is spherically symmetric about any one point (isotropic) and the same in all points (homogeneous). Although isotropy and homogeneity is assumed for space, when we look at distant galaxies, they appear to be receding from us; the universe is apparently not static, but changing with time. Therefore, any cosmological model of the universe must assume a homogeneous and isotropic universe in space but not in time. Spacetime can therefore be considered as $\boldsymbol{T} \times U$, where $\boldsymbol{T}$ represents the time direction and U is a homogeneous and isotropic three-manifold. The usefulness of homogeneity and isotropy is that they imply that U must be a maximally symmetric space, taking the form of a metric

$$ds^2 = -dt^2 + a^2(t)\gamma_{ij}(u)du^i duj, \tag{1.9}$$

where t is the timelike coordinates, (u^1, u^2, u^3) are the coordinates on U and γ_{ij} is the maximally symmetric metric on U. The dimensionless scale factor $a(t)$ is a function of proper time t, representing the scale of the space-like slice of spacetime at the present moment.

The geometrical interpretation of the cosmological principle can be shown to take a similar form to that of equation 1.8 as the Friedmann-Robertson-Walker (FRW) metric—a metric tensor which describes a homogeneous and isotropic spacetime that evolves as a function of time (see [8,10] for an in-depth review). The three line elements of the metric tensor can be written in a unified form to give the well known FRW metric,

$$ds^2 = -dt^2 + a^2(t)\left[\frac{dr^2}{1-kr^2} + r^2(d\theta^2 + sin^2\theta d\phi)\right], \tag{1.10}$$

where r, θ and ϕ represent the co-moving polar coordinates. The parameter k represents the curvature of the universe, where +1, 0, -1 is for a closed, flat or an open universe respectively, corresponding to a positive, zero or a negative curvature of space.

The FRW model assumes a cosmological fluid consisting of three non-interacting components: pressureless matter, relativistic particles and radiation, and vacuum. This can be modelled by an energy-momentum tensor of a perfect fluid, specified by an energy density, ρ, and isotropic pressure, p, given as

$$T_{\mu\nu} = (\rho + p)u_\mu u_\nu + pg_{\mu\nu}, \tag{1.11}$$

where u^μ is the fluid four-momentum. Under the boundaries imposed by the cosmological principle, whereby the energy-momentum tensor takes the form of a perfect fluid 1.11, the Einstein field equation 1.8 reduces to the Friedmann equations [5,9]:

$$H^2 \equiv \left(\frac{\dot{a}}{a}\right)^2 = \frac{8\pi G}{3}\rho - \frac{kc^2}{a^2} + \frac{\Lambda}{3}, \tag{1.12}$$

$$\frac{\ddot{a}}{a} = -\frac{4\pi G}{3}(\rho + 3p) + \frac{\Lambda c^2}{3}. \tag{1.13}$$

Examining these equations under certain assumptions can lead to useful cosmological quantities. In assuming a flat spacetime, where spatial curvature $k = 0$, and one which is static ($\Lambda = 0$), leads to the quantity known as the critical density,

$$\rho_{crit} \equiv \frac{3H^2(t)}{8\pi G} \simeq 1.88 \times 10^{-29}\, h^2 \text{ g cm}^{-3} \text{ [11]}. \tag{1.14}$$

The cosmological density parameter, a useful definition in comparing different cosmological models is defined as

$$\Omega_{tot} = \frac{8\pi G}{3H^2}\rho = \frac{\rho}{\rho_{crit}}. \tag{1.15}$$

Under the conditions where $\Lambda = 0$ and by using 1.15, the Friedmann equation (1.12) can be shown to take the form

$$\Omega_{tot} - 1 = \frac{kc^2}{a^2H^2}, \tag{1.16}$$

where the sign of spacetime curvature parameter, k, is determined by whether Ω_{tot} is greater than, equal to, or less than one. This reduction leads to a picture in which $\rho < \rho_{crit}$, $\rho = \rho_{crit}$ and $\rho > \rho_{crit}$, equate to a universe that is respectively open ($k = -1$), flat ($k = 0$) or closed ($k = +1$).

The observational determination of the density parameter is an area of intense investigation and it is often necessary to distinguish different contributions to the overall density. One can conveniently define the present-day density parameters for pressureless matter as Ω_m, relativistic particles and radiation as Ω_r and the quantity $\Omega_\Lambda = \Lambda/3H^2$. Thus, the total density of the universe may be defined as,

$$\Omega_{tot} = \Omega_r + \Omega_m + \Omega_\Lambda. \tag{1.17}$$

The Friedmann equation then takes the form

$$\frac{kc^2}{a_0^2H_0^2} = \Omega_r + \Omega_m + \Omega_\Lambda - 1 \tag{1.18}$$

where the subscript 0 indicates present day values.

The conclusion one takes is that the curvature of space denoted by the left side of equation (**??**) depends on the sum of densities in matter, relativistic particles, and vacuum. The Ω_{tot} parameter as given in 1.16, plays an important role in the evolution of universe through its gravitational potential. The observational determination of the density parameter and its constituents will highlight which of the three Robertson-Walker geometries describes our universe. In a simplified scenario in which $\Lambda = 0$ and universe is filled with fluids of positive energy ($\rho > 0$) and non-negative pressure ($p \geq 0$), equation 1.13 leads to $\ddot{a} < 0$. Since the expansion of the universe is verified by the motion of distant galaxies, where $\dot{a} > 0$, this leads to the conclusion that the rate at which the

universe is expanding is negative, hence the expansion is decelerating. This is as expected, since the gravitational attraction of the matter content of the universe works against expansion. In tracing the evolution backwards in time, a singularity is reached at $a = 0$. If $\ddot{a}$ were exactly zero, the age of the universe would be H_0^{-1}. The singularity represents a point in which the universe began from a singular state and this point in history is commonly known as the *Big Bang*.

1.2 Evidence for Dark Matter

The evolution of the universe is governed by the total density content, and by extension, the interplay between matter, radiation and vacuum densities. The cosmological inflation theory requires a universe that is flat, hence $\Omega_{tot} = 1$. With the premise that the universe is flat and by taking into account complementary theoretical and experimental techniques, it becomes possible to quantify the matter density of the universe. By examining the universe on different cosmological scales via Big Bang Nucleosynthesis (BBN), the Cosmic Microwave Background (CMB) and Gravitational Lensing, a picture emerges as one which roughly 95% of the total energy density of the universe still lacks scientific exploration and largely remains a mystery. This section will examine some of the leading cosmological and astronomical observations in more detail, concluding that the levels of observed or luminous matter in the universe do not account for the total matter and that the majority of the matter content of the universe is non-baryonic and non-luminous.

1.2.1 Cosmic Microwave Background

The cosmic microwave background radiation, first discovered in mid-1960s [12], is a primordial radiation from the early universe. In the hot Big Bang model, the early universe is extremely hot and dense, leading to a constant scattering of particles and radiation. At a redshift of around 1100 and roughly 380,000 years of age, the expansion of space cooled the plasma, allowing the first atoms to form through recombination, effectively decoupling the radiation from matter and making the universe transparent to photons. The collisions of these photons with electrons before last scattering ensures that the photons were in equilibrium. Travelling freely through space, this radiation is still present today but has been redshifted due to the expansion of the universe. The CMB photons have been detected on earth with a spectral distribution same as that of a black body function with $T = 2.725$ K [13]. The CMB as observed from earth is roughly homogeneous and isotropic but at scales of around 10^{-5}, it contains small

temperature fluctuations (or anisotropies). The most detailed observation to-date of the CMB anisotropies comes from the Planck collaboration [14], where an all sky map of the temperature anisotropies measured by their space observatory is shown in figure 1.1.

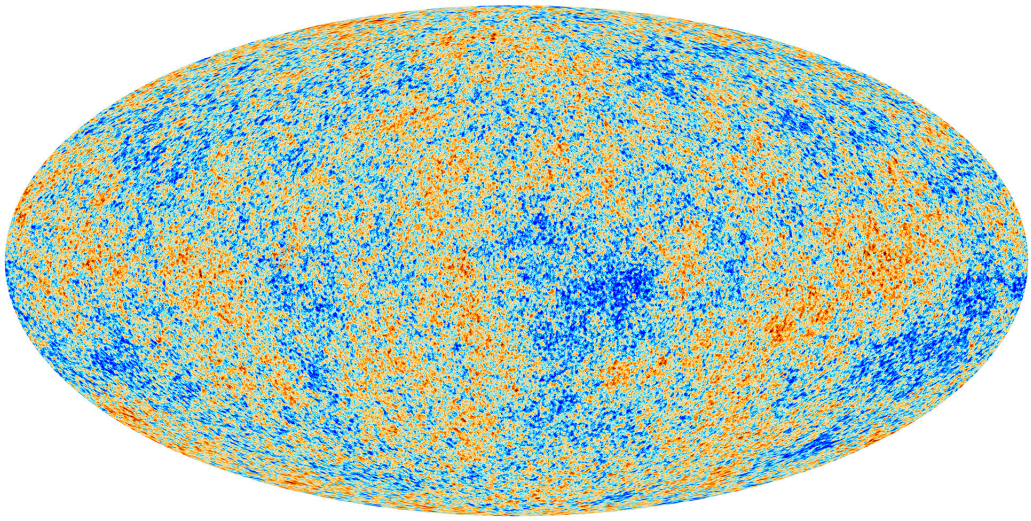

Figure 1.1: The map of the all sky CMB radiation as illustrated by the Planck collaboration, showing in detail the temperature anisotropies. The temperature difference between blue and red in the figure is a few thousandths of a Kelvin and correspond to matter density fluctuations in the distribution [14].

The anisotropies observed in the CMB can be mapped at different angular scales. These angular scales are representations of the physical size of anisotropies at the time of the last-scatter. The angular scales of the fluctuations can be parametrised as the multipole moments, l, of a spherical harmonic, which determines the wavelength, $\lambda = 180^{\circ}/l$, of the mode on the sphere of the CMB. The mapping of the different scales are given as the power spectrum of the CMB and shown in figure 1.2.

The primary anisotropies of the CMB are due to the last scattering of photons in the recombination epoch. Perturbations in the primordial plasma instigated a settling of matter into regions of over-density. The gravitational collapse lead to an increase in radiation pressure of the photon-baryon plasma, which eventually counteracted local gravitational wells, giving rise to acoustic oscillations. Photons from high-density regions at last scattering were redshifted climbing out of these potential wells. Furthermore, adiabatic fluctuations in these regions lead to an increase in temperature and velocity fluctuations within the plasma would have further resulted in Doppler shifts in frequency. The peaks observed in the power spectrum correspond, roughly, to resonances in which the photons decouple when a particular mode is at its peak amplitude.

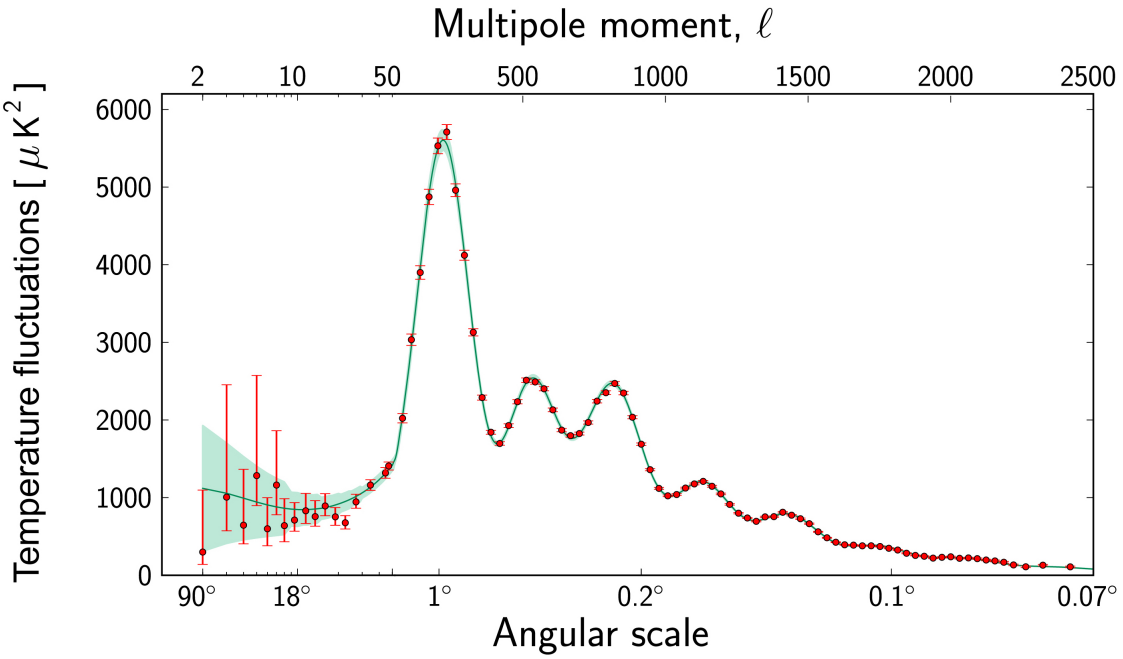

Figure 1.2: The angular power spectrum of the CMB temperature fluctuations as measured by Planck. The green line fitted onto the seven acoustic peaks is the six-parameter ΛCDM model. The shaded area around the best-fit curve represents cosmic/sample variance, including the sky cut used [7].

The ability to probe and image the very early universe via the CMB at the moment of recombination opens the way to understand, model and extract information about the contents of the early universe. The amplitudes and positions of the peaks observed in the power spectrum are dependent on the baryonic and non-baryonic matter content of the early universe, and on the geometry of space. Since light propagates along geodesics in space, and the size of the horizon at recombination can be inferred by the properties of the plasma, the geometry of space can be determined by the understanding of the the expansion history. A flat space-time corresponds to a first peak around $l \approx 220$. The higher order peaks of the spectrum can provide information on the baryonic and non-baryonic matter densities in the early universe. In particular the third peak is sensitive to the density ratio of matter to radiation. The dampening observed as l increases is due to the washing out of fluctuations initially set by inflation. The third peak however, is boosted relative to the rest, demonstrating the domination of matter in the plasma before the time of recombination and encapsulates the information present on the dark matter content of the early universe.

The power spectrum of the CMB is well described by the Lambda Cold Dark Matter (ΛCDM) model as shown in figure 1.2. ΛCDM emerged as the standard model of cosmology

in describing the evolution of the universe with its matter content [10]. In explaining and parametrising the Big Bang cosmological model, ΛCDM requires a cosmological constant, Λ, associated with the vacuum energy contribution—also known as dark energy, and the presence of ordinary and non-baryonic Cold Dark Matter (CDM). In fitting this model to the power spectrum, Planck extracts some of the density parameters defined in section 1.1.2, where $\Omega_\Lambda = 0.6847 \pm 0.0073$ and $\Omega_m = 0.3153 \pm 0.0073$ [7,15]. Furthermore, Planck extracts the baryon and cold dark matter densities from the ΛCDM model fit parameters to give $\Omega_b h^2 = 0.02237 \pm 0.00015$ and $\Omega_c h^2 = 0.1200 \pm 0.0012$. Normalising these with the the Hubble constant given in equation 1.3 results in $\Omega_b \sim 0.049$ and $\Omega_{CDM} \sim 0.265$. The information captured by the CMB and its power spectrum points towards a universe that is $\sim 68\%$ dark energy and $\sim 32\%$ matter. The non-baryonic cold dark matter further contributes to $\sim 84\%$ the total matter content of the universe.

1.2.2 Big Bang Nucleosynthesis

The radiation temperature of the universe moments after the big bang were above the MeV binding energies of nuclei and way above the KeV binding energies of atoms. Any nuclei or atom present would have quickly disintegrated into electrons, protons and neutrons. Within the first few minutes, when the temperatures dropped below nuclear binding energies, nuclear reactions lead to the formation of the very first nuclei via the process known as Big Bang Nucleosynthesis. The relative primordial abundance of isotopes such as D, ^{3}He, ^{4}He and ^{7}Li synthesised minutes after the big bang and depend on the cosmological parameters of the universe [16].

As the baryon number is conserved at and below MeV temperatures, the process of nucleosynthesis and the abundance of primordial isotopes depend on the total baryon number and thus the baryon density, Ω_b, in the early universe. The relative abundances can be measured today in places such as old stars, low mass local galaxies and the edges of distant galaxies, where a small change in primordial abundance is presumed. The primordial abundances of D, ^{3}He, ^{4}He and ^{7}Li as predicted by the standard model of Big-Bang nucleosynthesis is shown in figure 1.3. The figure shows the theoretical dependency of primordial isotopic ratios on the baryon/photon ratio, η, in the early universe and by extension on Ω_b.

Deuterium is usually entirely deployed when it is cycled into stars, and the only significant production mechanism is the process of BBN [16]. Hence, any detection of deuterium provides an upper limit on η_{10} and lower limit on the ratio of D/H. The local interstellar value of $\mathrm{D/H} = (1.56 \pm 0.40) \times 10^5$ sets a limit of $\eta_{10} < 9$ [18]. Although the η range

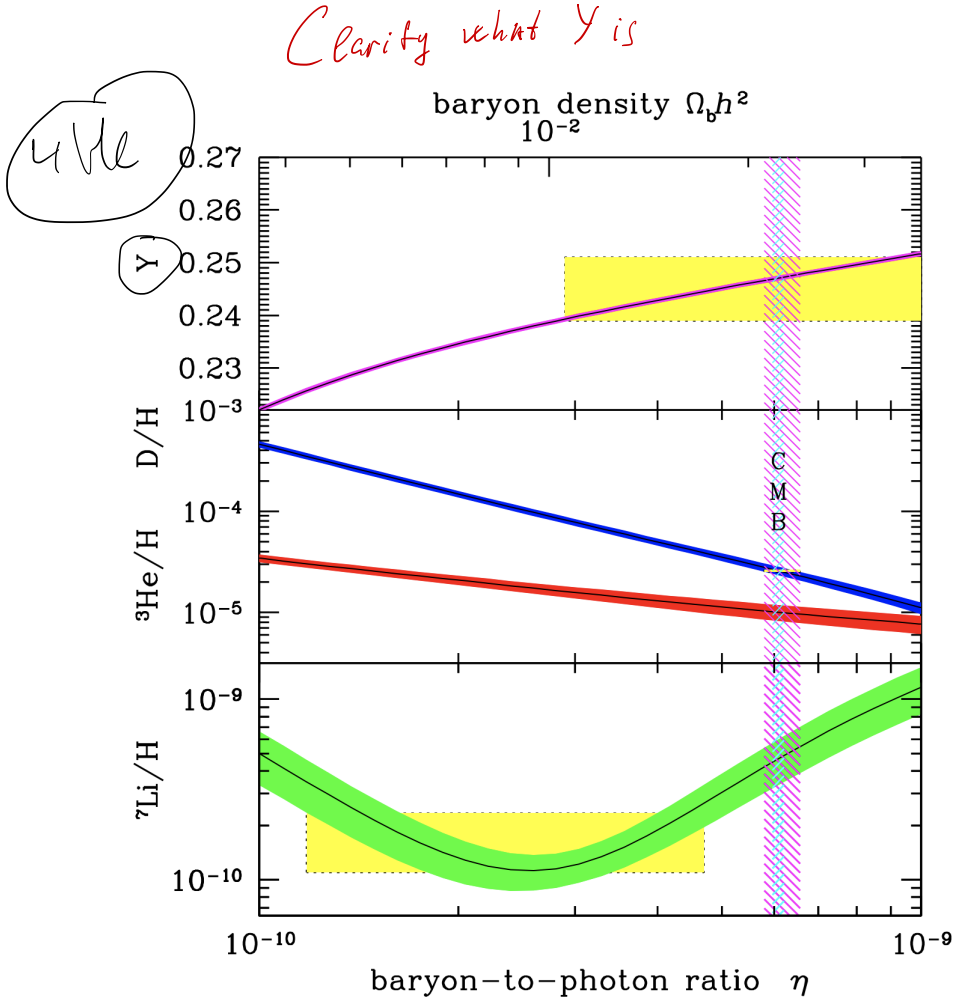

Figure 1.3: The primordial abundances of ^{4}He, D, ^{3}He, and ^{7}Li as predicted by the standard model of Big-Bang nucleosynthesis with the bands highlighting the 95% CL range. Yellow boxes indicate the observed light element abundances and the vertical band indicates the CMB measure of the cosmic baryon density [17]

.

measurements as illustrated by the boxes on figure 1.3 do not all overlap, they are all within a factor of ~ 2 from each other. In particular, the discrepancy between the lithium abundance in comparison to the D/H and less-constraining ^{4}He abundance is often referred to as the 'lithium problem' and could simply reflect the difficulty in determining the primordial lithium abundance (discussed in detail here [19]). The measured D/H and ^{4}He abundances are in great agreement when the lithium measurement is excluded due to unknown systematic. The η range extracted from the more-precise measurement of D/H gives

$$5.8 \leq \eta_{10} \leq 6.6\ (95\%\ CL), \tag{1.19}$$

which provides a measure for the baryon density of the universe in the range

$$0.021 \leq \Omega_b h^2 \leq 0.024\ (95\%\ CL). \tag{1.20}$$

Despite the lithium problem, by using only well-established microphysics, the theoretical predictions of the BBN model is in good agreement with both the observations of the D/H abundance and with the baryon density parameter obtained from the CMB by Planck. As an independent observation to that of the CMB, measurements of the primordial isotopic abundances and the BBN model suggest that luminous baryonic matter density $\Omega_{lum} \simeq \Omega_b$. This can be seen as further evidence to that obtained from the CMB power spectrum and ΛCDM, suggesting that the total matter content of the universe cannot be explained by only the presence of baryonic matter alone and the matter density parameter $\Omega_m = \Omega_b + \Omega_{CDM}$, where a substantial degree of the mass density is comprised of cold dark matter.

1.2.3 Galaxy Rotation Curves

There is considerable cosmological evidence that most of the mass content of the universe is neither luminous matter nor radiation. Luckily, mass can be detected even if the constituents of this mass is 'unseen'. The very early evidence for dark matter comes from studies in the early 1930s, where in studying galaxy cluster dynamics and applying the virial theorem to the coma cluster, Zwicky [3] noticed an unusual discrepancy between luminous mass and estimated mass, making the first claim for unseen matter in galaxies. It was not until the 1960s when Ruben and Ford showed further evidence to support Zwicky's claims by studying the rotation curves of starts in spiral galaxies [20, 21].

Galactic scale physics, such as the behaviour of stars orbiting spiral galaxy can readily be explained by Newtonian mechanics. Assuming spherical symmetry, the circular velocity, v_{circ}, of stars or hydrogen gas clouds orbiting a spiral galaxy at a distance, r, can be determined using a simple Newtonian relation

$$v_{circ} = \sqrt{\frac{GM(r)}{r}}, \tag{1.21}$$

where G is the gravitational constant and $M(r)$ is the mass of the galaxy contained within r. The relationship above can be written in a form to give the total mass encapsulated up to a specific radius $M(r)$, if the velocities of stars at a distance r can experimentally be obtained. For galaxies that are inclined to the line of sight, spectroscopic radial velocities

and radio observations of the 21 cm line of neutral hydrogen at a number of positions on the galactic disc can be used to determine and map out the velocity rotation curves of such galaxies.

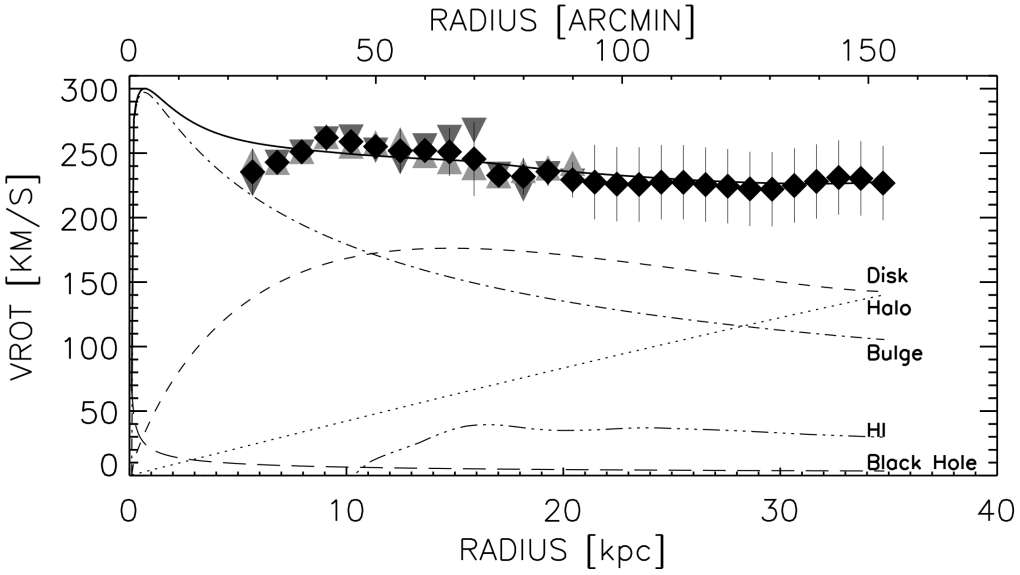

Figure 1.4: The galactic rotation curve of the Andromeda galaxy (M31) as measured by the Effelsberg and GBT 100 m telescoped. The solid black line represents best fit to data and the corresponding lines below are models illustrating the sub-contributions from the galactic disk, dark matter halo and other factors as labeled on the plot [22].

The traditional view on the mass density of spirals galaxies implied that most of the mass would be contained within the central luminous region, as observed visibly, and rotational velocities measured beyond this point would be proportional to $1/r^2$. The observations presented in figure 1.4, show the rotation curve of the Andromeda galaxy (M31). The plot suggests that rotational velocities of M31 certainly are not proportional to $1/r^2$, but rather remains fairly constant after the central bulge ($\geq$ 10kpc). The constancy of rotational velocities can be explained by the addition of a dark matter halo into galaxies. If the dark matter halo were to extend beyond the boundaries of the luminous bulge, this could explain the results of the rotation curves as shown for M31. A similar behavior seen in M31 has been observed in many other galaxies, including our own milky way [22, 23]. Unless our understanding of gravity needs modification, as proposed by MOND and other modified gravity theories (such as [24, 25]), the overwhelming data from such galaxies indicate that dark matter halos can account for a significant proportion of the mass contained within galaxies. Combining these observations with those presented in previous sections, further indicate the need for non-baryonic matter in the Universe.

1.2.4 Summary

The vast amount of observational data from different facets of cosmology and particle-astrophysics point towards a universe that is flat in geometry, and one which is comprised of dark energy, dark matter and ordinary matter—as presented in the standard model (SM) of particles. The primary evidence comes from the early universe physics encoded into the CMB, the formation of primordial isotopes as demonstrated by BBN, galaxy dynamics and rotation curves, and various other observations and realisations, such as large scale structure of the universe and the need for a form of dark matter to accommodate for the observed structure and galaxy formation [26]. In collating together our understanding of gravity, as outlined by General Relativity and the cosmological data presented, ΛCDM model of cosmology offers a framework which describes a universe with key cosmological parameters; $h_0 \sim 0.674$, $\Omega_\Lambda \sim 0.685$, $\Omega_m \sim 0.315$ and $\Omega_{CDM} \sim 0.265$. Our understanding of the particle content of the universe, as given by the SM of particle physics is insufficient in offering a candidate for the CDM content of the Universe, leaving $\sim 85\%$ of the matter content yet to be discovered.

1.3 Dark Matter & WIMPs

In an attempt to explain the discrepancy between Ω_m and Ω_B, a vast number of hypotheses have been proposed. These models predominantly fall under three categories; dark matter explained via the introduction of new particles—stemming from beyond the standard model (BSM) physics, astrophysical objects, and by questioning the fundamentals of cosmology and gravity and explaining DM by alternative gravity models. The most promising is Weakly Interacting Massive Particles (WIMPs).

1.3.1 Non-WIMP Dark Matter Candidates

Axions

The axion is a pseudo-Nambu-Goldstone boson, proposed by the Peccei–Quinn theory as an extension to the QCD Lagrangian in the SM to solve the strong Charge-Parity (CP) problem [27]. The QCD Lagrangian is given as

$$\mathcal{L}_{QCD} = -\frac{1}{4} G^a_{\mu\nu} G^{a\mu\nu} + \sum_{n}^{j=1} \left[\bar{q}_j \gamma^\mu i D_\mu q_j - (m_j q^\dagger_{Lj} q_{Rj} + h.c.) \right] + \frac{\theta g^2}{32\pi^2} G^a_{\mu\nu} \tilde{G}^{a\mu\nu}, \quad (1.22)$$

where the CP violating term $\mathcal{L}_\theta = \bar{\theta}(\alpha_s/8\pi)G^a_{\mu\nu}\tilde{G}^{a\mu\nu}$, in which $-\pi \leq \bar{\theta} \leq +\pi$ is the effective $\bar{\theta}$ parameter after diagonalising quark masses. Although the last term of the Lagrangian does not contribute in perturbation theory, it does however contribute through non-pertubative effects, associated with QCD instantons [28]. The QCD Lagrangian contains terms that may lead to CP violation in scenario where none of the quark masses vanish, leading to a non-zero θ dependence [29, 30]. If $\bar{\theta} \neq 0$, then QCD violates both Parity (P) and CP symmetry. However, the presence of CP violation in QCD leads to an electric dipole moment (EDM) of the neutron. The experimental bounds placed by neutron EDM experiments currently suggest an absence of CP violation in strong interactions, yielding an upper limit of $\bar{\theta} \leq 10^{-10}$, where $\bar{\theta} = \mathcal{O}(1)$ is otherwise completely satisfactory [31]. The question then is: given that $\bar{\theta}$ can take any value between $-\pi$ and π, why is $\bar{\theta}$ so close to zero? This presents a naturalness problem for SM, where the fine-tuning required here is presented as the strong CP problem of QCD.

The spontaneously broken global Peccei-Quinn $U_{PQ}(1)$ symmetry was introduced to solve the strong CP problem [27]. The axion is the pseudo-Nambu-Goldstone boson associated with the spontaneous breaking of the $U_{PQ}(1)$ symmetry. This symmetry is broken due to the anomalous triangle coupling of the axions to the gluons,

$$\mathcal{L}_\theta = \left(\frac{\phi_A}{f_A} - \bar{\theta}\right)\frac{\alpha_s}{8\pi}G^a_{\mu\nu}\tilde{G}^{a\mu\nu}, \tag{1.23}$$

where ϕ_A is the axion field and $f_A = v_a N$ the axion decay constant; v_a is the vacuum expectation value of the spontaneously broken $U_{PQ}(1)$ and N is an integer normalisation factor expressing the colour anomaly of $U_{PQ}(1)$. The introduction of this new symmetry results in the induction of a potential ϕ_A from the non-perturbative fluctuations of the gluon fields, whose minimum is at $\phi_A = \bar{\theta} f_A$, thereby canceling the $\bar{\theta}$ terms in the QCD Lagrangian and restoring CP symmetry.

The nature of axions in interacting with fermions, gluons and photons at loop level lead to a rich experimental approach in looking for these particles and placing bounds on their mass. Although most of these bounds place axion at a sub-eV mass scale, axions are non-baryonic and non-relativistic, as cold populations are produced out of equilibrium at the time of $U_{PQ}(1)$ symmetry breaking in the early universe; hence satisfying two major conditions for CDM and may well contribute towards the dark matter burden of the universe. In searching for axions in the plausible CDM mass range, galactic halo axions may be detected via a resonant conversion into monochromatic microwave signal in a high-Q electromagnetic cavity [32]. The Axion Dark Matter Experiment (ADMX),

utilises this approach to probe the axion mass range of 10^{-6} to 10^{-2}eV [33]. All such searches have yielded in upper bounds and as of yet, no positive signal has been observed.

Standard Model & Sterile Neutrinos

The implementation of neutrinos in the formulation of the SM of particle physics, meant that the neutrinos were massless as a consequence of gauge invariance and the renormalisability of the theory. Moreover, the lepton numbers associated with the three flavour generations, e, μ and τ are separately conserved. However, results from solar and atmospheric neutrino oscillation experiments have concluded that neutrinos of different flavours mix with each other, indicating a positive mass-squared difference between the three neutrino flavours (for a review see [34]), providing significant evidence in flavour physics beyond the SM.

The massive nature of neutrinos along with the fact that they are neutral in charge, make them a suitable candidate within the confinements of the standard model. The original assumptions with three massless, relativistic, neutrino species that obey Fermi-Dirac statistics suggested that neutrinos will add a contribution to Ω_r, however, the recent developments in neutrino mass means that Ω_m should contain a neutrino density parameter Ω_ν. The neutrino density parameter for neutrinos in the mass range of 5×10^{-4} eV to 1 meV is predicted as [35]

$$\Omega_\nu h^2 = \frac{\sum m_\nu}{94eV}. \tag{1.24}$$

Although cosmological observation can tightly constrain the absolute neutrino mass scale of neutrinos [36], these limits are highly model dependent. The most direct constraint with limited model dependence comes from the KATRIN experiment, which aims to measure the mass of the anti-electron neutrino from examining the spectrum of electrons emitted from the beta decay of tritium [37]. From their latest run, the KATRIN experiment has set an upper limit of 1.1 eV (90% CL) on the absolute mass scale of neutrinos [38]. Using such upper limits on the absolute neutrino mass scale and the equation prided for Ω_{nu}, it becomes evident that although massive neutrinos will contribute towards Ω_m; Ω_ν is much less than Ω_m, hence does not provide a solution to the dark matter problem.

A way of explaining the massive nature of neutrinos is through assuming a new unseen particle. Being the only neutral fermions in the SM with respect to all conserved charges, namely electric and colour, they can possess a Majorana nature in which mass can arise through a seesaw mechanism (for a review see [39]). Although inconclusive, recent

too strong of a statement

findings of anomalies in short-baseline neutrino oscillation experiments indicate the presence of an additional neutrino that mixes with ordinary active states, eluding the existence of such neutral particles [40, 41]. It is evident that there is fundamental gap in our understanding of neutrinos, and sterile neutrinos with the current limited theoretical understanding could still serve as the simplest model that can accommodate a viable non-baryonic dark matter candidate [42].

1.3.2 WIMP Dark Matter

A well motivated class of candidates for non-baryonic cold dark matter is Weakly Interacting Massive Particles (WIMPs). A WIMP would broadly be a new fundamental particle beyond the standard model, coupling weakly to standard model particles via the weak nuclear force or some other unknown force carrier, and interacting via the gravitational force. The main motivation for WIMPs as dark matter candidates stem from early Universe physics, where WIMPs in chemical equilibrium naturally result in the right abundance to fully account for Ω_{CDM}. Furthermore, the interactions that give rise to the right WIMP density allows for a viable means to test the WIMP hypothesis through detection.

Motivation for WIMPs

In the early universe just after inflation, all particles are assumed to have existed in a thermal plasma. WIMPs in the standard scenario are assumed to be produced as the bi-product of the early collisions between particles in this radiation-dominated era. Some of the important reactions that took place in this era would have been the production and the annihilation of WIMP pairs ($\chi\bar{\chi}$) in particle-antiparticle collisions to produce some of the SM particles, such as e^+e^-, $\mu^+\mu^-$, $q\bar{q}$, W^+W^-, ZZ, HH, etc. The production of WIMPs from particle collisions in the plasma and the inverse reaction that converted WIMPs to SM particles were initially in thermal equilibrium as the temperatures were much higher than the WIMP mass, $T \gg m_\chi$. This resulted in a common rate for both of these processes, given by

$$\Gamma_A = \langle \sigma_A v \rangle n_\chi^{eq}, \tag{1.25}$$

where σ_A is annihilation cross-section, v is the relative velocity and n_χ^{eq} is the number density in chemical equilibrium of the WIMP particles. The angle brackets represent the averaged WIMP thermal distribution.

The corresponding Boltzmann equation for a particle species of number density, n, is given by [43]

$$\frac{dn_\chi}{dt} = -3Hn_\chi - \langle\sigma_A v\rangle(n_\chi^2 - n_\chi^{2\,eq}), \tag{1.26}$$

where H is the Hubble constant as discussed in section 1.1.2. The terms on the right hand side of equation 1.26 take into account the expansion rate of the universe and the change in number density due to the annihilation and the production of WIMPs, respectively. The expansion of the universe in this era reduced the temperature of the plasma below the WIMP mass. While annihilation and production processes remained in equilibrium, the expansion exponentially decreased the number of WIMPs produced, as dictated by the Boltzmann factor, $e^{-m_\chi/T}$. Since the temperature of the plasma dropped below the WIMP mass, only those particle collisions in the tail of the Boltzmann distribution lead to the production of WIMP pairs.

As the universe expanded, this decreased the number density of particles n_χ and as a result, the WIMP annihilation rate, Γ_A, became smaller than the expansion rate, H, of the universe. This lead to the ceasing of WIMP-producing collisions, effectively locking in the total number of WIMPs in the comoving volume to an approximate constant. To map out the transition from an equilibrium scenario where the temperature of the plasma is $T > m_\chi$ to that which $T < m_\chi$ and calculate the WIMP relic density of the universe, equation 1.26 can be combined with the equation of law of entropy conservation, given as [44]

$$\frac{ds}{dt} = -3Hs, \tag{1.27}$$

where s is the entropy density and H is the Hubble parameter from equation 1.26. Substituting in $Y = n_\chi/s$ and $x = m_\chi/T$ and combining the two equations above gives [44],

$$\frac{dY}{dx} = \frac{1}{3H}\frac{ds}{dx}\langle\sigma_{ann}v\rangle(Y^2 - Y_{eq}^2). \tag{1.28}$$

Using the Hubble parameter as defined in the Friedmann equations by the mass-energy density ρ, and the energy and entropy densities as related to the photon temperature by the equations [44],

$$\rho = \frac{\pi^2}{30}g_{eff}(T)T^4, \quad s = \frac{2\pi^2}{45}h_{eff}(T)T^3, \tag{1.29}$$

$$g_*^{1/2} = \frac{h_{eff}}{g_{eff}^{1/2}} \left(1 + \frac{T}{3h_{eff}} \frac{dh_{eff}}{dT}\right). \tag{1.30}$$

where g_{eff} and h_{eff} are the effective degrees of freedom for the energy density and the entropy density respectively. Equation 1.31 then takes the form,

$$\frac{dY}{dx} = -\left(\frac{45}{\pi M_P^2}\right)^{-1/2} \frac{g_*^{1/2} m_\chi}{x^2} \langle \sigma_A v \rangle (Y^2 - Y_{eq}^2). \tag{1.31}$$

where, $M_P^2 = 1.22 \times 10^{19}$ GeV is the Planck Mass from the Hubble parameter. The evolution of WIMP density with time and its dependence on cross-section can be extracted by numerically solving the equation above to give the outcome in figure 1.5.

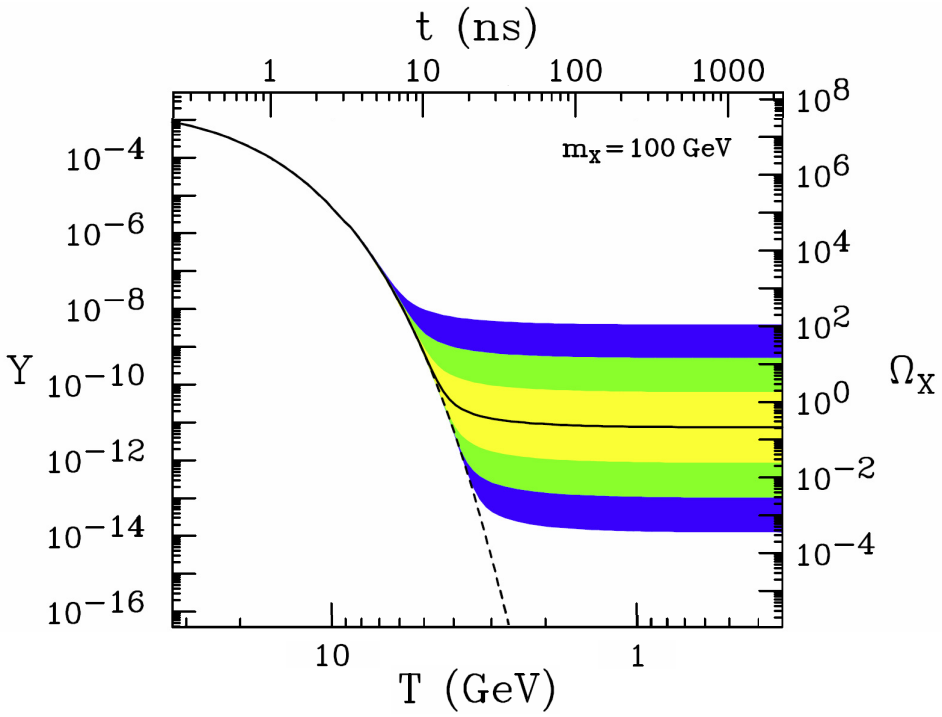

Figure 1.5: The plot represents the change in WIMP yield Y as a result of the temperature T in the early universe, which is equivalent to time t, governing the rate of expansion. The yellow, green and blue shaded regions represent the impact of changing the cross-section by a factor of 10, 10^2 and 10^3 respectively [45].

As shown in the figure above, as the temperature approaches the freeze-out temperature, T_{fo}—the point in which WIMPs are chemically decoupled—the annihilation rate becomes of the order of the Hubble expansion rate and the WIMP production becomes negligible, bringing the WIMP abundance per comoving volume to a constant value. The freeze-out temperature can be generalised as $T_{fo} \simeq m_\chi/20$ for varying WIMP masses and the

velocity at which this freeze-out is reached calculated by $v_{fo} = (3T_{fo}/2m_{\chi})^{1/2} \simeq 0.27c$. The WIMP relic density, as illustrated above, is inversely proportional to the annihilation cross-section and is independent of the WIMP mass. Smaller annihilation cross-sections lead to a larger relic density. Remarkably, an annihilation cross-section of an order of magnitude lower than that of the weak force will allow the relic density to match the current value of Ω_{CDM} as stated from cosmological observations. This rather unexpected connection between particle physics and cosmology has been commonly referred to as the "WIMP miracle".

WIMP Candidates

One of the most favoured candidates for a WIMP comes from a Supersymmetry (SUSY) model called the Minimal Super-symmetric Standard Model (MSSM). MSSM is an extension of the Standard Model that introduces a new global symmetry between fermions and bosons. As well as containing all of the known fields of the standard model, the theory requires partners to form supersymmetric multiplets. These partners are associated as a "superpartner" for each particle of the Standard Model, which has the same internal quantum number apart from spin that differs by one half. Hence, every boson has a supersymmetric fermion partner while every fermion has a boson superpartner.

The most important ingredient for supersymmetric dark matter is the newly defined global symmetric of SUSY called R-parity, expressed as [35],

$$R = (-1)^{3(B-L)+2S} \tag{1.32}$$

where B, L are the baryon and lepton number operators and S is the spin. The R parity in this model produces the Standard Model particles for $R = +1$ and their supersymmetric partners for $R = -1$. The conservation of this new symmetry dictates that there must always be two SUSY particles in the vertices that contain them and annihilation or creation can occur only within pairs. If R parity is broken, there are no special rules to present the supersymmetric partners to decay with masses of order few GeV or larger. This leads to the decay of heavier SUSY particles into lighter ones until they are locked in as a Lightest Supersymmetric Particle (LSP), which cannot decay further due to the conservation of energy. Thus, the LSP is stable, and its neutrally charged colourless nature makes it an ideal candidate for dark matter.

At low energies, there are four neutralinos that are fermions and are electrically neutral, the lightest neutralino ($\tilde{\chi}_1^0$) is stable in an R-parity conserved scenario of MSSM and the search for neutralinos are of interest in many accelerator searches [46]. Having been created in the early universe along with other SUSY particles, neutralinos are believed to exist in abundance to account for the missing matter content of the universe and hence are good candidate for WIMP dark matter.

1.4 Detection of WIMP Dark Matter

The phenomenological landscape of particle dark matter gives rise to many candidates, some of which are mentioned in section 1.4. This translates to a vast range of experimental techniques and methodologies in searching for these dark matter candidates, predominantly governed by the interaction mechanics of the proposed candidates. The nature of WIMP dark matter as postulated in section 1.3.2 provides three search avenues: direct detection, indirect detection and production. Focus of many indirect searches are geared towards detecting annihilation events of dark matter candidates in galaxies, such as gamma rays, neutrinos, positrons, or anti-protons. Particle collider searches are aimed at producing dark matter via SM collisions and looking for missing transverse energy event topologies, as dark matter particles are expected to leave the detector undetected. The main topic of this section however is the direct detection of galactic dark matter particles that are present in the Milky Way galaxy.

1.4.1 Local WIMP Halo Kinematics

Local WIMP Density

The density and distribution of dark matter in the Milky Way provide critical information on the dynamics of our galaxy and are particularly important for both direct and indirect dark matter searches. The local WIMP density, ρ_0, is an average over a volume of few hundred parsecs around the solar radius $R_o = (8.0 \pm 0.5)$ kpc [47]. The differential event rate is directly proportional to the expected density, hence any observational uncertainty in ρ_0 translates into an uncertainty in the event rate and the inferred constraints on the measured scattering cross-section.

The exclusion limits calculated by many direct detection experiments use a canonical local WIMP density of $\rho_0 = 0.3$ GeV cm^{-3} to allow for easy comparison between different results. Although the estimations of this parameter has fluctuated over the past few

decades, most estimates are of order two in agreement with one another [48]. Some of the more recent calculations using the second data release from the Gaia space mission [49] place the DM density at around $\rho_0 \simeq 0.47$ GeV cm^{-3}, highlighting the sensitivity of this parameter on the methodology and the data-sets used in determining the local density [50].

WIMP Velocity Distribution

Another quantity from the phase space distribution of DM that impacts the constraints on dark matter mass models of the Milky Way are the local circular speed, v_c, and the escape velocity, v_{esc}. The conventional approach used in calculating exclusion limits on signals, assumes an isotropic, spherically symmetric Maxwellian velocity distribution, known as the Standard Halo Model (SHM) and is given by,

$$f(\boldsymbol{v}) = \frac{1}{(2\pi\sigma^2)^{1/2}} \exp\left(-\frac{|\boldsymbol{v}|^2}{2\sigma^2}\right), \tag{1.33}$$

where the speed dispersion is related to the local circular speed by $\sigma = v_c\sqrt{3/2}$. The local circular speed is the measure of the Sun's velocity with respect to the center of our galaxy and is usually measured with respect to objects assumed to be at rest with the center [51]. These methods yield velocities of $v_c = [218, 246]$ km s^{-1} with the canonical taken as $v_c = 220$ km s^{-1}, yielding a standard deviation $\sigma \simeq 270$ km s^{-1} [52]. The local escape velocity of the galaxy has been calculated by sampling high velocity stars from the RAVE survey to be $v_{esc} = 544$ km s^{-1} [53].

In order to fully understand and map out the kinematics of the WIMP distribution as observed by a detector on earth, one has to also take into account the WIMP velocity distribution in the rest frame of the detector. This is achieved by carrying out a time-dependent Galilean transformation, where,

$$\boldsymbol{v} \to \tilde{\boldsymbol{v}} = \boldsymbol{v} + \boldsymbol{v}_E(t). \tag{1.34}$$

The velocity contributions from earths motion relative to the galactic rest frame, $\boldsymbol{v}_E(t)$, is a time dependent contribution to the overall velocity distributions with three sub-components: motion of the local standard of rest (LSP), given as $(0, v_c, 0)$ km s^{-1} for an axi-symmetric Milk Way; the Sun's peculiar motion with respect to the LSP, determined by observing motions of stars in the solar neighbourhood and is $\sim (10, 5.2, 7.2)$ km s^{-1} [54];

and the Earth's orbit about the Sun, $v_E = 29.8$ km s^{-1}, provided the ellipticity of the Earth's orbit and the non-uniform motion of the Sun is ignored.

Although these contributions all play a role in the signal models of direct detection experiments, the main characteristics of the WIMP signal can accurately be modeled by using only the motion of LSP. The other variables become important for time-dependent searches. Furthermore, in a scenario in which DM is observed by direct detection experiment, the accuracy and precision of the DM distribution and kinematics on Earth will require further investigation.

1.4.2 WIMP-Nucleon Scattering

Provided that the Milky Way is populated by a WIMP dark matter halo as detailed in section 1.4.1, then the WIMP flux on Earth is of the order $(100\ \text{GeV/m}_\chi) \times 10^5\ \text{cm}^{-2}\text{s}^{-1}$. Even though WIMPs are postulated to interact only weakly with SM particles, the WIMP flux as dictated by the WIMP halo is sufficiently large enough for a potential detection of a small faction of these particles, as they elastically scatter off of atomic nuclei. Many direct detection experiments aim to detect the recoils of WIMPs via their nuclear recoil, and measure the rate, R, along with the energies, E_R, of these recoils to determine the nature of dark matter (as proposed in [55]).

The differential event rate of WIMPs with masses m_χ, scattering off of atomic nucleus with mass m_N, usually expressed in terms of counts kg^{-1} days^{-1} keV^{-1} (often referred to as dru), is given by [44],

$$\frac{dR}{dE_R} = \frac{\rho_0}{m_N m_\chi} \int_{v_{min}}^{\infty} v f(\boldsymbol{v}, t) \frac{d\sigma_{WN}}{dE_R}(v, E_R)\, dv, \tag{1.35}$$

where ρ_0 is the local WIMP density, $f(v)$ is the WIMP velocity distribution in the detector frame and $\frac{d\sigma_{WN}}{dE_R}(v, E_R)$ is the WIMP-nucleus elastic scattering differential cross-section. The relative speed at which the scattering takes place is of the order 100 km^{-1} s^{-}1, hence the WIMP-nucleus scattering occurs in a non-relativistic limit and results in recoil energies that are characterised in the center of mass frame, θ^*,

$$E_R = \frac{\mu_N^2 v^2 (1 - cos(\theta^*))}{m_N}, \tag{1.36}$$

where the reduced WIMP-nucleus mass is given by $\mu_N = m_\chi m_N/(m_\chi + m + N)$. The total event rate given as per kilogram per day in a typical detector can then be calculated

by integrating equation 1.37 between the limits of the smallest recoil energy—resulting from the minimum WIMP speed, $v_{min} = \sqrt{(m_N E_R)/(2\mu_N^2)}$—and infinity, resulting in,

$$R = \int_{E_T}^{\infty} \frac{\rho_0}{m_N m_\chi} \int_{v_{min}}^{\infty} v f(\boldsymbol{v}, t) \frac{d\sigma_{WN}}{dE_R}(v, E_R)\, dv, \tag{1.37}$$

where E_T is the threshold energy as a result of the smallest recoil. Its important to note that in practice, most detectors will have a detector specific threshold which is almost always greater than the minimum detectable recoil.

The particle physics and the interaction properties of the WIMP-nucleus scattering is encoded into the differential cross-section as part of the equation above. This is often calculated from the effective Lagrangian describing the interaction of the particular WIMP model with the quarks and the gluons in the nucleus. The hadronic matrix elements that entail the quark-gluon content of the nucleus is usually a large source of uncertainty. The WIMP-nucleus differential cross-section can further be represented as a two part differential, entailing the spin-dependent (SD) and the spin-independent (SI) contributions from the nucleus and by encoding the form factor, $F(E_R)$, that depends on the momentum transfer, $q = \sqrt{2 m_N E_R}$, and accounts for the suppression caused by the coherence loss for event rates of heavier nucleus or WIMPs. The generalised form of the WIMP-nucleus scattering cross-section is given by

$$\frac{dR}{dE_R} = \frac{m_N}{2\mu_N^2 v^2} \left(\sigma_0^{SD} F_{SD}^2(E_R) + \sigma_0^{SI} F_{SI}^2(E_R) \right), \tag{1.38}$$

where $\sigma_0^{SD/SI}$ represents the spin-dependent and spin-independent cross-sections at zero momentum transfer.

The difference between the spin-dependent and -independent processes are best understood by examining the WIMP-quark interactions at the Lagrangian level. The contributions that arise from the spin-dependent interactions are due to the axial-vector couplings, whereas the spin-independent contributions are from scalar and vector couplings to quarks.

Spin-dependent Scattering

The spin-dependent contribution to the WIMP-nucleus differential cross-section arises from coupling of the WIMP field to the quark axial-vector current, $\bar{q}\gamma^\mu\gamma_5 q$ [35]. If for example the WIMP is a Majorana or Dirac fermion, such as the lightest neutralino in MSSM, the Lagrangian for the WIMP-nucleon axial-vector interaction can be represented

as

$$\mathcal{L}_A \supset \alpha_q^A(\bar{\chi}\gamma^\mu\gamma_5\chi)(\bar{q}\gamma_\mu\gamma_5 q). \tag{1.39}$$

The resultant spin-dependent WIMP-nucleus differential cross-section can be represented by taking into account the contribution of different quarks of the quark spin matrix elements to the angular momentum, that is related to the matrix elements of the axial-vector current in the nucleus and the total angular momentum $\boldsymbol{J}$ of the nucleus, to give

$$\left(\frac{d\sigma_{WN}}{dE_R}\right)_{SD} = \frac{16m_N}{\pi v^2}\Lambda^2 G_F^2 J(J+1)\frac{S(E_R)}{S(0)}. \tag{1.40}$$

where G_F is the Fermi constant, $\boldsymbol{J}$, is total angular momentum of the nucleus, and Λ is a quantity that represents the product of the contributions from different quarks of the proton, a_p, and the neutron, a_n, and the expectation value of the spin content of the proton or the neutron group in the nucleus, $\langle S_{p,n}\rangle$. Λ is given as

$$\Lambda = \frac{1}{J}[a_p\langle S_p\rangle + a_n\langle S_n\rangle], \tag{1.41}$$

where a_p and a_n is,

$$a_p = \sum_{q=u,d,s}\frac{\alpha_q^A}{G_F\sqrt{2}}\Delta_q^p; \quad a_n = \sum_{q=u,d,s}\frac{\alpha_q^A}{G_F\sqrt{2}}\Delta_q^n, \tag{1.42}$$

where the quantities $\Delta_q^{p,n}$ are related to the matrix element of the axial-vector current of the nucleon ($\langle n|\bar{q}\gamma_\mu\gamma_5 q|n\rangle = 2s_\mu^n$); s_μ is the spin of the nucleon, and $\Delta_q^{p,n}$ are values obtained using experimental data on lepton-proton scattering or simple nuclear models.

The exact coupling of WIMPs to protons or neutrons is not known, and although in reality there are probably contributions from the two types, it is standard to consider *proton-only* and *neutron-only* interactions separately. Consequently, heavy isotopes with an odd number of neutrons will have in general a much larger SD sensitivity to the WIMP-neutron channel.

Spin-independent Scattering

The spin-independent contribution to the WIMP-nucleus differential cross-section arises from coupling of the WIMP field to the scalar-scalar and vector-vector currents in the

Lagrangian,

$$\mathcal{L}_{SV} \supset \alpha_q^S \bar{\chi}\chi\bar{q}q \; + \; \alpha_q^V \bar{\chi}\gamma_\mu\chi\bar{q}\gamma^\mu q. \tag{1.43}$$

Under the assumption of a neutralino WIMP, the neutralino-nucleon scattering will have contributions from the squarks and the Higgs exchange [35]. By taking into account the contributions of the scalar-scalar and vector-vector interactions and the resultant matrix elements, the generalised spin-independent WIMP-nucleus scattering with both scalar and vector interactions would read,

$$\left(\frac{d\sigma_{WN}}{dE_R}\right)_{SI} = \frac{2m_N}{\pi v^2}\left[[Zf^p + (A \not\frown Z)f^n]^2 + \frac{B_N^2}{256}\right] F^2(E_R). \tag{1.44}$$

where Z is the number of protons, $(A-Z)$ is the number of neutrons, f_p and fn are the effective WIMP-proton and WIMP-neutron couplings, and $F^2(E_R)$ is the nuclear form factor for coherent interactions and is understood as a Fourier transformation of the nucleon density and is usually parameterized in terms of the momentum transfer [56]. The individual contributions from the scalar and vector couplings to the cross-section are given by,

$$\sigma_{S,0} = \frac{4\mu_N^2}{\pi}[Zf^p + (A-Z)f^N]^2, \tag{1.45}$$

$$\sigma_{V,0} = \frac{mu_N^2 B_N^2}{64\pi}, \tag{1.46}$$

with,

$$B_N^2 \equiv \alpha_u^V(A+Z) + \alpha_d^V(A-Z), \tag{1.47}$$

representing the contributions of the valence quarks.

In most instances, the WIMP coupling to the neutrons and protons is approximately equal, where $f_n \approx f_p$, and thus the spin-independent contribution scales as the square of the number of nucleons, A^2, whereas the spin-dependent contribution is proportional to the nuclear angular momentum, $(J+1)/J$. Due to the much larger enhancement from A^2, the spin-independent searches for heavier targets such as germanium, iodide or xenon, where $A > 20$, dominate the the SUSY parameter space.

1.4.3 Direct Detection Searches

The fundamental principle behind direct detection experiments is to design an experiment that has the potential to detect the recoiling of dark matter particles that transverse through the Earth, as the Earth travels through the dark matter halo present in our galaxy. These searches rely on a non-zero weak interaction between WIMPs and nuclei present in the detector volume. The main modes of detecting such a recoil signal lies in the ability of the detector to detect either the scintillation, ionisation or heat (phonons) that dissipates into the detection volume as a result of a WIMP-nucleus interaction. Ever since its proposal [55], there has been many experimental concepts developed using different target nuclei and detection techniques to probe for WIMP dark matter.

The recoil energies expected from WIMPs as specified in section 1.36 is $\mathcal{O}(10 - 100\ \text{keV})$ and the expected rates in a typical detection volume for a WIMP mass of $\sim 100\ \text{GeV/c}^2$ is $\leq 1\ \text{event}\,\text{kg}^{-1}\,\text{year}^{-1}$ [57]. To overcome the difficulty of detecting such event rate, many experiments aim to build detectors at ultra-low background levels, especially in regions of energy-space that overlay a WIMP signal; and often, install the detectors in deep underground facilities. To detect recoil energies at keV-scale or below, a combination of signals are often used in reconstructing the energy deposition from a recoil medium, i.e. scintillation light and ionisation, or other combinations. Such an approach can allow for experiments to distinguish between different interactions, such as electron recoils (ER) and nuclear recoils (NR) and improve 3D position reconstruction of events; all of which can be used to reduce background rates to lower levels.

Sodium-Iodide & Cryogenic Detectors

A popular avenue for dark matter detection has been the use of thallium-doped sodium iodide (NaI(TI)) crystals. Experiments such as DAMA/LIBRA make use of such crystals to avoid background discrimination by modelling and observing the expected annual modulation of dark matter due to Earth's motion around the Sun [58,59]. To the surprise of the community, they have been detecting an annual modulation at $\sim 12\sigma$, claiming this to be a dark matter signature. Its important to note that this signature has not been seen in other dark matter experiments that has probed much more of the signal space of a possible WIMP signature. Experiments such as COSINE-100 [60] and SABRA [61] are building detectors with similar detection technology to probe the DAMA/LIBRA discovery claim and conclude the saga once and for all.

Cryogenic detectors operating at near-zero kelvin temperatures EDELWEISS [62], CDMS [63] and CRESST [64] can use a different combination of signal channels to achieve event-by-event discrimination between nuclear and electron recoils. The EDELWEISS and CDMS experiments extract the ionisation and phonons produced in an interaction site, while the CRESST experiment relies on scintillation and phonons. One of the downfalls of such experiments is to grow radio-pure crystals at much larger scales, limiting their ability to probe dark matter at ever-more sensitive cross-sections, but are capable at probing WIMP masses at much lower energies by reducing their energy thresholds to sub-keV regimes, as demonstrated by the CRESST-III experiment [65].

Liquid Noble Gas Detectors

The history of liquid noble gases as a media for scintillation in search for galactic dark matter spans across several decades. Over this period, the experiments in this domain have narrowed their speciality in focusing on liquid -xenon (LXe) and -argon (LAr), as primary media for detecting scintillation and ionisation from particle interactions. The ability to detect both scintillation and ionisation is a unique feature of these liquids, in comparison to various other detection media. The capacity to scale-up to large mass with relatively trivial technology, has made LXe and LAr popular targets for dark matter, solar neutrino and neutrinoless double beta decay experiments.

The advantage of using LXe and LAr as a detection media lies on their ability to scintillate in the vacuum ultraviolet (VUV) at $\sim$178 nm and $\sim$128 nm, respectively, making it relatively easy to detect such photons using photo-multiplier tubes (PMTs). The first noble gas detectors ran primary as single-phase detectors, making use of only the scintillation photons produced from interaction sites. Some of these experiments include the single-phase LXe ZEPLIN-I [66] and XMASS [67] experiments, and the single-phase LAr DEAP/CLEAN [68] experiment. Although, running singe-phase experiments simplify detector design, they come at a cost of scientific performance. For LXe, this is primarily in the reduction of discrimination power between ER and NR events, as the ionisation signal can serve as a way to distinguish these two event types. Furthermore, both LXe and LAr will endure more background leakage as a result of worst position reconstruction, as the outer edges of the liquid-scintillator usually serve as a self-shielding layer for backgrounds coming off of the TPC and detector walls.

To overcome some of these limitations, dark matter searches with LXe detectors progressed towards dual-phase LXe time-projection chambers (TPCs). Experiments such as ZEPLIN-II/III [69,70], XENON [71] and PandaX [72] used dual-phase chambers to extract both the

LUX should be mentioned?

scintillation (S1) and ionisation (S2) signals by the use of electric-fields. The scintillation photons were detected using PMTs and the ionisation electrons were drifted towards the surface of the LXe and extracted through a gas-phase to generate S2 photons through electroluminescence. This technique allowed for much better ER/NR discrimination and 3D position reconstruction, reducing backgrounds leaking into the WIMP nuclear recoil signal region from both ERs and wall backgrounds, by precisely fiducialising the active LXe region into a virtual central detection region of lower background, effectively rejecting the background dominated regions of the LXe. Some of the leading exclusion limits in the search for SI-WIMP-nucleon cross-section are shown in figure 1.6. These experiments can effectively probe WIMP masses spanning a range of $\mathcal{O}(1 - 1000\ \mathrm{GeV/c^2})$. Limitations at low-masses are usually due to the S1 signal thresholds, where at least a single-photon S1 has to coincide with an S2 signal. At these low recoil energies, coincidence backgrounds due to PMT dark-count rates usually dominate and hence thresholds are usually set higher.

The latest results from the XENON1T [73] experiment are now the most stringent limits set for the spin independent WIMP dark matter, proceeding the PandaX-II [74] and LUX [75]; demonstrating the effectiveness of this technology. The XENON collaboration are now in the process of upgrading their detector, aiming to probe down the WIMP parameter space with a larger detector, XENONnT [76]. The ZEPLIN and LUX collaborations have now formed a larger collaboration, the LUX-ZEPLIN (LZ) collaboration, to build their next-generation dual-phase LXe detector, holding a total of 10 tonnes of LXe and aiming to begin operations in late 2020. The next chapter will outline the design and operational conditions of the LZ experiment, located in the Davis Cavern of the Sanford Underground Research Facility (Lead, South Dakota).

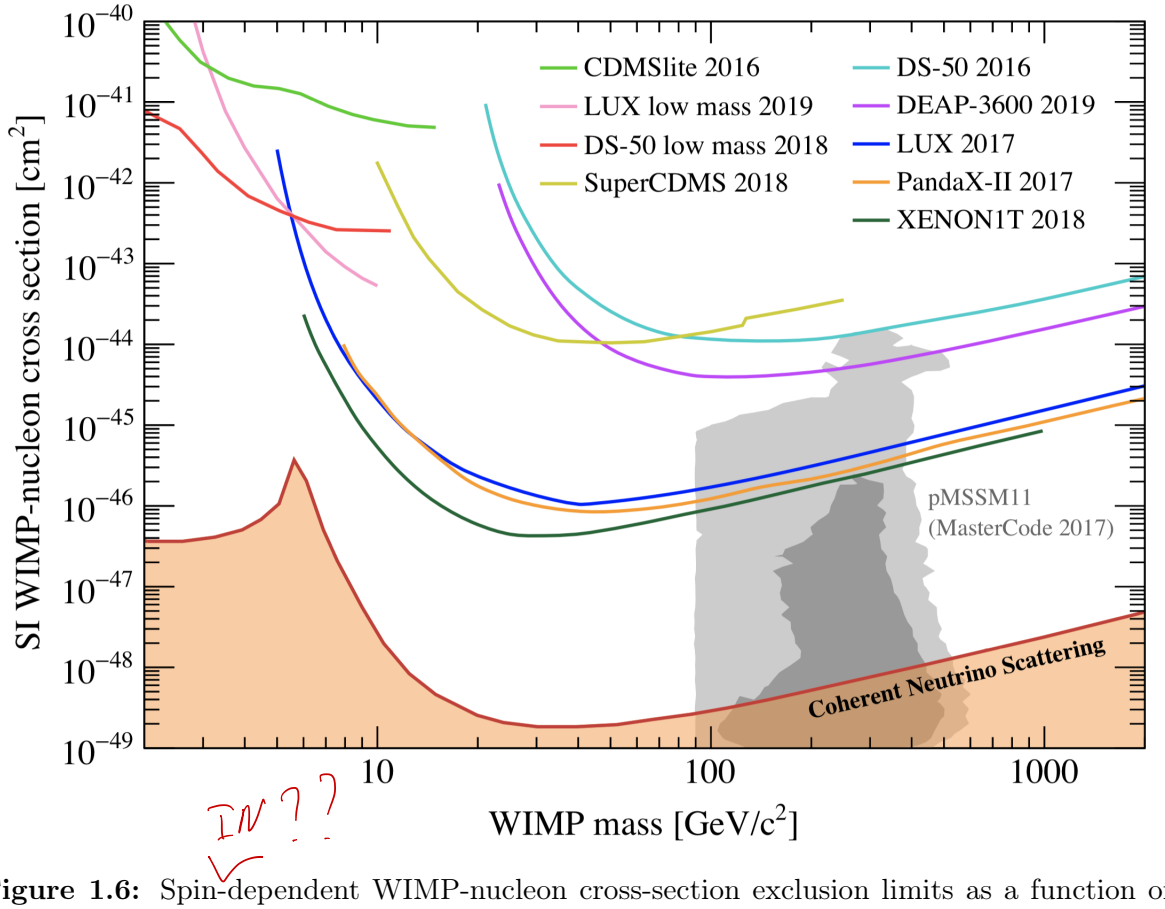

Figure 1.6: Spin-dependent WIMP-nucleon cross-section exclusion limits as a function of WIMP mass for some of the leading noble gas dark matter experiments and cryogenic crystal searches. The CDMSlite [77] and the SuperCDMS [78] limits are from cryogenic crystals. Low-mass WIMP analysis limits are from noble liquid detectors [75, 79]. And the remaining limits that span across most of the WIMP mass space are from liquid argon ([80, 81]) and dual-phase liquid xenon TPCs [73, 74, 82]. The irreducible background from neutrinos, denoted as the *neutrino floor* is shown as the brown shaded region [83] and the 1σ and 2σ favoured contours from a recent global fit scan based on a pMSSM model are shown in grey [84].

.

Chapter 2

The LUX-ZEPLIN Experiment

The introduction of dual-phase liquid xenon time-projection chambers, the origins of which date back to the 1970s, paved the way for substantial progress in the exploration of WIMP dark matter. The effective use of this technology made the LUX experiment the first sub-zeptobarn detector, placing stronger constraints on WIMP dark matter than all its predecessors. The next generation LUX-ZEPLIN (LZ) dark matter experiment, located in the Davis Cavern of the Sanford Underground Research Facility (Lead, South Dakota), 4850 feet under the ground, aims to build on this success in reaching ever-so sensitive WIMP-nucleon cross-sections. This section will introduce the concept of using xenon TPCs for direct detection dark matter searches; detailing the particle interactions, the detection mechanisms and providing an overview of the LZ detector.

2.1 Dual-Phase Xenon TPCs

The introduction of dual-phase TPC technology into the domain of direct detection over the past decade has dramatically improved the pace at which the sensitivity to WIMP dark matter has progressed. Dating back to the 1970s [85], TPC technology has made possible the use of liquid and gaseous xenon as a scintillation media to detect particle interactions, leading to ever-more stringent limits on SI and SD WIMP-nucleon cross-sections across a wide range of WIMP masses. The two main variables that strongly impact the sensitivity to WIMPs are the background rates as observed in the WIMP region of interest (ROI) and the amount of xenon held within the TPC.

In comparison to other noble elements, xenon offers several advantages. The large atomic number of xenon, $A = 131$, allows for a high sensitivity to SI-WIMP interactions due to the coherent scattering enhancement, $\propto A^2$, as given by equation 1.44. At relatively

low energy thresholds (e.g. $\sim$17 keV for 100 GeV/c^2 WIMPs), xenon is the most sensitive noble element of these targets. A comparison of the SI differential event rate for a collection of targets is shown in figure 2.1. The large atomic number also gives xenon excellent self-shielding properties in slowing down and stopping backgrounds originating from instrumental surfaces within a relatively short distance. The natural abundance of odd-neutron isotopes found in sourced xenon also provides a sensitivity for SD interactions. A major strength for these detectors is the possibility of precise fiducialisation of the xenon volume due to the 3D position reconstruction, allowing for an effective way to reject backgrounds from radiogenic walls and surfaces of the TPC. Furthermore, interaction lengths for gammas and neutrons in LXe are $\sim$10 cm and $\sim$15 cm, respectively; hence identifying and rejecting multiple scatters are of critical importance in reducing backgrounds.

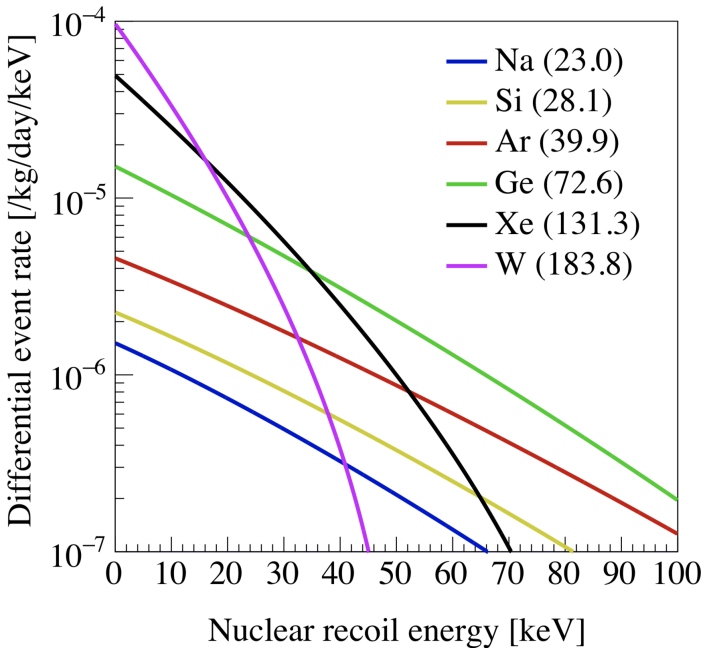

Figure 2.1: Comparison of differential event rates of a 100 GeV/c^2 WIMP interaction with several different target material with an assumed WIMP-nucleon cross-section of $\sigma_N^{SI} = 1$ zb. The averaged atomic mass of each target element at natural abundance is indicated next to its symbol in the legend. your plot? [res]

The interactions taking place inside the TPC generate three types of signals, of which two can be read out by detectors alike. The first of these are the scintillation photons that are produced in the LXe volume via a mechanism that allows these photons to propagate through the liquid and be detected by VUV-sensitive PMTs that cover the top and bottom of the TPC. The interaction also produces ionisation electrons that

are drifted upwards via a vertical electric field of several 100 V/cm. Once they reach the liquid surface, these electrons are extracted and accelerated through the gaseous phase, producing electroluminescence light, that which is detected by the PMTs. The following sections will cover in detail the mechanisms in which these signals are produced and how they lead to a precise 3D position reconstruction and an effective background discrimination.

2.2 Particle Interactions & Detection in a Dual-Phase Xenon TPC

Interactions of particles inside a xenon TPC result in electron and nuclear recoils. The majority of the backgrounds originating from radioactive isotopes, such as beta or gamma particles interact mostly via electron recoils, leading to a significant ER rate. Neutral particles, such as neutrons or WIMPs are expected to undergo nuclear recoils. Electron recoils are interactions in which the incoming particle interacts with the orbital electrons of the xenon atoms, whereas nuclear recoils are kinetic interactions off of the atomic nucleus. The recoiling particles in both cases deposit their energy through multiple short-ranged interactions, forming a track in which a cascade of interactions take place. The end result of this cascade converts the initial particle energy into scintillation photons, ionisation electrons and atomic motion (heat), latter of which is undetectable by current TPCs. The following sections will discuss in detail the mechanisms of energy transfer and signal production in such interactions.

2.2.1 Primary Energy Transfer

In rare gases, such as xenon and argon, the energy deposited by radiation is expanded into the production of a number of electron-ion pairs, N_{ion}, excited atoms, N_{ex}, and thermalised free electrons, known as sub-excitation electrons liberated in the ionisation process. The deposited energy, E_0, can be expressed into ionisation, excitation, and sub-excitation electrons by the use of a Platzman equation [86, 87]:

$$E_0 = N_{ion}E_{ion} + N_{ex}E_{ex} + N_{ion}\eta, \tag{2.1}$$

where E_{ion} and E_{ex} are the mean ionisation and excitation energies, N_{ion} and N_{ex} are the number of ionised and excited atoms, and η is the mean kinetic energy of ionised electrons. The energy required to produce a single electron-ion pair can be taken as an

averaged value, defined as the W-value, where,

$$W = E_0/N_{ion} = E_{ion} + E_{ex}(N_{ex}/N_{ion}) + \eta. \tag{2.2}$$

The average energy loss in ionisation is slightly larger than the ionisation potential or the band gap energy, resulting in the ratio of the W-value to that of ionisation potential or band gap to be 1.6-1.7 [88]. In general, the W-value is smaller in the liquid phase, and in LXe, in comparison to liquid argon and neon. As a consequence, the ionisation yield in LXe is the highest of all noble liquids.

Although the above equation is believed to apply for electronic recoils, in the case of nuclear recoils, a large fraction of the deposited energy is spent in nuclear collisions, which do not result in either excitations or ionisations. Hence, an additional term may be considered in equation 2.1 to account for this loss. The ratio of N_{ex}/N_{ion} has been measured to be $\sim$0.2 for electronic recoils and yields a value of $\sim$1 for nuclear recoils upon fitting to data [87, 89]. This difference in the initial ratio of exciton and electron-ion production is thought to be the underlying principle of discrimination between electron and nuclear recoils in two-phase TPCs. Further discussion on discrimination will follow in section 2.2.5.

2.2.2 Primary Scintillation (S1)

The primary scintillation light—often referred to as an S1 signal—is produced via a process known as self-trapping, in which an excited xenon atom (Xe^*) forms a molecular dimer (Xe_2^*) with a neighbouring atom; the decay of which produces a VUV photon. Upon initial recoil, there are two distinct processes in particular that lead to S1 light production. The first of these are when an incoming particle creates an excited xenon atom, which leads to the creation and decay of an excited xenon dimer molecule [87]:

$$p_i + Xe \rightarrow Xe^* + p_i, \tag{2.3}$$
$$Xe^* + Xe \rightarrow Xe_2^{*,v}, \tag{2.4}$$
$$Xe_2^{*,v} + Xe \rightarrow Xe_2^* + Xe, \tag{2.5}$$
$$Xe_2^* \rightarrow Xe + Xe + \gamma, \tag{2.6}$$

where p_i is the incoming particle, representative of any of the primary particle candidates present in such detectors, i.e., electrons, gamma rays, neutrons and so on. The superscript v is used to distinguish vibrationally excited states from purely electronic excitation.

The de-excitation of a vibrational state is mostly non-radiative but emission of infrared photons are also possible. The process detailed above is often referred to as *exciton luminescence*.

An alternative process to exciton luminescence is *recombination luminescence*. Although the end result of this process is identical to that of the process above, the initial interaction results in an ionised xenon atom, which undergoes recombination:

$$p_i + Xe \rightarrow Xe^+ + p_i + e^-, \tag{2.7}$$
$$Xe^+ + Xe + Xe \rightarrow Xe_2^+ + Xe, \tag{2.8}$$
$$Xe_2^+ + e^- \rightarrow Xe^{**} + Xe, \tag{2.9}$$
$$Xe^{**} + Xe \rightarrow Xe^* + Xe + (heat), \tag{2.10}$$
$$Xe^* + Xe \rightarrow Xe_2^{*,v}, \tag{2.11}$$
$$Xe_2^{*,v} + Xe \rightarrow Xe_2^* + Xe, \tag{2.12}$$
$$Xe_2^* \rightarrow Xe + Xe + \gamma. \tag{2.13}$$

The emission spectrum of the VUV scintillation photons originating from these two processes are similar as they share a common final stage. In a single event, both of these processes contribute in creating the summed S1 pulse—the collection of the VUV photons originating from an interaction site. However, it is important to note that the rate of recombination luminescence is heavily dependent on the initial energy recoil and more importantly, the electric field applied [89]. Application of an electric field serves as a mechanism to drift away any free electrons from the interaction site, hence suppressing recombination luminescence.

Although there exists a probability for an optical transition of the excited atoms to undergo a transition to the ground state, the collision rates in liquid xenon often result in the formation of strongly bound two-atomic xenon molecules. These molecules are only bound in their excited states and can exist either in a single state, $^1\Sigma_u^+$, or a triplet state, $^3\Sigma_u^+$, thereafter transitioning to the repulsive ground state, $^1\Sigma_g^+$, where the two molecules separate into two neutral xenon atoms and emit a VUV photon centered at $\sim$178 nm [90]. Thus, there is no re-absorption of the emitted photon, making xenon highly transparent to its own scintillation light—an important feature for a scintillator. The decay time constants of singlet and triplet states are very short, roughly 2.2 ns and 27 ns, respectively [87]. But recombination as highlighted in equation 2.3 is a slow process and can impact the shape of the S1 pulse by adding a non-exponential third

component, besides the fast (singlet decay) and the slow (triplet decay) components. The application of an electric field usually serves to reduce this third component by extracting the free electrons, hence suppressing recombination.

Furthermore, particle interactions at high energies ($\geq$ MeV), such as α-particles, can lead to the emergence of higher order processes that can decrease the number of primary scintillation photons. At these energies, the particle tracks formed due to high linear energy transfer (LET) increases the density of excited xenon atoms, thereby increasing the probability of interaction between two exited atoms. This process often leads to an increase in the ionisation rate in the track via a process called *bi-excitonic quenching* [91], where

$$Xe^* + Xe^* \rightarrow Xe^+ + Xe + e^-, \tag{2.14}$$

A similar process dubbed as *penning ionisation* can also take place if a single excited xenon atom has enough energy to ionise a neutral xenon atom from the ground state [89], where

$$Xe^* + Xe \rightarrow Xe^+ + Xe + e^-. \tag{2.15}$$

In such processes, the excited xenon atoms have enough kinetic energy to ionise another atom upon a collision. These processes on average usually lead to the suppression of the summed S1 pulse at higher energy recoils, as the process reduces the probability of exciton luminescence, which often leads to the creation of a VUV photon.

2.2.3 Ionisation & Secondary Scintillation (S2)

The electrons which escape recombination are drifted up by a vertical electric field, effectively removing the electrons from the interaction site. The drift velocity of the electrons depend on the strength of the applied electric field. For liquid xenon, a field strength of $\sim$1 kV/cm can lead to a 2.25 mm/μm drift velocity. After about 10 kV/cm, this dependence no longer holds and the drift velocity saturates at $\sim$2.8 mm/μm [92]. An accurate understanding of the drift velocity and hence the applied electric field is important in reconstructing the depth (z or the t axis) at which the interaction took place, as this is proportional to the time difference between the S1 signal and the S2 signal—or put it another way, the time it takes for the electrons to travel to the surface of the liquid, as depicted in figure 2.6.

The ionisation electrons drifting in a TPC will also experience diffusion in all three spacial dimensions. Diffusion taking place across the x-y plane dubbed as transverse diffusion, D_T, and the z plane, also known as longitudinal diffusion, D_L. The transverse diffusion usually has no first-order effect on the shape of the summed S2 pulse, whereas despite being an order of magnitude smaller, where $D_L/D_T \simeq 0.1$, the longitudinal diffusion in LXe has a critical effect on the S2 shape as it dictates the photon time of arrival at the photo-detectors. Hence modelling this accurately is crucial for realistic simulations of pulses and for the determination of the depth of the interaction.

Furthermore, electronegative molecules such as O_2, H_2O and N_2O can dramatically decrease the mobility of drifting electrons. These molecules can capture free electrons and form negative ions with extremely low mobility, resulting in drift velocities of a few mm/s at practical electric fields. The probability of a capture by such species depend on the concentration, the reaction rate constant and the path length of the electron as it drifts towards the anode. These species are usually present in sourced xenon and often outgas from detector material, constantly contaminating the LXe. Hence, the purification of liquefied rare gases to contaminant levels that are O(ppb) or lower is of great significance, especially for events at lower energies.

In reaching the liquid surface, the electrons have to overcome a potential barrier to be extracted over into the gas phase. This process is energetically unfavourable and hence an electric field of several kV/cm is usually applied between a grid just below and just above the liquid surface. Upon extraction, the electrons are accelerated through the gaseous layer to sufficient energies to excite the gas atoms, thus produce secondary scintillation, also known as *electroluminescence*. This process allows very high amplification gains to be achieved, where signals from a single electron to be detected. The mechanism in which secondary scintillation photons are produced is similar to that explained for primary scintillation. A schematic diagram of a toy TPC, highlighting signal generation from an S1 and an S2 signal is depicted in figure 2.6.

2.2.4 Energy Reconstruction and Signal Yields

Although the underlying principles that go into S1 and S2 production are relatively trivial, the modelling of these processes and correlating the output signal from a detector to a set of initial conditions depicting reality is less so. Taking into account the above, the number of emitted VUV photons, n_γ, and the escaped electrons, n_e, from an interaction

site after recombination can be expressed as,

$$n_\gamma = N_{ex} + rN_{ion}, \tag{2.16}$$

$$n_e = (1 - r)N_{ion}, \tag{2.17}$$

where N_{ex} and N_{ion} are the total number of excited and ionised xenon atoms prior to recombination, respectively, and r is the probability of recombination. In dual-phase TPCs, the detection of scintillation or ionisation due to a particle interaction is observed as an electronic signal that is proportional either to the number of emitted VUV photons, $S1 \propto n_\gamma$, or the number of escaped electrons, $S2 \propto n_e$.

On an event-by-event basis, number of excitons, N_{ex}, and ionisations, N_{ion}, produced, is subject to statistical fluctuations—however, not independently. Therefore reconstructing the energy deposited by using only S1 or S2 light is also subject to the same fluctuations. In realising that, $n_\gamma + n_e = N_{ex} + N_{ion}$, for any value of r, and the anti-correlation of S1 and S2 light, a linear combination of S1 and S2 could be used to construct a combined

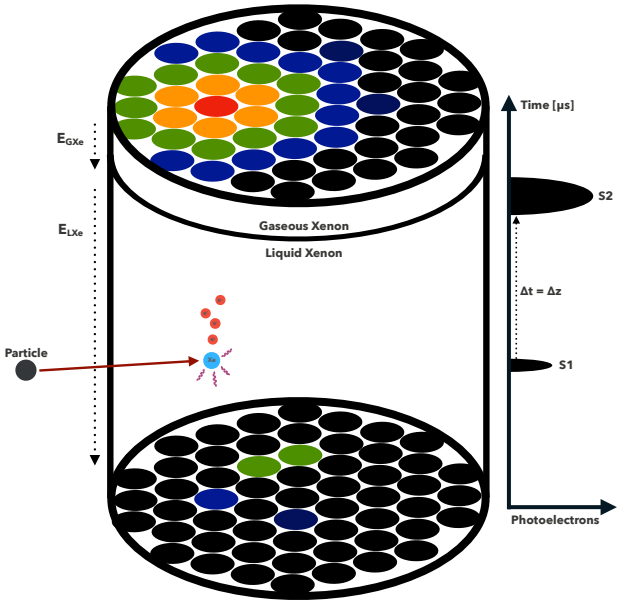

Figure 2.2: Schematic of a single scatter event inside a dual-phase toy TPC, showing the S1 signal production and the drift of free electrons towards the gas layer. The top and the bottom of the TPC is covered by PMTs that eventually detect the VUV photons created both in the liquid and in the gas phase. The diagram also depicts how TPCs allows for a 3D position reconstruction; where z is determined by the drift time of electrons and x-y determined by the PMT hit pattern.

signal to form an improved energy estimator,

$$E_0 = \mathcal{L}W(n_\gamma + n_e). \tag{2.18}$$

The W-value in this case represents the average energy required to produce either an exciton or a electron-ion pair, and has an approximated value of 13.7 eV in LXe [89]. $\mathcal{L}$ is referred to as the *quenching factor*, representing the fraction of the recoil energy that is transferred to electronic excitation instead of atomic motion. For electron recoils, this fraction is assumed to be negligible; whereas for nuclear recoils, a large amount of energy is lost as atomic motion. The commonly used model in estimating for this fraction comes from Lindhard's theory, which is based on heavy ion quasi-elastic collisions and gives the energy dependent nuclear recoil quenching factor as [93, 94],

$$\mathcal{L} = \frac{kg(\epsilon)}{1 + g(\epsilon)}, \tag{2.19}$$

where k is a constant of proportionality between electronic stopping power and the recoil velocity of the nucleus and $g(\epsilon)$ is a function that models the ratio of electronic-to-nuclear stopping powers. $\mathcal{L}$ is sometimes referred to as the *Lindhard factor* and the energies corresponding to ER or NR events are commonly reported as keV_{ee} and keV_{nr}, highlighting the electronic and nuclear recoil equivalent energies.

Light & Charge Yields in Liquid Xenon

In a xenon TPC, where searches are conducted across a wide range of recoil energies, it is often useful to define the light, L_y, and charge, Q_y, yields, as the number of photons emitted in scintillation or the number of electrons ionised, per keV of recoil energy, respectively, where

$$L_y = n_\gamma / E_0, \tag{2.20}$$

$$Q_y = n_e / E_0. \tag{2.21}$$

The prediction of the liquid xenon yields under the assumed drift electric fields of 180 V/cm and 310 V/cm are presented as the dashed and solid lines in figure 2.3. These electric fields are highlighted in particular to represent the fields operated by the LUX experiment and that which the LZ experiment aims to operate under, respectively. The figure also overlays measurements made by the LUX and the PIXeY experiments for both electron and nuclear recoils, down to a few keV of recoil energy, showing a good

agreement with the predictions from NEST (Noble Element Simulation Technique) [95,96]. NEST is a simulation package developed as an extension to GEANT4 [97] to simulate the non-linear behaviour of the energy dependence of scintillation and charge yields as seen by liquid noble detectors. Under its hood, NEST can be seen as a collection of models and approximations that predict the light and charge yields of noble gas elements as a function of recoil energy, electric field, particle type, temperature and pressure. A new version of the NEST software package was released in 2018 (v2.0.0) [98], moving away from the initially proposed semi-empirical models, towards a more data-driven approach to match the extensive collection of global data that exists.

The anti-correlation of light and charge yields for both electron and nuclear recoils are apparent from the solid and dashed NEST lines. The increased recoil energy under a fixed electric field, yields in more ionised electrons, increasing the probability of recombination, and hence increases the light yield. Furthermore, the quanta produced per keV of deposited energy for NR interactions are shown to be quenched across the same energy range. The figure also shows a subtle but noticeable difference between the yields as predicted for 180 V/cm and 310 V/cm; the larger field reduces the recombination probability for both ER and NR events, resulting in a larger charge yield across the energy range.

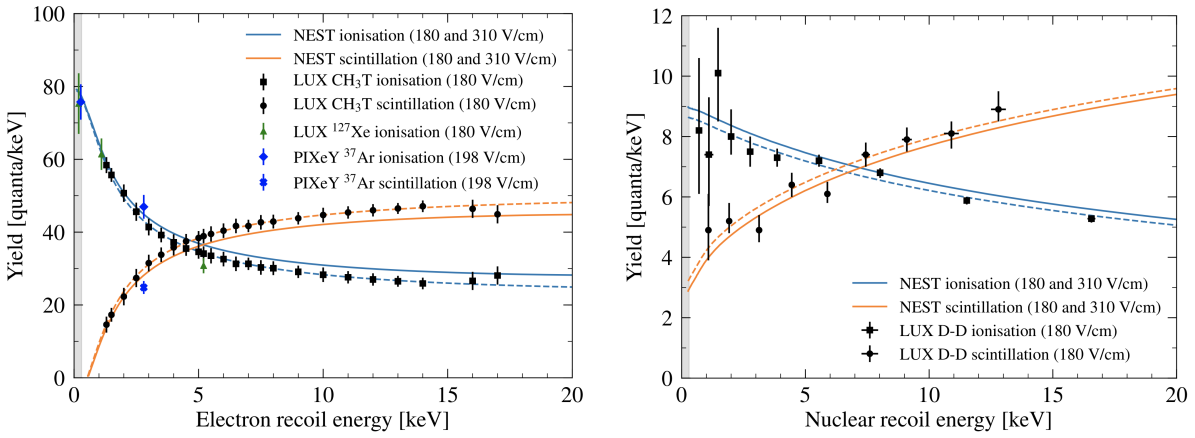

Figure 2.3: Liquid xenon scintillation and ionisation yields for electron recoils (left) and nuclear recoils (right). The NEST prediction of the scintillation and ionisation yields at drift electric field of 180 V/cm (dashed) and 310 V/cm (solid) are represented as the orange and blue lines, respectively. Measurements from LUX CH_3T [99] and ^{127}Xe [100] calibrations, along with the PIXeY ^{37}Ar source measurements [101] are overlaid. Figure adapted from Ref. [102].

Combined Energy Scale

The reconstruction of deposited or recoil energy as seen by the detector has to take into account detector specific efficiencies. Upon creation, a single VUV photon will reflect off of surfaces many times, before being successfully recorded by a PMT. The inefficiencies in this process, i.e., absorption of photons upon reflection, the quantum efficiency of PMTs, etc., serves to reduce the overall S1 size. Similarly, inefficiencies for the S2 light is also present, i.e., presence of electronegative molecules, efficiency of extraction into gas phase, etc., reduces the overall S2 size. Therefore, true S1 and S2, as seen by the detector can be defined as,

$$S1 = g_1 n_\gamma, \tag{2.22}$$

$$S2 = g_2 n_e. \tag{2.23}$$

Here g_1 represents the total light collection efficiency in liquid and g_2 represents the electron detection efficiency, which can be further represented as $g_2 = n_e N_{ph} \epsilon g_{1(gas)}$, where ϵ is the electron extraction efficiency, N_{ph} is the number of electroluminescence photons produced per electron, and $g_{1(gas)}$ is the light collection efficiency in the gas phase. By using the combined energy estimator defined in equation 2.20, energy as reconstructed by a detector takes the form,

$$E_0 = \mathcal{L} W \left(\frac{S1}{g_1} + \frac{S2}{g_2} \right). \tag{2.24}$$

Both g_1 and g_2 can be measured experimentally by the use of known calibration sources, as detailed in [103] for the LUX experiment. Due to the difference in the quenching factors between ER and NR events, calibration sources using γ-rays, are presented in electron equivalent energies, keV_{ee}. As an example of the way these scales work, a γ-ray induced electron recoil of 6 keV_{ee} would produce roughly the same total light and charge as a nuclear recoil of a $\sim$30 keV_{nr}.

2.2.5 ER & NR Discrimination

As mentioned previously, electron and nuclear recoils tend to appear in different regions of the energy-space, as seen by dual-phase LXe detectors. The conventional way in which events are displayed in such detectors is to plot directly in S1-S2 space. An example of such a plot from the LUX calibration data is shown in figure 2.4 [103]. When plotting in $\log_{10}$(S2/S1) verses S1 space, a clear band structure for ER and NR becomes apparent.

The discrimination as seen in this plot is thought to be a consequence of the difference in energy dissipation mechanisms for ER and NR events, as energy is deposited into LXe. To first order, the discrimination originates from the ratio of N_{ex}/N_{ion}, where more excitons, for the same energy deposition, are expected to form for a NR than for an ER, hence pushing the NR band lower in the $\log_{10}$(S2/S1) axis. The quantification of discrimination for LXe is conventionally taken as the fraction of ER events that leak below the NR mean, divided by the total ER events. Although discrimination varies across S1 or at higher energies, this quantity can be averaged in a desired energy range, i.e. WIMP region of interest. LZ is expected to reach an ER-NR discrimination of 99.5%.

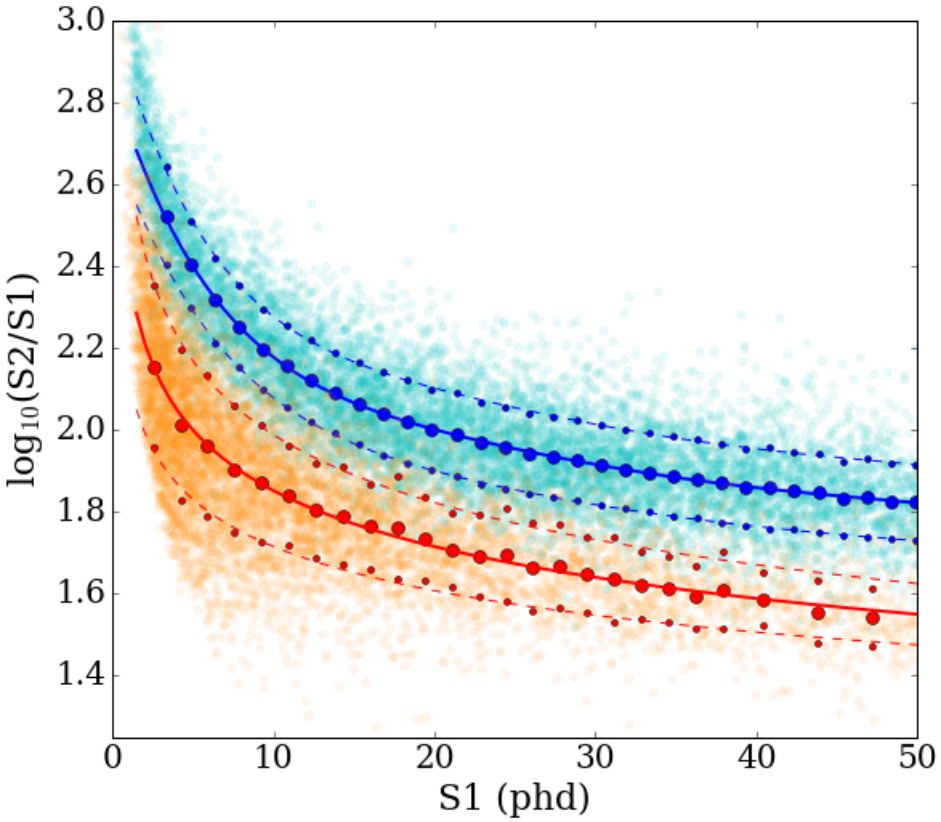

Figure 2.4: Calibration data from the LUX experiment, highlighting the ER and NR band formation (cyan and orange, respectively) in the S1-S2 space. Large filled circles show the fitted band Gaussian mean and small filled circles indicate the fitted Gaussian $\pm 1\sigma$. Power law fits to the means and $\pm 1\sigma$ are shown with solid and dashed lines [103].

2.3 The LUX-ZEPLIN Experiment

The LUX-ZEPLIN dark matter experiment is housed in the Sanford Underground Research Facility (SURF) in Lead, South Dakota, USA. The detector design is inspired from the LUX and ZEPLIN—III experiments that independently operated dual-phase LXe detectors at much smaller scales [70, 104]. In search for WIMP dark matter, the LZ detector at its core will operate a dual-phase xenon TPC with an active mass of 7 tonnes. To achieve optimal sensitivity, the detector is placed 4850 feet underground inside a water tank; shielded from cosmogenic and atmospheric backgrounds. In operating a LXe skin veto system (dubbed as the skin veto) that surrounds the TPC, and additionally, an outer veto system—dubbed as the outer detector (OD), which utilizes a gadolinium-loaded liquid scintillator (GdLS), the LZ experiment is projected to exclude spin-independent WIMP-nucleon cross sections above 1.4×10^{-48} cm^2 for a 40 GeV/c^2 WIMP mass at a 90% confidence level [105]. The following sections will detail the experimental design of LZ, highlighting key operational elements in its search for dark matter, some of which are displayed in figure 2.5.

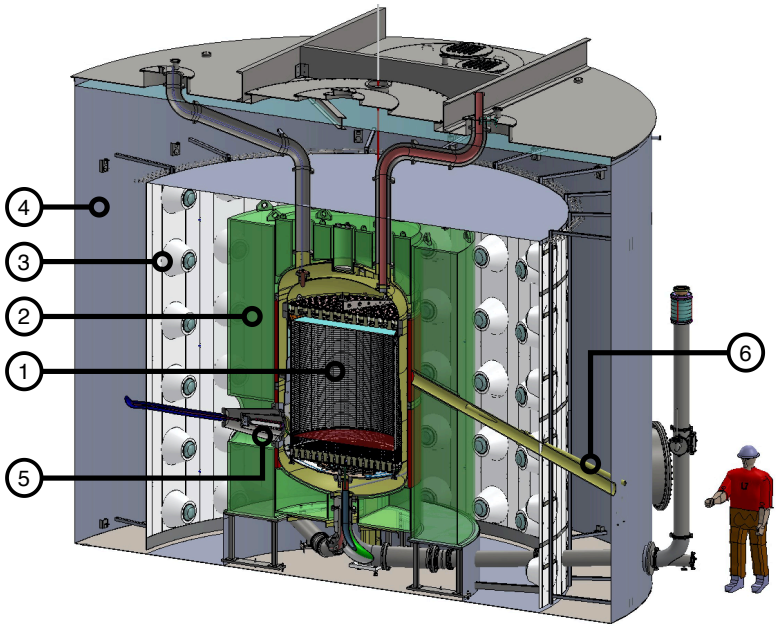

Figure 2.5: Cross-sectional cad model of the LZ experiment, highlighting the major detector subsystems. The LXe TPC (1) is located at the center with PMT arrays covering the top and the bottom. The TPC is sealed within a double-walled vacuum-insulated titanium cryostat that is surrounded by gadolinium-loaded liquid scintillator (GdLS) outer detector (2), surrounded by a suite of 8" PMTs (3) inside the water tank (4). The cathode high voltage (5) and the neutron calibration source conduit (6) are also depicted [106].

2.3.1 Liquid Xenon TPC & Skin Detector

The xenon detectors operated by LZ are housed in a double-walled vacuum-insulated titanium cryostat. The inner cryostat vessel (ICV) contains within it the TPC and the skin region. In operation, LZ handles a total of 10 tonnes of liquid xenon; 7 tonnes held inside the TPC and an additional ~ 2 tonnes held in the skin region. The TPC volume is usually referred to as the active volume which constitutes the WIMP target, and the skin volume refers to the region between the inner cryostat vessel and the outer surface of the TPC—both of which are instrumented with PMTs.

The TPC volume measures approximately 1.5 m in diameter and height, with a primary objective of detecting S1 and S2 light that are produced both in the liquid and the gaseous layers of this volume. To optimise the collection efficiency of S1 light, the TPC walls as seen by the photons are coated by highly reflective PTFE with a reflectivity of $\geq 97.3\%$ when immersed in LXe [107]. The S2 electrons produced within the liquid are handled by the operation of four horizontal electrode grids, woven from stainless steel wires, splitting the TPC into three different regions of electric field.

The drift field region (DFR) with a length of 145.6 cm extends from the cathode grid at the bottom of the detector, to the gate grid, located just below the liquid surface, and is shaped by 58 equally spaced titanium field-shaping rings that are embedded into the PTFE panels of the TPC wall. The DFR provides a vertical drift field for ionised free electrons to drift to the liquid surface. The extraction field region (EFR), also known as the electroluminescence region, is located between the gate (5mm below liquid surface) and the anode (8 mm into the gas). Electrons drifted to the surface of the liquid are extracted by this region and accelerated through the gas layer to generate ~ 820 electroluminescence photons per electron, of which the S2 light is constructed. The final region, known as the reverse field region (RFR) is located between cathode and another grid that sits just below. This space uses 8 field-shaping rings and serves to protect the bottom PMT array from the high potential of the cathode grid, while also drifting the electrons created in this region downwards, hence removing the S2 signal from events occurring below the cathode. A diagram of the TPC with key highlights are shown in figure 2.6.

The active volume of the TPC is monitored by two arrays of PMTs. A total of 494 PMTs are divided between the top array with 253 PMTs, and the bottom array with 241 PMTs, respectively. The 3-inch PMTs (model No. R11410-22) were manufactured by Hamamatsu for operation in cold liquid xenon. Furthermore, they were optimised

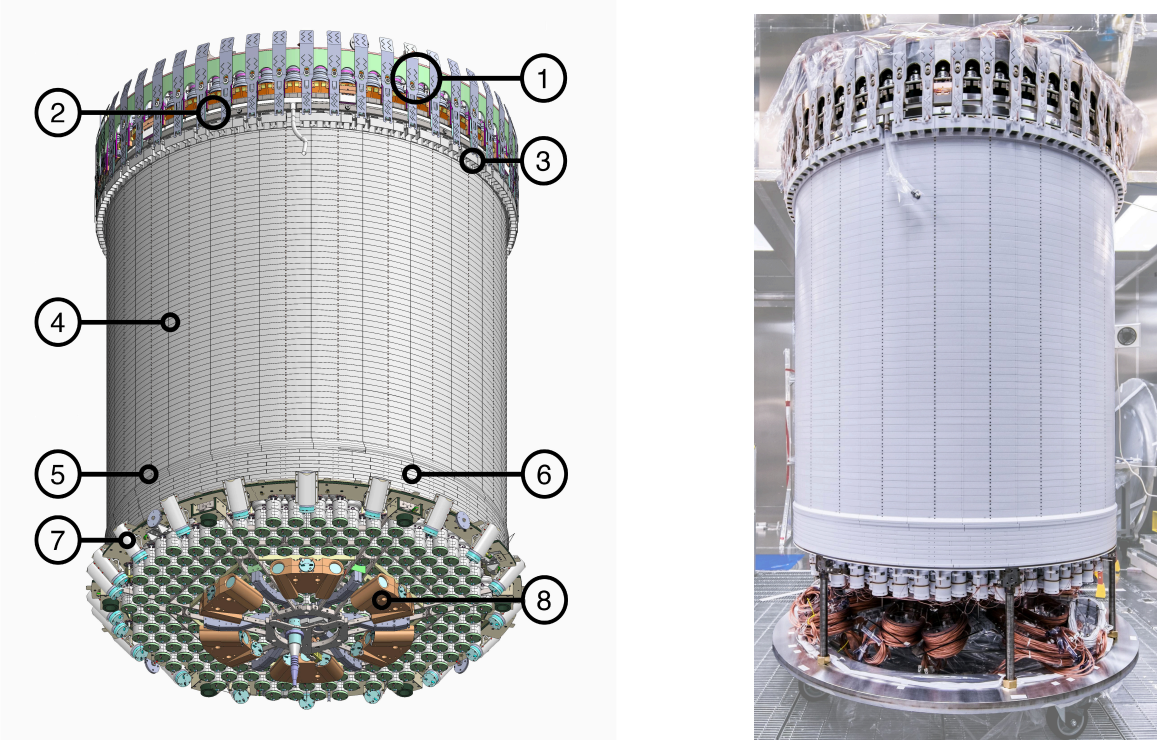

Figure 2.6: A diagram showing the CAD (left) and the fully constructed TPC (right), detailing the key components of the system. 1- Top PMT array; 2-Gate-anode and weir region (liquid level); 3-Side skin PMTs (1-inch); 4-Field cage; 5-Cathode ring; 6-Reverse field region; 7-Lower side skin PMTs (2-inch); 8-Dome skin PMTs (2-inch). Photographed by Matthew Kapust, Sanford Underground Research Facility [106].

for the detection of VUV luminescence, with an average quantum efficiency of 30.9% while operating in liquid xenon temperatures, and for low-radioactivity, an excellent single photo-electron (SPE) resolution, and low dark noise. At an operating voltage of 1500 V and 12 dynode stages, a nominal gain of 3.5×10^6 is expected at the end of the signal cable. The PMTs are arranged in close-packed hexagonal patterns to maximise the photocathode coverage and position reconstruction of the S2 signal for interactions near the TPC wall. The array structures are made from low-background titanium sourced as part of the R&D efforts for LZ [108]. The exposed titanium between the PMTs are covered by interlocking PTFE pieces to maximise VUV reflectance.

The skin region, sitting outside of the TPC is an important component of the xenon detector. The primary purpose of this region is to serve as a dielectric insulation between the TPC and the ICV. In addition to this, this region is also instrumented with VUV sensitive PMTs to serve as a scintillation-only veto detector, highly effective for γ-rays. The skin veto is composed of two regions: the outer layer of xenon outside of the TPC known as the skin, and the region below the TPC, known as the dome. The skin is

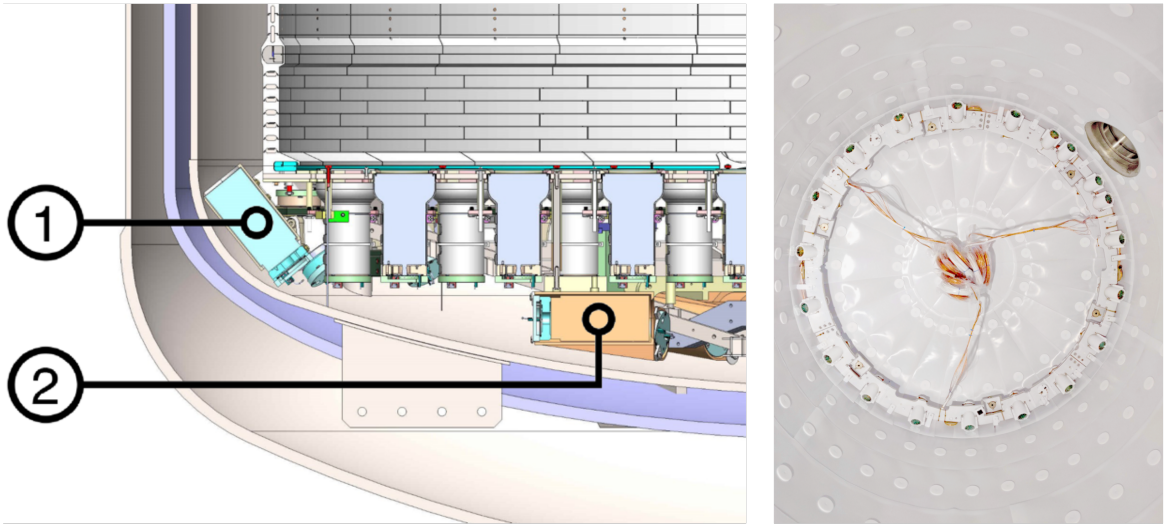

Figure 2.7: Left: CAD section of the TPC below the cathode showing the location of the 2" bottom side skin (1) and lower dome (2) PMTs. Right: Photograph showing the inner ICV with PTFE panelling on the walls and the lower side skin PMT structure at the bottom of the vessel [106].

monitored by three sets of Hamamatsu PMTs. First of these are a ring of 93 1-inch PMTs (model No. R8520) located at the top of the TPC looking down into the skin, and a further 20 2-inch PMTs (model No. R8778) located at the bottom of the TPC looking up and 18 2-inch PMTs mounted right below the TPC looking into the dome. A schematic of this region is shown in figure 2.7.

2.3.2 Cryogenics & Xenon Handling

The LZ cryogenic system is designed to contain $\sim$10 tonnes of LXe at 175 K. The xenon detector and majority of the LXe payload is held inside the ICV, and vacuum coated with the outer cryostat vessel (OCV). The OCV is supported at the bottom by three legs and the ICV is suspended from the top head of the OCV with a mechanism enabling its levelling from above. The cryostat vessels are fabricated from commercially available pure grade-1 titanium, chosen after an extensive screening campaign to identify the most radio-pure sample within a series of samples taken from different manufacturers, as detailed in [108].

The ICV consists of a top head and a tapered bottom vessel, connected via a large flange near the top. Its tapered shape is to reduce the electric field near the cathode. The top and the bottom heads of the ICV contain ports for cabling and heat exchancer conduits, with a larger port sitting on the front of the vessel for the high voltage (HV) conduit

connection. Whilst the size of the ICV is constrained by the Yates shaft, the OCV is constructed of three segments to overcome this restriction. Similarly, the OCV contains a HV port that aligns with the HV port of the ICV. Furthermore, the OCV also has a port opening to accommodate for the deployment of low energy neutrons that's crucial for calibration.

An overview of the cryogenic and xenon handling systems are shown in the schematic in figure 2.8. The temperature inside of the ICV is maintained by a set of closed-loop thermosyphon heat pipes with nitrogen as the process fluid. In operation, the liquid inside of the TPC is drained through the weir pipes, flowing into the xenon tower, which is a cryogenic system sitting outside of the water tank. The tower consists of four vessels:

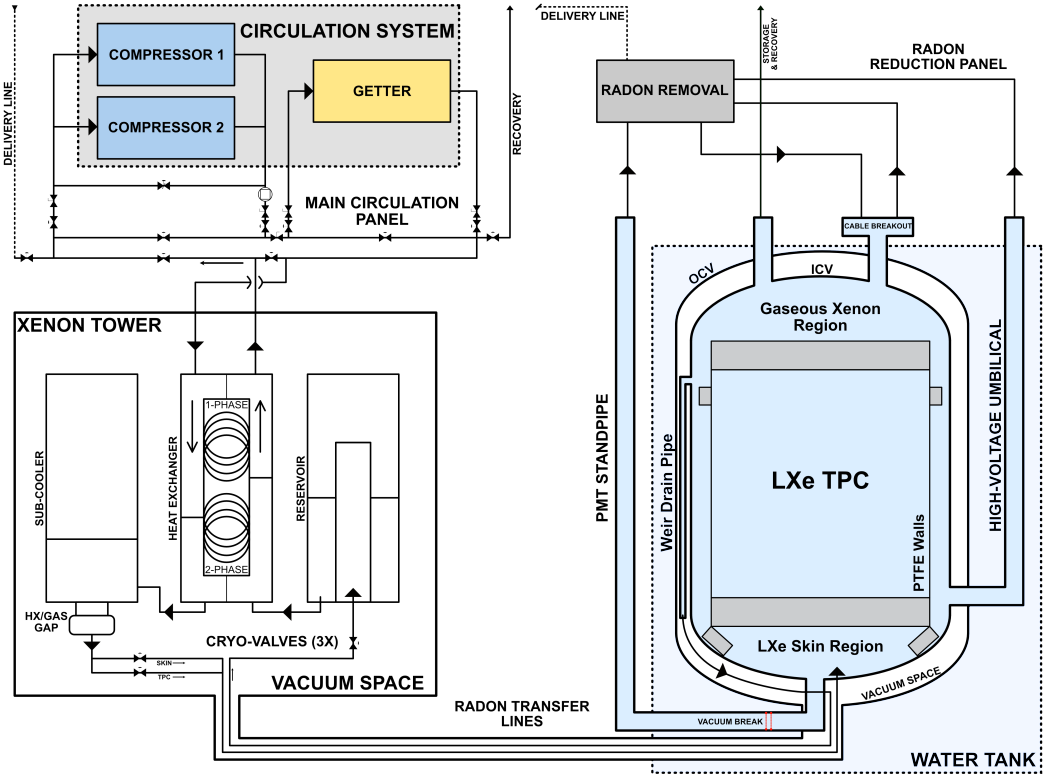

Figure 2.8: A simplified overview of the LZ circulation system. Majority of the xenon is held within the TPC, mostly in the liquid phase, with the gaseous region starting just above the weir drain opening. The LXe spills into the weir drain and through the xenon tower, which serves to heat the LXe using a two phase heat exchanger. The gaseous xenon is pumped through a hot zirconium getter, and returned to the detector after condensing. A radon removal system treats Xe gas in the cable conduits and breakout feed-throughs before sending it to the compressor inlet.

the reservoir vessel, the two-phase heat exchanger (HEX), the subcooler vessel, and the subcooler HEX. The tower acts as a system to convert xenon from either a liquid-to-gas phase or a gas-to-liquid phase. The circulation is established by the use of two all-metal diaphragm gas compressors (model No. A2-5/15) from Fluitron, circulating the gas through a hot zirconium getter at a design flow rate of 500 standard liters per minute (SLPM), taking 2.4 days to purify the full 10 tonne Xe inventory in a single pass. After the removal of electronegative species and calibration sources such as tritium or ^{14}C, the xenon is pumped through the cryogenic tower and back into the TPC and the skin region.

2.3.3 Outer Detector

The outer detector (OD) system consists of a set of 10 segmented acrylic tanks surrounding the ICV, as highlighted in figure 2.9. The segments are filled with a total of 17.3 tonnes of liquid scintillator. The scintillation medium consists of a linear alkylbenzene (LAB) solvent doped at 0.1% by mass with gadolinium [109]. The primary purpose of the scintillation system is to veto neutrons and γ-rays originating from radioactive impurities in material immediately adjacent to the TPC. The OD is designed to optimise the capture and tagging of neutrons within a time window that allows the signals to be correlated with the NR in the TPC. The secondary purpose of the system is to serve as an additional detector in constructing more accurate background rates for both neutrons and γ-rays.

Most neutrons ($\sim$90%) are detected predominantly through a neutron capture process with the ^{155}Gd and ^{157}Gd isotopes. Upon capture, multiple γ-rays emitted, totaling 7.9 MeV (^{155}Gd) or 8.5 MeV (^{157}Gd). The remaining neutrons ($\sim$10%) are captured on hydrogen, emitting a single 2.2 MeV gamma. The emitted gammas induce scintillation within the GdLS, which are collected by 120 8-inch PMTs arranged in a cylindrical array of 20 ladders that sit on support structures inside of the water tank. The light collection efficiency is further optimised by the use of Tyvek curtain that coat above, below and behind the PMT structure, and a layer surround the cryostat.

2.3.4 Calibrations

The calibration campaign developed for LZ is a multi-purpose effort to understand accurately and precisely the response of instruments, different detection regions and the underlying xenon response for both ER and NR interactions at varying energy scales. To achieve this, LZ will utilise on internal and external calibration sources, using a range of

radioactive nuclide sources. A list of these sources with key highlights are summarised and presented in table 2.1.

The deployment of internal calibration sources is necessary due to the self-shielding properties of LXe. To overcome this, known amounts of specific isotopes are injected into the circulation system, from which a uniform mixing with LXe in the active region can be achieved. The baseline set of internal sources include short-lived isotopes such as ^{83m}Kr, ^{131m}Xe and ^{220}Rn that are stored in the form of their parent nuclide that can be handled and stored in a compact solid form. Additionally, long-lived sources such as ^{3}H and ^{14}C can be stored as pressurised gas with purified Xe serving as the carrier. The removal of long-lived isotopes is critical and hence their form of deployment must be in a chemical form that can be effectively removed by the getter. Both long-lived and short-lived gaseous sources require precise dose control on the injected activity, accomplished via a gas handling system dedicated to injection control.

The external sources are predominantly used to calibrate nuclear recoil response and are achieved via two distinct methods. The first of these lower sources into the vacuum region between the ICV and the OCV with a deployment system which raises and lowers the source through three conduits with a position accuracy of ± 5 mm. A selection of photoneutron, γ, n, as listed in table 2.1, are planned to calibrate the nuclear recoil

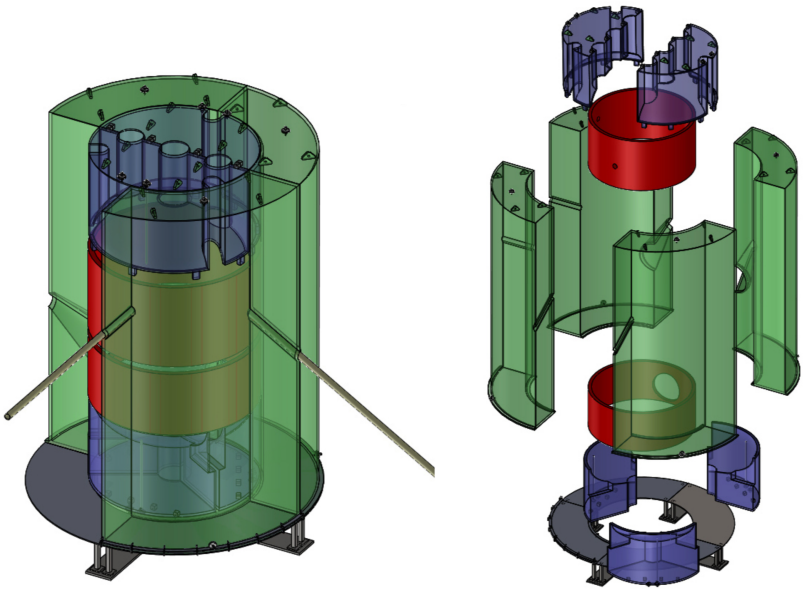

Figure 2.9: Schematic diagram of the liquid scintillator acrylic tanks. The four green tanks will cover sides, while the blue will cover above and below the OD. Displacer cylinders are shown in red [110].

energy range from below 1 keV up to about 4.6 keV. This energy region is of particular interest as ^{8}B solar neutrino coherent scattering falls within this window. A second method to calibrate higher energy NR response is by using a deuterium-deuterium (DD) neutron generator that produces up to 10^{8} neutrons per second. The setup will sit outside of the water tank delivering neutrons through the outer detector via a dedicated neutron conduits. This source has already been used by LUX to obtain a precise, in-situ calibration of the low-energy nuclear recoil response [111].

Table 2.1: Overview of the radioactive nuclide sources planned for LZ calibration, highlighting the type of interaction, energy deposition range, half-life of the isotopes and their intended purpose. The partitioned sections represent different deployment techniques. 1^{st}: Internal gaseous sources. 2^{nd}: Sealed sources lowered down small-diameter conduits to cryostat side vacuum, 3^{rd}: (γ, n) sources that are deployed as indicated in (2), but require dense shielding. 4^{th}: DD generator sources, in which neutrons travel through conduits from the generator.

Isotope	**Type**	**Energy [keV]**	$\tau_{1/2}$	**Purpose**
^{3}H	β	18.6 endpoint	12.5 y	ER band
^{14}C	β	156 endpoint	5730 y	ER band
^{83m}Kr	γ	9.4, 32.1	1.83 h	TPC (x, y, z)
^{131m}Xe	γ	164	11.8 d	TPC (x, y, z), Xe skin
^{220}Rn	α, β, γ	various	10.6 h	Xe skin
^{22}Na	γ	511, 1275	2.61 y	TPC and OD sync
^{54}Mn	γ	835	312 d	High-energy ER response
^{57}Co	γ	122	0.74 y	Xe skin
^{60}Co	γ	1173 , 1333	5.27 y	High-energy ER response
^{133}Ba	γ	356	10.5 y	ER response
^{228}Th	γ	2615	1.91 y	High-energy ER response
^{124}AmLi	(α, n)	1500 endpoint	432 y	NR band
^{124}AmBe	(α, n)	11,000 endpoint	432 y	NR band
^{252}Cf	n	Watt spectrum	2.65 y	NR efficiency
^{88}YBe	(γ, n)	152	107 d	NR response
^{124}SbBe	(γ, n)	22.5	60.2 d	NR response
^{205}BiBe	(γ, n)	88.5	15.3 d	NR response
^{206}BiBe	(γ, n)	47	6.24 d	NR response
DD	n	272 $\rightarrow$ 400	—	NR light and charge yields
DD	n	2450	—	NR light and charge yields

Chapter 3

Radiogenic backgrounds in LZ

The understanding of backgrounds and their origin in a low-background dark matter detector is critical for the search for dark matter. Without fully understanding and mapping all background sources, the ability to ascribe a statistical significance on any potential excess becomes ever more difficult. Moreover, this understanding is extremely important in sourcing detector materials, strategising cleanliness protocols for construction, and approximating the expected background rates for a potential search. This chapter will discuss background sources in LZ and their origin, highlighting the techniques used for the extensive screening campaign for material selection and detector construction.

3.1 Overview

The backgrounds as seen by the LZ detector can predominantly be characterised under two classes: electron recoils that occur when radioactive species interact with the electrons of the xenon target; and nuclear recoils, which occur when species interact with the nucleus of the xenon target. WIMPs are expected to scatter via nuclear recoils, hence any background that undergoes this type of interaction is WIMP-like, thus has the largest impact to WIMP sensitivity. Although electron recoils can be discriminated to a degree, recombination fluctuations as described in section 2.2.2 can lead to ER leakage into the NR band. Therefore, any and all sources that contribute towards ER and NR backgrounds are subject to extensive examination before and during detector construction.

The sources of backgrounds contributing to overall ER and NR rates can be categorised as those that are internal and external to the detector. Internal backgrounds are defined to

be those that are locked into the detector; originating from fixed material contaminants, surface contaminants and xenon contaminants. External backgrounds include those from laboratory and cosmogenics. This chapter will predominantly focus on fixed contaminants, surface contamination and contributions from the laboratory. Backgrounds from radon emanation—a dispersed xenon contaminant—will later be discussed in detail in chapter 4. Additional backgrounds, such as those from solar and atmospheric neutrino, or the double-beta decay of ^{127}Xe are search specific and will become more relevant in chapter 5.

To achieve design sensitivity to a WIMP-nucleon cross section below 3×10^{48} cm^2, LZ requires very low radio-contaminants, both intrinsic to materials and as a result of environmental exposure. At an early stage of the project, a requirement of 0.4 NR counts and below 1 µdru (event/kg/day/keV) of ER background was set for single scatter rates within the fiducial volume and WIMP search energy range from fixed contamination in the detector components. The LZ radioassay program was constructed to screen and source the most radio-pure materials available. The techniques used in the screening process include various forms of gamma and mass spectroscopy; to probe the intrinsically locked radiogenic species. Furthermore, upon completion of material selection, material handling in the transportation and construction process is of great importance in reducing surface contamination. The following sections will give an introduction to the origin of these backgrounds, the techniques used to screen, and the cleanliness protocols developed to monitor and keep surfaces clean in the construction process.

3.2 Background Origins

3.2.1 Fixed Contaminants

Naturally occurring radioactive species are often embedded in raw materials with unknown levels of activity. The most prevalent are those of ^{238}U, ^{235}U, ^{232}Th and their progeny, which eventually decay down to a stable isotope of lead via the emission of multiple α, β and subsequent γ-rays. The ^{238}U and ^{232}Th chains are particularly dangerous as they often lead to electron and nuclear recoils within the WIMP energy region of interest, the latter through (α, n) reactions within detector materials. Measuring the entirety of these chains present a challenge as they contain a number of isotopes with half-lives ranging from milliseconds to billions of years. Often it can be assumed that these chains are in secular equilibrium; a situation that arises due to the relatively long half-lives of parent

nuclei in comparison to their daughter nuclei. Hence, a measurement of the activity in one part of the chain can be used to infer the activity of the rest. However, ^{238}U and ^{232}Th chains, as shown in figure 3.1 are divided into *early* and *late* chains, representing the activity of U/Th as approximated by measurements on isotopic decays above or below the radium isotope on both chains. This distinction is particularly important for ^{238}U as the ^{226}Ra has a half-life of 1600 years; hence a breakage in secular equilibrium due to a chemical process will take thousands of years to be restored. $^{238}\mathrm{U}_e$ will refer to the ^{238}U activity as measured above ^{226}Ra, and $^{238}\mathrm{U}_l$ will represent the activity measured from ^{226}Ra and below. A similar approach is taken for ^{232}Th, with $^{232}\mathrm{Th}_e$ and $^{232}\mathrm{Th}_l$ representing activities above ^{228}Ra isotope and the latter part of the chain.

Furthermore, γ-ray emitting isotopes such as ^{40}K, ^{60}Co and ^{137}Cs are also present in many materials and are a part of the material screening process. ^{40}K is present within natural potassium at levels of 0.012%, whereas ^{60}Co can be produced via neutron activation of naturally occurring ^{59}Co, and ^{137}Cs is often formed as one of the more common fission products by the nuclear fission of ^{235}U. While these isotopes are often identified and measured by their γ-ray emissions, they all emit β particles at range of energies, with the highest endpoint of 1.311 MeV from the β-decay of ^{40}K. Hence, they often result in electron recoils with a wide energy spectrum.

3.2.2 Surface Contaminants

Fixed contaminants as highlighted in section 3.2.1 are naturally found in materials, with their isotopic activities expected to stay constant from the point of screening, to their implementation and usage inside the detector. This however does not hold true if a chemical process was conducted between the period of screening and construction. In addition, there are other mechanisms at play which can change the global activity of a material through surface contamination.

Contamination of surfaces can take place whenever a detector material is exposed. Contamination can occur through multiple mechanisms: contamination due to exposure to other material, environmental dust, and isotopic plate-out. However, the specific isotope of importance is the ^{210}Pb ($\tau_{1/2} = 22.3$ y) isotope in the ^{238}U decay chain. Due to the relatively long half-life of ^{210}Pb, the isotope can serve as another point of breakage in secular equilibrium. Material exposure to air with ^{222}Rn can result in the plate-out of radon daughters onto surfaces [112, 113]. This process serves as a mechanism to increase the activity of ^{210}Pb relative to the intrinsic activity driven from fixed contamination. Exposure to other materials, and more importantly environmental dust, can also yield as

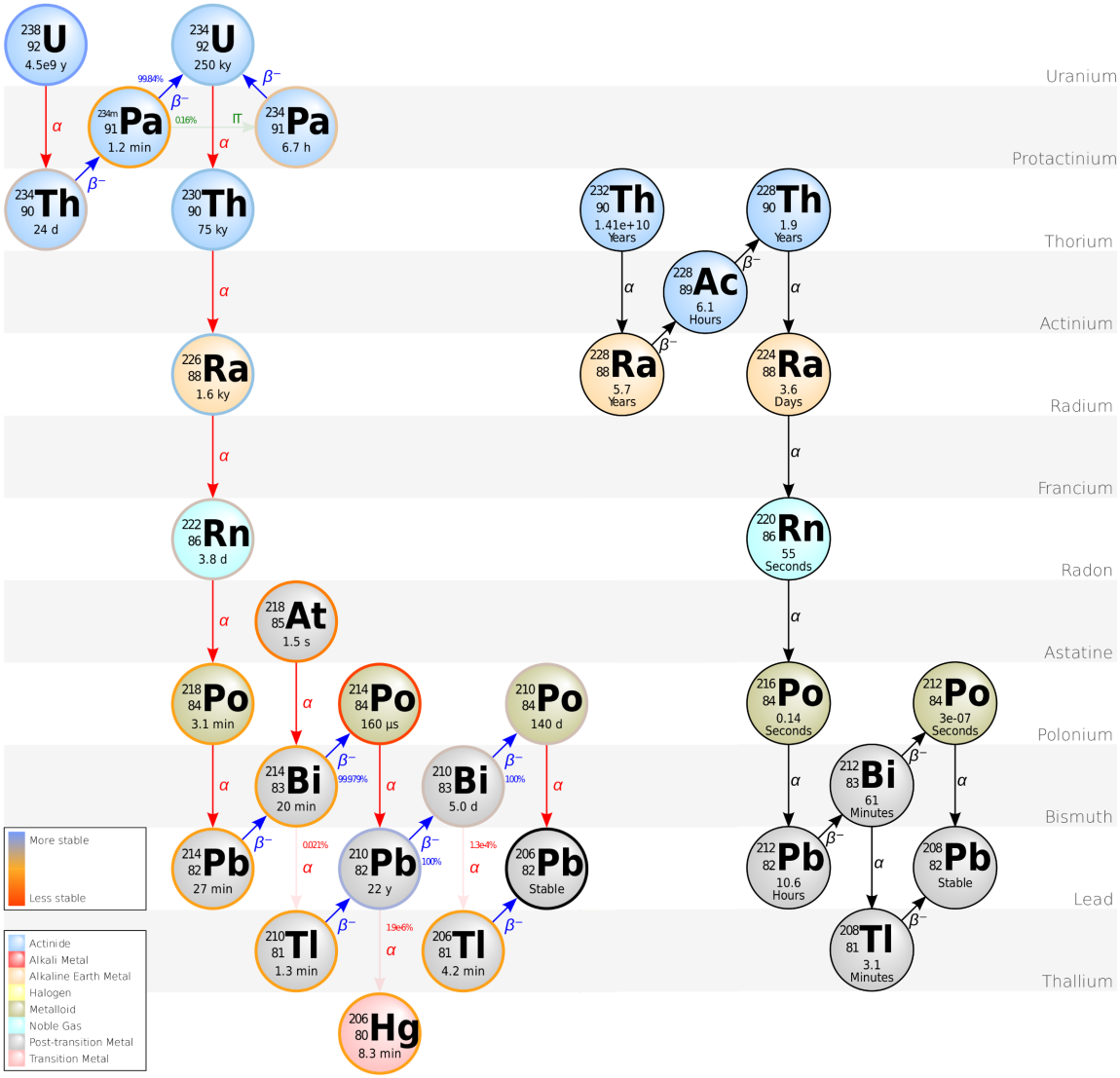

Figure 3.1: Isotopes of the ^{238}U and ^{232}Th decay chains, detailing their half-lifes and decay types. Its important to note that this is a simplified diagram and decays detailed here may occur through other mechanism.

a mechanism to increase the activity of isotopes in the late chain. The later contaminant not only increases the activity of ^{210}Pb, but the entire late chain, as the dust particulates will be locked into surfaces with specific concentrations of ^{238}U and ^{232}Th.

Plate-out and dust accumulation leads to the generation of both ER and NR backgrounds. ER backgrounds originate from the ^{214}Pb naked betas in the ^{222}Rn sub-chain, leading to a continuous ER background down to the WIMP energy window. NR backgrounds are increased due to the increase in the α-rate, which in turn increases the rate of (α, n) processes that release neutrons into the xenon. Furthermore, ^{210}Po ions from the ^{210}Pb

sub-chain originating at the edge of the TPC are likely to be misreconstructed as NRs within the fiducial volume. ^{210}Po on material surfaces will recoil into the LXe volume producing a complicated wall background (0 to 103 keV in energy). The impact of the latter depends critically on the performance of position reconstruction and drives the 4 cm radial fiducial volume cut. LZ has instituted a target for plate-out of ^{210}Pb and ^{210}Po of less than 0.5 mBq/m^2 on the TPC walls and below 10 mBq/m^2 everywhere else. LZ has also instituted a requirement limiting generic dust contamination to less than 500 ng/cm^2 on all wetted surfaces in the detector and xenon circulation system.

3.2.3 Other Source Origins

Xenon Contaminants

Natural xenon includes trace levels of ^{85}Kr and ^{39}Ar, both of which disperse throughout the liquid and are β-emitters that lead to ER events in the ROI. To reduce the levels of ^{85}Kr within the LZ xenon, a purification campaign using chromatography to remove krypton from xenon has been implemented [110]. The system has been shown to reduce ^{nat}Kr/Xe concentration to 0.075 ppt g/g. A further reduction in the levels of argon has also been observed, with an expected concentration of ^{nat}Ar/Xe below 0.45 ppb g/g.

Cosmogenic activation of xenon isotopes can also lead to an overall increase in background rates. The activation rate depends heavily on the depth at which the xenon is stored, as more activation is expected at sea level due to the cosmic ray flux. The equilibrium decay rate of ^{127}Xe ($\tau_{1/2} = 36.4$ d), a cosmogenic background, was measured by LUX to be (2.7 ± 0.5) mBq/kg after xenon was exposed to cosmic rays on the Earth's surface [114]. Further contaminants include ^{129m}Xe ($\tau_{1/2} = 8.9$ d), ^{131m}Xe ($\tau_{1/2} = 11.9$ d) and ^{133}Xe ($\tau_{1/2} = 5.3$ d). Due to their short half-lives, a short cooling period ($\sim$8-months) of the xenon underground before data taking reduces this background significantly.

Cosmogenic Activation of Materials

Cosmogenic activation can also impact detector materials, especially during the sourcing and construction phase, which predominantly takes place in the Earth's surface. At SURF, the location of LZ operations, the muon flux was measured at $(1.149 \pm 0.017) \times 10^{-2}$ s^{-1}cm^{-2}sr^{-1} [115]. The primary concern from cosmogenic material activation is the production of ^{46}Sc ($\tau_{1/2} = 83.8$ d). Generated by either muon capture or an (α, n) reaction in titanium, ^{46}Sc decays via a β-decay with an endpoint energy 0.357 MeV, with a subsequent emission of two γ-rays of energies 889 keV and 1,121 keV. The production

and the decay modes are given as,

$$^{46}_{22}\mathrm{Ti} + \mu^- \rightarrow {}^{46}_{21}\mathrm{Sc} + n + \nu_\mu, \tag{3.1}$$

$$^{46}_{22}\mathrm{Ti} + n \rightarrow {}^{46}_{21}\mathrm{Sc} + p, \tag{3.2}$$

$$^{46}_{21}\mathrm{Sc} \rightarrow {}^{46}_{22}\mathrm{Ti} + e^- + \nu_e. \tag{3.3}$$

Muon-Induced Neutron Background

Despite 4850-foot (4300 m w.e.) of Earth sitting above the Davis laboratory at SURF, although suppressed in comparison to surface level, a muon flux of $(4.4 \pm 0.1) \times 10^{-9}$ $\mathrm{s}^{-1}\mathrm{cm}^{-2}$ is still present [116]. In detector material and xenon, this flux generally generates internal backgrounds as discussed above. In the laboratory, neutrons from muon-induced electromagnetic and hadronic cascades within the cavern walls can generate background events. The neutron flux from the laboratory walls have been estimated using simulations of muon transport through rock around the laboratory and detector geometry. Attenuation through the water tank and the outer detector scintillators reduces the integrated neutron flux by more than 6 orders of magnitude [117] resulting in a negligible contribution to backgrounds in LZ. Its important to note that this mode of background generation may become more significant, if experiments were running closer to the surface.

3.3 Fixed Contaminant Screening Techniques

Approximating and modelling the expected backgrounds originating from fixed contaminants, as covered in detail in section 3.2.1 has been a high priority for the LZ experiment; initially in selecting radio-pure material for the LZ detector, but also to inform the background model through a combination of screening results, attained from many different screening techniques and detector. The ability to radioassay materials to ever increasing levels of sensitivity, within a short time period is of great importance as the next-generation low-background experiments are probing evermore sensitive parameter spaces.

In screening for fixed contaminants, the LZ screening campaign has made use of various techniques, including but not limited to an array of high-purity germanium (HPGe) detectors and inductively-coupled plasma mass spectrometry (ICP-MS). The following sections will summarise these techniques within the scope of LZ; focusing on the Boulby

underground germanium suite (BUGS) [118] and the ICP-MS facility at University College London (UCL) [119].

3.3.1 High-Purity Germanium Screening

Gamma ray spectroscopy is a technique that uses the principles of interaction of gamma radiation with matter to interpret and measure the activities of specific radio-isotopic impurities within material. The incoming γ-ray photons often deposit their energy by transferring up to all of its energy to the absorbing material through the mechanisms of photoelectric absorption, Compton scattering and pair production. The resultant secondary particles, often electrons, will then induce excitation and ionisation within the material to elude to the nature of the incoming photon. There are various different absorption material, detector design and types of operation to probe a wide range of photon energies but, the primary focus in this section will be germanium semiconductor diodes detectors. Details into the wider theoretical and practical use cases of γ-ray spectroscopy are provided in [120].

Germanium Detectors

Germanium detectors are a class of semiconductor detectors that are widely used in γ-ray spectroscopy. Their relatively high atomic number, Z; capacity for large crystalline growth with impurity levels of 10^{10} atoms/cm^3 or lower; and the energy resolution achieved due to their very low bandgap ($E_g \approx 1$ eV), make them a prime candidate for keV–MeV γ-ray detection.

The periodic lattice formation in germanium crystals lead to distinct band formation for electrons that exist within the solid. The *valence band* corresponds to outer-shell electrons that form covalent bonds within the crystal; the *conduction band*, sitting at a higher energy level, represents the band in which electrons are free to migrate through the crystal. The excitation of an electron from the valence band to the conduction band often takes place due to thermal energy. In doing so, it places an electron into the conduction band that is free to drift, but also creates what's known as a vacancy (hole) in the otherwise full valence band—the combination of these is called an *electron-hole* pair. The electron in the conduction band and the subsequent hole can both be drifted if an electric field is applied to the crystal; though in opposite directions, as the hole represents a net positive charge. The resultant drifted charge is then collected using electrodes.

The electrical properties of commercial crystals is often dominated by the small residual impurities that remain within such crystals. The nature of these impurities determine the type of semiconductor present; often labeled as an n- or p-type. In n-type crystals, the impurities occupy sites within the lattice and have extra valence electron in their outer-shell. Often referred to as *donor impurities*, they readily contribute electrons to the conduction band. In such material, the majority charge carriers are electrons. In p-type, the impurities often have one less valence electron relative to the crystal, effectively increasing the number of holes within the entire crystal. Referred to as *acceptor impurities*, these sites capture electrons excited to the conduction band; hence the majority charge carrier in such material are the excess holes that are formed within the material. Materials can often be doped with specific impurities to determine the nature of the crystal.

Boulby Underground Germanium Suite (BUGS)

The Boulby Underground Germanium Suite (BUGS) hosts seven gamma spectroscopy detectors, 1.1 km underground, at the Boulby Underground Laboratory in a class 1000 cleanroom, constructed and developed primarily for LZ. Since 2013, majority of the gamma spectroscopy screening efforts in LZ were conducted by the Chaloner (Mirion BE5030 broad-energy ultra-low background (ULB) HPGe detector), Lunehead (Mirion ULB SAGe well-detector), and Lumpsey (Ortec p-type detector) detectors. In addition to these detectors, BUGS has installed additional Mirion *specialty ultra-low background* (S-ULB) detectors which have been used to screen later LZ samples since 2017. These comprise two p-type detectors, Belmont and Merrybent, with relative efficiencies of 160% and 110%, respectively, and Roseberry, a BE6530 BEGe type detector.

The shielding of such detectors is detrimental to their operational output. The idea behind these detectors is to limit the γ-rays hitting the crystals strictly to those originating from the sample of interest. γ-rays originating either from detector material or external sources are considered to be background. The BUGS detectors are housed in custom shields designed and built by Lead Shield Engineering Ltd. The shields comprise 9 cm thickness of lead and 9 cm thickness of copper with interlocking retractable roofs to simplify sample loading. The lead used in these shields has mostly been recycled from lead used to shield previous low-background experiments hosted at the Boulby Underground Laboratory. The characterizations and sensitivities of these detectors are discussed in [118].

γ-rays originating from the ^{222}Rn sub-chain in the air can also contribute towards the background rate. To reduce such background, the shields used for all detectors are purged

using nitrogen from a Wirac NG6 gas generator. The Boulby Underground Laboratory benefits from a low baseline radon level (averaging $\sim$2.5 Bq/m^3). To remove residual radon in the nitrogen purge gas, charcoal traps containing approximately 6 kg of Carboact activated charcoal are deployed in a Labcold ULTF416 -80°C chest freezer. This radon reduction system is based on the design of a radon emanation detector developed at the Centre de Physique des Particules de Marseille (CPPM) [121].

Check it is indeed Carboact

Other γ-ray Screening Facilities for LZ

Other than BUGS, LZ employs various other γ-ray screening facilities, including the Black Hills Underground Campus (BHUC) [122], located at the 4850-foot level of SURF, which hosts a class 2000 clean-room containing seven low and ultra-low background HPGe detectors; the Lawrence Berkeley National Laboratory (LBNL) [123], which operates two HPGe detectors devoted to assay; and University of Alabama operating two above-ground Canberra p-type low-background HPGe detectors [124].

The LZ radioassay program uses a total of 12 detectors from the facilities mentioned above. A more detailed description of these facilities and their housed detectors can be found in *The LUX-ZEPLIN (LZ) radioactivity and cleanliness control programs* paper [1]. A summary of the 12 detector used by LZ, detailing the type of detector and some key characteristics can be found in table 3.1.

HPGe Cross-Calibration

The screened samples in LZ were distributed amongst the 12 detectors detailed in table 3.1, all with different backgrounds, shielding arrangements and operational history. To evaluate the systematic uncertainties and be able to correlate results from one detector to that of another, a sample of Rhyolite with well-characterized uranium, thorium and potassium content was used for cross-calibration. The material has been used by LBNL for over 30 years, with a well established uniformity across the sample.

An S5 Marinelli beaker of this mineral was prepared and sealed, with the content and its activity unknown to the collaboration. The comparison of results from different detectors uncovered some issues with several analyses, mostly due to problems with the Monte Carlo simulations of the detectors. These issues were identified and corrected without knowledge of the true calibration source material. The results were again compared across all the detectors. It is important to note at this point that when a concentration is reported, in parts per value (*e.g.* ppm, ppb, ppt) it is no longer pertinent to refer to

Table 3.1: Key characteristics of the 12 detectors used in the LZ HPGe screening campaign. Crystal mass and volume is included to give an idea of the relative sizes of the crystal. In addition the relative efficiency is given for the p-type detectors and the area of the front face is given for the BEGe detectors [1].

Location	Detector	Type	Volume [cm^3]	Mass [kg]	Relative Efficiency (%)	Face Area [cm^2]
BUGS	Belmont	p-type	600	3.2	1.92	-
	Merrybent	p-type	375	2.0	1.87	-
	Lunehead	p-type	375	2.0	1.86	-
	Roseberry	BEGe	170	0.9	-	181.1
	Chaloner	BEGe	150	0.8	-	1053.0
	Lumpsey	SAGe well	263	1.4	-	-
LBNL	MERLIN	n-type	430	2.2	3.59	-
BHUC	MAEVE	p-type	375	2.0	3.19	-
	MORGAN	p-type	375	2.0	2.68	-
	MORDRED	n-type	253	1.3	2.44	-
	SOLO	p-type	113	0.6	5.52	-
Alabama	Ge-II	p-type	260	1.4	3.6	-
	Ge-III	p-type	406	2.2	2.71	-

late chain or early chain values as the concentration defines the concentration of the progenitor isotope (^{238}U , ^{235}U, ^{232}Th) assuming secular equilibrium [125]. Table 3.2 lists reference values for each isotope; compares results from each detector; and gives their combined average and standard deviation. The cross-calibration effort confirmed that the modeling of detector geometries and efficiencies were correctly handled and provides a reasonable estimate on the systematic variation among the assays of $\sim$10% thus giving the collaboration confidence that each individual facility is able to produce consistent and accurate assay results.

3.3.2 Inductively-Coupled Plasma Mass Spectrometry

Inductively-Coupled Plasma Mass Spectrometry (ICP-MS) allows very precise direct measurement of the elemental abundances of uranium and thorium in small samples. The assays can be very quick, taking hours to days depending on requisite sensitivity down to sub-ppt (g of U/Th per g of material) levels and depending on related sample

Table 3.2: Results from the HPGe cross-calibration performed using a sample of Rhyolite. For the $^{238}U_e$ and $^{238}U_l$ columns, the contamination reported is that of the progenitor isotope ^{238}U assuming secular equilibrium and for the $^{232}Th_e$ and $^{232}Th_l$ columns, the contamination reported is that of ^{232}Th assuming secular equilibrium [1].

Detector	**$^{238}U_e$ (ppm)**	**$^{238}U_l$ (ppm)**	**$^{232}Th_e$ (ppm)**	**$^{232}Th_l$ (ppm)**	**K (%)**
Reference	8.87(4)	8.5(1)	12.1(1)	12.1(1)	2.82(1)
MERLIN	8.92(9)	-	12.4(1)	12.4(1)	2.81(3)
MAEVE	8.6(1)	8.6(1)	11.9(1)	11.9(1)	2.74(3)
MORDRED	7.92(5)	10.2(1)	11.3(2)	11.3(1)	2.66(6)
SOLO	6.16(1)	-	12.5(7)	9.94(1)	2.91(1)
Chaloner	8.73(5)	7.9(2)	11.1(1)	11.1(1)	2.81(1)
Lunehead	8.5(1)	-	11.8(1)	11.8(1)	2.85(1)
Ge-II	9.6(13)	11.4(15)	12(16)	12.2(17)	3.4(4)
Ge-III	9.2(9)	10.3(10)	12.1(12)	12.8(13)	3.3(3)
Average	7.61(3)	9.2(2)	11.9(1)	10.54(0.5)	2.84(2)
Std. Dev.	0.98	1.26	0.46	0.84	0.25

preparation protocols. ICP-MS has been used extensively in LZ to quickly measure ^{238}U and ^{232}Th in small samples to either reject or clear materials for use, or to pre-screen materials prior to assay with gamma spectroscopy which can determine the complete activity through the ^{238}U and ^{232}Th decay chains. In addition to constraining systematic uncertainty and directly determining activity at the top of the ^{238}U and ^{232}Th chains, ICP-MS has been used in LZ as part of our QC and QA program to ensure radioactivity and cleanliness compliance through component manufacture and delivery. The speed of ICP-MS allowed for rapid analysis of test pieces provided by manufacturers at specified points in the production processes, to detect potential issues and to ensure radioactivity and cleanliness compliance.

The majority of ICP-MS assays for LZ were performed using a dedicated mass spectrometry laboratory at UCL, housed in a class 1000 cleanroom facility and operating an Agilent 7900 spectrometer installed in 2015 exclusively for LZ [119]. Sample preparation and analysis procedures have been developed for materials with U/Th concentrations in the ppt to 1 ppb range. Samples are microwave-digested in pre-cleaned modified-PTFE (TFM) vessels using ultra-high purity acids. They are then diluted, without further chemical treatment, into disposable 50 ml polypropylene (PP) vessels ready for ICP-MS analysis. Fractional recoveries of ^{230}Th and ^{233}U spikes added prior to digestion are used to correct for ^{232}Th and ^{238}U signal loss from a range of sources. In particular, this enables accurate analysis of samples with high total dissolved solids (TDS) where

the instrument response degrades throughout the run. A full assay including digestion, ICP-MS measurement and analysis can be completed in a single day. The UCL facility was upgraded in 2019 with an Agilent 8900 ICP-MS.

In addition to the system at UCL, some material samples were assayed using facilities at the University of Alabama, the Centre for Underground Physics in Korea, and the Black Hills State University. At the University of Alabama, the LZ group set up a sample preparation laboratory in a Class 500 cleanroom equipped with a cryogenic mill, microwave digestion system, and digestion bomb. Further processing of samples, including spiking and resin-based extraction of U/Th isotopes was carried out in a separate cleanroom. The samples were then given to the Department of Geological Sciences which processed the samples using a Perkin-Elmer SCIEX-ELAN 6000 system. At Korea and Black Hills State, samples were measured using Agilent 7900 spectrometer, as was used at UCL.

3.4 LZ Cleanliness Protocols & Surface Contamination

Surface contamination through dust and radon daughter plate-out can lead to ER and NR generation as detailed in section 3.2.2. This class of contamination can take place from the moment a material is manufactured, up until it is mounted onto the detector and protected from exposure. This section will entail dust deposition and plate-out on LZ material, focusing on the protocols used in mitigating against such contamination; techniques used in handling, modelling and estimating exposure rates on critical surfaces of the detector.

3.4.1 LZ Cleanliness Protocols

Often, manufacturing of detector components are sourced out to experienced companies tailored for specialty instrumentation, such as Hamamatsu for PMTs, Loterios for the LZ cryostats and Axon for cables. And in other cases, specific instrumentation was designed and built by some of the universities involved in the project. Despite efforts in monitoring these environments for dust and radon plate-out, levels of contaminants in such environments are well above the baseline contamination requirements of the LZ project. To tackle this issue, most of the detector components after manufacturing were sent to a certified precision cleaning company, AstroPak Inc. The cleaning process involves chemical passivation or electropolishing—both of which are intended to etch surface layers of the material, removing any dust or plate-out isotopes on the surface.

After these procedures, the material are sealed with radon-proof bags, either aluminised Myler or Nylon bags with reduction factors of 2500 ± 1042 and 130 ± 3, respectively [126], and purged under nitrogen gas. The components are then stored safely up until their use-case in the construction process.

Majority of LZ assembly and construction took place in the surface assembly laboratory (SAL), in SURF. The laboratory was engineered as an ISO 6 class cleanroom with an average particulate count of ≤ 10 per cubic foot. The air filtration system was fitted with large activated charcoal columns to scrub the radon within the cleanroom to reduce the averaging activity of ambient radon level ≤ 0.5 Bq/m^3. The radon reduced cleanroom (RCR) in particular was designed with a high recirculation rate of 240.7 m^3/min in order to sweep out most of the radon daughters—in particularly ^{218}Po—before plate-out can occur. The cleanroom was under constant dust and radon monitoring.

Upon their use-case, the material components were taken into the RCR with their outermost seals removed, inspected for dust by ultra-violate (UV) light and fully unsealed under de-ionising fans that served to reduce any static buildup, which was shown to be effective in reducing dust accumulation on surfaces. Majority of the critical assembly was then completed under these de-ionising fans. For situations which required further cleaning, non-shedding mini-filament (Abgenics Essence Gold) wipes saturated with 99% pure IPA was used as cleaning agents.

Cleanroom garbs worn by personnel working on the assembly were changed after every work shift and wiped off with a lint roller multiple times during work to remove particulates that could deposit onto detector surfaces. Small detector components were sealed in double nylon bags which prevented plate-out since the components were then no longer in contact with the radon-laden air. Larger components like the cryostat vessels or PMT arrays had bespoke airtight enclosures, enabling additional filtered air and N_2 purges while in storage within the cleanroom to further mitigate against radon plate-out.

3.4.2 Surface Dust

The predominant source of dust that components are exposed to are as a result of outdoor air flowing into the SAL and that carried in from personnel, equipment and material. Dust monitors (Met One GT-526S particle counters) fitted in different locations of the cleanroom indicate increased levels of detection proportional to the activity within the cleanroom. While regular cleaning of the cleanroom and the air filtration system removes most of the dust, some still deposits on surfaces, including some of the most critical

regions of the detector, i.e. PMTs and TPC walls. To approximate deposition levels on surfaces and locked in dust amounts, two techniques have been utilised in measuring and modelling surface dust; the use of witness plates and tape-lifts.

Witness Coupons

Witness coupons made of PTFE and glass; cleaned with isopropyl alcohol (IPA) soaked non-shedding wipes are placed in multiple locations within the RCR, serving as controlled surfaces for dust collection. Fresh coupons are often used for specific phases of the construction with the assumption that the coupons would accumulate dust at a similar rate to that of the detector surfaces exposed during that phase of construction. The PTFE and glass coupons are then screened under fluorescence and optical microscopy, respectively, and processed via an ImageJ software [127] to reveal smaller particulates to determine the size distributions and their relative contributions to the dust density accumulated on the coupons' surfaces. Once the dust particulates size distribution is determined, as shown in figure 3.2, the dust density accumulated on the coupon (in n/cm^2) is calculated by dividing the accumulated mass (assuming particulates are spherical in shape with density of $1g/cc$) by the surface area of the coupons. Blank rates from unexposed coupons prepared in the same manner are taken into account in the analyses by background subtraction. The results from witness plates are a good measure on average dust levels during operation but are not precise enough to estimate the actual dust accumulation on surfaces.

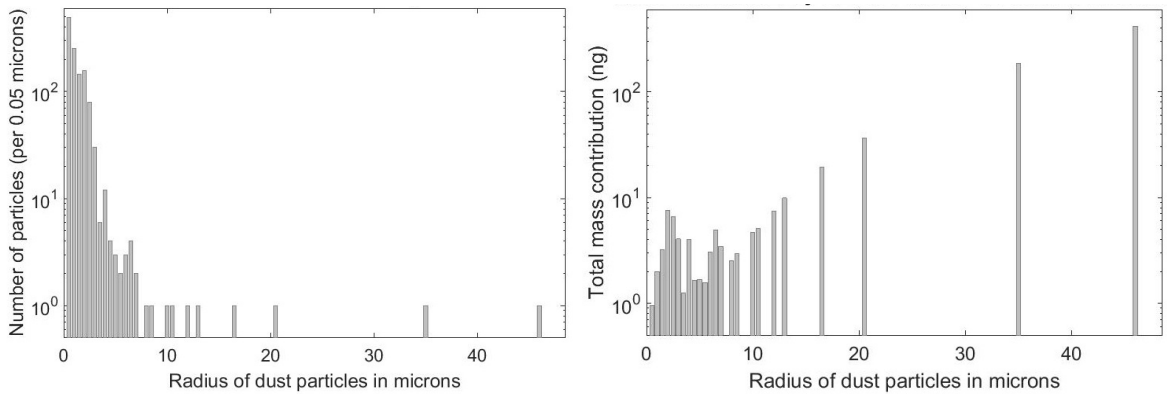

Figure 3.2: Dust particulate size distribution (left) and mass distribution (right) from fluorescent image analysis of a witness plate. Majority of the mass on the coupon is from a small number of larger particles. Particulates of size > 50 µm are rarely recorded.

Tape-lifts

In order to fully assess the dust levels on surfaces post-construction, surfaces of detector material were sampled with acetate or carbon tapes. The tapes were applied onto surfaces to remove the accumulated dust and assayed using the same fluorescence microscopy technique utilized for the witness coupons. The choice of tape material depends on the surface roughness of the component; acetate tape works better on smooth surfaces, like PTFE, while, for rougher surfaces like titanium, carbon tapes were found to perform better. However, tape-lifts cannot be taken on particularly sensitive parts of the detector, and therefore, they do not negate the need for coupons, but rather complement them. Both tape-lifts and coupons are necessary for a full history of the dust deposition on every component during the assembly process.

3.4.3 Radon Plate-out

The presence of primordial ^{238}U and the effect of radon emanation from the environment can vary radon levels in the air from 5–15 Bq/m^3 and to much higher levels in indoor environments. Once in air, the consequent α-decay of ^{222}Rn and daughters can lodge into material surfaces due to the kinetic energy carried as a result of the decay. As described in section 3.4, LZ limits the plate-out rate by assembling most of the background-prone instrumentation from plate-out in the RCR, with a continuous filtration system constantly circulating to reduce the concentrations of ^{222}Rn and daughters in the air. Absolute plate-out prevention is however not possible, and the remaining ^{218}Po that plates out is problematic due to the long-lived ^{210}Pb daughter which will decay over time in the detector. Therefore, the estimation of plate-out rates during assembly is crucial for operational control and background modelling.

Plate-out rates onto material are estimated using the Jacobi model [128, 129], describing particle deposition on surfaces from a balance of in- and out-flux of concentration in a maximally mixed air model. The model assumes that all surfaces within a given enclosure have equivalent plate-out rates per area, which is a function of air circulation rate, Rn concentration, volume, and surface area within the enclosed space the material surfaces reside. The plate-out rate is given as Becquerel per unit area and time of ^{210}Pb, where

$$R_p = C_{Rn}\lambda_{Pb_{210}}\frac{\Lambda_d}{(\Lambda_d + \Lambda_v)}\frac{V}{A}. \tag{3.4}$$

The ^{222}Rn concentration as obtained by radon monitors within the RCR (Durridge RAD7) is given by C_{Rn}, where $\lambda_{Pb_{210}}$ is the decay rate of ^{210}Pb. $\Lambda_d = v\frac{A}{V}$ is the deposition rate that depends on the diffusion velocity, v, of radon daughters measured to be between 5–15 m/h [129], $\Lambda_v = \frac{R}{V}$ is the air ventilation rate obtained by dividing the recirculation rate, R, by the volume, V, of the cleanroom, and A is the surface area of the RCR at SAL where most of the assembly work has been performed. The ratio, $\frac{\Lambda_d}{(\Lambda_d+\Lambda_v)}$, corresponds to the probability that a radon daughter will plate-out before removal through ventilation and is calculated to be 0.17.

In estimating a plate-out rate, the Jacobi model does not differentiate between types of material. This assumption is shown to be incorrect for material with highly negative triboelectric charging—a type of contact electrification on which certain materials become electrically charged—such as PTFE [130]. Measurements on PTFE indicate a factor of 50–100 times higher plate-out rate than for neutral metallic materials [131]. PTFE surfaces within LZ therefore have a multiplicative correction factor $M = 100$ as an upper-limit to reflect this correction. To reduce this effect for the PTFE surfaces within the TPC, multiple de-ionisation fans (Simco 4008630) were utilised above the assembly, continuously supplying ionised air through corona discharge, thus neutralizing the otherwise negatively charged PTFE material. Electrostatic field measurements taken at regular intervals indeed verified the neutralisation of PTFE surfaces with consistent reading of 0 kV/inch within the uncertainty of the measurement device.

The weighted plate-out rate R_w within an exposure time period (T) of assembly work is thus given by,

$$R_w = \frac{\sum A^i_{exposed}(MR_p)T}{\sum A^i_{total}}, \tag{3.5}$$

where M is the plate-out rate multiplicative factor described above, A the surface area of the individual parts making up the assembly, and R_p the Jacobi plate-out rate given in equation 3.4. The overall plate-out, R_O, accumulated for all the work shift time periods for that assembly is obtained by combining all the weighted rates as was done previously for the dust estimation. Overall, the average plate-out for the inner TPC PTFE surfaces in contact with the LXe is $R_{avg} = 158 \pm 13$ µBq/m^2, which is below the LZ requirement of 500 µBq/m^2.

3.5 γ-ray Background in the Davis Cavern

3.5.1 Overview

The radioactivity produced within the walls of the Davis cavern, the location in which the entirety of the LZ detector is located, is of great importance for background estimations for the WIMP search and other relevant rare event searches, and in particular $0\nu\beta\beta$. The ^{238}U and ^{232}Th chains contained within the environment leads to γ-ray emissions from excited states of the daughters, which under secular equilibrium leads to an average of 2.2 and 2.7 γ-rays, respectively [132]. In addition, ^{40}K within the walls emit a 1461 keV γ-ray with a branching ratio of about 10%. Due to the possibility of high levels of these isotopes both within rock formations and construction materials, characterisation of the γ-ray background in the cavern, and more importantly, as seen by the water tank, is crucial for background rates observed in the OD and within the TPC. In particular, high background rates from external sources within the OD can increase the false veto rate and the amount of excluded data.

The LZ detectors will be housed within a water tank of height 591 cm and radius 381 cm. Further shielding is provided by 6 octagonal steel plates of 5 cm thickness, inlaid beneath the floor of the water tank with an inverted pyramid hierarchy, directly below the xenon target. The water tank and the steel pyramid are aimed at reducing the environmental radioactivity. Geological and radiometric surveys of the Homestake mine indicate that most rock at the 4,850 level is of the Homestake formation, a metamorphic rock of relatively low uranium and thorium content [133], with additional intrusions of rhyolite segments—an igneous, volcanic, silica-rich rock, with higher natural radioactivity. The estimation of the rhyolite layers as present across the north wall, west wall and the floor are shown in figure 3.3. The walls and the ceiling of the cavern is lined with a layer of $\sim$12.7 cm thick sprayed concrete (shotcrete) with a thickness variance of factor two. The floor is covered with a 15 cm low-radioactivity concrete with the exception of two rooms at the end of the cavern, away from the water tank. Prior to this measurement, the radiological contents of the rock formation and construction material were measured with high purity germanium (HPGe) screening; these results are shown in table 3.3. The table also include two recent measurements of samples collected during this measurement. The following sections will summarise the details of the Davis cavern γ-ray measurements, highlighting the experimental setup, detector calibration, data collection and the results. A more detailed overview of these measurements are presented in [2].

3.5.2 Experimental Setup

The γ-ray flux within the cavern was measured using a thallium-doped sodium iodide (NaI) scintillating crystal ($5 \times 5 \times 5$ inches) coupled with a PMT. The detector, manufactured by Harshaw, was connected to a NOMAD 92X-P portable γ-ray-spectroscopy unit. The MAESTRO software was used to produce spectra. A total of 130 lead bricks ($8 \times 4 \times 2$ inches) were used in three different configurations for direction specific measurements while shielding away γ-rays from unsought directions, providing at least 8 inches of lead on the sides that were not exposed. A picture of the detector and lead brick configurations in which exposures from above and below are shielding is shown in figure 3.4.

Detector Calibration and Efficiency

A ^{60}Co source calibration was performed before each measurement to relate PMT channels to deposited energy and adjust for fluctuations in gain of the NOMAD unit. Using

Figure 3.3: Diagram of the Davis cavern highlighting the naming conventions of the wall locations and the rhyolite intrusion layers in orange with the estimated percentage coverage of rhyolite. The water tank is marked with a grey circle. The ceiling is estimated at 0% rhyolite, the south wall at 5% and the east at 2% [133]. Diagram adapted from [2].

Table 3.3: HPGe screening of rock, shotcrete and gravel samples from the Davis cavern laboratory. The first four materials were radioassayed during construction of the Davis cavern and give the average and range for several samples. The latter two samples were taken during the time of the γ-ray measurements. When not stated, overall uncertainties are estimated to be 10–20%.

Sample		^{40}**K** [Bq/kg]	^{238}**U** [Bq/kg]	^{232}**Th** [Bq/kg]
Homestake	ave.	297	2.7	1.3
	range	31–601	0.7–9.5	1.0–6.5
Rhyolite	ave.	1291	108	44
	range	523–2127	99–135	7.7–61
Concrete	ave.	381	27	13
	range	368–393	22–27	13–14
Shotcrete	ave.	272	23	12
	range	127–393	22–28	8.1–14
Shotcrete	-	220 $\pm$30	21 $\pm$1	11.4 $\pm$0.4
Gravel	-	35.0 $\pm$0.6	26.3 $\pm$0.1	1.7 $\pm$0.8

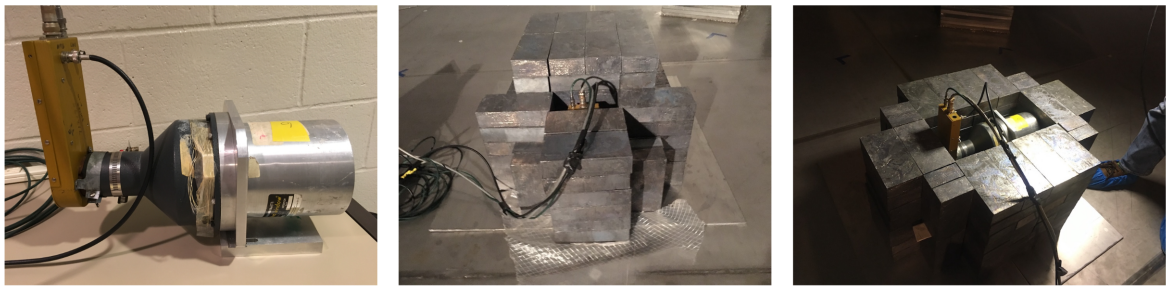

Figure 3.4: A photograph of the 5-inch NaI(Tl) detector (left), showing the pre-amplifier, PMT and NaI crystal. The right two images are showing the lead shielding configuration in measuring γ-rays from the bottom (centre) and from above (right).

the 2505 keV peak from ^{60}Co ensured a dynamic range that fully contained the energy spectrum up to the 2614 keV peak from ^{208}Tl. The detector efficiency and energy resolution were determined by using three calibration sources with their associated energy peaks: ^{60}Co (1173 keV, 1332 keV, 2505 keV), ^{137}Cs (662 keV) and ^{208}Tl (2614 keV). Each of the energy peaks was fitted with a Gaussian and exponential backgrounds in order to determine the location and resolution of the respective peaks. Calibrations were performed from the same central location within the water tank without shielding. Background measurements from the same location were subtracted from the calibration source spectra to account for γ-rays from the cavern.

The absolute efficiency of the detector, ϵ_A, is given by,

$$\epsilon_A = \frac{N(E)}{ATP_\gamma(E)} \tag{3.6}$$

where $N(E)$ is the number of counts in a photopeak of energy E, A is the activity of the source, T is the live time and $P_\gamma(E)$ is the probability of a single decay producing a γ-ray of energy E. ϵ_A is a product of the geometric acceptance due to the fractional solid angle expose of the detector, the γ-ray conversion efficiency within the crystal, and the PMT light collection efficiency. Simulations of calibration sources at varying distances from the detector were performed and source activities were used to calculate the rates in each simulated photopeak. Comparison to data revealed an over-estimation of rates in data, likely as a result of the unaccounted light collection effects in simulations. A correction factor of 0.90 ± 0.06 was calculated and applied to further simulations. The resolution, R, of each peak was calculated from the full width at half maximum (FWHM) and the energy, E, of that peak, using,

$$R = \frac{FWHM}{E} \equiv \frac{\Delta E}{E}. \tag{3.7}$$

The energy dependent resolution scale was then determined by fitting a resolution model, which took into account the light transmission from the scintillating crystal to the photocathode, α, statistical fluctuations in photon production, attenuation, conversion and amplification, β, and the noise contribution, γ, [134], where,

$$R = \frac{\Delta E}{E} \cong \sqrt{\alpha^2 + \frac{\beta^2}{E} + \frac{\gamma^2}{E^2}}. \tag{3.8}$$

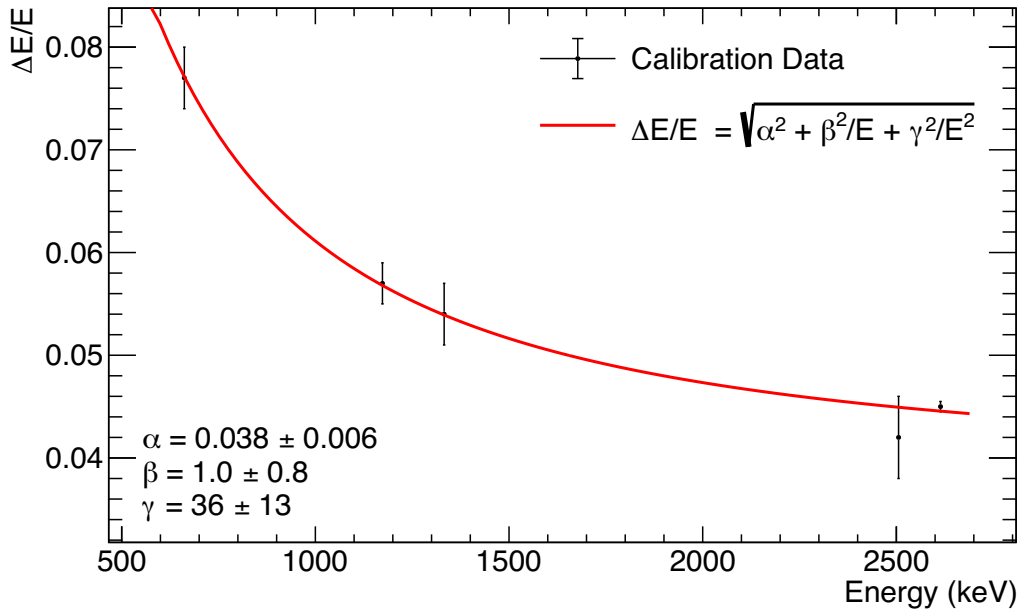

Figure 3.5: Resolution of the NaI(Tl) detector obtained from the calibration source peaks of ^{60}Co, ^{137}Cs and ^{228}Th. The fit to data using the resolution model given in equation 3.10 is also shown.

The resolution model as applied to the calibrations performed during this measurement are presented in figure 3.5 and were later used to correct the true Monte Carlo energy depositions from the simulations in an effort to directly compare with the data from NaI(Tl) detector.

Data Collection

A total of nine measurements were conducted to fully map the γ-ray flux within the Davis cavern, focusing primarily on the flux as seen by the water tank as shown in figure 3.6. Seven of these were conducted within the water tank; five of which were measurements from the centre of the tank. Locations from the centre consisted of an unshielded measurement (a) and shielded measurements looking down with 30 cm of steel pyramid beneath (f), looking up (g), looking west (h) and looking east (i). The remaining two within the water tank were shielded measurements looking down at the edge (d) and looking down halfway from the centre to the edge with 15 cm of steel pyramid beneath (e). The two measurements outside of the water tank were conducted unshielded in the Upper Davis above the water tank (b) and on the floor of the counting room (c). Measurements looking down within the water tank were aimed at measuring the effectiveness of the steel pyramid, whereas those facing the walls aimed at assessing

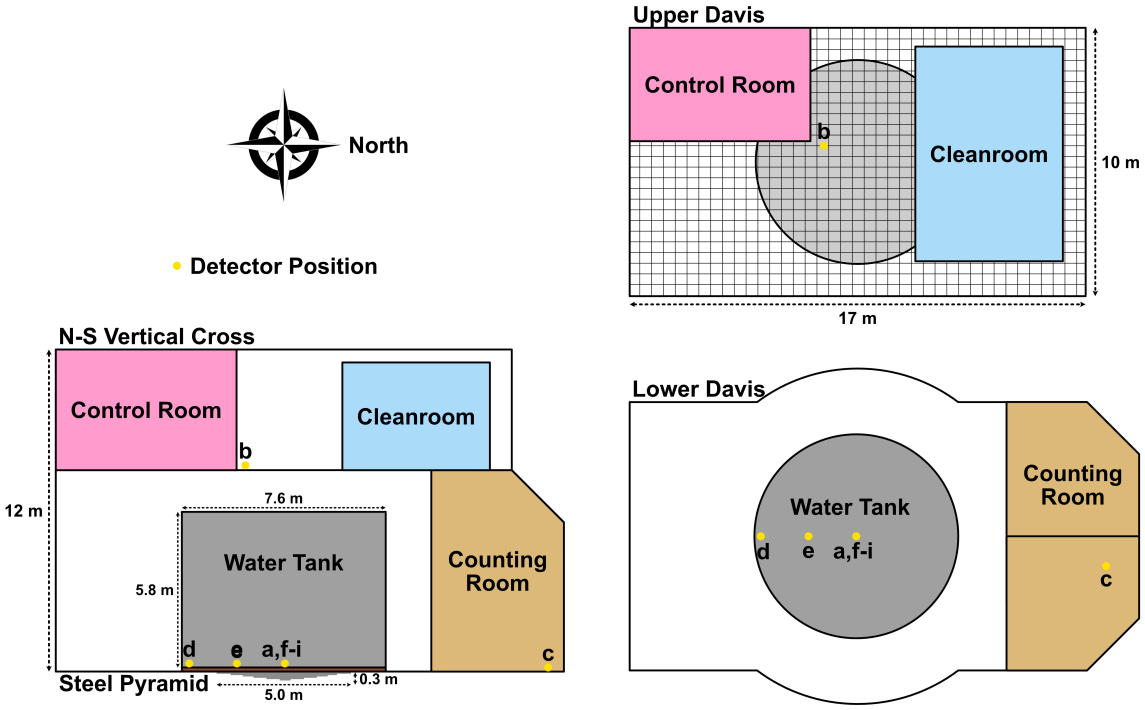

Figure 3.6: Schematic layout of Davis cavern at the time of the measurement, highlighting key dimensions and the measurement positions with yellow dots. The labels of the positions directly map to measurement results within table 3.4.

the asymmetry due to the presence of rhyolite. The measured energy spectra from all of the 9 positions are shown in figure 3.7 and their integrated rates, along with differing exposure times and measured ambient radon levels are summaries in table 3.4. The lowest rates observed are from two measurements inside of the water tank, at the centre (f) and halfway to the edge (e), both facing down. Despite the much longer exposure time for (f) and the differences in the thickness of pyramid shielding below, the rates observed for these two measurements are comparable. This suggests that the rates observed in these positions are intrinsic to the experimental setup—essentially a background of the experiment, as NaI(Tl) crystals and PMTs are known to have intrinsic ^{40}K, ^{238}U and ^{232}Th contamination [135]. Measurements facing east and west are comparable in rate, signalling no significant asymmetry due to the difference in rhyolite intrusion within the walls. This may imply that the difference observed in the directional flux ($\sim$ 10%) may be due to unevenness in shotcrete thickness since the shotcrete is approximately 10 times more radioactive than the Homestake formation in ^{238}U and ^{232}Th. The measurement at the edge of the water tank looking down (d) does show a higher rate than both (e, f) suggesting that the steel pyramid is in fact reducing the flux from below. The rates were

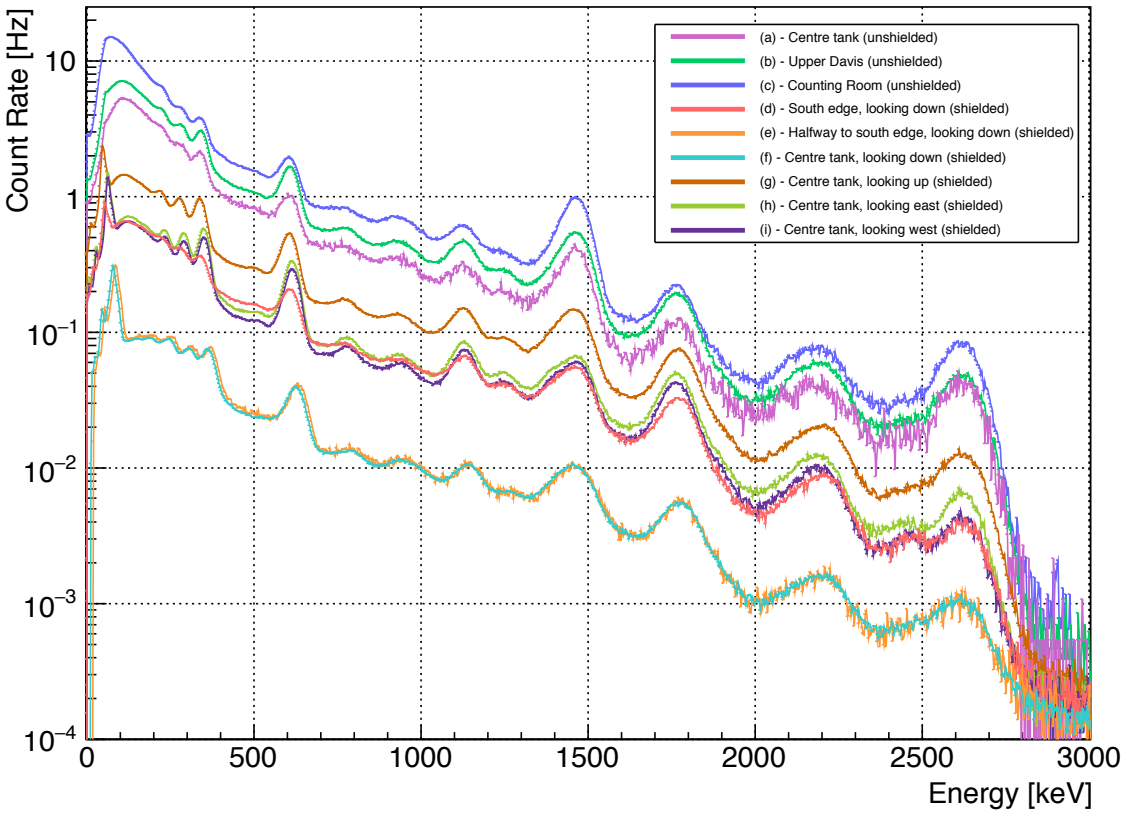

Figure 3.7: The energy spectra for all nine measurements labeled with their corresponding positions in the energy range 0–3000 keV.

highest in the east counting room, followed by the upper level of the Davis cavern and the centre of the water tank—all unshielded.

Decays from the ^{222}Rn sub-chain make up a majority of the γ-rays in the ^{238}U chain, hence the activity of radon within the cavern air must be considered. The average radon concentration, taking into account seasonal dependence in the Davis Campus, is expected to be within 150–310 Bq/m^3 [133]. However, unusually high radon levels were recorded (measured with an AlphaGuard detector) some of the days, possibly as a result of the air flow and air circulation fluctuations within the mine drift. The recorded levels from an area outside the main entrance to the cavern known as the common corridor during each dataset are also shown in table 3.4. Although there may be uncertainties due to the differences in location, the concentrations were significant enough that γ-rays from airborne-radon was included in the analysis.

Table 3.4: Dates, live times, radon concentrations and integrated count rates for each measurement position. The centre of tank measurements were shielded from all directions except the intended direction as stated. Stated uncertainties are Poisson counting errors. Data adapted from [2].

Measurement Position	Label	Date	Live time [hours]	Ave. ^{222}Rn Act. [Bq/m^3]	Rate (total) [Hz]	Rate (>200 keV) [Hz]
Centre of tank (unshielded)	a	24/10/17	4.0	422 ± 34	595.7 ± 0.2	386.0 ± 0.2
Upper Davis (unshielded)	b	26/10/17	3.6	868 ± 222	794.4 ± 0.2	512.0 ± 0.2
Counting Room (unshielded)	c	26/10/17	2.1	929 ± 70	1355.0 ± 0.4	750.9 ± 0.3
South Edge, looking down	d	16/10/17	18.2	358 ± 80	94.17 ± 0.04	64.40 ± 0.03
Halfway to South Edge, looking down	e	17/10/17	17.9	336 ± 55	17.15 ± 0.02	10.70 ± 0.01
Centre of tank, looking down	f	19/10/17	117.0	500 ± 155	16.715 ± 0.006	10.427 ± 0.005
Centre of tank, looking up	g	18/10/17	20.2	372 ± 76	203.57 ± 0.05	139.0 ± 0.04
Centre of tank, looking west	h	24/10/17	17.3	359 ± 37	95.11 ± 0.04	51.77 ± 0.03
Centre of tank, looking east	i	25/10/177	22.3	316 ± 46	106.33 ± 0.4	59.14 ± 0.03

3.5.3 Simulation & Analysis

Simulations of the γ-ray background within Davis cavern are performed using the BACCARAT framework, a GEANT4 (v.10.03) [97] package developed primarily for LZ background simulations—detailed further in section 5.2. Electromagnetic processes were modelled using the *G4EMLivermorePhysics* class, a sub-package that models interactions of γ-ray and electron cross-sections [136, 137], focusing on low energy processes, such as Rayleigh, Compton scattering, bremsstrahlung and the photoelectric effect.

A custom geometry featuring the cavern, steel pyramids, water tank and the NaI detector was created, with additional shielding geometry, taking into account the three different configurations. The cavern was modelled as a cuboid to have internal dimensions of $20 \times 14 \times 12$ m; slightly larger than stated in figure 3.6 to account for the unevenness of the cavern walls. The cavern walls were defined as a mixture of oxides, primarily SiO_2, Al_2O_3, FeO and water [138]. Decays from the ^{238}U and ^{232}Th chains and the ^{40}K decay were all initiated within a 30 cm thick layer of material surrounding the cavern. The ^{238}U and ^{232}Th chains were simulated using an event generator developed for LZ background simulations. The generator assumes secular equilibrium and initiates a chain of decays beginning at ^{238}U or ^{232}Th and ending at the stable ^{206}Pb or ^{208}Pb, initiating all of the α, β and γ-decays for the entire chain with correct energies and branching ratios. Moreover, the ^{222}Rn chain was also simulated within the cavern air and the water tank to account for the elevated levels of radon at the time of the measurement and the rates normalised using the measured concentrations. The simulated dataset recorded energy depositions of the γ-rays within the NaI crystal and further smeared the data

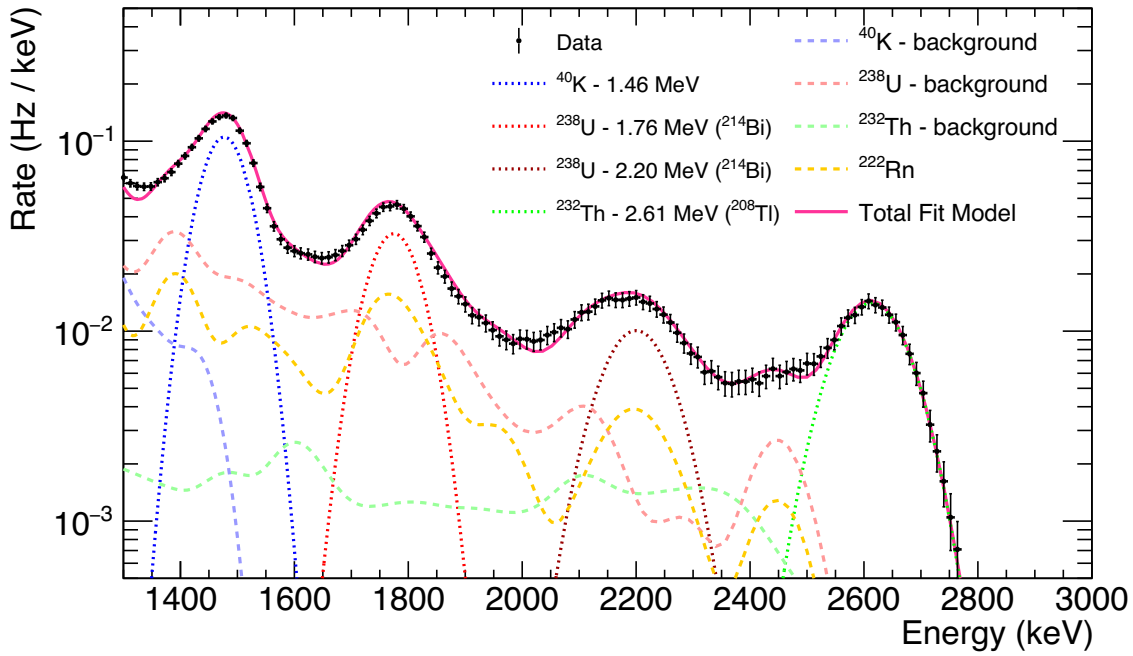

Figure 3.8: Fitted energy spectra for position (a) showing the 1461 keV ^{40}K peak, 1764 keV and 2204 keV peaks from ^{238}U and the 2614 keV peak from ^{232}Th, with background contribution PDFs from less dominant lines, air-borne radon and Compton scattering. Diagram adapted from [2].

using a Gaussian function; accounting for the energy resolution by using the resolution model fit to calibration data as shown in figure 3.5.

An equivalent of 1 Bq/kg was simulated to calculate the activity necessary for each isotope of interest within the cavern walls to reproduce the rates observed in data. The simplest technique to scale the simulations to data was by fitting a Gaussian to each of the prominent peaks at 1461 keV (^{40}K, BR: 10.66%), 1764 keV (^{214}Bi, BR: 15.30%) and 2614 keV (^{208}Tl, BR: 99.75%). Focusing on the photopeaks was done in order to select those γ-rays produced near to the surface of the cavern to reduce the effects of the Compton background leaking into each peak. The analysis further focused on γ-rays with energies of 1400 keV or above where the Compton background is less dominant. The Compton backgrounds overlaying the peaks of interest contain γ-rays from all energies and peaks from the uranium and thorium chains. To model for this, a background probability distribution function (PDF) was created using the simulated spectra of each isotope with the prominent lines removed and signal PDFs were produced from Gaussian functions with widths constrained within error bars obtained from the resolution function. A background PDF was also constructed for the ^{222}Rn decay chain γ-rays to account

for the ambient radon. The fit was constrained by fixing the branching ratio of ^{214}Bi, allowing the rate from radon to float within 20% uncertainty due to location dependent uncertainties, and the peak-to-continuum ratio was constrained to float within 20% of the simulated value for each contribution. An example of the fit to the unshielded data taken in the centre of the water tank is shown in figure 3.8.

The corresponding activity of ^{238}U, ^{232}Th and ^{40}K within the wall shell was calculated for each measurement position by using the three isotopic decays by comparison to the simulated rates. The activity for each isotope (denoted by the subscript i) and measurement position (denoted by the subscript p) is given by

$$A_{i,p} = \frac{R_{i,p} - R^{bkg}}{\epsilon R^{sim}_{i,p}}, \tag{3.9}$$

where $R_{i,p}$ is the signal peak in data as determined by the Gaussian fit, R^{bkg} is the internal background rate of the setup as measured in locations e and f, ϵ is the aforementioned efficiency correction determined from calibration and $R^{sim}_{i,p}$ is the simulation normalisation factor calculated using,

$$R^{sim}_{i,p} = \frac{N_{i,p}}{N^{tot}_{i,p} B_p M}. \tag{3.10}$$

Here $N_{i,p}$ is the raw number of counts in a given peak for isotope i and position p, $N^{tot}_{i,p}$ is the total number of events simulated, B_p is the event biasing multiplicative factor and M is the mass of the simulated shell. The event biasing multiplicative factor is as a result of a biasing technique used to increase γ-ray statistics hitting the detector by saving γ-rays on a predefined surface and then propagating a larger quantity onward with the same momentum in a second simulation. The fit results for each peak in activity $A_{i,p}$ are given in table 3.5.

3.5.4 Results & Discussion

In assuming that each measurement is an independent observation of the same flux within the cavern, the averaged activities across the positions of interest result in 220 ± 60 Bq/kg of ^{40}K, 29 ± 15 Bq/kg of ^{238}U and 13 ± 3 Bq/kg of ^{232}Th. The results from the HPGe screening of the shotcrete samples taken during the measurement indicate activities of 220 ± 30 Bq/kg of ^{40}K, 21 ± 1 Bq/kg of ^{238}U and 11.4 ± 0.4 Bq/kg of ^{232}Th, all of which are in good agreement within uncertainties with the results of this analysis.

Table 3.5: Results from the fits on the three signature peaks from the ^{40}K, ^{238}U and ^{232}Th decay chains. The best fit activities, A_m, of the resultant activity within the wall shell from each measurement are given for the positions of interest. The uncertainties are from fit results only, but systematic uncertainties are expected from the simplified simulation geometry. The average values are show at the bottom with their standard deviations. Data adapted from [2].

Measurement Position	Label	^{40}K (1461 keV) A_p [Bq/kg]	^{238}U (1764 keV) A_p [Bq/kg]	^{232}Th (2614 keV) A_p [Bq/kg]
Centre of tank (unshielded)	a	285 ± 1	36.9 ± 0.4	15.2 ± 0.14
Upper Davis (unshielded)	b	135 ± 4	10.4 ± 0.2	8.8 ± 0.1
Counting Room (unshielded)	c	264 ± 1	18 ± 0.2	12.2 ± 0.2
South Edge, looking down	d	182 ± 2	31.4 ± 0.2	16.7 ± 0.1
Centre of tank, looking up	g	214 ± 1	48.4 ± 0.2	9.5 ± 0.1
Averaged activities	-	220 ± 60	29 ± 15	13 ± 3

However, large variations are observed when taking a closer look at the activities from each measurement; although not fully understood, this could be a result of multiple factors. The first of these could be the uncertainty of the radon concentration within the cavern. The activity of radon used in the simulation were measured outside of the Davis cavern and without a model of the airflow into the cavern, it is difficult to account for this uncertainty. Since most of the γ-rays are emitted from the ^{222}Rn sub-chain, this uncertainty is expected to account for the observed large variations. Furthermore, the simulation does not take into account some of the key features of the cavern, such as the steel grating diving the two floors, walls of the counting room and the control room. Lastly, the variation in different activities may indicate towards a non-uniformity in the concentrations of each isotope spatially within the cavern walls, especially in places where the fluctuations in Shotcrete thickness may lead to γ-rays leaking from the highly active non-uniform Rhyolite layers. Despite the variations between measurements, the results can be used to estimate the background contribution from the Davis cavern for the LZ dark matter experiment.

The overall contribution of γ-rays from the cavern result in a total of < 5 ER events within the WIMP search region of interest, equating to a small fraction of the total expected ER events, as summarised in table 5.2. Nevertheless, as discussed in detail in chapter 5, this contribution is taken into account in determining the sensitivity of the LZ experiment to WIMPs. However, it is important to note that Cavern wall γ-rays make up around a third of all backgrounds for the $0\nu\beta\beta$ search in LZ [139].

Chapter 4

Radon Emanation in LZ

The discovery of radon dates back to 1900, when Friedrich Ernst Dorn reported results showing the emanation of a radioactive gas from radium compounds [140]. Since then we now know that all isotopes of radon are radioactive, and only four are found in nature. With advancements in reducing cosmogenic and detector backgrounds in low-background dark matter experiments, emanation of radon is now the largest background contributor for the WIMP search ROI [105]. The focus of this chapter is to highlight the relevance of radon for the LZ experiment; detailing the radon screening campaign of LZ, predominantly focusing on the work done at UCL and presenting the total expected radon emanation of the LZ detector.

4.1 Overview

Radon is a chemical element with an atomic number 86 found in the 6^{th} period of the noble gases. It occurs naturally in trace amounts in the radioactive decay chains through which uranium and thorium decay into lead and various other short-live radioactive elements, as shown in figure 3.1. It is found as a monatomic gas due to its full outer valence shell with solely radioactive isotopes. A consequence of its inert nature is that radon often exhibits a long diffusion length through solids. Its inert nature makes it extremely difficult for any filtration via chemical means, hence most removal attempts are achieved through physical methods.

Radon is a colourless and odourless gas under standard temperature and pressure (STP). Its melting and boiling points are comparatively high for a noble gas, at -71°C and -61.7°C, respectively, and is densest of the noble gases with a density of 9.7 kg/m^3. Activity of radon can vary substantially due to the composition of the environmental

conditions. Typical atmospheric activities are $\sim$10 Bq/m^3 and around 30–50 Bq/m^3 for indoor environments. In underground laboratories, such as SURF, the activities can vary between 200–1000 Bq/m^3 [133], with significant fluctuations due to the variance in ventilation rate of the underground facility. Salt mines report amongst the lowest activities of all underground laboratories, such as the Boulby mine with $\sim$3 Bq/m^3 [141].

The significance of the radon background in LZ motivates a need for material screening and selection. γ-ray spectroscopy can help elude to the activities of (^{238}U & ^{232}Th)$_e$ and (^{238}U & ^{232}Th)$_l$, but without material specific radon diffusion coefficients, its difficult to understand the radon emanation rate of materials purely from γ-spectroscopy. LZ utilises four facilities for radon emanation screening, built to collect and directly measure the emanated radon from screened samples, leading to a more accurate result in constructing the radon-induced background rate. The following sections will focus primarily on the operation of the UCL facility, highlighting important results measured for the LZ experiment. Thereafter, summaries of the other facilities will be detailed and the total radon budget of LZ will be taken into account.

4.2 Radon Backgrounds in LZ

4.2.1 Origin of Radon Emanation

4 in prev. page

All isotopes of radon are radioactive and only five are naturally found in minute quantities in nature. Those of interest for the LZ background model and often other low background experiments in search for WIMP dark matter or $0\nu\beta\beta$ experiments are ^{222}Rn ($\tau_{1/2}$ = 3.8232 d) from the ^{238}U decay chain and ^{220}Rn ($\tau_{1/2} = 55.8$ s) from the ^{232}Th decay chain; hereafter called radon and thoron, respectively. Due to the long lifetime of their progenitor isotopes, radon and thoron are produced at a near-constant rate within detector material. They can then diffuse out, mixing with the GXe or LXe, and inevitably decaying within the active volume of the detector. The emanation rate of a material can be broken down into two parts: emanation due to recoiling radon atoms (i.e. ^{222}Rn or ^{220}Rn) from their subsequent radium parent isotopes (i.e. ^{226}Ra or ^{224}Ra), E_{recoil}, and emanation due to diffusion, $E_{diffusion}$. The total emanation rate is then given by the sum total of the two components,

$$E_{tot} = E_{recoil} + E_{diffusion}. \tag{4.1}$$

Emanation due to diffusion can vary drastically depending on chemical and lattice structures of a material, density, surface roughness, and temperature; whereas the emanation from recoiling radon atoms depend heavily on the density of the material and the kinetic energy carried by the radon atom from the subsequent radium decay. ^{222}Rn (^{220}Rn) recoils with a kinetic energy of 86.26 (103.4) keV, with recoil ranges varying between 20–30 nm for materials such as Zircon or Quartz, and 60–65 µm for air and water [142]. The diffusion length, $L(m)$, is given as,

$$L(m) = \sqrt{D/\lambda}, \tag{4.2}$$

where D is the diffusion coefficient and λ the decay constant. A diffusion coefficient of 10^{-24} m^2 s^{-1} corresponds to $0.7(9 \times 10^{-3})$ nm for ^{222}Rn (^{220}Rn). Due to the much shorter half-life of ^{220}Rn, the emanation of ^{220}Rn in almost all material used in LZ is assumed to be dominated by the recoil emanation, whereas for ^{222}Rn both factors are assumed to play a role in the total emanation rate, with the ratio $E_{diffusion}/E_{recoil}$ expected to be suppressed in colder temperatures.

4.2.2 Radon Emanation Background in LZ

In LZ, the material and surfaces of interest for radon emanation are those that are in direct contact with either GXe or LXe. Upon emanation, due to its relatively long half-life, ^{222}Rn is expected to mix homogeneously within the active volume. Although the same assumption is made for ^{220}Rn, due to its much shorter half-life and diffusion length, a significant suppression is expected relative to ^{222}Rn, hence the assumed activity for ^{220}Rn is 5% that of the expected activity of ^{222}Rn as measured and estimated by radon screening. This assumption is made as a conservative measure as its extremely difficult to screen for ^{220}Rn emanation due to its short half-life.

The background from radon emanation for the WIMP search ROI is dominated by the ground-state to ground-state or *naked* β-emission from the ^{214}Pb progeny of the ^{222}Rn sub-chain, as it decays to ^{214}Bi. This results in a uniform ER background with a β-spectrum of up to 1019 keV. Similarly, the background from ^{220}Rn is from the *naked* β-emission from ^{212}Pb, as it decays into ^{212}Bi with a β-spectrum of up to 569.9 keV. The remaining decays from the sub-radon chain are either too high in energy—in the case of α-decays—or decay with a subsequent particle, i.e., a γ-ray or an α particle, and hence can be vetoed via coincidence tagging, as such is the case for the β-decay of ^{214}Bi, which is subsequently followed by the α-decay of ^{214}Pb with a half-life of $\tau = 162.3$ µs [114, 143].

The details of the decay of each isotope in the radon and thoron sub-chain are summarised in table 4.1.

Radon emanation requirements for the LZ experiment are predetermined to ensure that the background due to radon does not significantly dominate over the irreducible *pp* solar neutrino background, in order to maximise the WIMP search sensitivity in the low mass region. A total of 20 mBq of ^{222}Rn activity is set as the threshold, of which 13.4 mBq is within the 7 tonnes of the active volume and 11.2 mBq in the 5.6 tonne fiducial volume. The radon emanation background from the latest projections account to $\sim$66% of the projected ER background in the WIMP search region of interest in LZ [105], predominantly from a projected ^{222}Rn(^{220}Rn) specific activity of 1.83(0.09) µBq/kg that corresponds to approximately 18.3(0.9) mBq in the 10 tonnes of xenon. The methodology used in estimating the projected activity of ^{222}Rn and ^{220}Rn will be highlighted in later sections.

Table 4.1: Details of isotopes in the ^{222}Rn and ^{220}Rn decay chains, starting from ^{226}Ra (upper) and ^{224}Ra (lower), down to ^{214}Po and ^{212}Po, respectively. The table also details the progenitor isotopes of the radon and thoron chains; ^{238}U and ^{232}Th.

Isotope	**Decay**	**Q-value [MeV]**	$\tau_{1/2}$		**Daughter**
^{238}U	α	4.270	4.47(10^9)	y	-
⋮	⋮	⋮	⋮		⋮
^{226}Ra	α	4.871	1600	y	^{222}Rn
^{222}Rn	α	5.590	3.8232	d	^{218}Po
^{218}Po	α	6.115	3.071	m	^{214}Pb
^{214}Pb	β	1.019	26.9	m	^{214}Bi
^{214}Bi	β	5.621	19.8	m	^{214}Po
^{214}Po	α	7.833	162.3	µs	^{210}Pb
^{232}Th	α	4.081	14.02(10^9)	y	-
⋮	⋮	⋮	⋮		⋮
^{224}Ra	α	5.789	3.631	d	^{220}Rn
^{220}Rn	α	6.405	55.8	s	^{216}Po
^{216}Po	α	6.906	0.148	s	^{212}Pb
^{212}Pb	β	0.570	10.64	h	^{212}Bi
^{212}Bi	β	6.207	60.54	m	^{212}Po
^{212}Po	α	8.954	300	ns	^{208}Pb

4.3 UCL Radon Emanation System

Material screening for radon emanation is often interpreted as the activity of radon released from the measured sample. Depending on the material at hand, the units are therefore either given in becquerels per surface area, mass or quantity of a given item. Most of the screening efforts are conducted on fractional quantities of the final material usage and the activities are scaled assuming to apply to the entirely of the material, provided they come from the same manufacturer and undergo the same cleanliness treatments as those screened.

Radon activity is reconstructed by measuring the radon sub-chain daughter isotopes, often ^{218}Po and ^{214}Po. Although commercial radon detectors are readily available—such as the Durridge Rad7 devices, their sensitivity is restricted to 0.5 Bq/m^3, which is orders of magnitude away from the sensitivity required for a reliable measurement of radon activities in the µBq–mBq range, as required by LZ. The UCL radon emanation system, initially designed and constructed for the SuperNEMO $0\nu\beta\beta$ experiment, utilises on a custom-made electrostatic detector, specially developed for use in many low background experiments. The following sections will briefly highlight the design and the operation of this system; outlining the detection technique, detector specifications and calibration measurements. More details on the construction of this system can be found in [144, 145].

4.3.1 Radon Detection & Techniques

The techniques involved in screening for radon generally reconstruct the radon emanation rate by measuring the radon sub-chain daughter isotopes. An indirect way of achieving this uses gamma spectroscopy to measure the ^{214}Bi and ^{214}Pb decay rates, from which the radon decay rate can be inferred. Although some useful constraints can be derived, it is extremely difficult to distinguish between radon daughters decaying in the bulk of the material and those that decay outside of the material. Thus, emanation rates cannot be deduced without a material-specific diffusion model.

A more direct and accurate approach, one that has been utilised in the UCL system, is to directly measure the activity of radon that has emanated out of detector material. The sample material is initially enclosed in an air-tight chamber that is filled with a low-radon carrier gas, typically helium or nitrogen. This carrier gas prevents recoiling radon atoms from embedding themselves in the walls of the chamber. After an emanation period that allows the radon concentration in the chamber to approach equilibrium, the

emanated radon atoms are transferred into a detector that can directly measure the rates of ^{218}Po and ^{214}Po. The emanation rate is reconstructed by correcting for the detection and transfer efficiencies measured during dedicated runs with radon sources of known activity.

The radon emanation rate is often determined by detecting the α-particles of the radon progenies ^{218}Po and ^{214}Po in electrostatic detectors. In using the progenies to reconstruct the emanation rate, its important to understand the relationship between the activities of these isotopes to that of their parent isotope ^{222}Rn. In a radioactive decay chain, the number of atoms of a given isotope is dictated by the homeostasis between the number of atoms decaying from the parent isotope and those that are decaying into new daughter isotopes. When considering the decay chain, it is useful to introduce the following notation to identify the number of atoms and decay constant for each isotope:

$$\begin{array}{ccccccccc} ^{222}\mathrm{Rn} & \rightarrow & ^{218}\mathrm{Po} & \rightarrow & ^{214}\mathrm{Pb} & \rightarrow & ^{214}\mathrm{Bi} & \rightarrow & ^{214}\mathrm{Po} \\ N_0, \lambda_0 & & N_1, \lambda_1 & & N_2, \lambda_2 & & N_3, \lambda_3 & & N_4, \lambda_4 \end{array}$$

The number of atoms of a given isotope in the chain can be represented as,

$$\frac{dN_i}{dt} = \lambda_{i-1} N_{i-1} - \lambda_i N_i. \tag{4.3}$$

The activity of isotopes down the entire decay chain and its evolution with time can then be calculated by iteratively solving the above differential equation, provided $i = 0$ represents ^{222}Rn and appropriate starting conditions are assumed; i.e. at $t = 0$, $N_0 = x$ Bq, $N_{1-4} = 0$. The full deviation of activities down to ^{214}Po can be found here [144] and the evolution of activities of the chain starting from ^{222}Rn with an assumed activity of 1 mBq is shown in figure 4.1. Its important to note that the activity of ^{218}Po quickly reaches an equilibrium with ^{222}Rn, whereas it takes $\sim$4.5 hours for ^{214}Po. Hence, this slight delay needs to be taken into account if the emanation from a sample is transferred into the detector prior to equilibrium. Provided equilibrium is reached, the measured activity of both ^{218}Po and ^{214}Po will be equivalent to the activity of ^{222}Rn.

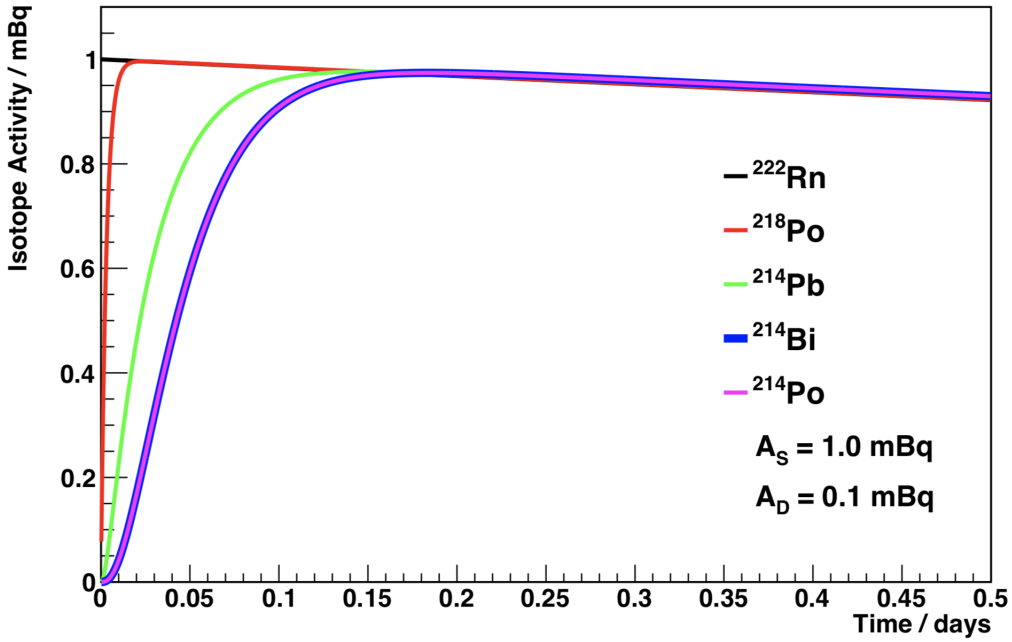

Figure 4.1: The evolution of activities of the ^{222}Rn decay chain with respect to time under the starting condition of 1 mBq of ^{222}Rn. A_D represents the intrinsic background activity of the detector. Figure adapted from [144].

4.3.2 Electrostatic Detector

The electrostatic detector used in this work has been specially developed for the use of ELEGANT V and Super-Kamiokande experiments in measuring low-levels of radon [146, 147]. A detector with identical specifications developed by the same group was later acquired for SuperNEMO for background studies, as detailed in [144]. Its design capability can measure radon activities to 1-2 mBq/m^3, 2 orders of magnitude improvement upon commercially available radon detectors. The schematics of the system are shown in figure 4.2.

The simple design of the detector consists of an electro-polished stainless steel chamber with a 70 litre volume with a silicon PIN-diode attached to the top of the detector as shown schematically in figure 4.3. The associated detector electronics are housed in the lid of the detector, separated from the measurement chamber by a sheet of perspex with a feedthrough for the PIN-diode. The detector has an inlet and an outlet valve for gas flow, all either metallic or have been coated with styrene butadiene rubber (SBR) to reduce the internal radon background that diffuse out or through material and into the detector volume. An electric field is generated inside the chamber by applying a negative high voltage (typically 1500 V) onto the PIN-diode.

Figure 4.2: Pictorial diagram of the electrostatic detector used for the radon emanation results published in this work. Left shows the detector in full operational mode and the right shows it without its lid, where the feedthrough for the PIN-diode can be seen.

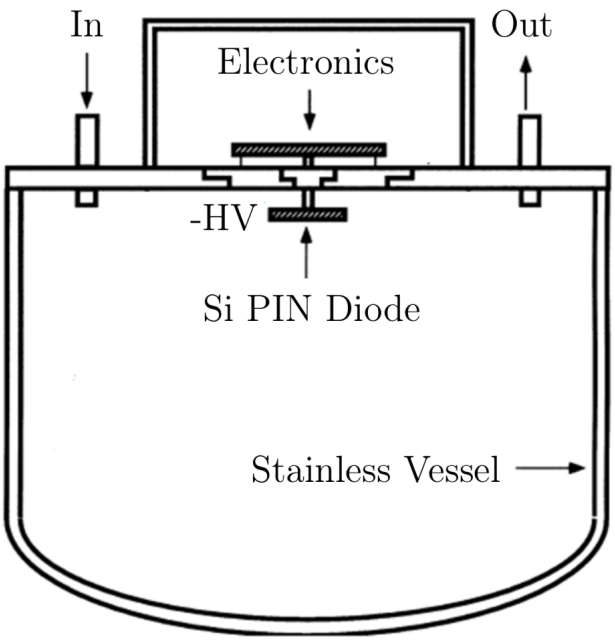

Figure 4.3: A schematic diagram of the electrostatic detailing the electronics.

In a standard operation, a sample is usually left to emanate for a set amount of time after which the gas content is transferred into the detection volume. The radon atoms decay within the volume result in daughter nuclei that are predominantly positively charged ions ($87.3 \pm 1.6\%$ [148]). These ions are effectively collected by the PIN-diode as a result of the applied electric field. The α particles emitted from the ^{218}Po and ^{214}Po ions are detected by the PIN-diode as they undergo α-decay and are distinguished by the energies they deposit; 6.1MeV and 7.9MeV, respectively.

4.3.3 Detector Efficiency

Understanding the response of the detector to a known activity of radon is vital in modelling the detector response and correcting the measured activity for detector related efficiencies. In modelling this, a calibration source of ^{226}Ra (Pylon Electronics, RN-1025) with a known activity of 1.32 kBq was used. The source is designed to allow for gas flow through the material to transfer the emanated radon effectively into the detector volume, ensuring all of the radon to be exhausted.

The method used in calibrating the detector is sometimes referred to as the *spike* method. The source volume is initially flushed out by the use of a helium carrier gas by around 10–100 times the volume of the source to ensure all of the radon is exhausted thoroughly. The volume is then sealed for a set amount of time to allow for a set amount of radon to build up. In a typical calibration, helium is used as a carrier gas to move 2.5 Bq of radon into the detector. The background spectrum of the electrostatic detector without and with a typical calibration source injection is shown in figure 4.4.

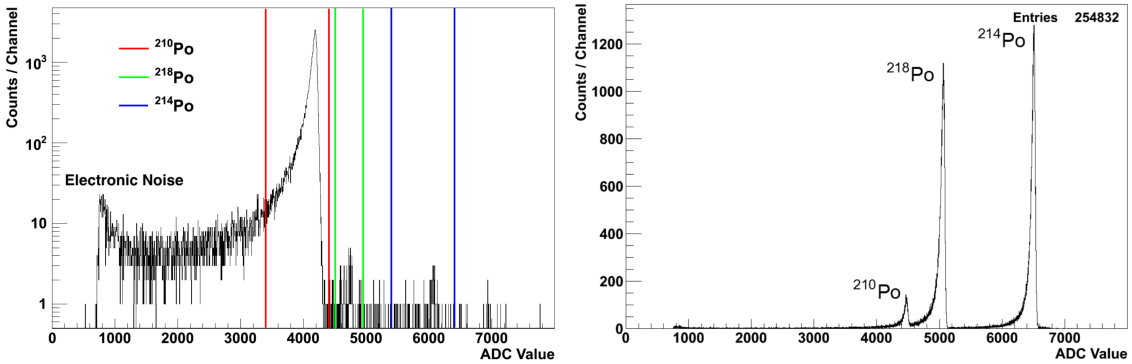

Figure 4.4: Spectrum from the electrostatic detector without (left) and with (right) 2.5 Bq of the calibration source present. The spectral peaks of ^{210}Po, ^{218}Po and ^{214}Po are displayed from left to right. The red, green and blue windows are used to select regions of the spectrum associated with the isotopes of interest for further analysis.

In an event where the ionised radon progeny attaches onto the PIN-diode and undergoes α-decay, the kinetic energy carried by the α-particle can be identified by the induced amplitude of the signal. The energy resolution of these detectors is such that the peaks observed for the three isotopes of polonium are clearly visible after the source injection. Although some ^{210}Po is present as a result of the calibration source, the majority of its observed activity is as a result of residual exposure of the PIN-diode and its longer half-life of $\sim$140 days. This residual activity is more apparent on the background spectrum of the detector prior to source injection, as seen on the left in figure 4.4. Although one may naively think that the peaks of ^{214}Po and ^{214}Po should be identical in activity (counts), this is often not the case. This apparent difference in efficiency is thought to be as a result of ^{214}Po decay taking place after multiple intermediary isotopic decays. The intermediate isotopes ^{214}Pb and are assumed to be predominantly created as ions and as a result are collected by the PIN-diode. This results in more ^{214}Pb either on the PIN-diode or close to the PIN-diode, reducing the probability of neutralisation, which often takes place under trace amounts of impurities, such as nitrous oxide (N_2O). Although α-decay counts from both ^{218}Po and ^{214}Po can be used to reconstruct the radon activity, the activities quoted are from ^{214}Po due to its higher detection efficiency. Furthermore, despite the energy resolution, some overlap between the ^{218}Po and ^{210}Po peak is unavoidable.

To calculate the detection efficiency, the peaks of ^{218}Po and ^{214}Po are initially selected with predetermined windows, and their respective activities are fit using decay equations derived from equation 4.3 and shown in detail in [144]. A typical result from a 2.5 Bq of radon injection into the detector is shown in figure 4.5. The detection efficiency was then calculated as $27.1 \pm 1.4\%$ and $31.6 \pm 1.6\%$ for ^{218}Po and ^{214}Po, respectively. Its important

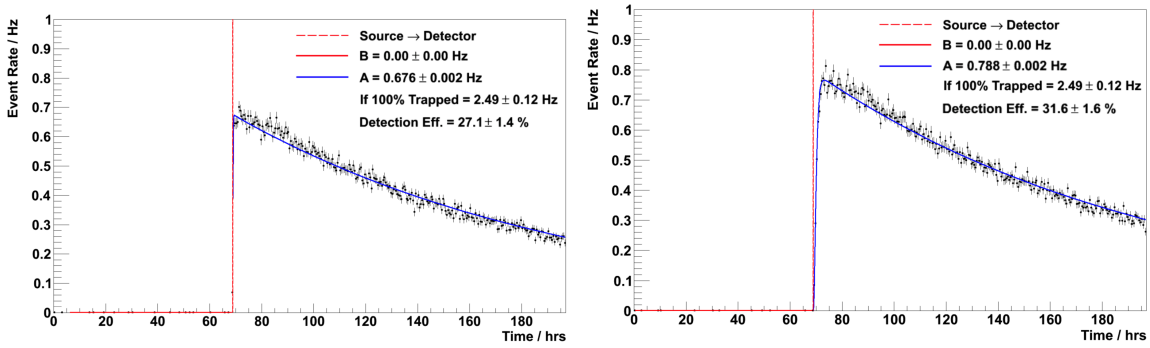

Figure 4.5: ^{218}Po (left) and ^{214}Po (right) event rates for a calibration injection of 2.5 Bq of radon into the detector via a helium carrier gas. The fitted black line shows the expected response for the given isotope with all half-lives fixed to their known values.

to note that the maximum detection efficiency achievable using this technique is 50%, as half of the α-particles are emitted away from the PIN-diode and hence never measured.

4.3.4 Detector Background Measurement

The sensitivity of the detector and the measured activities are not limited to the efficiency of the detector alone but also the detector background rate. In general, a typical measurement would include a measurement of the background rate of the detector ~ 5 days prior to the transfer. This background rate is then subtracted from the measured activity post transfer. Additionally, much longer background measurements are performed periodically to ensure the stability of the detector. In such measurements, the detector is fully sealed to both the gas line and the environment and the radon activity is continuously measured. The energy spectrum from this type of run is different to that of a calibration run as can be seen in figure 4.6.

The observed spectrum is similar to that of a typical material measurement with a dominant ^{210}Po that has accumulated onto the PIN-diode from prior calibration runs. The ^{218}Po and ^{214}Po peaks are visible on a logarithmic scale and a smaller peak from ^{212}Po at 8.9 MeV from the thoron chain is also visible. The peaks are selected with pre-determined windows as shown by the vertical lines on figure 4.6 and the activity of ^{214}Po, along with that of ^{210}Po is shown in figure 4.7.

The inferred ^{214}Po rate, which is the primary channel to reconstruct the radon emanation rate shows an averaged daily rate of 6.2 ± 0.7 counts-per-day (cpd). The detector in this measurement is initially flushed thoroughly and filled with helium gas, so by using the detector efficiency of 31.6% for ^{214}Po, the intrinsic activity of the detector is determined

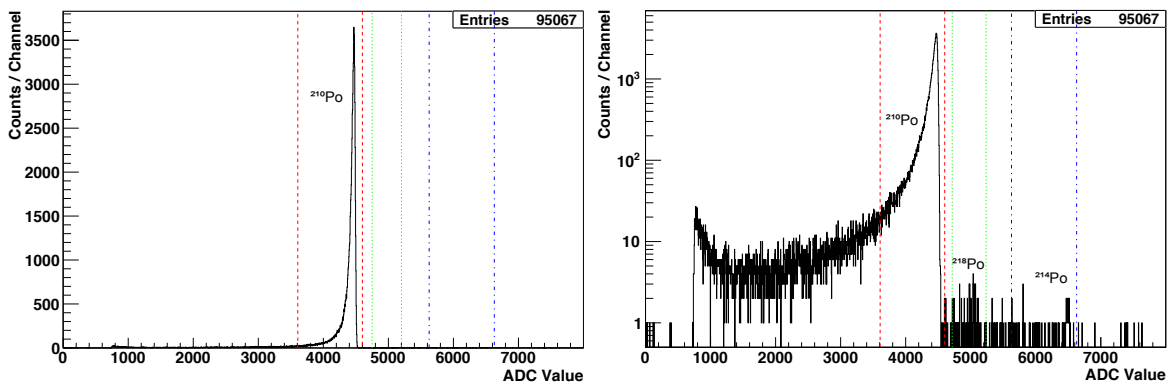

Figure 4.6: Energy spectrum of a long detector background measurement with linear and logged y-axis. The peaks of ^{210}Po, ^{218}Po and ^{214}Po are displayed accordingly.

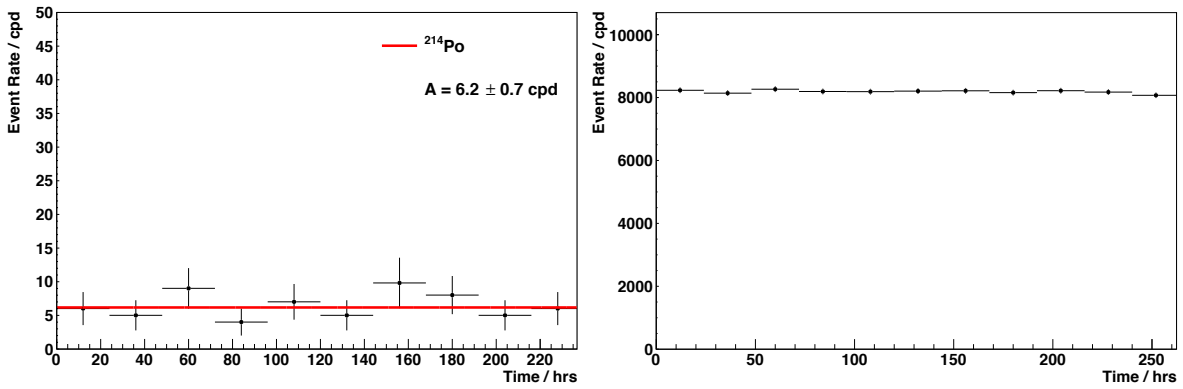

Figure 4.7: ^{214}Po (left) and ^{210}Po (right) event rates for a typical background measurement run. The ^{214}Po rate shows a relatively low background level, whereas the ^{210}Po shows the stability of the detector.

to be 0.20 ± 0.02 mBq. Besides the ^{214}Po rate, the ^{210}Po rate is also measured as shown in figure 4.7. Although this does not inform on the radon activity, it is a useful measure in checking the stability of the detector and the DAQ over time, as this rate is expected to be constant over a measurement period.

4.3.5 System Design and Schematics

The electrostatic detector as detailed in the previous sections is part of a large system that handles gas flow in and out of the sample chamber and detector. A pictorial and a schematic diagram of the design is shown in figures 4.8 & 4.9.

The system is design to facilitate a high degree of flexibility in operation. The carrier gas enters from the location marked as *He* and can either flow through the radon emanation chamber (REC) or by-pass the chamber; crucial for calibration source injection or flushing the system without impacting the source emanation with the REC. Although helium has been used as the primary gas carrier, nitrogen can also be injected through the same flow path. Prior to entry, the gas is initially passed through an activated charcoal trap stored in an ultra-low temperate freezer (193 K) with 0.5 micron stainless steel particulate filters fitted on both ends to reduce particulate contamination. The charcoal trap scrubs the radon generated from the cylinders of the gas carriers to supply radon-free gas into the entire system. The carrier gas is then directed by a series of valves, with a flow meter determining the flow rate. All pipework is made from stainless steel and all valves are fully metallic, which reduces radon emanation.

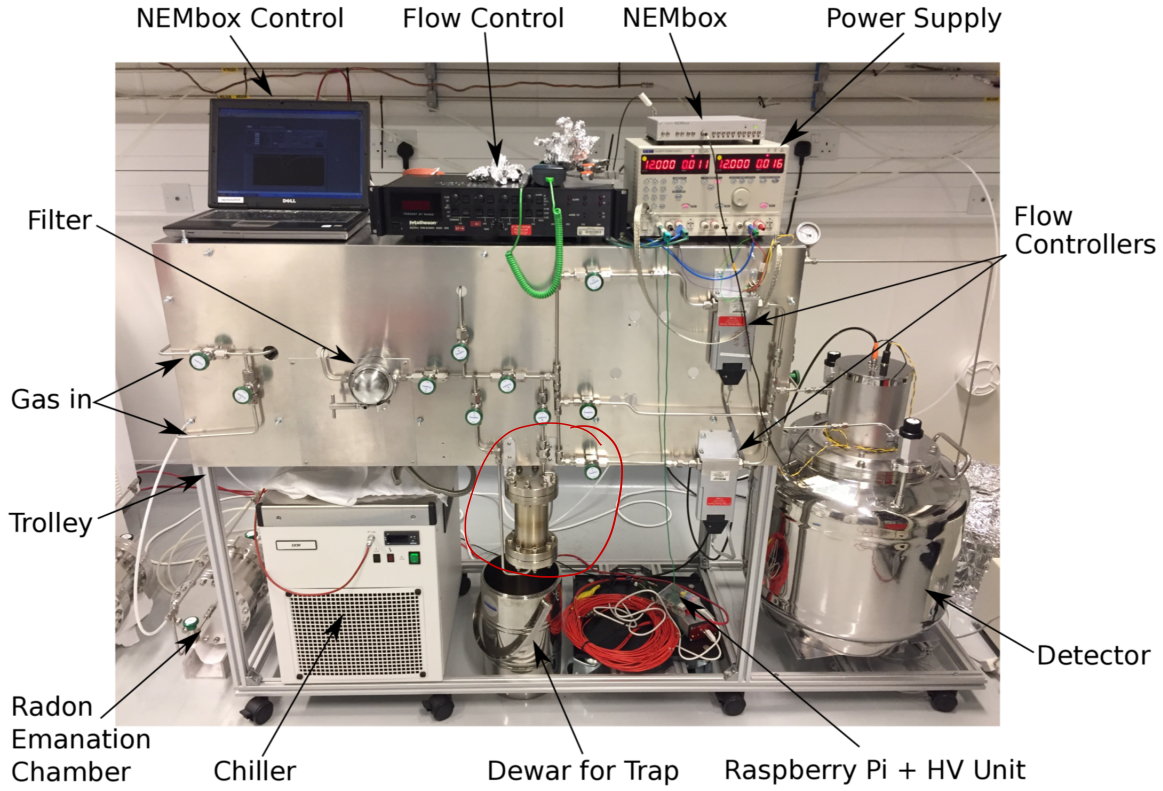

Figure 4.8: A pictorial diagram of the UCL radon emanation system with key components highlighted.

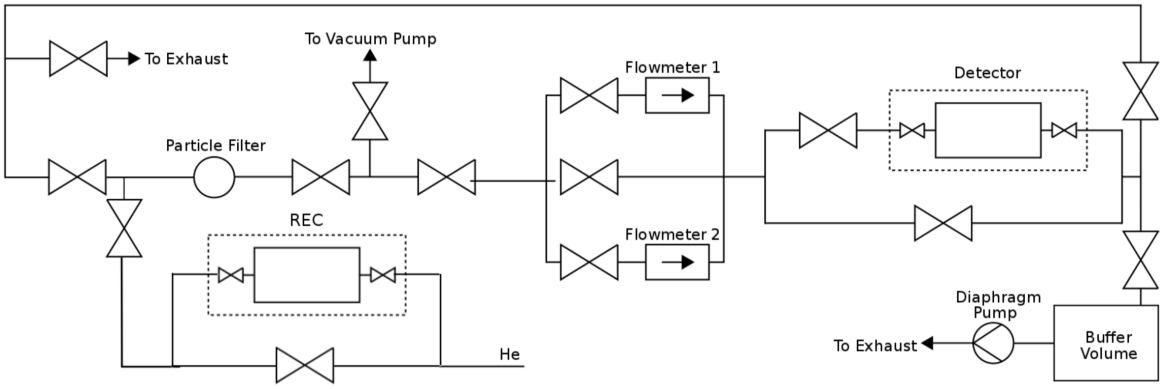

Figure 4.9: A schematic diagram of the UCL radon emanation system.

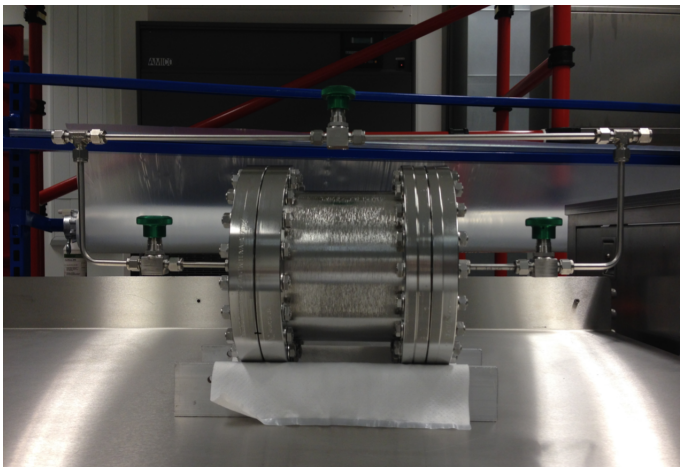

Figure 4.10: A pictorial diagram of the 2.7 L stainless steel radon emanation chamber used to house samples for emanation.

The system operates two 2.7 L stainless steel chambers as the emanation media, as shown pictorially in figure 4.10. Once the sample is sealed inside the chamber, the chamber is flushed thoroughly to remove any ambient radon trapped inside and checked for leaks using a helium leak detector (GasCheck Tesla Helium Leak Detector)—ensuring no leaks above 10^{-6} cc/s is observable. The larger detector volume and the small chamber volume allow a single step transfer process, where helium gas is flushed through the emanation chamber, carrying the emanated radon from the sample within the chamber directly into the detector. A carrier gas volume of ten times the chamber volume is used in this process to ensure a near 100% transfer efficiency from the chamber into the detector. This mode of operation has been the primary way samples were screened for LZ.

A second mode of operation for the system uses 57 g of activated carbon (a synthetic charcoal sourced from Carbo-Act International [149]) as a radon collection trap. In larger emanation volumes, the radon is initially absorbed into the cooled trap while the carrier gas passes through. The trap is then heated to release the radon and the carrier gas is then used to transfer the concentrated radon into the detector volume. The trapping efficiency for this setup has been measured to be $\approx 93\%$ at 248 K [145].

4.4 Radon Emanation Measurements for LZ

Screening key components of the LZ detector that are in direct contact with the xenon circulation system for radon emanation has been one of the primary focal points in the LZ screening campaign. The UCL radon emanation system has been used extensively for

several of these key measurements; including various PMT bases that are located inside the ICV and the TPC, the raw titanium and titanium welding used for the cryostats and several other structural segments with the ICV, and various other items. This section will highlight some of these results in detail.

4.4.1 PMT Bases

The LZ detector will use a total of 500 3", 39 2" and 94 1" PMT bases, all of which reside in the xenon volume of the detector. The components used in these bases are mostly (both in mass and area) made up of Cirlex (Kapton) printed circuit boards (PCBs), solder, capacitors, resistors and receptacles; together adding up to a considerable surface area within the xenon. Assays of these individual components have previously been conducted with γ-screening and radon emanation to build a *bottom-up* model of the expected radon from the fully assembled bases. The solder and the receptacles were excluded as they yielded low $^{238}U_e$ activities with γ-screening; and emanation results from the other components yielded a *bottom-up* approximation of 1.01 mBq for all bases used in LZ. This corresponds to 1.65 µBq and 1.25 µBq per a 3" and 1" base respectively. The pictorial diagram of the 1" and 3" bases used in this study are shown in figure 4.11.

Table 4.2: Relation of components in the different kind of LZ bases. The Cirlex mass is proportional to the Cirlex surface since all the bases are made of a 1.5 mm thick Cirlex PCB. All resistors and capacitors have the same dimensions. Regarding the solder, please refer to the text.

Components	**3" PMT Bases**	**2" PMT Bases**	**1" PMT Bases**
Cirlex PCB	3300 mg	3300 mg	1680 mg
Resistors	15 units	15 units	13 units
Capacitors	5 units	5 units	3 units
Receptacles	19 units	20 units	3 units
Solder	180 mg	180 mg	300 mg

Although the bases are all constructed from the same material, they do differ in the quantity of components use. These differences are highlighted in table 4.2. The 3" and 2" PMT bases are essentially identical in size and component use, with the only minor difference being the additional receptacle used on the 2" PMT base. Hence, the results obtained for 3" bases are also assumed for 2" bases. The 1" bases are substantially

different and hence were separately screened. The 180 mg value quoted for the total mass of solder used per 3" base was measured by weighing the bases before and after solder was applied. However, the same approach was not conducted for the 1" bases. The difficulty in doing a similar measurement was due to the variation in the amount of solder used for an individual 1" base. The 1" bases use similar number of components and in addition to this, they contain two reinforced solder tracks, hence a 300 mg was adopted as a best estimate.

Emanation of 3" Bases

A total of 124 3" bases were packaged inside radon tight bags at the Imperial College cleanroom and transported to the radon facility cleanroom at UCL. Each base was then carefully taken out of the radon tight packaging and placed inside the emanation chamber with caution to avoid scratching or damaging base components. After the emanation period, the radon was transferred into the electrostatic detector and measurements on the decay rates of ^{214}Po and ^{218}Po were made. A second measurement was followed before the bases were transported back to Imperial College. The pre-corrected ^{214}Po

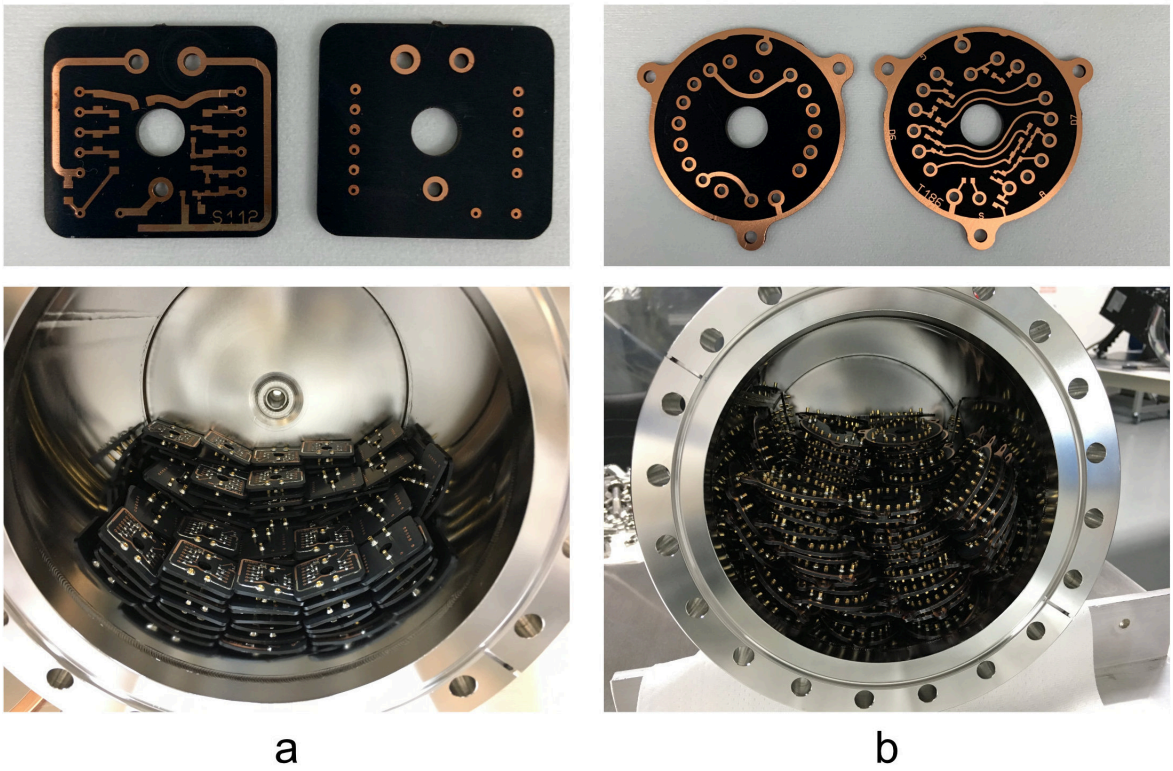

Figure 4.11: A pictorial diagram of the 1" (a) and 3" (b) PMT base boards and their positioning within the UCL emsanation chamber.

rates from these two measurements are shown in figure 4.12. Although not provided, the ^{218}Po rates were checked for completeness and was found to agree within error with those obtained from ^{214}Po. The output from the ^{214}Po result was then corrected by applying the detector efficiency corrections detailed in section 4.3.3 to give a total radon emanation rate of 0.62 ± 0.11 mBq and 0.70 ± 0.11 mBq for 124 3" bases for the first and the second measurement respectively.

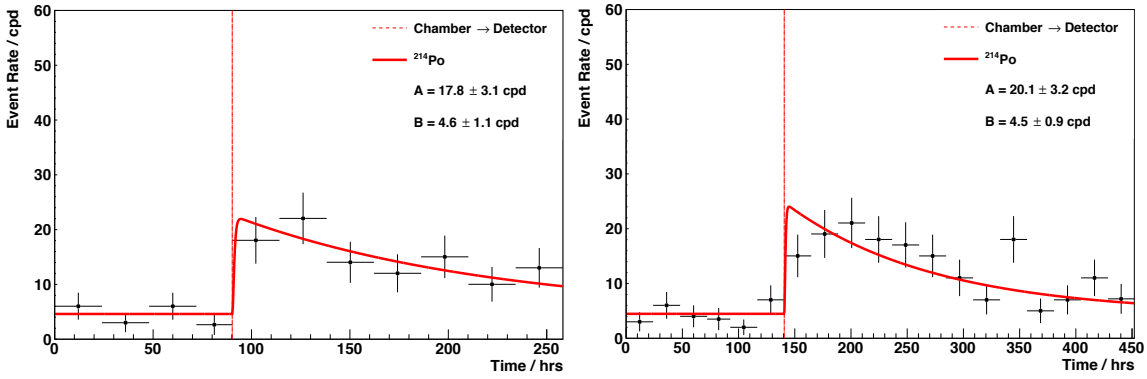

Figure 4.12: Pre-corrected ^{214}Po event rates of 124 3" PMT bases screened using the UCL radon emanation system. The bases were prepared and cleaned with a procedure identical to those used in the LZ detector.

rationale behind two measurements.

Emanation of 1" Bases

The emanation results from the 3" bases yielded a large discrepancy between the bottom-up estimations, hence 120 1" bases were emanated at the UCL facility to determine the radon background from these bases, as the bottom-up estimations were no longer reliable for the LZ background projections. Furthermore, the instrumental differences between the 3" and 1" could help understand why such a large discrepancy was observed; whether some of the components making up the bases were more radioactive than expected. These bases were treated identically to the 3" bases; initially cleaned at the Imperial College cleanroom to remove any surface contamination, and later transported to the UCL facility in radon tight packaging to minimise radon plate-out. The pre-corrected results obtained for ^{214}Po and ^{218}Po rates are in agreement within error and their rates within the detector are shown in figure 4.13. The output from the ^{214}Po decay rate is then corrected by applying the detector efficiency corrections and the radon emanation rate of 120 1" bases are calculated to be 0.53 ± 0.11 mBq.

Need more detail. the length of emanation, BKGR in chamber etc.

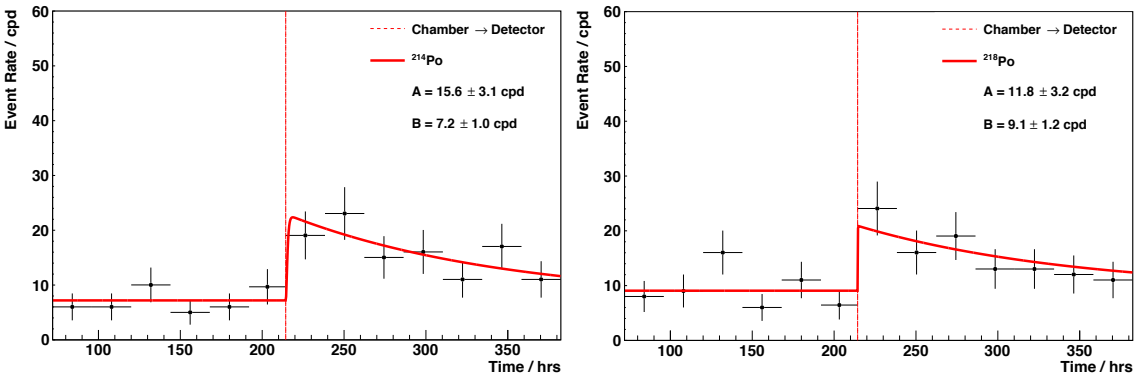

Figure 4.13: Pre-corrected ^{214}Po (left) and ^{218}Po (right) event rates of 120 1" PMT bases screened using the UCL radon emanation system. The bases were prepared and cleaned with a procedure identical to those used in the LZ detector.

Discussion & Conclusion

The radon emanation results from the 3" and the 1" bases, along with their bottom-up estimates are highlighted in table 4.3 for comparison. The results indicate a radon emanation activity of 5.33 µBq and 4.42 µBq per 3" and 1" base; which is 3.68 µBq and 3.17 µBq above the bottom-up estimation respectively. Although the 1" bases have less Cirlex and electronic components, the activity in comparison to the 3" bases are relatively high, suggesting the solder to have a non-zero activity comparable to some of the components taken into account. In assuming the 3" bases emanation rate also applied to the 2" bases, the contributions from all LZ bases together returns a total contribution of 3.21 ± 0.35 mBq. Furthermore, a cross-calibration campaign between all of the radon facilities used by LZ, as highlighted in section 4.5, indicated an upwards

Table 4.3: Radon emanation results as obtained from the UCL system for the 3" and the 1" bases with bottom-up comparisons. All the results are given per respective base. A measurement from the XENON1T collaboration for 3" bases with almost identical design and component usage is provided for comparison [150].

Measurement	3" Bases [µBq/base]	1" Bases [µBq/base]
Bottom-up	1.65	1.25
1^{st} Measurement	5.00 ± 0.86	4.42 ± 0.90
2^{nd} Measurement	5.65 ± 0.90	-
Averaged	5.33 ± 0.63	4.42 ± 0.90
XENON1T Bases	3.0 ± 0.6	-

systematic for the UCL radon emanation system of 1.53 when compared to the base rate of the sample. In considering this systematic, the total radon emanation rate of the bases go down to 2.10 ± 0.23 mBq. This equates to an activity of 3.38 ± 0.41 µBq/[3" base]—in good agreement with the result obtained by XENON1T [150]. It is important to note that these values do not assume any reduction in rate due to temperature and the actual rate in LZ may be lower due a temperature suppression.

4.4.2 Cryostat Titanium & Titanium Welding

In the early stages of the LZ experiment, an extensive R&D campaign was conducted to source and produce enough titanium for the cryostat vessels of the detector. The ICV and the OCV, which contain the TPC and the 10 tonnes of LXe, make up a significant bulk of the LZ detector. Due to their scale and proximity to the TPC, it was necessary to ensure ultra-low levels of radiopurity for ^{238}U and ^{232}Th isotopes as well as ^{40}K and ^{60}Co. A detailed analysis using ICP-MS and gamma-ray spectroscopy of 22 different titanium samples was conducted, and the sample of the HN3469 product manufactured by TIMET was found to have the lowest background. The measured activities for $^{238}\mathrm{U}_e$, $^{232}\mathrm{Th}_e$, ^{60}Co and ^{40}K from the sample are significantly lower than requirements and were the lowest reported to date [108].

Assuming chemical equilibrium within the titanium for both the uranium and thorium series, the ultra-low activities measured by the ICP-MS facility for $^{238}\mathrm{U}_e$ (<0.13 ppb) and $^{232}\mathrm{Th}_e$ (0.069(7) ppb) lead to a negligible amount of radon emanation, with the assumption that diffusion would be heavily suppressed due to the dense metallic nature of titanium. To this day, there are no known measurement of radon emanation from titanium, however, results from steel sheets and welding have previous been reported by the GERDA collaboration with activities in $\mathcal{O}(10)$ µBq/m^2 [151, 152].

Although the OCV is relevant for γ-rays, backgrounds for radon emanation is only expected from the ICV and its inner content. The ICV uses a total of 950 kg of titanium with several other titanium pieces used for structural support of PMTs, both in the skin region and within the TPC. Furthermore, the ICV is made up of several smaller segments welded together using $\sim$6 kg of titanium welding rods. After the installation of the skin region at SURF, the ICV was sealed and left to emanate. The results obtained from the harvested radon from the ICV indicated an emanation rate of 28.3 ± 2.0 mBq; in comparison to this, the expected bottom-up emanation from individual measurements of components within the ICV was only $2.3^{+3.7}_{-0.9}$ mBq. This large discrepancy was unexpected and prompted a radon screening campaign to examine some of the potential sources;

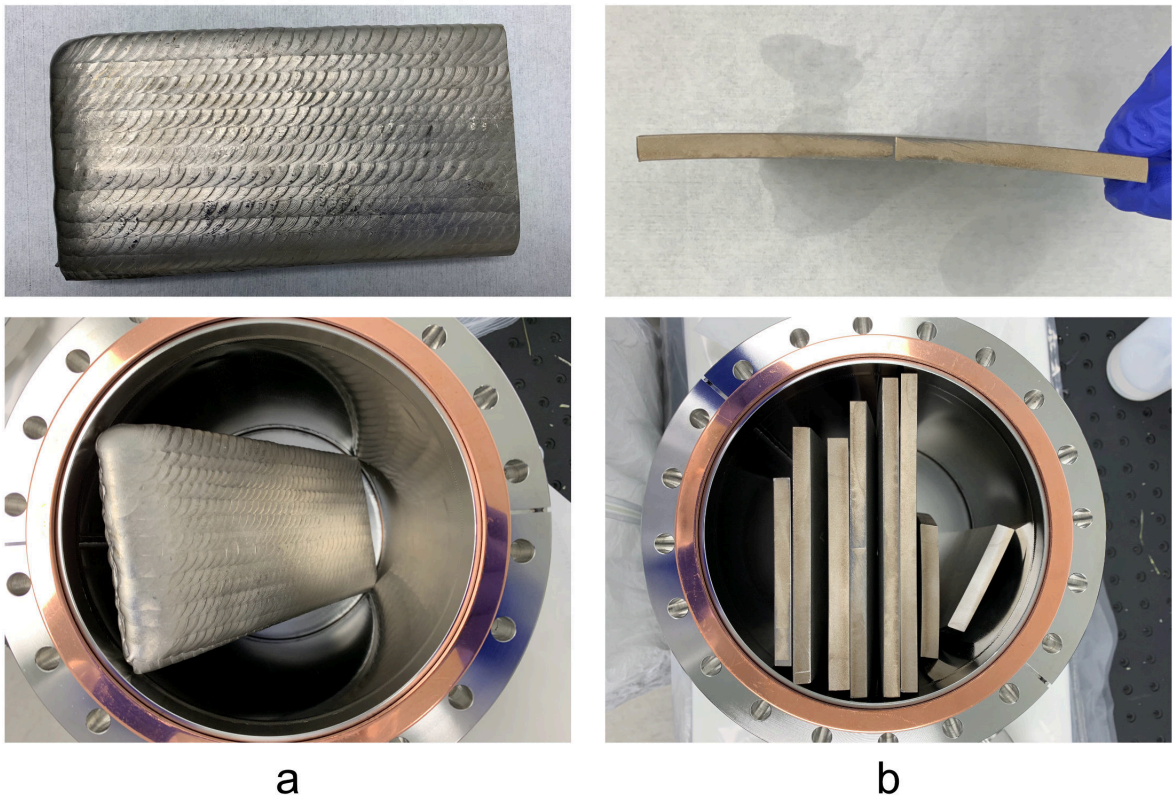

Figure 4.14: A pictorial diagram of welded titanium block (a) and the titanium sheets (b) cut-off from the LZ OCV.

emanation from dust accumulation and from unaccounted components (i.e. titanium cryostat and welding).

To examine radon emanation from the welded surface and the raw titanium surface, a 7 mm titanium plate welded with titanium and several titanium cutouts from the OCV were shipped to the UCL radon facility. A pictorial diagram of these two samples can be seen in figure 4.14 just before their respective emanation periods. The welded block was originally constructed from the LZ stock to study abnormally high ICP-MS measurements, detailed in [1].

Titanium Welding

To examine radon emanation from a titanium welded surface, a sample of 7 mm Ti plate with a large TIG weld on both sides with a total welding surface area of 325 cm^2 was assayed at the UCL facility. The sample is one of four blocks originally prepared for quality control during the ICV and OCV manufacturing. Studies on this sample using ICP-MS yielded concentration of 0.16 ± 0.04 ppb $^{238}U_e$ and 3.20 ± 0.16 ppb $^{232}Th_e$. The

higher levels of $^{232}Th_e$ were attributed to the inadvertent use of thoriated electrodes, which was later corrected as a result of this study with no impact on background. The final welding used inside the ICV was from the same titanium stock but used lanthanated elecrodes. ^{222}Rn is strictly coming from the ^{238}U decay chain and hence the results highlighted here are assumed to apply to lanthanated welding. Two sets of measurements were performed on the welded block: emanation prior to etching and post etching by AstroPak—a certified professional precision cleaning company. Results obtained for the pre-etched and post-etched block are shown in figure 4.15 and 4.16, respectively. Pre-etched block was measured once, whereas the post-etched block was measured twice.

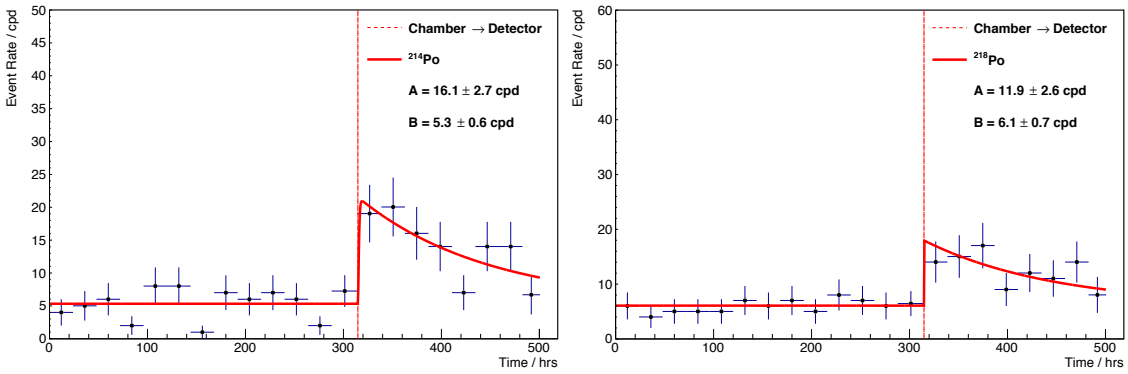

Figure 4.15: Pre-corrected ^{214}Po and ^{218}Po event rate results obtained from the single measurement made on the pre-etched titanium welded block. The block was initially wiped extensively with wet cleanroom wipes and ultrasonic bathed.

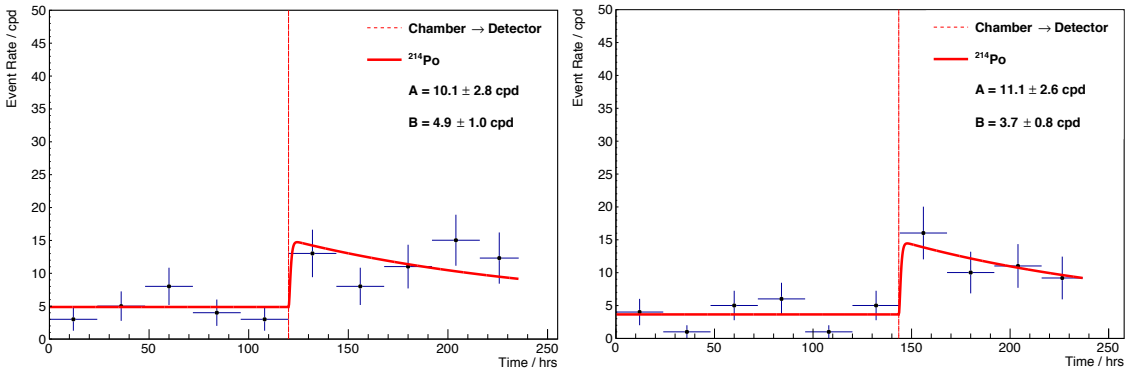

Figure 4.16: Pre-corrected ^{214}Po event rate results obtained from the two measurement made on the post-etched titanium welded block.

The output from the ^{214}Po rate of the pre-etched welded block indicated an emanation rate of 560 ± 97 µBq, which was in good agreement with ^{218}Po within error. The averaged

output from the post-etched block indicated a rate of 370 ± 68 µBq. Although the errors are relatively large and the dataset is constrained by so few measurements, the result seems to indicate that there is a substantial amount of radon emanating out of the block.

Titanium Sheets

To examine radon emanation from the cryostat titanium, a collection of titanium cutouts from the OCV were assayed. 8 pieces totalling to an area of 2350 cm^2 were initially wiped down with cleanroom wipes and ultrasonic bathed to remove any dust residue. There sheets are identical to those used in the ICV. Two sets of measurements were performed on the sheets: pre-etched and post-etched measurements. The slight curvature on the sheets, as shown on figure 4.14, was used to minimise overlaps, which in theory could reduce emanation from recoil, as radon atoms from one surface can lodge into another surface. Results obtained for the pre-etched and post-etched sheets are shown in figure 4.17 and 4.18, respectively. Pre-etched block was measured once, whereas the post-etched block was measured three times.

The output from the ^{214}Po rate indicates an emanation rate above the background measured prior to transfer, corresponding to a corrected activity of 380 ± 88 µBq. However, the ^{218}Po rate suggests a background only measurement. This behaviour has previously been observed and is attributed to outgassing of certain samples, for example the ^{218}Po in comparison to ^{214}Po has been shown to be suppressed under the presence of (N_2O). Although a signal has been observed, the presence of neutralising agents may add a systematic error that's currently difficult to determine.

The ^{214}Po activity measured from the same sample after etching at AstroPak has also shown a signal above the measured background. The two measurements are in good

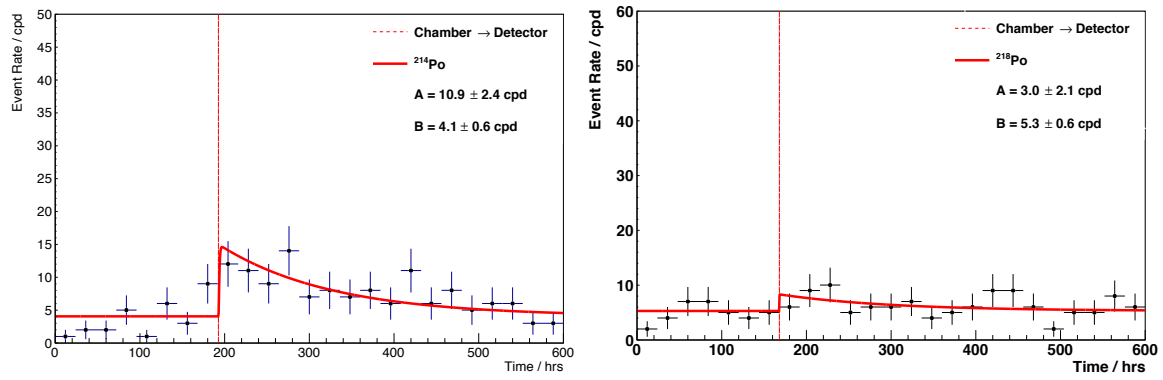

Figure 4.17: Pre-corrected ^{214}Po and ^{218}Po event rate results obtained from the single measurement made on the pre-etched titanium welded block.

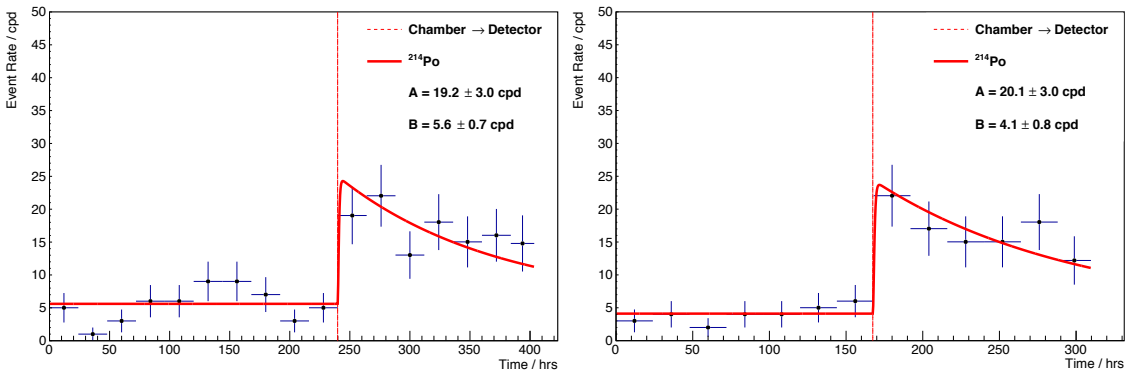

Figure 4.18: Pre-corrected ^{214}Po event rate results obtained from the two measurements made on the post-etched titanium sheets.

agreement and the averaged rate is calculated to be 685 ± 81 µBq. The averaged observed for ^{218}Po for these two measurements were 476 ± 79 µBq. Although there was a clear signal above background, the suppression in comparison to ^{214}Po still indicates an outgassing induced neutralisation.

Discussion & Conclusion

The pre- and post-etched emanation rates from the titanium welded block normalised for surface area result in 17.2 ± 3.0 mBq/m^{2}and 11.4 ± 2.1 mBq/m^2, respectively. The surface area normalisation for the titanium sheets for pre- and post-etched measurements give 1.62 ± 0.37 mBq/m^{2}and 2.91 ± 0.35 mBq/m^2, respectively. The titanium results obtained from this study, and for comparison, similar results obtained for stainless steel are highlighted in table 4.4.

The findings from these measurements are unexpected and surprising. The initial expectation for emanation from the titanium was in the order of that measured for stainless steel, but despite the etching, the titanium results in an activity that is ~ 3 orders of magnitude higher. A small reduction in activity is observed on the titanium welding post etching, but this effect is reversed for the raw titanium sheets, were the activity rises; thus suggesting an ineffectiveness of the etching process on metallic surfaces. Recent results published by the XENON1T collaboration also seem to indicate relatively high emanation rates for titanium. The untreated titanium sheets measured by XENON1T (supplied from Nitronit) are in good agreement with the emanation rates measured for the LZ titanium [153]. They however demonstrate that electropolishing of the titanium surface and removing ~ 30 µm from the surface, eliminates all of the measured activity, indicating that the emanation rate is predominantly due to a form of

surface contamination. Although electropolishing is known to be a very effective way of removing surface contamination, the size of the LZ detector restricted the use of this technique—leading to alternative forms of etching.

The total titanium surface within the ICV is 15.1 m^2 and a further 0.66 m^2 of titanium welding is present in multiple locations. Scaling the etched results from this study to the ICV results in a total emanation rate of 43.9 ± 5.3 mBq and 7.5 ± 1.4 mBq at room temperature for the raw titanium and welded surfaces respectively. For comparison, the bottom-up radon emanation projection prior to the titanium measurement was ~ 20 mBq from the entire detector. Applying the cross-calibration correction of the UCL detector results in 28.7 ± 3.5 mBq and 4.9 ± 0.9.

Table 4.4: Radon emanation results as obtained from the UCL system for the titanium welded block and titanium sheet assays. The results do not take into account the cross-calibration systematic of the UCL detector. For comparison, radon emanation results of titanium (middle rows) and stainless steel welding and foil (bottom rows) are provided, as measured by the XENON1T[1] collaborations [153] and the GERDA[2] [151, 152], respectively.

Sample Description	^{222}Rn emanation rate	
Titanium welded block (untreated)	17.2 ± 3.0	mBq/m^2
Titanium welded block (etched)	11.4 ± 2.1	mBq/m^2
Titanium sheets (untreated)	1.62 ± 0.37	mBq/m^2
Titanium sheets (etched)	2.91 ± 0.35	mBq/m^2
Titanium sheets[1] (untreated)	2.81 ± 0.19	mBq/m^2
Titanium sheets[1] (electropolished)	< 80	µBq/m^2
Steel welds[2] (untreated)	0.24 ± 0.03	mBq/m^2
Steel welds[2] (etched & passivated)	< 0.1	mBq/m^2
Stainless steel foil[2] (untreated)	10.2 ± 0.8	µBq/m^2
Stainless steel foil[2] (etched & passivated)	4.6 ± 0.9	µBq/m^2

4.4.3 Other Measurements

The UCL radon facility has been used to assay several other components for the LZ experiment. The procedure followed for these assays are identical to those detailed in the former sections. Samples are initially cleaned by cleanroom approved wet wipes prior to the placement into the emanation chamber and left to emanate for ~ 2 weeks. One week of background data is recorded prior to each transfer and the background rate is

subtracted from any observed signal. Results from these measurements are summarised in table 4.5.

Cirlex PCBs

The Cirlex boards screened here are from the same batch of material to those assayed in section 4.4.1, but without all of the electronic components highlighted in table 4.2. In an effort to distinguish the radon emanating out of the Cirlex alone a total of 124 3" and 7 1" PCBs, totalling 421 grams were assayed twice. The averaged rate was determined to be 636 ± 77 µBq, equating to 1.51 ± 0.18 µBq/g.

HV Components

A mixture of HV components were assayed at UCL including; 90" peek rods, 4.5 feet polyethylene tubes, 18 polyethylene displacer discs, 9 feet of fluorinated ethylene propylene (FEP) and 54 polyethylene insulating boomerangs, each provided at a quantity 1.5 times more than required by the LZ detector. Although the activity of the individual components cannot be quantified, an emanation rate of 369 ± 85 µBq were measured for the entire batch.

DB25s

As part of the radon screening campaign for the excess ICV radon, a pair of DB25s were assayed. These items were temporarily used in the ICV during the skin installation and hence was an unaccounted item. The measurements resulted in an upper limit of <0.13 mBq.

Nitrile O-rings

A total of 90 nitrile rubber o-rings were assayed. The total surface area of the assayed rings were 9.15 cm^2. An emanation rate of 17.6 ± 1.7 mBq was measured per ring. LZ will use a total of 2 nitrile rubber o-rings.

Polyoxymethylene (Delrin) Discs

A collection of 50 Delrin discs with a total surface area of 0.54 m^2 was assayed for radon emanation. An emanation rate of 450 ± 11 µBq/$m^2$was measured. LZ requires a total of 200 cm^2 as part of the installation of the HV umbilical cord, resulting in a contribution of 9 ± 2 µBq.

Titanium Rods

As part of the radon emanation cross-calibration campaign of the four facilities used by LZ, a set of titanium rods were procured and screened at the various facilitates. A total of 20 rods, 16 cm in lenth and 1 mm in diameter were screened along two small aluminium plates used for structural support. The emanation rate for the sample was measured at 404 ± 98 µBq.

Summary of Emanation Results

A summary table of the key measurements made by the UCL system are provided in table 4.5. The results are provided in easily scalable units for future use and multiple measurements are combined to a single emanation rate.

Table 4.5: Radon emanation results as obtained from the UCL system for all the components measured for the LZ experiment. These results do not include the cross-calibration correction ratio of 1.53.

Sample Description	^{222}Rn emanation rate	
Titanium welded block (not treated)	17.2 ± 3.0	mBq/m^2
Titanium welded block (etched)	11.4 ± 2.1	mBq/m^2
Titanium sheets (not treated)	1.62 ± 0.37	mBq/m^2
Titanium sheets (etched)	2.91 ± 0.35	mBq/m^2
1" PMT Bases	4.42 ± 0.90	µBq/base
3" PMT Bases	5.33 ± 0.63	µBq/base
Cirlex PCBs	1.51 ± 0.18	µBq/g
HV Components	369 ± 85	µBq/batch
DB25s	< 0.13	µBq/unit
O-rings (Nitrile)	17.6 ± 1.7	µBq/ring
Polyoxymethylene (Delrin) Discs	450 ± 11	µBq/m^2
Titanium Rods ($\times$ 20, L=16 cm, D=1 mm)	404 ± 98	µBq

4.5 Other Radon Emanation Assays for LZ

The LZ radon emanation screening campaign utilises on four different facilities in measuring small and large scale samples: the UCL facility as detailed in section 4.3, South Dakota School of Mines and Technology (SDSMT), University of Maryland and

University of Alabama facilities. More in-depth discussion and details on these facilities and their operational methods are highlighted in [1].

The facilities operate under similar approaches in measuring emanation rates, where samples are initially enclosed in air-tight emanation chambers and the radon is harvested into their respective detectors after the equilibrium period. SDSM&T and Maryland facilities make use of electrostatic PIN-diode detectors to measure the α-particles from the ^{214}Po and ^{218}Po isotopes to reconstruct the radon emanation rate. The Alabama facility operates an organic liquid scintillator detector with a low-activity 3" Hamamatsu R-1307 PMT. Boil-off nitrogen with low intrinsic radon content is used to transfer the radon from an emanation chamber into 150 mL of scintillator. The emanation rate is reconstructed by detecting the scintillation light from the delayed ^{214}Bi-^{214}Po coincidences.

LZ also makes use of two portable radon collection systems for equipment that is too large or are part of the construction in the SURF Surface Assembly Laboratory (SAL); i.e. radon emanation measurements from the ICV post skin region and TPC installation. Emanated radon is transferred to a cold trap consisting of copper beads or wool that is double-sealed and then transported by car or overnight shipping to the radon facility at SDSM&T or University of Maryland. The collected radon is then transferred over into the respective radon detector with transfer efficiencies taken into account from portable-system specific calibrations. The activity is then reconstructed by correcting for the transportation time, transfer and detector efficiency. These portable systems were critical for measurements of radon emanation from the assembled LZ detector and from large instrumentation used in the circulation path. Harvesting of radon from the getter system at the SAL using one of the portable systems is displayed on figure 4.19.

4.5.1 Cross-Calibration Campaign

The LZ collaboration performed cross-calibrations for the four radon facilities deployed as part of the assay program. A rubber sample previously screened by the EXO collaboration [154, 155] was assayed at each of the radon emanation facilities. Prior to the emanation period, the sample was prepared under the same conditions to reduce the chances of environmental contamination. The surface of the sample was scrubbed with isopropyl alcohol-soaked lint-free wipes and inspected with UV-light to ensure no presence of surface contamination. The activity of the sample was 10mBq and was thus well above the minimal detectable activities of the radon systems. Table 4.6 presents the results of the cross-calibration and a summary of key details of the LZ radon screening facilities. The EXO emanation results indicated an activity of 4.94 ± 0.07 mBq. The

cross-calibration results are provided as a ratio between the EXO activity and that measured with the various systems. All but the UCL emanation system agrees with the EXO results within error.

If ε were overestimated A_{UCL} would've been even higher, goes wrong way.. !

There are several considerations for the discrepancy for the unknown systematic observed for the UCL system. Due to the size and geometry of the sample, the transfer efficiency from the chamber may be overestimated, as some radon may have been trapped in folded pockets of the rubber sample. The UCL system transfers the chamber content with 10 times the volume of the chamber; hence it is difficult to explain such a large discrepancy with this explanation alone. Another explanation could be the exposure of the sample to radium rich air, hence increasing the radon activity of the sample. Due to the uncertainties in understanding why the UCL system is behaving in such a way, it is difficult to conclusively explain this behavior and further tests will be conducted between the LZ radon emanation systems to fully understand if such an upwards systematic exists.

did you take into account system. error of UCL ?

Main systematics: background in Emanation chamber

Figure 4.19: A pictorial diagram of the portable radon harvesting system used at the SAL for the getter radon emanation measurement. The emanated radon is collected by transferring through one of the traps held under LN_2 temperature. The trap is later transported to a radon emanation facility for counting.

4.5.2 Large Scale Radon Emanation Studies

Room temperature measurements from individual material and components measured by various radon facilities are all presented in [1]. Furthermore, measurements from fully assembled sub-systems, such as the ICV, xenon purification and circulation system are also presented in figure 4.20. Measurements for three of these assemblies are discussed in the following sub-sections. These measurements were made possible by the portable radon harvesting system deployed at SURF.

Inner Cryostat Vessel

Radon emanation from the ICV was measured several times during various integration stages of the construction of the skin veto region and the TPC installation. The final assay was made following after the ICV was fully complete and sealed. The cryostat at this stage housed both the top and the bottom PMT arrays for the TPC and the skin veto regions, and their corresponding PMT bases and cables. Furthermore, the entire field cage, PTFE coating, various sensors, and conduit volumes of the cables were a part of these measurement.

A portable radon trapping system was deployed underground at SURF with minimal plumbing due to space constraints. After leak-checking and purging, the trapping system was opened to the ICV and the emanated gas was harvested over a 6.3 hour period—equivalent to 18.25% of the gas within the ICV. After the harvest, the trap was carefully

Table 4.6: Comparison of the key highlights of the four radon emanation facilities used by LZ. The chambers detailed are those used in containing the sample material, where radon is collected. Some facilities operate two chambers as detailed below. Chamber blank rates detail the emanation rate from the chambers alone and are background subtracted for sample measurements. Detector efficiency represents the fraction of activity measured from the total radon inside the detecting volume; independent of chamber usage and transfer efficiency. The cross-calibration figures represent the reconstructed emanation rate of a standard rubber sample previously used by other collaborations. When not stated, overall uncertainties are estimated to be 10-20%.

Detector	Type	Chamber Volumes [L]	Chamber Blank Rates [mBq]	Transfer Efficiency [%]	Detector Efficiency [%]	Cross-Calibration [Measured/EXO–activity]
SDSM&T	PIN-diode	13	0.2	94	25	0.89 ± 0.15
		300	0.2	80		1.11 ± 0.28
Maryland	PIN-diode	4.7	0.2	96	24	1.13 ± 0.19
UCL	PIN-diode	2.6	0.2	97	30	1.53 ± 0.15
		2.6	0.4	97		
Alabama	Liquid Scint.	2.6	<0.4	34	36	0.83 ± 0.17
		2.6				

Systematics discussion!!!

disconnected and transported to SDSM&T radon facility for screening. The radon trap also captures outgassing molecular species that would serve as neutralisers of positively charged radon-daughters, leading to a drop in detection efficiency. An in-house procedure was followed to separate out these species by transferring the sample from a cold trap held at -109°C to one at -196°C with sufficient flow to effectively transfer all of the radon atoms while leaving most of the contaminants behind. This process was repeated until measurements with a residual gas analyzer indicated no further reduction in contaminant concentration, after which the sample was transferred to the detection chamber via a secondary small cold trap. Results indicate a room-temperature emanation rate of $46.1^{+4.0}_{-3.8}$ mBq under the assumption of an even sampling of the radon within the ICV.

Xenon Circulation System

The xenon gas circulation system brings together multiple components and surfaces that are potential radon emitters. The system consists of two gas compressors, a heated zirconium getter, and a main valve and instrumentation panel. The compressors (model A2-5/15 from Fluitron) have two heads, each enclosing a flexible all-metal diaphragm sealed with copper plating. Check valves, accumulation bottles, and associated plumbing and instrumentation are also included in the compressor assemblies. The compressors operate in parallel to achieve a gas flow rate of 500 standard liters per minute. Much of the system was fabricated at the University of Wisconsin's Physical Sciences Laboratory. Whilst there, a portable radon trapping system was used to harvest emanation samples that were then shipped to shipped to the U. Maryland radon facility for counting.

Initial radon emanation measurements of compressor 2 found that the heads emanated $<$ 1mBq each, however, the integrated compressor skid assembly presented $\sim$17mBq. After replacing most of the welded stainless steel plumbing and etching the accumulation bottles in citric acid, the rate was reduced to 1.48 ± 0.31 mBq. A similar treatment was applied to compressor 1 but this compressor was not radon emanated and hence is assumed to have the same rate as compressor 2. The main circulation panel contains most of the valves and instrumentation exposed to the xenon in gas phase, and it was found to contribute 0.74mBq of radon. The fully loaded getter (model PS5-MGT50-R-535 from SAES) was emanated at its operational temperature of 400°C using helium carrier gas and its emanation rate was determined to be 2.26mBq. The entire circulation system amounted to a total emanation rate of 5.22 ± 0.75 mBq.

Xenon Tower

The xenon tower is a cryogenic system that thermally couples the gaseous and LXe portions of the purification circuit for efficient heat transfer, serving to vaporize and re-condense the liquid for continuous purification. It consists of a two-phase heat exchanger (supplied from Standard Xchange), three cryogenic valves (manufactured by WAKE), a sub-cooler/phase-separator vessel to hold LXe returning to the detector, a reservoir vessel to hold liquid exiting the detector, two liquid xenon purity monitors, and several custom liquid xenon heat exchangers. The tower can be viewed as having two sides: the heat exchanger assembly on one side and the weir reservoir, sub-cooler and purity monitor on the other. Radon emanation from sub-components was measured prior to full integration of the xenon tower and was found to contribute a total of <1mBq.

A preliminary measurement of the tower after integration found a very high radon activity in the reservoir side, possibly due to a leak into the system from laboratory air. As a precautionary measure, the reservoir vessel was flushed with a concentrated solution designed for removing radioactive contamination (Radiacwash^{TM}) and rinsed with deionized water. The portable radon trap was then deployed underground to measure the two sides of the complete xenon tower prior to the installation of the purity monitor and found a total emanation rate of $3.14^{+0.86}_{-0.81}$ mBq.

4.6 Radon Emanation Projection in LZ

Sensitivity projections for LZ presented in [105] include the effect of the online charcoal-based radon-removal system, operating continuously to scrub gaseous Xe [110, 149]. Although this system will not scrub majority of the xenon within the ICV, a volumetric gas flow of 2 slpm has been shown to eliminate 90% of the radon from cables and feedthroughs. LZ will utilise on a 7.0 kg charcoal trap to reduce radon emanation from instrumentation immersed in GXe; particularly, radon emanation from the top PMT array, cabling and sensors, along with all the titanium surfaces on the upper-side of the ICV.

Projections also assume an expected suppression of radon diffusion in certain materials at low temperatures, namely those suspended within the LXe were the operational temperature is 175.8 K (-97.4°C). Its important to note that the radon emanation assays from all the samples—whether individual components screened using emanation chambers,

or system-wide instrumentation's screened using a portable harvesting system—were all performed at room temperature ($\sim 20^{\circ}$C).

The projection of radon emanation from warm measurements to operational conditions is a difficult task involving multiple assumptions and approaches. In calculating an operational rate, both the radon reduction system and the suppression due to cold temperature has to be taken into account. The ratio of components sitting within the operational volume of the radon reduction system is well known, but there are still many uncertainties on the suppression rates obtained at cold temperature. Furthermore, these rates heavily depend on the type of material used; more emanation reduction is expected from porous materials like plastics and ceramics when cold. The sections below will initially construct a warm emanation rate projection of the entire detector, and a further attempt to quantify operational rates through literature-based educated assumptions on suppression.

4.6.1 Bottom-up Projection

Prior to large scale emanation results during construction, the radon projection was constructed entirely from a bottom-up approach from measuring components and material in fractional quantities and scaling the emanation results to quantities present in LZ. The results from this approach with various projections are detailed in table 4.7.

Although the table does not fully account for all of the items to be used in LZ, majority of the radon contributors are included. Components such as sensors and screws have previously been emanated but contribute negligible amounts to the total sum. The results obtained by UCL, i.e., the raw titanium, titanium welding and PMT base results, take into account the systematic correction of 1.53 from cross-calibrations. Components that are within the operational ground of the radon removal system are further suppressed by the previously determined 90% removal efficiency. The GXe suppression factor therefore is $S = 0.1$, where the LXe suppression factors are component specific: $S1 = 0.5,\ S2 = 0.1,\ S3 = 0.01,\ S4 = 0.001,\ S5 = 0.0001$. The cold reduction values for plastics (S3, S4, S5) originate from diffusivity data on Kapton, Acrylic and PTFE; where temperature dependence of diffusivities of Ar and Kr were evaluated from [156] by the EXO collaboration and a model for radon is constructed. Components using mixtures of material—such as the bases—use a conservative suppression value ($S2$); though its important to note that the majority of the emanation is from Cirlex ($\rho \simeq 1.42\text{g/cm}^3$), which has a similar density as PTFE ($\rho \simeq 2.2\text{g/cm}^3$).

Finally, ($S1$) is used for components with metallic surfaces; i.e. PMTs, but more importantly the titanium welding and cryostat. Material such as glass and metals are crystalline in nature and hence space for additional atoms is often limited, especially for the large radon atom. Hence diffusion through such material is suppressed as a nature of the material, as radon would then have to displace or significantly deform the lattice structure to squeeze through, which is heavily suppressed at room temperature. In such a case, emanation is dominated by recoil and hence no suppression at colder temperatures. However, this assumption only applies to perfect lattice structure. The lattice formation depends heavily on the cooling methods when forming the solid metal. A slow cooling process can lead to large crystalline grain formations, whereas a fast cooling process leads to small grains. The grain boundaries represent a surface of imperfect lattice that could be a route for radon to diffuse.

The expected radon emanation from the LZ detector that emanates directly into volumes in line with the GXe and LXe without any suppression factors result in a rate of $60.8^{6.0}_{-6.1}$ mBq. Although not detailed in table 4.7, by taking only into account the suppression from the radon removal system and omitting any cold suppression, an emanation rate of $41.3^{+4.4}_{-4.5}$ mBq is obtained. Taking into account the conservative cold suppression factors in table 4.7, this rate further drops to $21.6^{+2.3}_{-2.3}$ mBq. If a substantial amount of emanation from the cryostat and the welding is as a result of diffusion, a significant suppression due to cold could be expected. To reflect this, the conservative ($S1$) suppression factor was substituted with ($S2$), giving a total expected emanation rate of $11.0^{+1.0}_{-1.0}$ mBq for an optimistic scenario. The LZ detector is expected to take commissioning data operating fully in GXe and with LXe, hence the comparison of that data to estimations presented here is of utmost interest.

4.6.2 Large Scale Assay Projections

A second method to estimate for the total radon in LZ was by using the large scale measurements highlighted in section 4.5.2. Results obtained using this method for the sub-systems of interest is provided in figure 4.20. The main difference here is that the entire ICV and the xenon tower has been emanated after the installation of all sub-components. The comparison between large-scale and bottom-up ICV measurements obtained from table 4.7, result in a remarkably good agreement, with $46.1^{+4.0}_{-3.8}$ mBq and $48.5^{+5.9}_{-6.0}$ mBq, respectively. Combining the outcomes of the large-scale measurements result in a total emanation rate of $60.4^{+4.2}_{-4.0}$ mBq for the LZ experiment, which in good agreement with the bottom-up estimations when excluding suppression factors.

4.6.3 Discussion

The results obtained from bottom-up assays and large scale emanation measurements during sub-system installation at the SAL are in good agreement within error. A large proportion of the emanation rate is expected from the ICV, of which, the largest contribution comes from the cryostat, welding and the PMT-base pairings. The emanation rate measured from the cryostat titanium was unexpected. Exclusion of the titanium emanation rate from the bottom-up ICV results lead to a substantial underestimation of the emanation rate when compared to the large-scale ICV result. Furthermore, the issue around the UCL systematic adds another layer of complexity, but it is safe to say that this factor is indeed a systematic and not a result of external circumstances. This conclusion is reached when considering the comparison between the ICV bottom-up and total; if this correction was not applied, the bottom-up scenario will substantially overestimate the result from the complete ICV emanation. The agreement between the large scale emanation results and that of the bottom-up adds further confidence to the cross-calibration factor used to estimate radon emanation at operational conditions. Assuming the fraction of radon emanation coming from each sub-component is accurate and the suppression factors are conservative; the worst case scenario with only the radon removal suppression yields an emanation rate of $41.3^{+4.4}_{-4.5}$ mBq. This further reduces to $21.6^{+2.3}_{-2.3}$ mBq and $11.0^{+1.0}_{-1.0}$ mBq when less conservative ($S1 \rightarrow S2$) suppression factors for LXe are successively assumed. Chapter 5 will investigate the significance of the radon background for the WIMP search, studying the implications of these scenarios for the sensitivity and the discovery potential of WIMPs.

As discussed at the viva this chapter should be restructured: first detection and calibrations, then results.

Table 4.7: Results obtained from component and material radon emanation from various facilities used by LZ. The UCL results provided take into account the systematical fraction highlighted in table (4.6). Provided are the components and quantities used in LZ and emanation results obtained from same/similar samples. Fraction of components occupying either the GXe region of the detector—where radon removal system will operate, or the LXe region—where cold suppression is considered. Emanation rates expected from these two regions after applying the suppression factors is given in the last two columns. The GXe suppression factor is S=0.1, where the LXe suppression factors are component specific: S1=0.5, S2=0.1, S3=0.01, S4=0.001, S5=0.0001. Those components were neither suppression factor apply are left blank; i.e. xenon tower and circulation. The remaining results from the radon emanation campaign are detailed in [1].

Component	**Quantity**		**^{222}Rn**		**Location [%]**		**Suppression [µBq]**	
					GXe	LXe	GXe	LXe
ICV								
Titanium (Raw)[S1]	15.1	m^2	$2910.0^{+0.4}_{-0.4}$	µBq/m^2	0.25	0.75	35.90	10769.85
Titanium (Welding)[S1]	0.66	m^2	$7451.0^{+2.1}_{-2.1}$	µBq/m^2	0.10	0.90	2.46	2212.94
3" PMTs (R11410)[S1]	494	unit	$1.8^{+1.7}_{-1.8}$	µBq/unit	0.51	0.49	2.28	216.96
PMT Bases (3")[S2]	499	unit	$3.5^{+0.6}_{-0.6}$	µBq/unit	0.51	0.49	4.46	84.66
2" PMT (R8520)[S1]	48	unit	$1.8^{+1.0}_{-1.3}$	µBq/unit	0.00	1.00	0.00	43.92
PMT Bases (2")[S2]	49	unit	$3.5^{+0.6}_{-0.6}$	µBq/unit	0.00	1.00	0.00	17.07
1" PMT (R8778)	93	unit	$7.1^{+2.6}_{-3.0}$	µBq/unit	1.00	0.00	3.30	0.00
PMT Bases (1")[S2]	94	unit	$2.9^{+0.9}_{-0.9}$	µBq/unit	0.99	0.01	1.34	0.30
Cables (Axon)[S4]	14802	m	$0.6^{+0.1}_{-0.1}$	µBq/m	0.55	0.45	24.65	4.10
Cables (Koax)[S4]	1771	m	$0.03^{+0.23}_{-0.03}$	µBq/m	0.70	0.30	0.16	0.01
PTFE[S5]	84	m^2	$12.4^{+5.3}_{-10.0}$	µBq/m^2	0.00	1.00	0.00	0.10
Kapton Sheets	1.25	m^2	$56.0^{+104.0}_{-56.0}$	µBq/m^2	1.00	0.00	0.35	0.00
HV Feedthrough	21	unit	$37.0^{+12.0}_{-12.0}$	µBq/unit	1.00	0.00	3.89	0.00
Signal Feedhrough	31	unit	$23.0^{+18.0}_{-14.0}$	µBq/unit	1.00	0.00	3.57	0.00
Anode/Cathode Feedhrough	3	unit	$18.8^{+19.0}_{-18.8}$	µBq/unit	1.00	0.00	0.28	0.00
HV Umbilical								
Umbilical Cable[S3]	7.8	m	$52.0^{+8.0}_{-8.0}$	µBq/m	0.51	0.49	1.04	1.98
Mixed Components[S2]	0.67	batch	$369.0^{+85.0}_{-85.0}$	µBq/batch	0.20	0.80	0.25	19.68
Radon Removal & Transfer Lines								
Activated Carbon (Trap)	6	kg	$510.0^{+90.0}_{-90.0}$	µBq/kg	1.00	0.00	400.86	-
Radon Reduction Panel	1	unit	$290.0^{+110.0}_{-110.0}$	µBq/unit	1.00	0.00	1.45	-
Xenon Transfer Lines	1	unit	$220.0^{+70.0}_{-70.0}$	µBq/unit	0.00	1.00	0.00	220.00
Xenon Circulation								
Purification Getter	1	unit	$2260.0^{+280.0}_{-280.0}$	µBq/unit	-	-	2260.00	-
Compressors	2	unit	$1480.0^{+310.0}_{-310.0}$	µBq/unit	-	-	2960.00	-
Circulation Panel	1	unit	$740.0^{+200.0}_{-200.0}$	µBq/unit	-	-	740.00	-
Xenon Tower								
Xylem HEX	1	unit	$529.0^{+132.0}_{-132.0}$	µBq/unit	-	-	529.00	-
Subcooler HEX	1	unit	$300.0^{+140.0}_{-300.0}$	µBq/unit	-	-	300.00	-
WEKA Valves	3	unit	$60.0^{+10.0}_{-10.0}$	µBq/unit	-	-	180.00	-
Conditioning Heater	2	unit	$36.0^{+17.0}_{-15.0}$	µBq/unit	-	-	72.00	-
Misc Others	1	batch	$500.0^{+500.0}_{-500.0}$	µBq/batch	-	-	500.00	-
Sub-total [mBq]							$\mathbf{8.03^{+0.89}_{-0.93}}$	$\mathbf{13.6^{+2.1}_{-2.1}}$
Total [mBq]			$\mathbf{60.8^{+6.0}_{-6.1}}$				$\mathbf{21.6^{+2.3}_{-2.3}}$	

remind LZ goal in the caption

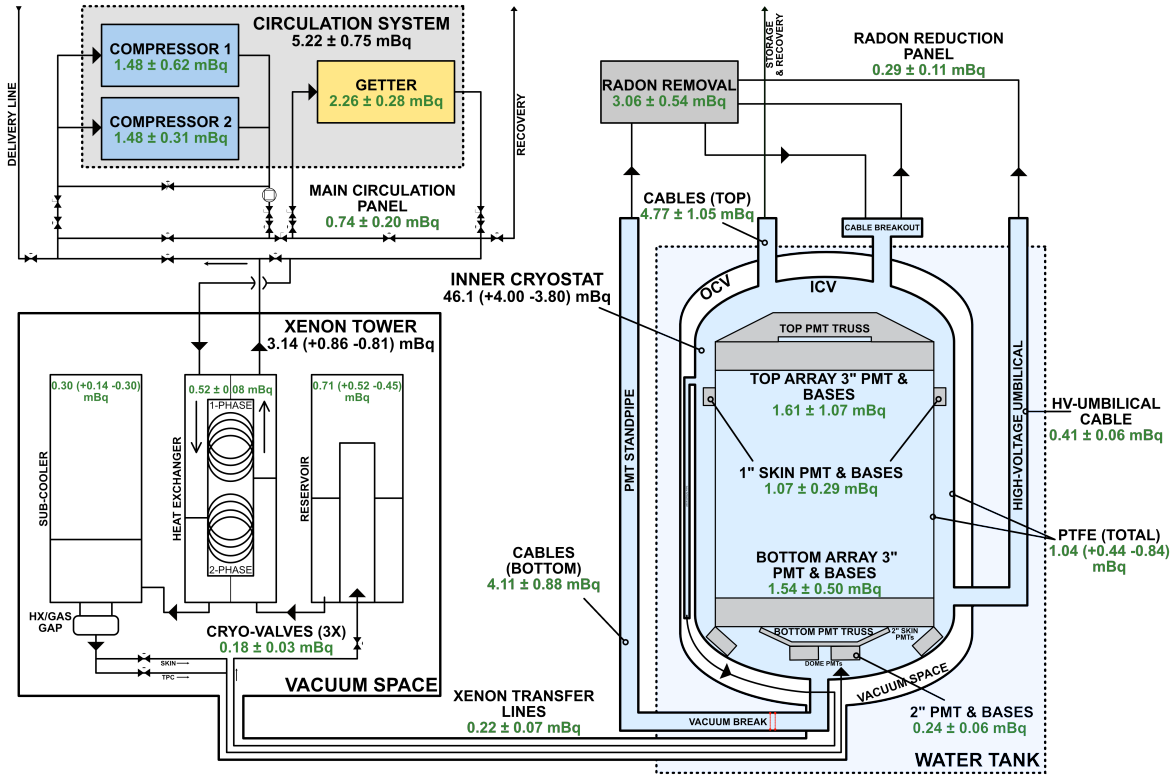

Figure 4.20: Approximate schematic of LZ highlighting key sub-systems and xenon circulation paths in and out of the ICV. The diagram condenses some of the key radon emanation measurements that will contribute to the overall radon budget of LZ. The results presented in green text are directly from measurements and those in black show summed results for that particular component. All of the results shown are measurements made at room temperature and does not include the cold suppression expected under full operation.

Chapter 5

LZ Sensitivity Studies

Understanding the physical response of a detector to its environment is key in assessing the capacity of the detector in looking for the desired physics objectives. Furthermore, detector design has to take into account this response to optimise construction and allow for the testing of theories and models by comparison to data. Over the past few years, the LZ simulation and statistical packages were developed alongside the design and construction of the experiment. The focus of this chapter is initially to give a brief introduction to these packages, focusing primarily on the statistical software package LZStats, which has been developed and used to study the sensitivity and discovery potential of the experiment to WIMP dark matter. Moreover, sensitivity studies are presented using the statistical framework, showing how varying levels of radon and other backgrounds in the detector impact our science reach; highlighting the essentiality of precision understanding and reduction of the backgrounds to maximize detector sensitivity.

5.1 Overview

The instruments used in pursuit of new physics becomes a playground in which new discoveries can be made. However, without fully understanding the internal dynamics of this playground and the precise response mechanics taking place as a result of known (background) and unknown (signal) interactions, the ability to claim a discovery is diminished. Simulation of detectors through the means of Monte Carlo modeling is an essential tool in physics to test theories and models by comparison to data, and more importantly, to understand the response dynamics of such a playground to these interactions.

Although the origin of background events and their response mechanisms in LXe are well understood, this alone is not enough to determine the actual rates observed by the entire system operating in unison. The simulation of events for LZ serves multiple purposes; the primary of which is to determine an optimal detector design that takes into account material specific background rates, and their physical and geometric features in constructing an ultra low-background detector optimised for the detection of WIMPs. Furthermore, upon a verified detector design, the simulations are used for the calculation of background rates in LZ with input from radioactivity measurements. Through the use of these rates and by utilising on a Profile Likelihood Ratio analysis (PLR), the sensitivity of the experiment to various rare event searches is predicted.

The LZ simulation chain brings together a class of packages that simulate the response of the detector beginning from the initial interaction point—the point of first energy deposition, all the way through the electronic and algorithmic response models in creating an ultra-realistic event topology. The chain starts with a GEANT4 based in-house code BACCARAT to track the passage of particles through the detector, identifying and recording their interaction points. The output from BACCARAT is further used in two separate chains as detailed in figure 5.1.

The fast simulation chain records energy depositions using BACCARAT and passes these depositions over to NEST, where the energy depositions are converted into S1 and S2 signals by using well understood light and charge yields in LXe, and applying detector-averaged quantities. In enabling fast generation of large datasets, this chain is often used in analysing background rates and informing sensitivity estimates. However, more minute details of events, such as, times of interaction and PMT photon hits

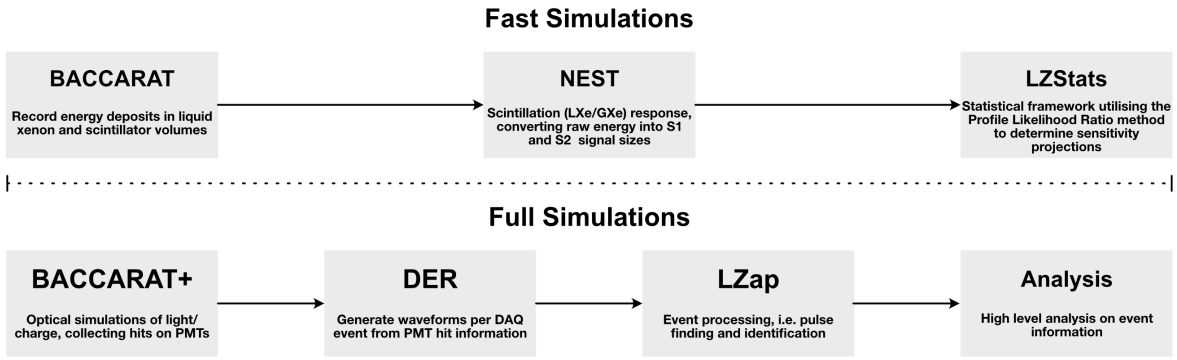

Figure 5.1: The LZ simulation packages, detailing the fast and the full processing chains of background simulations. The fast chain is primarily used in sensitivity studies, whereas the full chain is used to generate ultra-realistic pulses for Mock Data Challenges (MDCs).

are inaccessible. The full simulation chain includes the simulation of VUV photons and ionization electrons that are produced during xenon interactions, as well as the scintillation light generated in the skin and OD veto systems. Furthermore, a detector electronics response (DER) simulation is used to model the PMT response to VUV photons including quantum efficiency and dark noise, front-end and back-end electronics to generate realistic waveforms. These waveforms are stored in realistic data structure to that of expected data—facilitating a training dataset used to prepare for real data through Mock Data Challenges (MDCs). These waveforms are passed through the LZ Analysis Package (LZap), which reconstructs pulse and event level information through a multitude of algorithms for data analysis.

The simulation studies highlighted in this chapter focus predominantly on the fast simulation chain. The expected backgrounds from screening results are used as a bases to input into BACCARAT, where detector related background rates are determined. Dedicated particle generators are used to simulate surface and xenon contaminants; backgrounds from the cavern, cosmogenic muons and various physics backgrounds, such as solar, atmospheric and diffused supernova neutrinos. NEST is then used to generate background specific S1 and S2 signals that plug into the LZStats framework for the evaluation of sensitivity projections. The following sections will give a brief introduction to the fast simulation chain used in this work, a more in-depth highlight can be found in [157]. A description of LZStats framework and its statistical approach is detailed. Furthermore, projections made for the WIMP sensitivity of the LZ dark matter experiment and various other sensitivity studies, emphasising on the impact of the dominant radon background of LZ are presented.

5.2 LZ Simulation Framework & Detector Parameters

5.2.1 BACCARAT

Geant4 is a toolkit used extensively in the nuclear and high-energy physics community to simulate the passage of particles and particle interactions through detectors and materials. The LZ simulation package BACCARAT is an extension to the simulation package developed for LUX [158], providing a more user-friendly interface to Geant4 for low-background experiments. Simulations in low-background experiments differ to conventional particle colliders due to the origin of background sources. In low-background experiments, such as LZ, one of the main sources of background is embedded radioactive

isotopes scattered throughout detector material; placing the source of radiation across a three-dimensional volume. Furthermore, every material and component within the detector has a unique radioactive composition; the simulation of which requires a collection of sources with potentially complicated spatial and radioactive extent.

BACCARAT is a simulation framework designed and used by LZ that takes a component-centric approach to event generation and recording. It implements a C++ detector component object that allows for spacial origin for radioactivity across a three-dimensional component or material for a more accurate modeling of impurities. Furthermore, each component can independently have a material specific recording level for the amount of information required, such as position, scattering information or energy deposition—significantly improving memory usage. The defined geometry of the LZ detector, illustrated on figure 5.2 relies heavily on GEANT4 classes.

In modeling various physics processes, BACCARAT implements several modules that are contained in the GEANT4 toolkit, including *G4EMLivermorePhysics*—covering electromagnetic interactions for γ-rays and electrons down to $\sim 10\,\text{eV}$, where low energy processes, such as bremsstrahlung, the photoelectric effect, Rayleigh and Compton scattering are modeled [136, 137]. Furthermore, when run in full simulation mode, BACCARAT implements a custom-built physics list (NEST) directly into the GEANT4 interface under *G4S1Light* & *G4S2Light*, governing the detector specific generation of light and charge quanta in a xenon volume, respectively.

In addition to these, there are several other physics lists that have been implemented to simulate various other potential event topologies in LZ, such as, Cherenkov processes in non-xenon materials, rest and in-flight decay of radioactive nuclei via α, $\beta^{\pm}$, γ-emission or electron capture; and relaxation of excited atomic states via the emission of X-rays and electrons. The BACCARAT physics list, particle generators and processes such as charge transport within xenon are continually improved for more realistic simulations. The code is maintained via an LZ inclusive Git repository and the studies highlighted in this chapter are with BACCARAT verified against GEANT4 version 10.3.

5.2.2 NEST

The NEST package introduced in section 2.2.4 plays a key role in the fast simulation chain. NEST is a semi-empirical collection of models, relying on data from a multitude of past and present science and calibration datasets for β, γ and neutron-induced xenon recoils in varying electric fields, simulating the excitation, ionization, recombination, and

electron electroluminescence processes in liquid or gaseous xenon. The previous versions of NEST [95, 96] modeled light and charge yields as a function of energy inspired by the Thomas-Imel box recombination model at low energies [159] and Doke modification to Birks' law [160] at high energies, with coefficients as functions of field. The version used as part of this study, v2.0, uses a range of sigmoidal-class functions to model yields as functions of energy [98]. The yields are readily modeled as a function of particle and interaction type, energy, ionisation density, electric field and fluid density.

The output from BACCARAT; information on energy deposition, material media, type of interaction, is fed into NEST for a rapid conversion into the detector observable quantities. The conversion from deposited energy to detector observables (S1 & S2) is

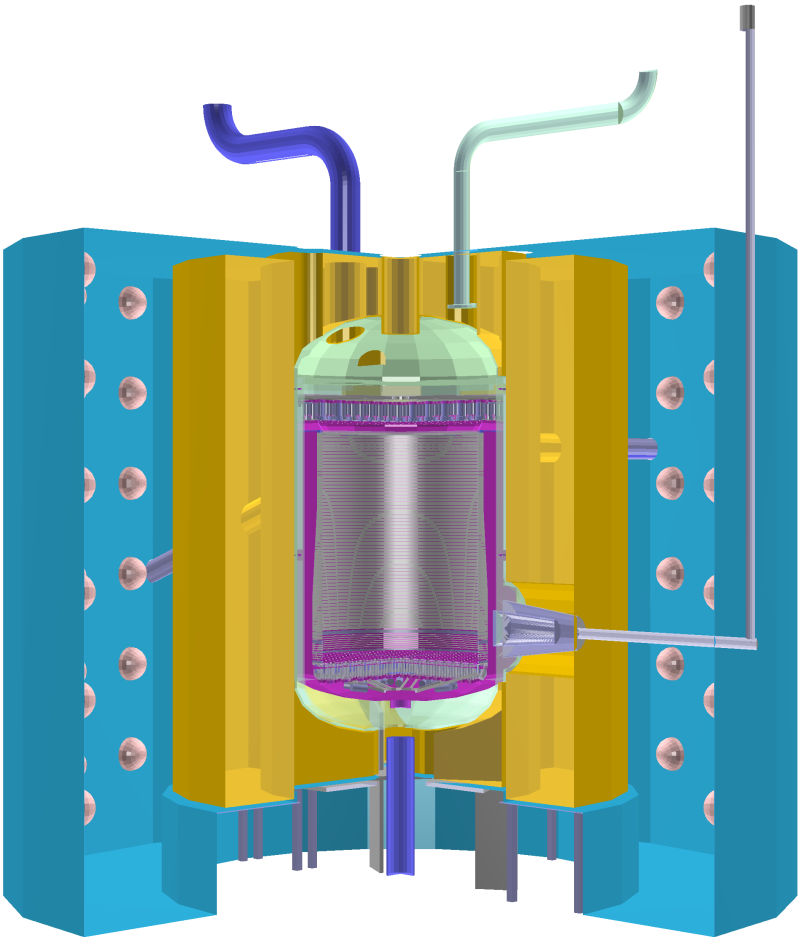

Figure 5.2: The geometry of the LZ detector as constructed by the BACCARAT simulation package illustrating some of the key components. The entire detector is immersed inside a water tank, with the inner part of the water tank shown in blue; holding the OD PMT structure, which face the GdLS outer detector tanks (yellow). The outer and the inner. cryostat (light green) holds the central TPC (magenta).

calculated in multiple steps, where the exciton-to-ion ratio is first considered to determine the amount of excitons, leading to primary scintillation (S1) and electron-ion pairs. Energy-specific recombination probabilities are then applied to determine the amount of electron-ion recombination, resulting in a reduction in S2 signal, but an increase in S1. For processes where energy is lost through heat, i.e., nuclear recoil events, a simple power law approximating the Lindhard factor is applied [93, 94]. The transportation of escaped electrons to the liquid-gas interface is handled by NEST through a parametrised electric field applying diffusion and a finite mean free path; where upon reaching this barrier, an extraction efficiency is applied through probabilistic quantities dependent on extraction field strength in the gas phase. The resulting output from NEST then takes into account detector specific quantities to produce a corrected $S1_c$ and $S2_c$ signal in *photons detected* (phd).

5.2.3 Detector Parameters

The detector parameters that are key in determining the actual observed signal for *S1, S2, x-y-z*, from the point of interaction and through the physical and electrical processes

Table 5.1: Key detector parameters for the LZ experiment. PDE refers to *photon detection efficiency*, SE to *single electron*, e to *electron*, ph and phd to *photon* and *photons detected*, respectively.

Detector Parameter	**Value**	
Drift electric field	310	V/cm
Electron lifetime	850	µs
Electron extraction efficiency	95	%
Average PMT efficiency	27	%
Average PDE in liquid (g_1)	0.119	phd/ph
Average PDE in gas (g_{1gas})	0.102	phd/ph
Electron extraction efficiency	95	%
Single electron size	83	phd
Effective charge gain (g_2)	79.2	phd/e
S1 coincidence level	3	ph
Single phe trigger efficiency	95	%
PTFE reflectivity in LXe	97.7	%
PTFE reflectivity in GXe	85	%

of LZ are summarised in table 5.1. Once an event occurs within the LXe volume, the photons that are produced—referred to as raw S1—traverse the volume, reflecting off of the PTFE walls before hitting a PMT successfully. The g_1 factor, formally known as the photon detection efficiency in the liquid represents the averaged successful recording of a single photon, taking into account reflectively and PMT quantum efficiencies; g_{1gas} is the equivalent detection efficiency for S2 electroluminescence photons generated in the gaseous extraction region. The current estimates derived from optical simulations based on reflectively measurements of the LZ PTFE [107, 161] for g_1 and g_{1gas} are 0.119 phd/ph and 0.102 phd/ph, respectively. These values include considerations of 3" Hamamatsu PMT quantum efficiency, double photoelectron emission probabilities [162], first dynode collection efficiency and photon absorption length in LXe motivated by the literature [103]. Single electron size represents the average number of photons detected per extracted electron, whereas the photons detected from a raw S2 signal is represented by the g_2 factor. g_2 takes into account the extraction efficiency at the liquid-to-gas boundary, adding an averaged correction for the lost electrons, resulting in an effective charge gain of 79.2 phd/e.

The detector parametrisation factors detailed in table 5.1 are evaluated alongside the BACCARAT input to the NEST framework in calculating corrected detector observable signals, $S1_c$ and $S2_c$. Although this process takes certain parameters as their averaged representations; excluding differences arising from event location, or PMT specific divergences on an event-to-event bases; it allows for fast generation of ($S1_c$, $S2_c$) probability density functions (PDF) that are representative of detector operational conditions. The PDFs of background and signal events are then fed into the LZ statistical framework, LZStats, for sensitivity studies. The event selection criteria and the representative background rates under projected operational conditions, as determined by the use of the LZ simulation framework are detailed in the next section.

5.3 Background Projections for WIMPs

The LZ detector is capable of detecting signals from a wide spectrum of event topologies and energy ranges. This wide range of energy-space is made accessible by exploiting the two signal types in LZ, measurement of scintillation light and charge production, in various search types; i.e. S2-only, S1-S2 and S1-only searches. At sub-keV energies, S2-only searches are used to probe for lighter WIMPs, sub-GeV hidden sector and asymmetric dark matter models. Low energy depositions at this regime usually result in

free electrons extracted without any accompanying S1 signal. At much higher energies, LZ is capable of probing the ^{136}Xe $0\nu\beta\beta$-decay with a $Q_{\beta\beta}$ value of 2458 keV [139].

The observation of a WIMP signal is conducted in the S1-S2 space in the LZ detector, coming from an excess of single-scatter nuclear recoil events taking place within a WIMP centric fiducial volume and a pre-defined energy region of interest (ROI), optimised for the signal-to-background ratio. The full ROI can be seen as a selection of detector-specific cuts applied to the outcome of the Monte Carlo simulations, which are dictated by measured material radioactivity and anticipated levels of dispersed and surface radioactivity. The following sections will highlight the WIMP search event selection criteria used for constructing the background model for the sensitivity projections, and present the integrated background rate for ER and NR counts in the 5.6 tonne fiducial mass for a 1000 live day run using a reference cut-and-count analysis; which was used for the purpose of tracking material radioactivity throughout the design and construction phase of the LZ experiment. The full ROI highlighted below is relevant for the PLR analysis, detailed in section 5.4, and used to calculate the sensitivity and the discovery potential for WIMPs using the LZ detector.

5.3.1 Background Selection Cuts

In the design and construction phase of the detector, the attribution of specific backgrounds to planned operational conditions and material radioactivity is vital in selecting the most appropriate materials and the final design of the experiment. Analysis of simulation results are used to determine the total number of background events and their distribution in the $S1_c$–$S2_c$ space, from which PDFs are generated for the PLR analysis. A set of cuts is applied to the simulated data to select WIMP-like events and determine the impact of backgrounds on the WIMP-search analysis. These cuts, which are aimed at imitating those that will be applied to real WIMP search data are as follows:

- Region of interest—**ROI**: Defines the energy window of the expected WIMP-like events in LXe. Backgrounds of interest for the WIMP search are those that fall into this energy region of interest.
- Single scatter–**SS**: Requirement of the energy deposition taking place in a single spacial (x-y-z) coordinate within expected detector resolution.
- Skin veto–**Skin**: Rejection of events in the active volume if an accompanying event occurring in the skin region.

- Outer detector veto–**OD**: Rejection of events in the active volume if an accompanying event occurring in the outer detector.
- Fiducial Volume–**FV**: The virtual volume within the active LXe TPC that an event is required to take place. This volume is defined to remove the overwhelming background from the walls of the TPC.

The region of interest for WIMPs is defined both in energy-deposition terms, i.e., in keV and in detector observables, S1-S2. In the energy space, where deposition-only simulations are considered without the implementation of NEST, this window is given as 1.5–6 keV_{ee} for ERs and 6–30 keV_{nr} for NRs. The difference between these energy terms is to represent the quenching that takes place for an NR event. The conversion between these two representative energy depositions is given by,

$$E_{dep}(keV_{ee}) = E_{ER} + \frac{1.5}{6.0}E_{NR} \tag{5.1}$$

$$E_{dep}(keV_{nr}) = E_{NR} + \frac{6.0}{1.5}E_{ER}. \tag{5.2}$$

The energy scale used is dependent on the type of simulated background; i.e., β and γ interactions are represented by keV_{ee}, whereas nuclear recoil interactions are given as keV_{nr}. In real data, there is no definite way to distinguish ER from NR events, hence interactions are usually represented in one or the other version. To better replicate the real impact of the detector on energy depositions and to simulate the treatment of real data, the ROI is also defined in terms of S1 and S2 space. In this space, the WIMP ROI is defined by $0 < \mathrm{S1}_c < 80$ phd, with a 3-fold S1 coincidence requirement within the TPC PMTs. The 3-fold cut is required to reduce background events leaking into the WIMP ROI from coincidences between PMT dark noise and S2-only events. In addition, the S2-raw signal is required to be greater than 420 phd—equivalent to ~ 5 extracted electrons. This is to ensure an adequate S2 size for an accurate x-y position reconstruction, reducing backgrounds due to misreconstruction of events into the fiducial volume.

Single scatter events are those that deposit all of their energy into a single interaction point, as expected from a WIMP interaction. Although on microscopic scales, the total energy deposition of background events may result from many micro-depositions taking place within a very small radial regime, these interactions cannot be resolved due to the expected spatial resolution of the detector. A single scatter cut applied on the energy-weighted standard deviations in the radial, $\sigma_r, and vertical directions, \sigma_z$, is used

to reject multi-scattering neutrons and γ-rays that fall outside of the energy-weighted clustering resolution. The energy weighted mean position is defined as,

$$\langle r_E \rangle = \frac{\sum_i E_i r_i}{\sum_i E_i}, \qquad \langle z_E \rangle = \frac{\sum_i E_i z_i}{\sum_i E_i}, \tag{5.3}$$

where r_i and z_i represent the radial and vertical interaction points and E_i, the energy deposited into each vertex, represented by i. The energy-weighted standard deviation (σ_z & σ_r) is then given by,

$$\sigma_r = \sqrt{\frac{\sum_i E_i (r_i - \langle r_E \rangle)^2 \times \sum_i E_i}{(\sum_i E_i)^2 - \sum_i E_i^2}}, \qquad \sigma_z = \sqrt{\frac{\sum_i E_i (z_i - \langle z_E \rangle)^2 \times \sum_i E_i}{(\sum_i E_i)^2 - \sum_i E_i^2}}. \tag{5.4}$$

The single scatter requirements used in the background selection of LZ simulations is developed through taking into account the PMT size and the array layout, and by incorporating previous LUX position reconstruction studies [163]. A conservative requirement of $\sigma_r < 3.0$ cm and $\sigma_z < 0.2$ cm is set for S2 signals at the detection threshold. Position resolution in real LZ data will make use of hit patterns and waveform shapes, and is expected to be < 1 cm radially and to vary with energy and radial position.

In addition, events occurring in the active volume of the TPC with a time-coincident event taking place within the skin or the outer detector veto system are also rejected. For the LXe skin veto, at least 3 phd must be observed within an 800 µs coincidence window, either before or after the TPC S1 signal. Whilst for the OD, a minimum of 200 keV must be deposited within a 500 µs interval. The primary purpose of the veto systems is to ensure the vetoing of both prompt γ and delayed signals from thermal neutron capture.

Lastly, the final crucial event selection criteria is the fiducial volume cut. This cut is designed to remove events near the edge of the TPC. A cylindrical virtual volume with boundaries defined to be 4 cm from the TPC walls, 2 cm above the cathode grids (with 14.8 cm of LXe below the cathode providing further shielding) and a further 13 cm below the gate grid. This volume contains a total of 5.6 tonnes of LXe and is largely motivated by the misreconstructed wall events leaking into the FV. This leakage probability has previously been studied using the Mercury algorithm—which is responsible for the x-y reconstruction from S2 PMT hits—and shown to be less than 10^{-6} for the smallest S2 signals at 4cm away from the walls, ensuring that wall events are a sub-dominant background [164, 165]. Simulated efficiencies after the application of the WIMP ROI cuts as a function of recoil energy for electronic and nuclear recoils is shown in figure 5.3.

5.3.2 Projected Background Rates

During the construction phase of the detector, a cut-and-count style analysis was performed on the simulated background dataset as a means of assessing the impact of design specific decision making. The integrated rates calculated for the ER and NR backgrounds were selected using the WIMP ROI in the energy-space, where ER events between 1.5–6.5 keV and NR events between 6–30 keV were selected in a full 1000 live day run with a 5.6 tonne fiducial mass. Although the analysis takes a different approach to that used by the PLR analysis, it nevertheless provides an insight into the rates expected for the WIMP search and in informing design specifications. The analysis simulates many of the backgrounds detailed in section 3.2 and various other event types that contribute towards the integrated background rate; such as physics backgrounds from astrophysical neutrinos. The contributions from the most relevant background components are listed in table 5.2, with the expected ER and NR counts for each entry.

Background events from *detector components* originate from naturally occurring radioactive isotopes found within the construction material of the experiment. Isotopes of interest for simulations are the decay chains of ^{238}U, ^{235}U, ^{232}Th; as well as, γ-emitting isotopes of ^{40}K, ^{137}Cs and ^{60}Co. The results from the comprehensive screening campaign of LZ ($>$ 1200 assays over 5 years) are used to quantify the activity of such isotopes within the component-centric BACCARAT framework. Due to the selective material sourcing process used by LZ, backgrounds from detector components are sub-dominant. Furthermore, isotopic *surface contamination*, through dust deposition (500 ng/cm^2) and

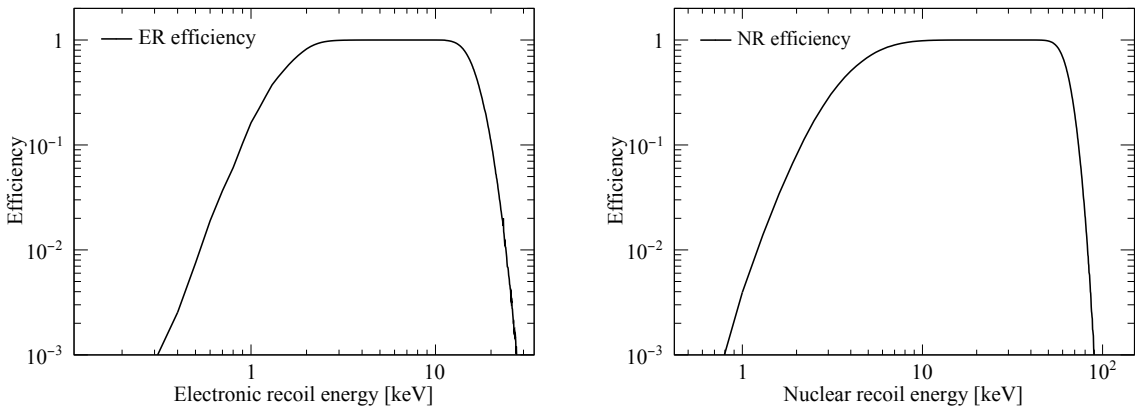

Figure 5.3: Simulated detection efficiency for electronic (left) and nuclear recoil (right) events after the application of the WIMP ROI event selection cuts. These cuts include the 3-fold S1 coincidence, S1$_c$ $<$ 80 phd and S2 $>$ 420 phd. Figure adapted from [105].

Table 5.2: Estimated background rates from all significant contributors in a 1000 live day run and a 5.6 tonne fiducial mass. The ER and NR counts are from a region of interest relevant to a 40 GeV/c^2 WIMP; approximately 1.5–6.5 keV for ERs and 6–30 keV for NRs; and after application of the single scatter, skin and OD veto cuts. Counts from the solar ^{8}B and hep neutrinos are given as a reference, as they are not significant above an NR energy of 6 keV. The ER discrimination is a conservative value taken from the LZ TDR [110], aimed at selecting events from the energy-space that is most relevant for NR interactions.

Background Sources	**ER**	**NR**
Detector components	9	0.07
Surface contamination	40	0.39
Laboratory and cosmogenics	5	0.06
Dispersed radioisotopes (Xenon)		
^{222}Rn (1.8 µBq/kg)	681	0
^{220}Rn (0.09 µBq/kg)	111	0
^{136}Xe ($2\nu\beta\beta$)	67	0
^{85}Kr (0.015 ppt g/g)	24.5	0
^{39}Ar (0.45 ppb g/g)	2.5	0
Astrophysical neutrinos		
Atmospheric (Atm)	0	0.46
Diffuse supernova (DSN)	0	0.05
Solar (^{8}B + *hep*)	0	38*
Solar (*pp* + ^{7}Be + ^{13}N)	191	0
Total	1131	1.03
Total (with 99.5% ER discrimination, 50% NR efficiency)	5.66	0.52

^{222}Rn plate-out (50 nBq/cm^2) leads to both ER events near the detector surface and NR events from (α, n) processes. Although a significant amount of wall events are rejected by the fiducial volume cut, some make it into this volume due to algorithmic spatial misreconstruction near the walls and mobility of ^{210}Bi. Wall backgrounds have been a huge focus during construction with extensive surface cleanliness protocols in place as detailed in section 3.2.2, thus the assumptions used in this study are expected to be conservative.

Environmental backgrounds either generated from cosmogenic activation or originating from the surrounding environment of the detector are combined under *laboratory and cosmogenics*. The ER background from this source is predominantly from γ-ray events

from the rock, as detailed in section 3.5; with a slight contribution from activation products ^{136}Xe and ^{46}Sc. The NR background is from muon-induced neutrons.

Although xenon is mostly radiopure, there are trace amounts of internal and external contaminants that contribute strictly in the ER band of the background spectrum. The dominant internal background comes from the $2\nu\beta\beta$ of ^{136}Xe, which exists in trace amounts within the sourced xenon. Xenon usually contains other isotopes, such as ^{85}Kr and ^{39}Ar. These isotopes are remnants from the production of xenon. The concentration of these isotopes provided in table 5.2 are estimated based on the expected performance of the a custom-made gas chromatography system designed and installed at SLAC to remove krypton [110]. The krypton requirement is ambitious, hence sensitivity studies using 0.30 ppt g/g concentrations have also been performed to quantify the impact. The largest contributor from xenon contaminants is the backgrounds originating from radon emanation. The ER contributions from ^{222}Rn and ^{220}Rn account to a total of 792 events—equivalent to $\sim$70% of all ER backgrounds from the cut-and-count analysis. This is based on a uniform ^{222}Rn(^{220}Rn) activity of 1.8(0.09) µBq/kg; which falls within the bounds of the optimistic and the conservative projections from section 4.20.

The last major background contribution to the WIMP search ROI is from *astrophysical neutrinos*. The elastic neutrino-electron scattering [166] and coherent elastic neutrino-nucleus scattering (CEνNS) [167] are the two main interaction types, leading directly to ER and NR events, respectively. There are several sources of neutrino backgrounds observed by the LZ detector; atmospheric neutrinos produced in muon and pion decays, neutrinos produced in distant supernovae events, and solar neutrinos originating from various fusion reactions within the sun. The solar neutrino background for WIMP masses greater than $\sim$20 GeV/c^2 is dominated by *pp* neutrinos, with contributions from the ^{7}Be and CNO (Carbon-Nitrogen-Oxygen) cycles. The observed rates from elastic neutrino-electron scattering leading to ER events in LZ are calculated using flux and spectra from [168], incorporating up-to-date oscillation parameters from [169]. To take into account the effect of atomic binding, a scaling factor based on the relativistic random phase approximation calculation in [170] is applied to the free electron scattering rate below 30 keV. The ^{8}B and hep neutrino rates are only relevant for NR energies $\lesssim$ 6 keV, equivalently for WIMP masses below $\sim$20 GeV/c^2. At this regime, CEνNS of neutrinos originating from the two fusion processes,

$$^8\mathrm{B} \rightarrow {}^7\mathrm{Be}^* + \mathrm{e}^+ + \nu_e \quad (^8\mathrm{B}\ \textit{neutrinos}), \tag{5.5}$$

$$^3\mathrm{He} + p \rightarrow {}^4\mathrm{He} + \mathrm{e}^+ + \nu_e \quad (\textit{hep}\ \textit{neutrinos}), \tag{5.6}$$

become dominant irreducible NR backgrounds. Although table 5.2 provides a reference event rate for ^{8}B and *hep* neutrinos, they do not contribute to the total cut-and-count rate observed for a 40 GeV/c^2 WIMP; nevertheless, they are included in the WIMP sensitivity calculations using the full PLR treatment described in section 5.4.

The cut-and-count analysis for a 40 GeV/c^2 WIMP results in a total of 1131 ER events and 1.03 NR events, prior to ER–NR discrimination. In applying a 99.5% discrimination selection on ER events as described in figure 2.4 and a 50% NR efficiency; the total sum of irreducible backgrounds in the signal region result in 6.18 events in a 1000 live day run within a 5.6 tonne fiducial volume. The spectral contributions from the background sources highlighted in table 5.2 for NR and ER events are shown in figures 5.4 & 5.5, respectively. These figures show spectral rates of single scatter events in the fiducial volume, excluding the energy ROI, skin, OD cuts to provide a wider picture of background rates. The S1–S2 PDFs are a bi-product of the rates shown here, after the application of WIMP-specific ROI cuts and are used as an input to the LZSTATS framework for sensitivity studies.

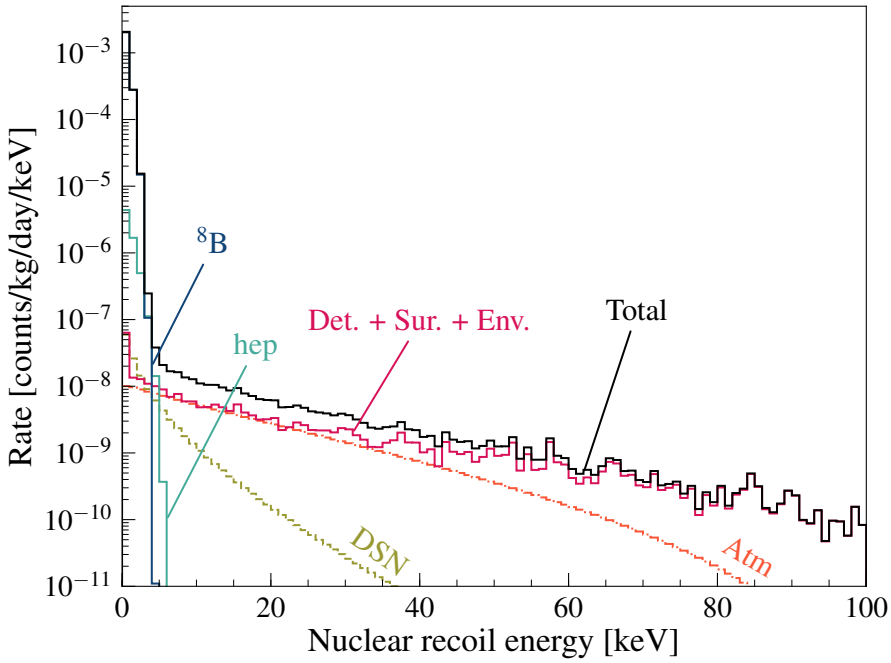

Figure 5.4: The projections of NR background spectra in the 5.6 tonne fiducial volume for single scatter events, including the skin and OD veto cuts. Detector efficiency and WIMP-ROI cuts on S1$_c$ are also excluded. Laboratory, cosmogenic and surface backgrounds are combined together as (Det. + Sur. + Env.). Figure adapted from [105].

Confusing. Suggest to use before/after cuts instead of including/excluding.

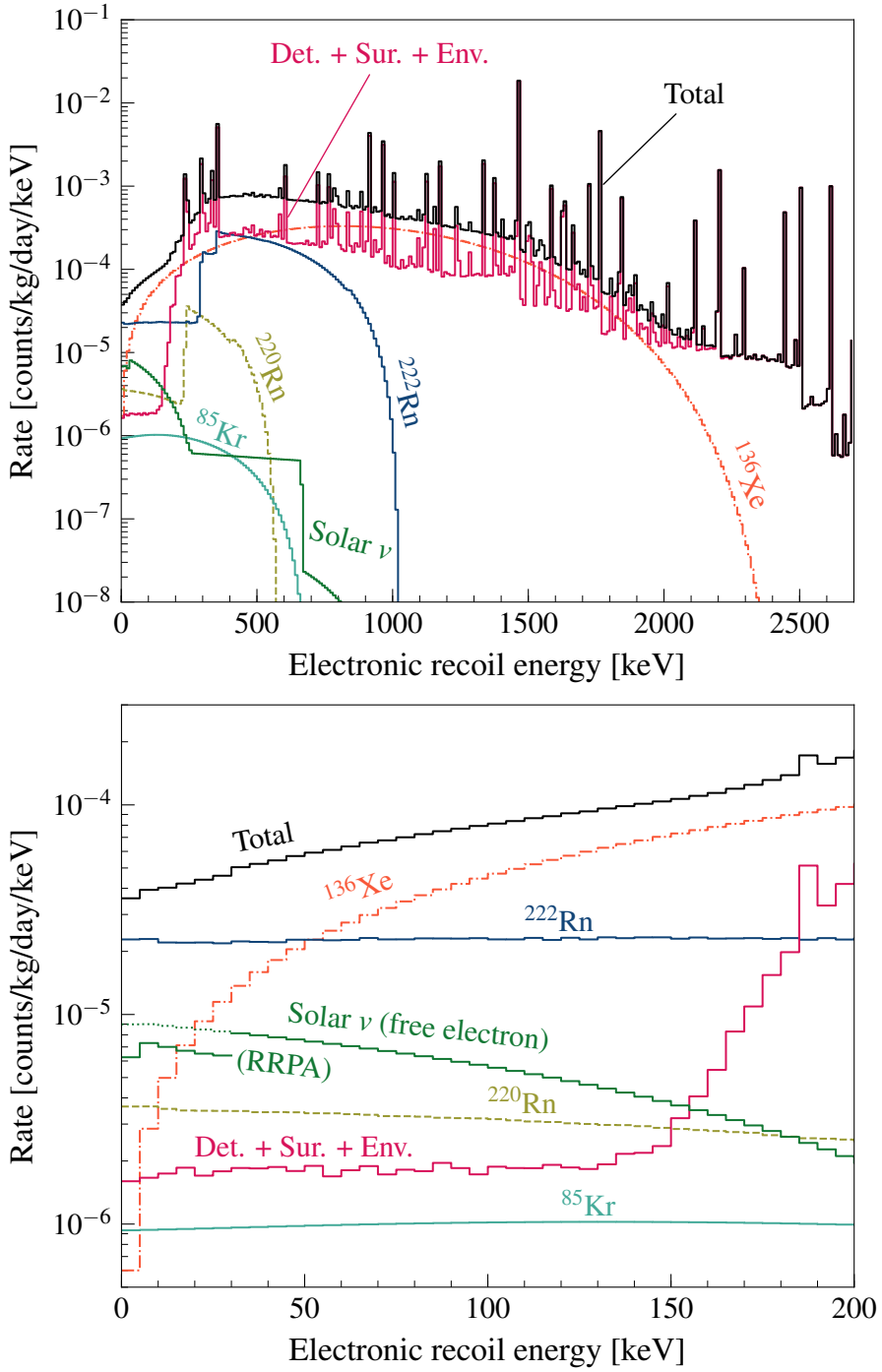

Figure 5.5: The extended (above) and the close-up (below) projections of ER background spectra in the 5.6 tonne fiducial volume for single scatter events, including the skin and OD veto cuts. Detector efficiency and WIMP-ROI cuts on $S1_c$ are also excluded. The scaling applied to the pp + ^{7}Be + ^{13}N from relativistic random phase approximation (RRPA)calculations is visible below 30 keV [170]. Laboratory, cosmogenic and surface backgrounds are combined together as (Det. + Sur. + Env.). Figure adapted from [105].

5.4 Statistical Approach

The eventual outcome expected from the LZ experiment is either to discover a dark matter signal that is significantly different from the expected background model—WIMP-like or otherwise, or in a less favourable scenario, verify the expected background model and set a statistical limit on the excluded model parameters. Often the outcome of the experiment is evaluated against the *null*, H_0, and the *alternative*, H_1, hypothesis in determining the compatibility of the observed experimental dataset with the hypotheses. In testing for a hypothesis, H_0 is assumed to be true until it is rejected by the observed dataset. The definition of the null and alternative hypothesis is dependent on the type of statistical statement being made; either claiming a significance for discovery or setting limits on model parameters.

Typically, new physics searches are looking for a signal that is adding on top of the expected background. The discovery of a signal is formulated by a hypothesis test where the background-only hypothesis plays the role of the null hypothesis and the signal-plus-background hypothesis plays the alternative. In claiming a discovery, the background-only hypothesis is rejected on the basis that it is incompatible with the observed data. When the observed dataset fails to reject the null hypothesis, hence failing to claim significance, there remains the question of what values of the theoretical parameter space is still allowed—holds potential for discovery, likewise, what values of the model parameter space is excluded with the available data. In the limit setting scenario, the null and the alternative hypothesis are flipped around, where the null hypothesis is defined as the signal-plus-background and the alternative is background-only. Hence, a series of null hypothesis are tested with increasing values of the parameter of interest until a median value is reached for the desired exclusion significance—also known as the confidence region/interval.

The approach taken in determining the discovery potential and the sensitivity of LZ to WIMPs is the Profile Likelihood Ratio (PLR) method [171] utilising an unbinned maximum likelihood. This method allows an event-by-event comparison of the observed (or pseudo) data to a given model, providing a near-optimal exploration due to its ability to discriminate between signal and background by utilizing a number of variables that may have limited discrimination power on their own. In utilising on this method, a statistical package, LZStats, was developed, that built upon the RooStats package frequently used by the HEP community [172]. A detailed description of the LZStats package can be found in [102]. The following sections will lay out the foundations of the

approach taken in LZSTATS, focusing on the PLR method, construction of the null and the alternative hypothesis for the WIMP search, which become the inputs to LZSTATS and finally, the output from this package and the construction of the sensitivity and discovery potential of the LZ experiment.

5.4.1 Profile Likelihood Ratio Method

Statistical Terminology

A detector usually records an extensive amount of data of which only a selected few are of interest. The selection criteria for the WIMP search in LZ has been described in section 5.3.1. The dataset used in the studies to follow are achieved by Monte Carlo techniques to generate pseudo-experiments under the condition imposed by the hypothesis. Each event is parameterised by a vector $\boldsymbol{x}$ of constructed quantities, known as observables. The observables in LZ data include $S1_c$, $S2_c$, x-y-z and t. The spatial quantities are assumed to be uniform due to fiducialisation and events are assumed to be time-independent; hence, these variables are not included in the list of PLR observables. The observables for the WIMP search study are selected as $\boldsymbol{x} = (S1_c,\ S2_c)$, following the definitions of these two quantities from the previous chapter.

The background and signal *event probability models* representing the hypotheses is then constructed as a parametric family of probability density functions (PDF) in obtaining a particular event for a particular background or signal component, c, and is expressed by,

$$f_c(\boldsymbol{x}|\boldsymbol{\theta}). \tag{5.7}$$

The parameters of the model given by $\boldsymbol{\theta}$ are intrinsic to the model, representing parameters of a physical theory, or an unknown property that can be estimated from data. The complete set of model parameters include the *parameters of interest* (POI), $\boldsymbol{\alpha}$ and the *nuisance parameters*, $\boldsymbol{\nu}$, which account for unknown experimental properties of the physical theory, such as uncertainties; carrying no intrinsic value but necessary for an accurate depiction of the model. The event probability model typically contains a number of background components and a signal component, each with their associated PDFs and an expected mean number of events, $\mu_c(\boldsymbol{\theta})$, the sum of which is given by $\mu(\boldsymbol{\theta})$. For a total number of N components, total probability model is then given as the weighted

sum of each individual component, where

$$f(\boldsymbol{x}|\boldsymbol{\theta}) = \sum_{c=1}^{N} \left(\frac{\mu_c(\boldsymbol{\theta})}{\mu(\boldsymbol{\theta})} \right) f_c(\boldsymbol{x}|\boldsymbol{\theta}). \tag{5.8}$$

In considering a dataset with n events, where $\mathcal{D} = \{\boldsymbol{x}_i\}_{i=1}^{n}$ where events are independently drawn from the same underlying distribution, the *joint probability distribution* of each events takes the form of the product of the individual probability distributions of each event. Furthermore, the overall Poissonian nature of observing n events given $\mu(\boldsymbol{\theta})$ has to be taken into account, resulting in

$$f(\mathcal{D}|\boldsymbol{\theta}) = Pois(n|\mu(\boldsymbol{\theta})) \prod_{i=1}^{n} f(\boldsymbol{x}_i|\boldsymbol{\theta}) \tag{5.9}$$

$$= \left(\frac{\mu(\boldsymbol{\theta})^n}{n!} e^{-\mu(\boldsymbol{\theta})} \right) \prod_{i=1}^{n} f(\boldsymbol{x}_i|\boldsymbol{\theta}). \tag{5.10}$$

(5.17) is what's really used.

The final form of the probability density model takes into account the nuisance parameters as approximated Gaussian constraints, which originate from auxiliary measurements. Due to the uncertain nature of these parameters, which contain a degree of uncertainty on the estimate, they are added as a *constraining term*, leading to the fully generalised form of the probability density model

$$f(\mathcal{D}|\boldsymbol{\theta}) = \text{Pois}(n|\mu(\boldsymbol{\theta})) \left[\prod_{i=1}^{n} f(\boldsymbol{x}_i|\boldsymbol{\theta}) \right] \prod_{j=1}^{N_c} g(\boldsymbol{\alpha}_j|\nu_j), \tag{5.11}$$

where the constraining term $g(\alpha_j|\nu_j)$ is given as the product of N_c constraining functions for each nuisance parameter, ν_j.

Profile Likelihood Ratio

The likelihood function $\mathcal{L}(\boldsymbol{\theta})$ is numerically equivalent to equation 5.11 with a fixed $\mathcal{D}$ and is used to determine the combination of model parameter values that maximize the probability of drawing the obtained dataset, $\mathcal{D}_{obs}$. It should be noted that the likelihood function does not represent the probability density for $\boldsymbol{\theta}$ and often does not normalise to unity. The likelihood function is used to investigate the measure of agreement between the observed data and a given hypothesis, through the construction of a function of the measured variables, called a *test statistic*, $t(\mathcal{D})$. Although a test statistic can be multidimensional, often it is constructed as a scalar function to lower the dimensionality of

the data without losing the ability to discriminate between hypotheses. Each hypothesis will imply a test statistic distribution, i.e., $f(t|H_0)$, $f(t|H_1)$; which may be calculated analytically or numerically. Commonly, Monte Carlo techniques are used to generate pseudo-experiments for complicated likelihoods, from which a test statistic distribution is obtained and a statement about the compatibility of the hypotheses is inferred.

A widely used test statistic for a given parameter of interest, μ, and a collection of nuisance parameters, ν, is the profile likelihood ratio (PLR) [171, 173], defined as

$$\lambda(\mu) = \frac{\mathcal{L}(\mu, \hat{\hat{\boldsymbol{\nu}}})}{\mathcal{L}(\hat{\mu}, \hat{\boldsymbol{\nu}})}. \tag{5.12}$$

The $\hat{\hat{\boldsymbol{\nu}}}$ represents the value of ν which maximises the log likelihood function for a fixed value of μ, known as the *conditional maximum-likelihood estimator*. The denominator is the maximised (unconditional) likelihood-function estimator of μ, where the single hat refers to the *maximum-likelihood estimators* (MLE), which are defined as the value that which maximises the likelihood function. The impact of the nuisance parameters broaden the profile likelihood as a function of μ, reflecting the lack of information about μ due to the systematic uncertainties.

In examining the comparability of hypotheses as a means for limit setting or assessing discovery potentials, it is convenient to use the test statistic

$$t_\mu = -2\log\lambda(\mu), \tag{5.13}$$

which is distributed between 0 and infinity, with larger values of the test statistic corresponding to increasing incompatibility between the two hypothesis of interest.

Hypothesis Testing

Once the distributions of the null and the alternative hypotheses are constructed through the test statistic, it becomes possible to define a hypothesis test to derive a statistical statement on whether the null hypothesis can be rejected. This is achieved through the definition of the p-value, defined as the probability of obtaining a result as the observed dataset under the assumption that the null hypothesis H_0 is true, i.e.,

$$p = P(t > t_{obs}|H_0), \tag{5.14}$$

$$= \int_{t_{obs}}^{\infty} f(t|H_0)dt. \tag{5.15}$$

A hypothesis test is constructed where a critical region is defined with a pre-declared size α such that the null hypothesis H_0 is rejected if the observed test statistic t_{obs} falls in this region, i.e., $p < \alpha$. The confidence level (CL) of the test is defined as $(1-\alpha)\%$, where the size of α is typically given as 5% or 10%. In direct detection of dark matter, and in this work, the CL is set to 90%. In particle physics, a common practice of reporting statistical results of a hypothesis test is via the significance Z, given as

$$Z = \Phi^{-1}(1-p), \tag{5.16}$$

where Φ^{-1} is the inverse of the cumulative distribution of a standard Gaussian. Z represents the number of standard deviations above the mean of a normal Gaussian distribution such that the upper-tail probability is equal to the p-value. The significance for evidence or a discovery correspond to $5\sigma > Z \geq 3\sigma$ and $\geq 5\sigma$, respectively.

5.4.2 Input

The background only hypothesis for the PLR analysis is constructed by an 11-component background model that is based on the analysis selection criteria detailed in section 5.3.1. The estimated number of counts per component in the extended $S1_c$–$S2_c$ space and their corresponding uncertainties that feed into the PLR analysis as the nuisance parameter terms is shown in table 5.3. The component specific uncertainties are estimated on a component-by-component basis. The *Det. + Sur. + Env.* uncertainties for both ER and NR contributions come from counting and simulation results, those on the neutrino components are primarily flux uncertainties, and the uncertainties on radon are from the branching ratio uncertainty of ^{214}Pb and ^{212}Pb to their respective ground states. Finally, those on ^{85}Kr and ^{136}Xe are estimates from uncertainties on the spectral shapes at low energies. Although these systematics are treated as nuisance terms in the LZ PLR with Gaussian priors, preliminary studies on their significance result in minimal shifts in the sensitivity results due to the low number of background counts expected in LZ. No other nuisance terms are included in the sensitivity calculation presented here.

The background-only event probability model for the WIMP search is constructed from the expected spectral background as given in figures 5.4 & 5.5, where component specific PDFs in the $S1_c$–$S2_c$ space, normalised to the background specific expected number of events is shown in figure 5.7. The background PDFs, $f_b(\boldsymbol{x_i})$, include no implicit dependence on any model parameters, i.e., no shape-varying nuisance parameters such as g_1 or g_2. These distributions are generated by taking samples from the corresponding

Table 5.3: Eleven background types considered in the PLR analysis, along with the integrated counts in the LZ 1000 day WIMP search exposure and the systematic uncertainties on their normalisations, included as nuisance parameters in the PLR. Counts are for the WIMP search ROI (S1 with $\geq$ 3fold coincidence, S1c $<$ 80 phd and uncorrected S2 $>$ 415 phd): approximately 1.5–15 keV for ERs and 4–60 keV for NRs; and after application of the single scatter, skin and OD veto, and 5.6 tonne fiducial volume cuts.

Background Components		**Counts (N)**	**Uncertainty (σ/N)**
ER			
Det. + Sur. + Env.	μ_{DetER}	152	20%
^{222}Rn	$\mu_{Rn\text{-}222}$	1705	10%
^{220}Rn	$\mu_{Rn\text{-}220}$	281	10%
^{136}Xe $2\nu\beta\beta$	$\mu_{2\nu\beta\beta}$	406	50%
^{85}Kr	$\mu_{Kr\text{-}85}$	74	20%
Solar ν (pp + ^{7}Be + ^{13}N)	μ_{pp}	548	2%
NR			
Det. + Sur. + Env.	μ_{DetNR}	0.77	20%
Atmospheric ν (Atm)	μ_{atm}	0.64	25%
Diffuse supernova ν (DSN)	μ_{DSN}	0.14	50%
hep ν	μ_{hep}	0.78	15%
^{8}B ν	$\mu_{B\text{-}8}$	29	4%

recoil energy spectra and converting them into the corrected (flat-fielded) S1 and S2 signals with the application of LZ specific detector parameters as detailed in section 5.4.3, by using NEST. As previously mentioned, the PLR analysis does not take into account any position related information, as majority of the background sources are expected to be uniformly distributed. The non-uniformity observed closer to the TPC walls, arising from detector the *Det. + Sur. + Env.* component is largely minimised due to fiducialisation.

The full LZ likelihood function for the WIMP search includes the signal spectrum for the WIMP recoils at varying WIMP mass, m_χ. The signal spectra are calculated using the standard halo model as discussed in detail in section 1.3.2 with v_0 = 220 km/s, v_{esc} = 544 km/s and $\rho_0 = 0.3$ GeV/c^2. The SI WIMP-nucleon recoil rate is calculated using the Helm from factor, as provided in [174], whereas the SD WIMP-nucleon recoil rate is driven from nuclear structure functions from [175]. The full sensitivity is calculated over a range of WIMP mass, m_χ, where a PDF for each mass is used as a standalone signal hypothesis to be tested. The power of the PLR technique arises from an optimal

weighting of the background-free and background-rich regions, and for all WIMP masses considered background rejection exceeds 99.5% for a signal acceptance of 50%. An example pseudo-experiment simulated from the total probability model in the $S1_c$–$S2_c$ space as expected by the LZ experiment after the completion of a full 1000 live-day run is shown in figure 5.6.

The simulated dataset in figure 5.6 corresponds to a background-only scenario in which majority of the events will occur in the ER band of the $S1_c$–$S2_c$ space. The ER and NR bands discussed previously in section 2.2.5, highlighting the discrimination power between the two event types, are shown here in blue and red, respectively. Furthermore, backgrounds expected from ^{8}B + *hep* neutrinos and a potential 40 GeV/c^2 signal as seen in the $S1_c$–$S2_c$ space is overlaid with their corresponding 1σ and 2σ contours. The signal contour is a direct consequence of the standard halo model of WIMPs. In setting limits, studying the sensitivity or the discovery potential of the detector, the parameter of interest is represented by the signal mean $\mu_s(\sigma)$ of a specific WIMP mass, which is directly proportional to the WIMP-nucleon scattering cross-section. Moreover, the expected mean of each background component μ_b assumes a degree of uncertainty as specified in table 5.3, thus is varied in the PLR analysis with a Gaussian variability constraint. The full log-likelihood function utilised by LZ for the WIMP analysis is thus given by the equation:

$$\begin{aligned} -2\log\mathcal{L}(\mu_s(\sigma),\boldsymbol{\nu}) = 2 &\left(\mu_s + \sum_{b=1}^{N_c}\mu_b\right) \\ &- 2\sum_{i=1}^{n_0}\log\left(\mu_s(\sigma)f_s(\boldsymbol{x}_i|m_\chi) + \sum_{b=1}^{N_c}\mu_b f_b(\boldsymbol{x}_i)\right) \\ &+ \sum_{b=1}^{N_c}\frac{(\mu_b - n_b)^2}{\nu_b^2}, \end{aligned} \tag{5.17}$$

where $\boldsymbol{\nu}$ represents the set of all nuisance parameters, n_b and ν_b refer to the estimated number of counts of a given background component in the WIMP search ROI and its associated uncertainty, respectively. The subscript, i, runs over each of the n_0 events in the dataset and b runs over each background component; evaluating the full LZ WIMP likelihood.

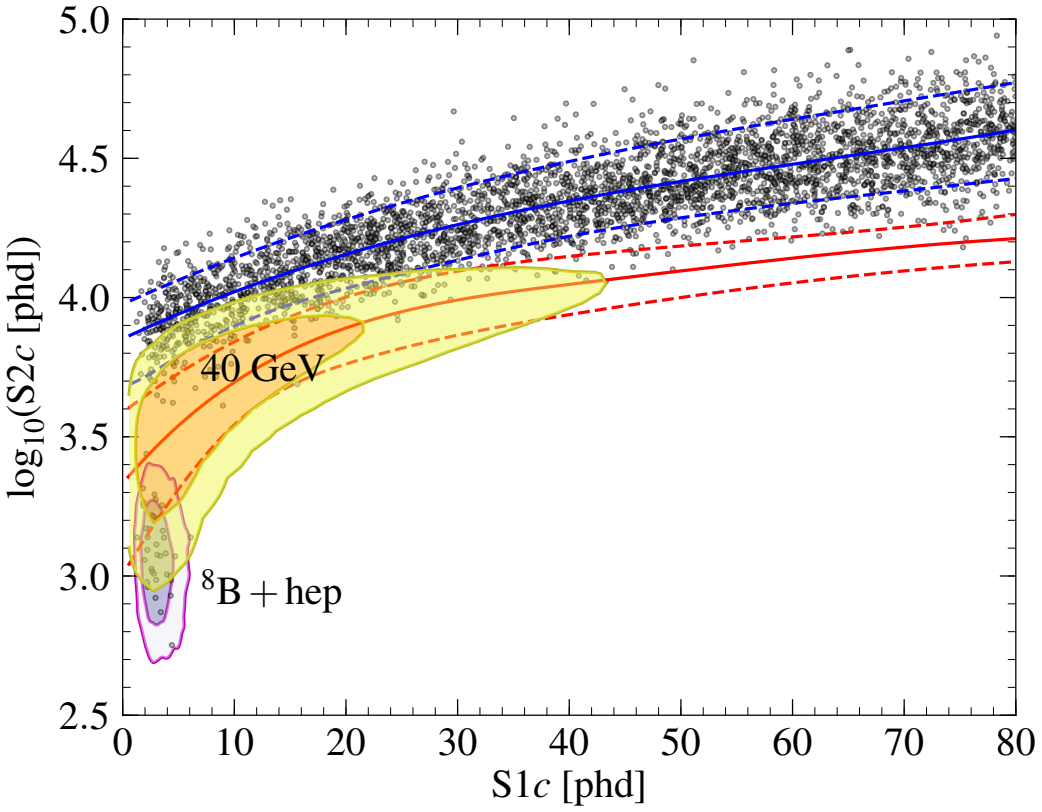

Figure 5.6: LZ simulated data set for a background-only 1000 live day run and a 5.6 tonne fiducial mass. ER and NR bands are indicated in blue and red, respectively (solid: mean; dashed: 10% and 90%). The 1σ and 2σ contours for the low-energy ^{8}B and *hep* NR backgrounds, and a 40 GeV/c^2 WIMP are shown as shaded regions. Diagram adapted from [105].

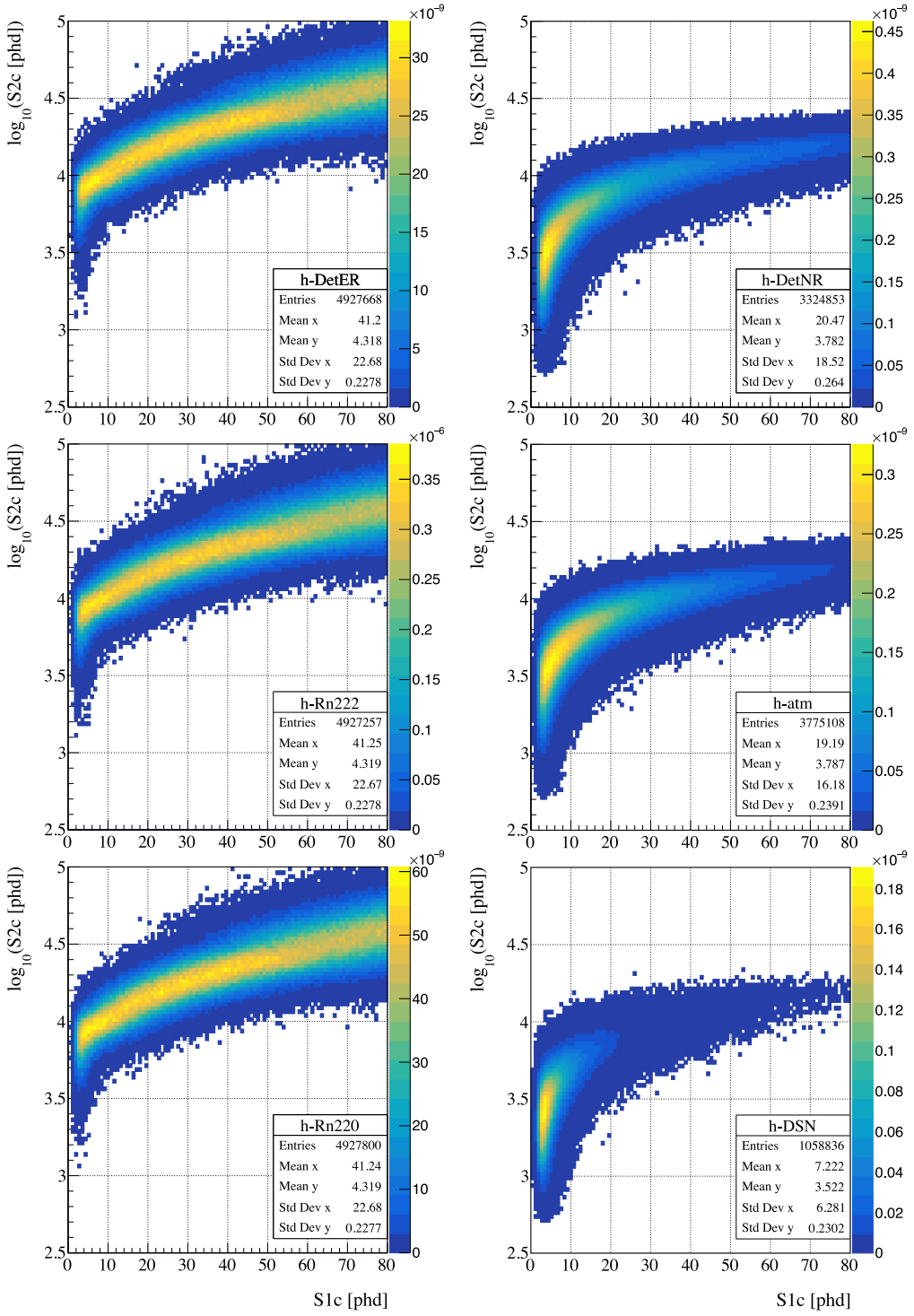

Figure 5.7: Background components of the event probability model for the WIMP search ROI with the electronic recoil background PDFs (left) and nuclear recoil background PDFs (right) normalised to their specific contribution in the corrected $S1$–$S2$ space (part 1).

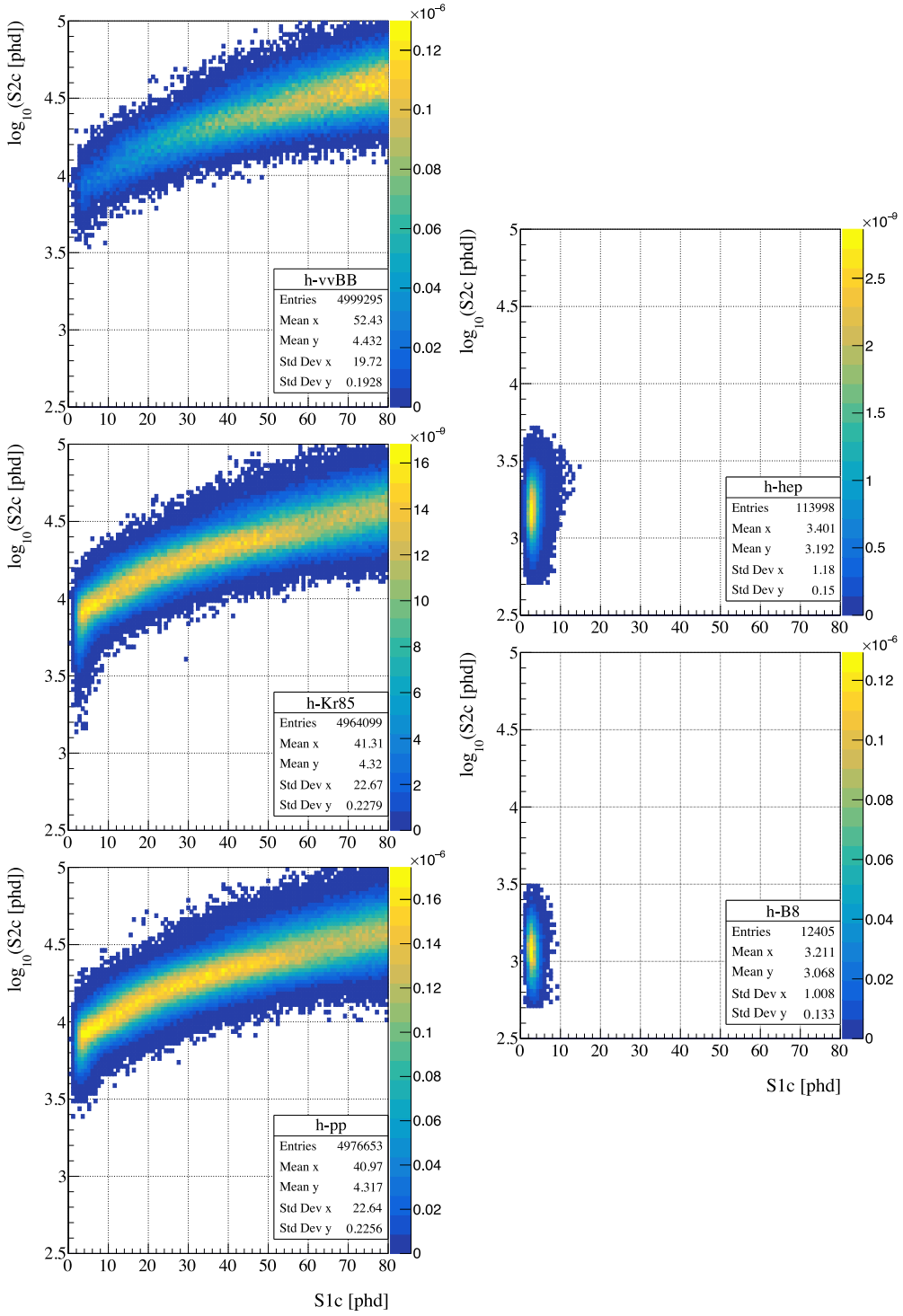

Figure 5.7: Background components of the event probability model for the WIMP search ROI with the electronic recoil background PDFs (left) and nuclear recoil background PDFs (right) normalised to their specific contribution in the corrected $S1$–$S2$ space (part 2).

5.4.3 Output

The statistical statement inferred by setting a limit or a sensitivity curve in the case of an experimental projection prior to data taking, is one which tries to determine the amount of a potential signal that can be present until the null hypothesis is no longer justifiable to a certain confidence level. Hence, the goal is to find the value of the POI, in this case, the number of detected WIMP particle interactions above which the signal plus background ($S + B$) hypothesis is incompatible with the background-only (B_{only}) hypothesis at a 90% CL. Therefore, the signal strength μ_s is scanned over to construct a multitude of test statistic distributions to determine the value of μ_s at which the statistical statement is achieved.

The corresponding one-sided PLR test statistic distributions from a 40 GeV/c^2 SI-WIMP interaction is shown in the upper panel of figure 5.8 for 16 values of the PIO where μ_s is scanned from 0–16. The null distribution corresponding to the $S + B$ hypothesis of an increasing μ_s is shown from top left to bottom right. The median of the alternative hypothesis representing the B_{only} scenario is taken as a proxy for the observed test statistic (vertical black line). The median alternative hypothesis test statistic used for a projected limit would otherwise be substituted for the observed dataset in the presence of real data. The lower panel in figure 5.8 represents the p-values (black dots) calculated from the pseudo experiments generated through the use of a Monte Carlo method of the above panel. A p-value is obtained for each hypothesis test, which represents the value of μ_s used in constructing the $S + B$ hypothesis. Moreover, for each value of μ_s that is tested, 1σ and 2σ deviations from the median of the alternative hypothesis is also obtained, represented in green and yellow, respectively. These are representative of the possible statistical and systematic fluctuations of the observed upper limit over repeated experiments.

The projected 90% CL upper limit on the POI, $\mu_s^{90\%}$, is obtained by determining the point at which the two hypotheses are no longer in agreement with one another; when the agreement between the two hypotheses fall to 10%. This is indicated as the point at which the p-value of a given μ_s is equal to 0.1, as shown by the horizontal red line in figure 5.8.

An alternative statistical test is to determine the projected discovery significance of an input signal model. In this case, the null hypothesis in the limit setting scenario is replaced by the background-only hypothesis and similarly, increasing values of the POI are considered. The projected discovery significance at a 3σ level is calculated by using

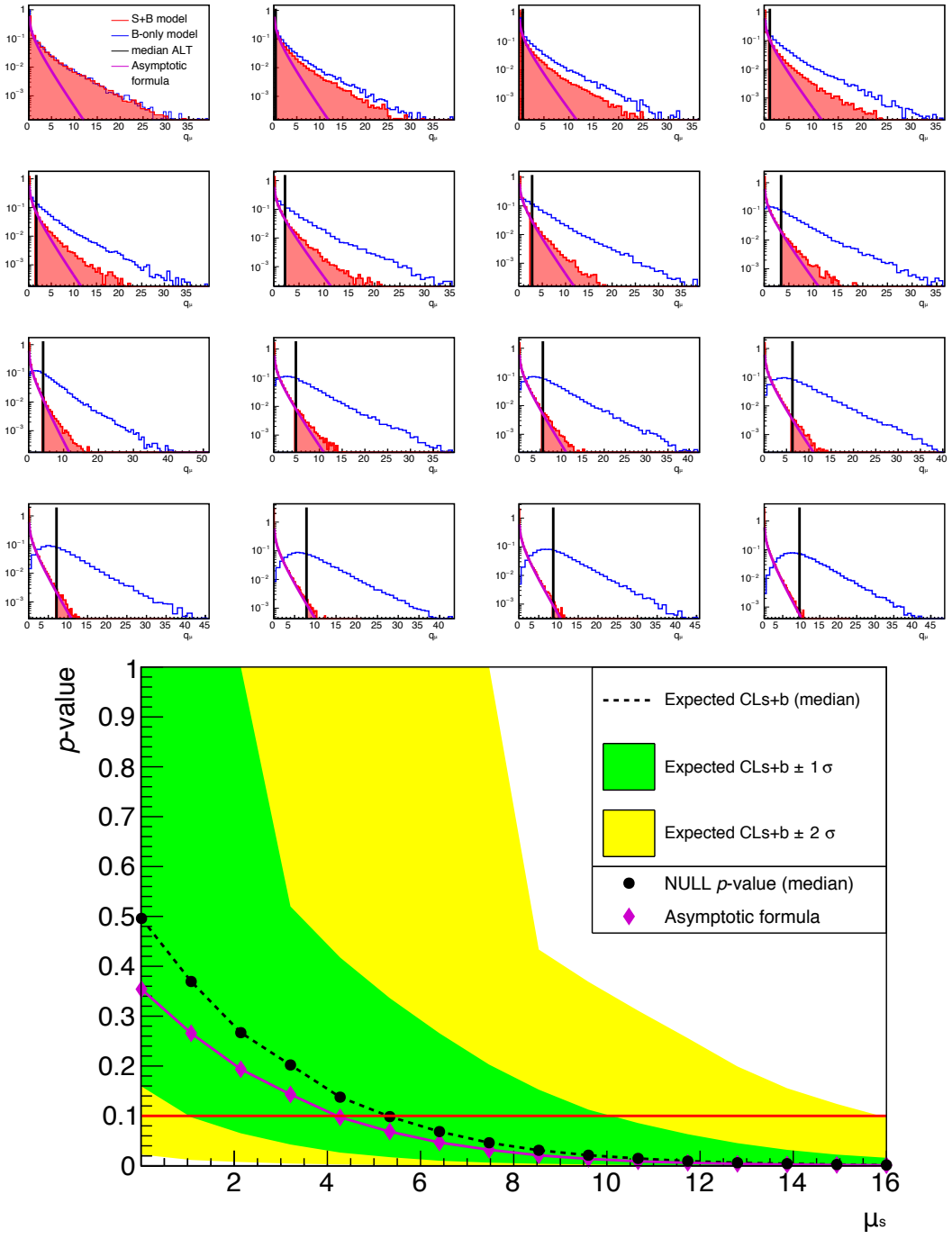

Figure 5.8: The projected sensitivity output of a 40 GeV/c^2 WIMP as analysed through the PLR analysis using LZStats. *Above*: Shows the test statistic distributions under the null (signal plus background in red) and the alternative (background-only in blue), constructed using the one-sided PLR test statistic in equation 5.13. The vertical black line indicates the median of the alternative distribution used in calculating the median p-value of the hypotheses. Increasing values of the POI, μ_s is tested from top left to bottom right. *Below*: Shows the calculated null p-value from both Monte Carlo (black dots) and the asymptotic formula (magenta diamonds). The p-value assuming 1σ and 2σ shifts from the median of the alternative distribution for each hypothesised μ_s are also indicated with green and yellow bands, respectively. The 90% upper limit on the POI is obtained when the two hypotheses result in a disagreement where the median p-value is equal to or less than 0.1; represented by the horizontal red line.

the median of the $S+B$ alternative hypothesis until a p-value of 0.14% is reached, where

$$\begin{aligned} p(\mu_s^{3\sigma}) &= 1 - \Phi(3) \\ &= 0.0014. \end{aligned} \tag{5.18}$$

The $\Phi(Z)$ in the above equation is the normal cumulative function. In addition, an alternative method in calculating sensitivity and discovery potential to that of the frequentest method using the asymptotic formula is represented by the magenta lines in figure 5.8. This alternative way is not the focus of this thesis, but more information on this can be found in [102]. The final sensitivity and discovery potential curves for the LZ experiment are computed across a range of WIMP masses using the statistical methodology described in this section. The following sections will highlight several of these studies, conducted due to the uncertainties arising as a result of the construction phase of the experiment. These are followed by the final projections of the LZ experiment to galactic WIMP dark matter.

5.5 Impact of Radon on Sensitivity and Discovery Potential

The simplified cut-and-count analyses detailed in section 5.3.2 resulted in a total of 1131 ER and 1.03 NR background events over the duration of a 1000 live day experiment in the WIMP region of interest. A significant proportion of these events are as a result of radon emanation from detector material. In assuming a ^{222}Rn(^{220}Rn) activity of 1.81(0.09) µBq/kg within the LXe active volume, the approximated events arising from these two sources add up to 792 ER interactions, making up $\sim$70% of all ER events, as summarised in table 5.2. However, as discussed in detail in section 4.6, the radon emanation projections arising from both the bottom-up and large scale screening efforts of detector materials in LZ come with a range of possible activities. These depend on the performance of the radon removal system in gas, the uncertainties of cold temperature suppression across different material and any systematics that may otherwise be unaccounted. Moreover, the unexpected radon emanation rate observed from the titanium cryostat risked the possibility of failing to reach the sensitivity requirement of 3.0×10^{-48} cm^2 for the SI-WIMP hypothesis as defined by the LZ technical design report [110].

In order to address these range of possibilities, the potential impact of unexpected radon emanation rates were examined for a range of radon activities, assessing the variability of sensitivity and discovery potential to the SI-WIMP hypothesis. The uniformity of the ^{222}Rn background in the fiducial volume lead to the realisation of an invariable spectral shape under a varying normalisation factor to the radon background. Therefore, a linear shift in normalisation—or the expected activity of radon—results in a vertical spectral shift of the ^{222}Rn and ^{220}Rn rates provided in figure 5.5. The LZSTATS framework was used to alter the levels of expected radon emanation of the background model, $\mu_{^{222}Rn}$, ranging from 0.1 µBq/kg to 10.0 µBq/kg of radon activity. Although the results are given in ^{222}Rn specific activity, the ^{220}Rn activity was also scaled by the same factor, keeping the ratio of ^{222}Rn/^{220}Rn constant at all times.

To accurately explore the potential impact of radon, roughly 200k pseudo-experiments were produced for each new background hypothesis driven from $\mu_{^{222}Rn}$ and repeated over 16 test values of the POI (μ_s) to calculate the p-value of the corresponding one-sided median 90% CL. The change in SI-WIMP sensitivity of a 40 GeV/c^2 WIMP as a function of ^{222}Rn activity and the corresponding 3σ discovery potential is shown in figure 5.9. These plots are overlaid with the best and the worst possible expected radon emanation scenarios driven from section 4.6; where scenario A (11.0 mBq) represents a rate assuming radon removal (RR) in gas and optimistic cold suppression (CS) factors; B (21.6 mBq) assumes RR and moderate CS factors. Scenarios C (41.3 mBq) and D (60.8 mBq) represent RR-only and warm emanation results, respectively, where CS is not assumed. The projected radon emanation rate given by the vertically dashed green line as assumed in [105] is given as 1.81 µBq/kg, situated between scenarios A and B. As observed from figure 5.5, both the sensitivity and the discovery potential gradually increases with an increasing radon activity. However, this increase is substantially slow over the range of possible radon scenarios, with the median 90% CL limit staying well below the LZ requirement of 3.0×10^{-48} cm^2.

At a ^{222}Rn activity of 1.81 µBq/kg, the achieved sensitivity is 1.43×10^{-48} cm^2; whereas with the best (A) and worst (D) possible scenarios, the sensitivity shifts from 1.34×10^{-48} cm^2 to 1.76×10^{-48} cm^2. A drastic increase of 3.4 times (scenario D) in comparison to the baseline radon projection seems to result in a subtle loss is sensitivity, this loss is equivalent to $\sim$23% of the baseline sensitivity. To further examine the impact of elevated radon activity within the active volume, statistical tests were conducted to quantify the time impact of such elevated rates; i.e., given an increase of a factor x, how much

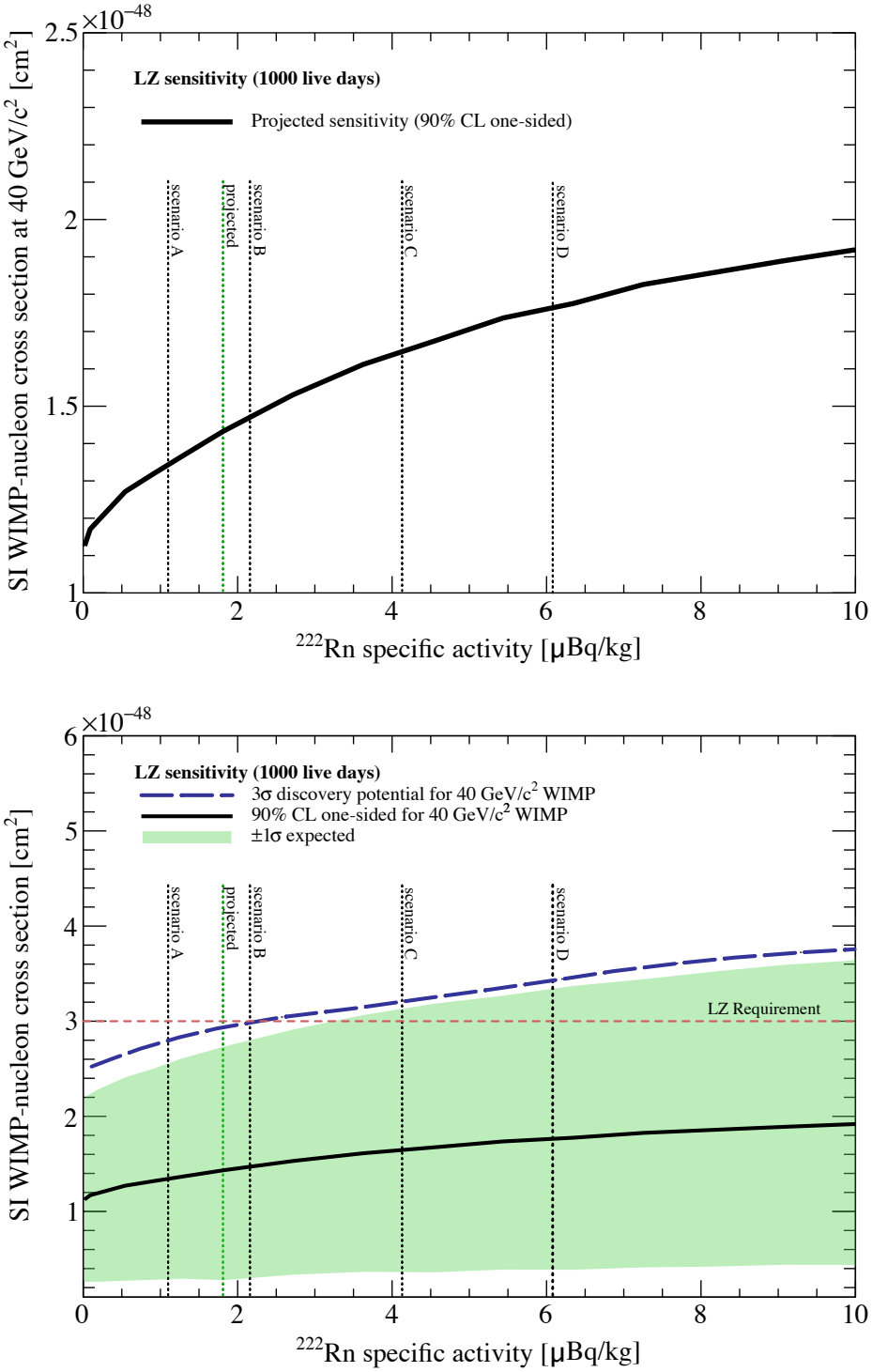

Figure 5.9: Projected SI sensitivity and discovery potential for a 1000 live-days run in 5.6 tonnes of fiducial volume as a function of ^{222}Rn activity as observed in the fiducial volume for a WIMP mass of 40 GeV/c^2 WIMP. *Above*: Shows the median 90% CL sensitivity with the projected estimate for ^{222}Rn activity of 1.81 μBq/kg marked with a green vertical line. Scenarios A, B, C and D (black vertical lines) are driven from emanation results in section 4.6, indicating the four scenarios ranging from the most optimistic to the pessimistic scenarios. *Below*: Shows the same result as above but with the variation observed on the 1σ band of the median sensitivity and the 3σ discovery potential as radon activity is increased. The LZ sensitivity requirement of 3.0×10^{-48} cm^2 is given with the horizontally dashed red line.

longer does the experiment have to run to reach the desired sensitivity under the baseline projection scenario.

The SI-WIMP sensitivity against live days of data taking is shown in figure 5.10 for a multitude of radon activities. The solid black line in figure 5.10 shows the time evolution of the baseline scenario for the SI-WIMP sensitivity assuming a ^{222}Rn activity of 1.81 µBq/kg across 0–2000 live days, overlaid with the 1σ band (solid green) of the median 90% CL. Furthermore, the median 90% CL sensitivity evolution of $x2$, $x4$, $x6$ radon activity factors in comparison to the baseline scenario is given as the dashed coloured lines, as indicated on the plot. As observed from the plot, doubling the ^{222}Rn activity to 3.6 µBq/kg results in an extra $\sim$48 days above 1000 live days to regain the sensitivity loss in comparison to baseline projection. At a much larger radon activity—6 times the baseline projection, the impact becomes more substantial, where the baseline sensitivity is reached with an extra $\sim$325 live days.

In conclusion, the sensitivity studies detailed above on elevated radon levels within the active LXe volume of LZ indicate that the sensitivity and discovery potential to the SI-WIMP is not substantially impacted by even the worst case scenario arising from screening efforts. Despite the gradual increase in both sensitivity and discovery potential, a ^{222}Rn activity of 60.8 mBq results in a median sensitivity that remains below the LZ requirement [105, 110]. Although the result is somewhat surprising, the ^{222}Rn background does indeed fall into the ER band, and ER-NR discrimination combined with the PLR analysis minimises the impact of such elevated radon levels. This is better understood when considering that although a shift in the ^{222}Rn normalisation increase the ER band population, it is the lower tail of the ER band distribution that leaks into the NR band. As can be seen from figures 5.6 & 5.7, the denser regions of the ER and NR distributions remain fairly separated. In a conventional cut-and-count analysis, the leaked events are evenly distributed in the signal region, whereas in a PLR analysis, their relative positions in the $S1$–$S2$ space is conserved, hence a large amount of the signal space remains undisturbed by larger ER backgrounds, resulting in a gradual loss in sensitivity and discovery potential. Although it appears that elevated levels of radon is not a large issue for the WIMP search, the impact of radon on signal models that are expected in the ER band will be much larger.

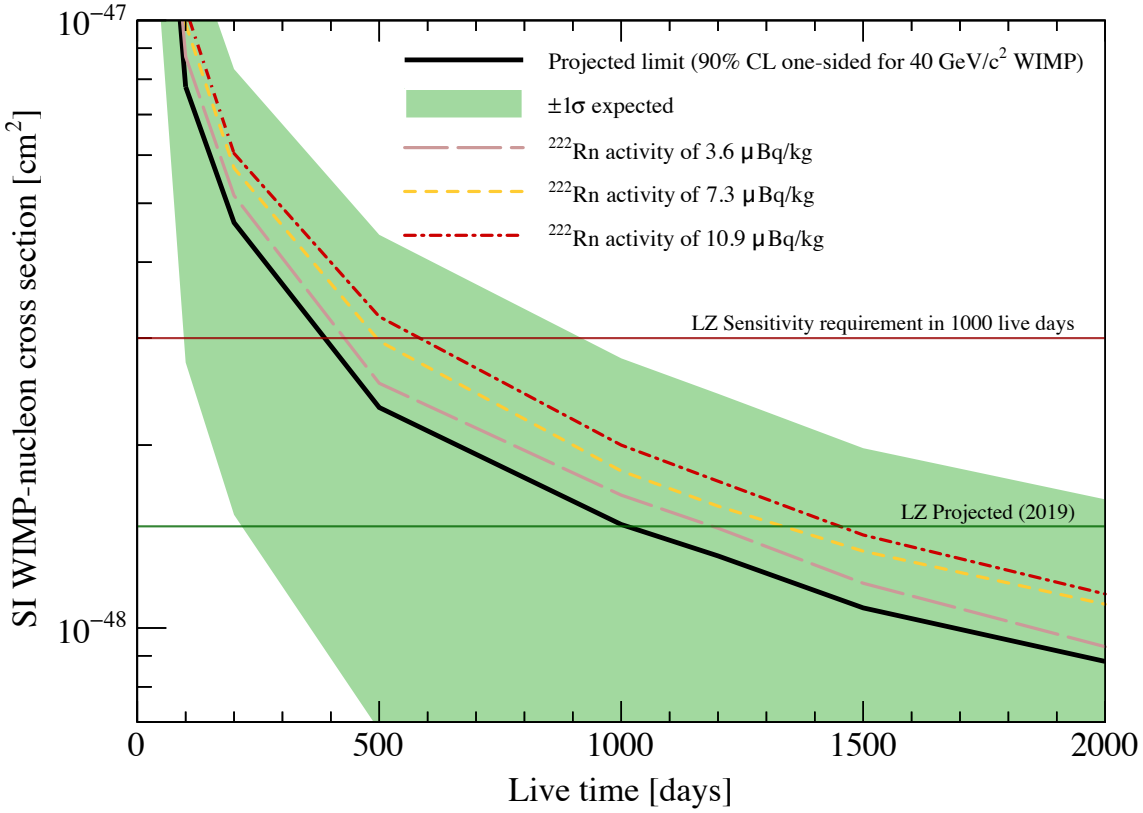

Figure 5.10: Projected SI sensitivity in 5.6 tonnes of fiducial volume as a function of live days of data taking, showing the evolution of the median 90% CL evolution for a range of ^{222}Rn activities for a WIMP mass of 40 GeV/c^2 WIMP. The baseline projected scenario with ^{222}Rn activity of 1.81 μBq/kg is given as the solid black line, along with the 1σ band (green). The median sensitivity evolution for radon activities increase by factors of x2, x4, x6 are displayed in dashed coloured lines. The LZ sensitivity requirement and the baseline sensitivity is overlaid with horizontal red and green lines, respectively.

5.6 Impact of Krypton on Sensitivity and Discovery Potential

During the construction of the LZ detector, a parallel effort in purifying the sourced xenon from its radioactive contaminants was in place to remove the ^{85}Kr by using a custom-made gas chromatography system. The removal of krypton is a time consuming process and reaching the ambitious requirement of 0.015 ppt of ^{85}Kr set by the LZ TDR [110] in line with the construction of the detector and the incorporation of the xenon into the circulation system was in question. To determine whether the experiment can save time on krypton removal and deliver the xenon in time, a similar statistical study to that of radon for elevated ^{85}Kr activities was conducted.

The sensitivity and discovery potential to a 40 GeV/c^2 was examined over a range of ^{85}Kr activities from 0.015–1.0 ppt. To incorporate the impact of elevated radon activity into this study, the ^{85}Kr scenarios were examined under the nominal radon projection of 1.81 µBq/kg and 3.62 µBq/kg of xenon—twice the nominal rate. The expected number of ^{85}Kr events showing up in the signal region of interest, derived from the cut-and-out analysis explained in section 5.3.2 and given in table 5.2, is 24.5 ER events in a 1000 live day run within the 5.6 tonne fiducial volume. As the krypton is expected to be uniformly dispersed within the LXe, the study was conducted by using the LZSTATS framework and altering the normalisation of the ^{85}Kr distribution in the background model, $\mu_{^{85}Kr}$, for two ^{222}Rn scenarios. The median 90% CL sensitivity and the 3σ discovery potential of varied ^{85}Kr activities for both the nominal and twice the nominal projected radon levels are shown in figure 5.11. The irregularity observed in figure 5.11 is as a result of the lower statistics ($\sim$10k pseudo-experiments per hypothesis) used in assessing the impact of krypton.

As can be seen in figure 5.7, the ^{85}Kr distribution is very similar to that of ^{222}Rn; with both residing in the ER band of the $S1$–$S2$, hence the implication of an increased ^{85}Kr to the SI-WIMP sensitivity is expected to be similar to that of radon. The objective key performance parameter (KPP) of 0.015 ppt and the threshold KKP of 0.3 ppt of ^{85}Kr activity as defined by the LZ project is shown in dashed green and red lines in figure 5.11, respectively. For both scenarios of ^{222}Rn, the elevated levels of ^{85}Kr activity results in a gradual increase in sensitivity and discovery potential; where the LZ sensitivity requirement is still achievable under the KPP threshold of 0.3 ppt of radon. The LZ sensitivity requirement remains to be achievable even at a much larger elevation of 1.0

ppt of ^{85}Kr and twice the nominal radon projection. Although the SI-WIMP search is not drastically impacted by elevated levels of ^{85}Kr, the overall goal of the experiment is to keep ^{85}Kr concentrations well below the KPP threshold of 0.3 ppt, so to reduce the impact of ^{85}Kr on ER physics searches.

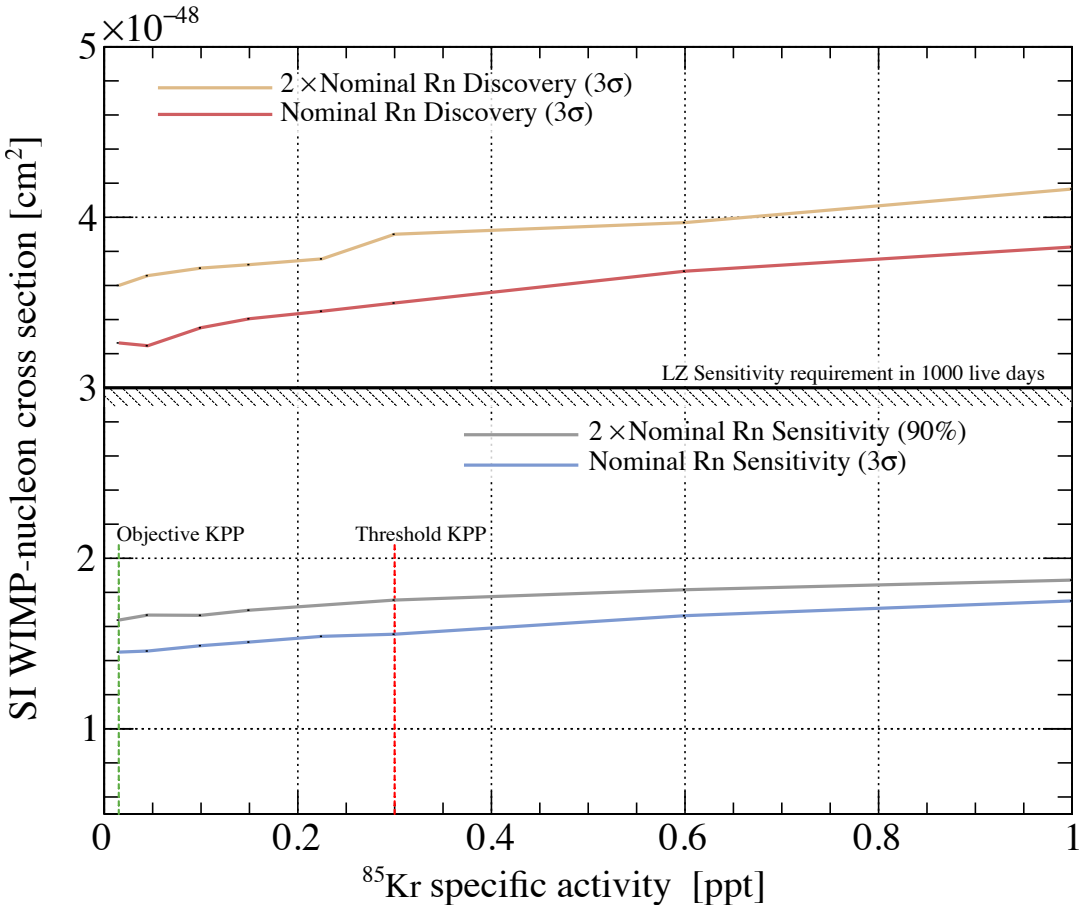

Figure 5.11: Projected SI sensitivity and discovery potential for a 1000 live-days run in 5.6 tonnes of fiducial volume as a function of ^{85}Kr as activity as observed in the fiducial volume for a WIMP mass of 40 GeV/c^2 WIMP. The median 90% CL sensitivity and 3σ discovery potentials of ^{85}Kr ranging from 0.015–1.0 ppt concentration are shown for two ^{222}Rn specific activities of 1.81 µBk/kg and 3.62 µBq/kg. The lower two curves show the variation in sensitivity, whereas the above two curves show the variation in discovery potential.

5.7 Projected WIMP Sensitivity and Discovery Potential

The projected LZ sensitivity and discovery potential to the SI WIMP-nucleon cross section at a 90% CL is shown in figures 5.12 & 5.13. The statistical studies are conducted over a wide range of WIMP masses varying from 5–2000 GeV/c^2. Each mass is taken as an independent signal model in constructing the null and the alternative hypotheses, where a set of pseudo-experiments are generated for 20 test values of the POI (μ_s), equally spaced between 0 to 30. In the limit setting scenario (above), for each mass, the test statistic distributions are used to determine the p-values of the median, 1σ and the 2σ bands at the 90% CL. In the case of discovery potential (below), the 3σ and 5σ potentials are determined, showing the region of parameter space above which the LZ experiment would have the ability to exclude the background-only hypothesis at the indicated significance.

The best sensitivity on the SI WIMP-nucleon cross section is expected for 40 GeV/c^2 WIMPs with a sensitivity of 1.43×10^{-48} cm^2, achieving a limit that is more than an order of magnitude lower than the limits set by recent LXe experiments [73, 74, 82]. As shown in figure 5.12, the projected median sensitivity, given as the solid black line, is expected to probe a significant fraction of the parameter space above the irreducible coherent neutrino scattering background, dubbed as the *neutrino floor*, indicated as the shaded orange region. At a region closer to the neutrino floor, the NR signal region of WIMPs across all masses are saturated with nuclear recoils from coherent elastic neutrino-nucleus scattering, significantly reducing the sensitivity improvements from experimental scaling. At lower WIMP masses ($\leqslant$ 10 GeV/c^2), the presence of neutrino backgrounds from ^{8}B and *hep* is already limiting the sensitivity gains made my larger scale experiments. However, although the coherent elastic neutrino-nucleus scattering is becoming significantly more constraining for WIMP searches in LXe, studying CEνNS with LXe detectors can pave the way for a better understanding of their flux and hence improve future WIMP searches with more precise modeling of these backgrounds. For LZ, the low energy event rates for background and signal modeling will ultimately depend on the low energy nuclear recoil efficiency of the experiment, which is currently capped at 1.1 keV due to the limitations of experimental data below this energy.

Furthermore, the 3σ and 5σ discovery potential for the SI WIMP-nucleon scattering is shown as a function of WIMP mass and compared with the 90% CL sensitivity in figure

5.13. In conducting these studies, the median of the alternative distribution is taken as the value of the observed test statistic and hence, these projections represent the outcome of the median experiment over repeated realisations. At 40 GeV/c^2, the median 3σ and 5σ significance is projected to occur at 3.4×10^{-48} cm^2 and 6.5×10^{-48} cm^2. Across all tested WIMP masses, the projected 3σ and 5σ significance is below the 90% CL limits from recent experiments, leaving a significant region of the parameter space open for the discovery of a SI WIMP signal with the LZ experiment.

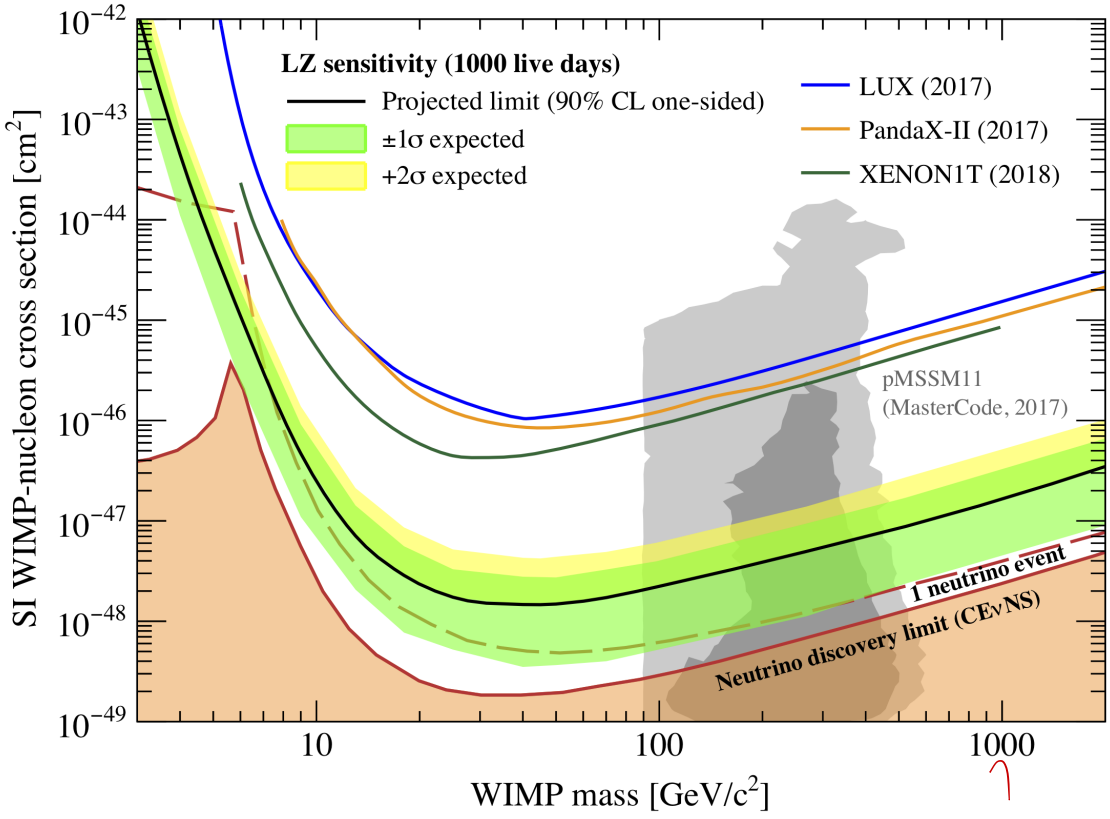

Figure 5.12: LZ projected sensitivity (above) and discovery potential (below) to the SI WIMP-nucleon elastic scattering for 1000 live days and a 5.6 tonne fiducial volume in WIMP search region of interest. The best median 90% CL sensitivity of 1.43×10^{-48} cm^2 is achieved at a WIMP mass of 40 GeV/c^2 (solid black line). The -2σ expected region is omitted based on the expectation that the limit will be power constrained [176]. Recent results achieved by other LXe experiments are also shown for comparison [73, 74, 82]. The lower shaded region and dashed line indicate the emergence of backgrounds from coherent scattering of neutrinos [83] and the gray contoured regions show the favored regions from recent pMSSM11 model scans [84].

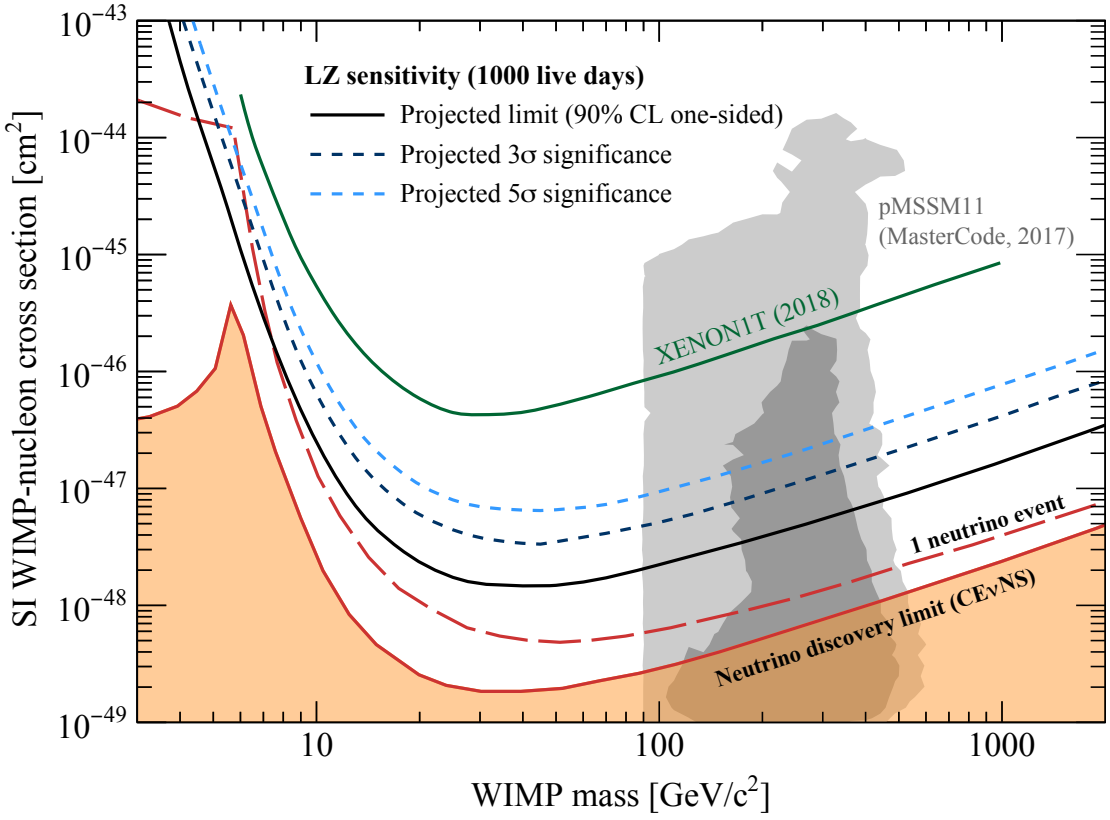

Figure 5.13: LZ projected discovery potential (below)? to the SI WIMP-nucleon elastic scattering for 1000 live days and a 5.6 tonne fiducial volume in WIMP search region of interest. The best 3(5)σ significance is achieved at $3.4(6.5) \times 10^{-48}$ cm^2 for 40 GeV/c^2 WIMPs. The current best limit XENON1T is shown for comparison [73]. Figure adapted from [105].

Chapter 6

Sensitivity Studies for G3 Dark Matter

Second generation dual-phase liquid xenon detectors due to go online, such as LZ and XENONnT, are projected to reach SI-WIMP sensitivities of $\sim 1.4 \times 10^{-48}$ cm^2 at a 90% CL [73, 105]. In comparison to their predecessors, they will probe the WIMP dark matter paradigm with orders of magnitude improvement. However, a significant amount of the parameter space prior to the cosmic neutrino background—the so called *neutrino floor*—will remain to be explored. In an effort to examine the necessary scale of a future LXe detector and the required background levels to probe down to the neutrino floor, a third-generation (G3) toy LXe detector was envisioned. This chapter outlines the rationale behind a G3 experiment and the assumptions made in constructing a potential sensitivity curve for the SI WIMP paradigm by using LZ as a model detector and the LZSTATS package to assess the statistical reach.

6.1 Motivation

The primary purpose of a third-generation (G3) dark matter experiment using dual-phase xenon technology will be focused towards designing a detector with optimal sensitivity for WIMPs. Furthermore, with the scale of a G3 experiment, there is a real possibility of transitioning from an experiment focusing mainly on WIMP dark matter, to one which operates as an observatory for a range of rare event physics searches. Some of these avenues include the search for neutrinoless double beta decay with pre-existing isotopes of ^{134}Xe and ^{136}Xe, and the study of solar and cosmic neutrinos, provided enough active LXe is present. The current generation experiments, such as LZ and XENONnT, are soon to begin data taking, with sensitivity projections for the SI WIMP-nucleon interaction around $\sim 1.4 \times 10^{-48}$ cm^2 for a 40 GeV/c^2 mass WIMP at a 90%

CL [76, 105]. Although these experiments are expected to probe a considerable magnitude of the favoured phenomenological MSSM parameter space [84], their reach is restricted by various backgrounds and the scale of the active LXe mass. However, a significant amount of the pMSSM parameter space prior to the cosmic neutrino background—which poses a hard boundary on the WIMP discovery potential—will remain to be explored. Exploring cross-sections below $\sim 10^{-49}$ cm^2 is extremely difficult given the uncertainties on the neutrino fluxes and their irreducible nature in the $S1$–$S2$ space; thus, precise measurements of different neutrino flux components are of utmost importance for a G3 experiment and beyond in reducing the impact of neutrino backgrounds on direct detection experiments [83].

what are the uncertainties ?

There are several sources of known background events expected in a potential G3 detector, similar to those expected in G2 experiments, as detailed in chapters 4 & 5. The degree in which these backgrounds impact the potentiality of a discovery varies with the search type and therefore the energy scale of the search region of interest. Despite their production mechanisms, these backgrounds are observed either as NRs or ERs for the WIMP hypothesis, and hence are more or less WIMP-like, respectively. Isotopic backgrounds originating from material and components, surface contamination and the environment are all expected to contribute to the overall background rates. Therefore, beyond the scaling of the detector, a G3 experiment will require similar or improved techniques of screening, handling and construction of the detector to reduce background rates. The rates expected from the material specific backgrounds depend on various factors: location of experiment, material selection and cleanliness, veto detector efficiency, xenon purification efforts and other variables; hence their rates can be altered and reduced through a multitude of approaches.

A major background contribution to the WIMP search ROI is from astrophysical neutrinos. The elastic neutrino-electron scattering [166] and coherent elastic neutrino-nucleus scattering (CEνNS) [167] lead directly to ER and NR events, respectively. There are several sources of neutrino backgrounds observable more prominently by a future G3 detector; atmospheric neutrinos produced in muon and pion decays, neutrinos produced in distant supernovae events, and solar neutrinos originating from various fusion reactions within the sun. The solar neutrino background for WIMP masses greater than ~ 20GeV/c^2 is dominated by *pp* neutrinos, with contributions from the ^{7}Be and CNO (Carbon-Nitrogen-Oxygen) cycles, and are expected to become the largest ER contribution at G3 scales. The ^{8}B and *hep* neutrino rates significant for NR energies $\lesssim 6$ keV—equivalent to WIMP masses below ~ 20 GeV/c^2—is expected to be observed in

$\mathcal{O}(100)$ events. The astrophysical neutrino background rates are independent of detector dependent approaches and hence are irreducible in nature and is expected to be the dominant source of background events for a future G3 experiment in both the ER and the NR bands. Although these signatures are backgrounds to the WIMP analysis, extensive studies on these signatures in theory can lead to improvements for the WIMP search and neutrino physics in general. Albeit, the primary focus of the study highlighted in this chapter is to consider the rates of these backgrounds as inputs into a potential G3 experiment in search for WIMP dark matter to determine the potential parameter space such an experiment can cover. The following sections will detail any potential improvements a G3 experiment can benefit from, the assumptions made in constructing the statistical models, and the results of such an experiment for the SI WIMP sensitivity.

6.2 Potential Improvements

A combination of cleanliness protocols and an ultra-selective screening campaign, likes of which has been demonstrated by the LZ collaboration [1], is expected to lead to substantial reductions on backgrounds from detector related radioactive isotopes. Moreover, a G3 experiment utilising an outer detector (OD) with a gadolinium load liquid scintillator (GdLS), and a LXe skin veto system with a more stringent fiducial volume that makes use of the self-shielding effect of LXe, is likely to benefit from a significant reduction in detector related backgrounds in comparison to G2 experiments. Furthermore, with more effective shielding—either by utilising a larger water tank or making use of lead-like shielding—a significant reduction on environmental backgrounds may also be expected. Improvements on dispersed xenon contaminants are more challenging in nature. The background rate from the $2\nu\beta\beta$ of ^{136}Xe is expected to be constant, unless isotopic purification of xenon is considered. Current experiments are making use of custom-made gas chromatography systems to expel the ^{85}Kr, and in theory can achieve ^{85}Kr concentrations of 0.015 ppt [110]. The krypton rate is already deemed to be highly ambitious, hence a significant improvement will be highly unlikely for a G3 experiment using tens of tonnes of LXe.

Without further development, the background from radon emanation, more specifically, the *naked-*β emission from ^{214}Pb in the ^{222}Rn sub-chain—the current most dominant background in G2 experiments—is expected to be a significant limiting factor in the science reach of a future G3 experiment. With a radon screening campaign selecting low-emanation material and a radon removal system deployed for the gas-phase of the

detector [1, 110], the LZ collaboration is projected to achieve a radon activity between 1.10–2.16 µBq/kg of xenon. Despite these efforts, the background contributions from radon are expected to make up $\sim$70% of all ER backgrounds for the WIMP search in LZ [105]. Accurate radon-induced background estimates and characterisation of their impact is challenged by poor understanding of material- and temperature-dependent radon diffusion coefficients and emanation rates. While radon diffusion is suppressed in some material at cryogenic temperatures, radon progeny recoiling out from surfaces is not. There is limited data available on the overall temperature dependence of radon outgassing from material, with even less distinguishing surface from bulk emission. Similarly, there is very limited data on potential radon barriers that could be applied to material surfaces to inhibit radon emanation. A future G3 experiment adopting more accurate radon screening methods, discussed in detail in chapter 7—aimed towards a better understanding of emanation out of varying detector material at LXe temperatures—can lower contributions through a more selective material sourcing process. In addition, the use of potential radon barriers applied on material surfaces can further reduce emanation out of surfaces. Combining these approaches with online radon removal techniques, as demonstrated in [177] by the use of cryogenic distillation and analytically-driven approaches in tagging and vetoing the *naked-*β emission from ^{214}Pb, a substantial reduction in radon-related backgrounds is possible. With a more driven campaign, G3 experiments will likely reduce the impact of radon backgrounds on the WIMP ROI, which will also positively impact any other physics searches in the ER band.

6.3 Toy G3 Detector & Background Assumptions

In an effort to examine what it takes to probe the remaining parameter space of the pMSSM model and exploiting the full discovery potential of dual-phase xenon TPC technology down to the so-called *neutrino floor*, a toy G3 detector was envisioned. To reach a cross-sectional sensitivity of $\sim 10^{-49}$ cm^2, a future detector would vaguely require a target mass 10 times that of current-generation detectors. The proposed toy detector is conceptualized to be similar to current G2 experiments for simplicity, with a diameter and an active length of 3.14 m, holding a total of 70 tonnes of LXe with the TPC. To reduce detector and wall related backgrounds, a virtual fiducial volume is assumed, cutting away 7.85 cm of active volume from the walls, below the cathode and above the gate, resulting in a fiducial volume of 60 tonnes. A TPC of this size is roughly twice as large as the current-generation detectors and offers a factor of $\sim$10 increase in active mass. In assuming a similar design to its predecessors, its likely that a significant fraction of

detector related backgrounds will originate from the top and bottom PMT arrays; which will require around 2300 3-inch-diameter PMTs to provide a similar coverage density as utilised in G2 detectors.

The detector parameters of a G3 experiment will play a big role in the expected signal and background rates as seen through the reconstructed observables *S1, S2, x-y-z, t*. These variables are fundamentally dependent on the photon detection techniques used in such detectors. A future G3 experiment will likely use a similar approach to G2 experiments in optimising for light and charge collection, through the use of PMTs or silicon photomultipliers [178] and PTFE coverings to reduce absorption. The end result of such techniques will result in a g_1, g_{1gas} and a g_2 factor as described in section 5.4.3. Although photon and charge collection efficiencies may improve as a result of technological advancements, as a conservative measure, the toy detector assumes identical parameters to that of the LZ experiment, where $g_1 = 0.119$ phd/ph, $g_{1gas} = 0.102$ phd/ph and $g_2 = 79.2$ phd/e, as detailed in table 5.1. These factors are used in converting the scaled background spectra from figures 5.4 & 5.5 to the $S1$–$S2$ representation needed to construct the background specific PDFs.

In calculating the sensitivity of a G3 detector to SI WIMPs, a total of 5 live years was assumed, equating to an exposure of 300 tonne $\cdot$ years. An 11-component background model including those detailed in sections 5.3.2 & 5.4.2 with projections of improvements for several of the sources are assumed. A simplified background table using a cut-and-count analysis, approximating the number of background counts from a region of interest relevant to a 40 GeV/c^2 WIMP, approximately 1.5–6.5 keV for ERs and 6–30 keV for NRs, is provided in table 6.1. The rates of detector related backgrounds and dispersed backgrounds from ^{222}Rn and ^{220}Rn were scaled by a factor of 0.1 in comparison to LZ. The remaining background contributors were kept at the same rate as LZ for the reasons given in section 6.2. With these assumed improvements, detector and dispersed radioisotopic backgrounds become sub-dominant to solar backgrounds for ER events. The largest impact to WIMP sensitivity above $\sim$20 GeV/c^2 is expected to come from atmospheric and solar (pp + ^{7}Be + ^{13}N) neutrino backgrounds. At energies below 6 keV the solar neutrinos from (^{8}B + hep) is dominant.

Furthermore, topologically non-standard backgrounds that are potentially dangerous for the WIMP search are considered. One of these is accidental coincidence events from PMT dark count and S2-only interactions. Dark count events can lead to fake S1-only events, and very low energy events can show up as S2-only without an S1 component; the combination of which can create an S1-S2 pair in the WIMP ROI. This background

Table 6.1: Estimated background rates from all significant contributors in a 5 live year run and a 60 tonne fiducial mass. The ER and NR counts are from a region of interest relevant to a 40 GeV/c^2 WIMP; approximately 1.5–6.5 keV for ERs and 6–30 keV for NRs; and after application of the single scatter, skin and OD veto cuts. Counts from the solar ^{8}B and hep neutrinos are given as a reference, as they are not significant above an NR energy of 6 keV. The ER discrimination of 99.9% is aimed at selecting ER events from the energy-space that is most relevant for NR interactions.

Background Sources	**ER**	**NR**
Detector (Det. + Lab. + Cosmo. + Surf.)	106	1.00
Dispersed radioisotopes (Xenon)		
^{222}Rn (0.18 µBq/kg)	1333	0
^{220}Rn (9×10^{-3} µBq/kg)	217	0
^{136}Xe ($2\nu\beta\beta$)	1311	0
^{85}Kr (0.015 ppt g/g)	528	0
Astrophysical neutrinos		
Atmospheric (Atm)	0	10.4
Diffuse supernova (DSN)	0	1.00
Solar (^{8}B + *hep*)	0	722*
Solar (*pp* + ^{7}Be + ^{13}N)	4990	0
Total	8485	12.4
Total (with 99.9% ER discrimination, 40% NR efficiency)	8.49	4.96

component can be estimated using the cold PMT dark count measurement of 25 Hz (reported in [179]) and a 1 mHz S2-only rate (twice that seen in LUX [180]). Taking into account the increased number of PMTs and live days for the proposed toy G3 experiment, the expected coincidental background when enforcing a 3-fold PMT coincidence level is expected to total 29.8 events. This is substantially more significant than that expected in LZ (less than 0.2 events). Increasing the PMT coincidence threshold to 4-fold will reduce the events to less than 0.05 events but this comes at the cost of increasing the low-energy threshold of the detector, thus reducing the sensitivity to lower mass WIMPs. A possible G3 experiment will require more stringent PMT dark count and S2-only rates to sustain a 3-fold coincidence level.

6.4 G3 SI WIMP Sensitivity

The component specific background spectra for the LZ WIMP search analysis, as shown in figures 5.4 & 5.5 was scaled and used to produce two dimensional probability density functions (PDFs) using NEST v.2.0.0 in $S1$–$S2$ space and fed into a profile likelihood ratio analysis framework used by LZ. The WIMP ROI for this analysis was defined by 0 $< \mathrm{S1}_c <$ 80 phd, with a 3-fold S1 coincidence requirement. The 3-fold cut is required to reduce background events leaking into the WIMP ROI from coincidences between PMT dark noise and S2-only events—although this background topology still contributes significantly with generation 2 rates for PMT dark noise and S2-only rates, it has been ignored for this study with an anticipation of improvements for a possible G3 experiment. In addition, the S2-raw signal is selected to be greater than 420 phd—equivalent to $\sim$5 extracted electrons. Furthermore, only single scatter events, passing the skin and the OD vetoing were selected and scaled.

The SI WIMP sensitivity of the toy G3 experiment is evaluated using the same PLR method as described in section 5.4, with an unbinned and extended likelihood, as shown in equation 5.18, providing optimal exploration between the signal and background models, based on 2-dimensional $S1$–$S2$ PDFs. A scan over the parameter of interest, μ_s—equivalent to the SI WIMP cross section—at a 90% confidence level was evaluated for WIMP masses ranging from 5 GeV/c^2 up to 20,000 GeV/c^2 by performing a frequentest hypothesis test inversion using the RooStats package [172]. The sensitivity projection uses a one-sided PLR test statistic in evaluating the upper limit.

The projected sensitivity for the toy G3 detector with the assumed background scaling and an exposure of 300 tonne $\cdot$ years to SI WIMP-nucleon scattering is shown in figure 6.1. The best sensitivity is achieved at a WIMP mass of 40 GeV/c^2 with a cross section of 1.2×10^{-49} cm^2. With this sensitivity, the remaining parameter space that G2 experiments will fail to examine above the coherent scattering of neutrinos from astrophysical sources is comfortably reached. For comparison, figure 6.1 also shows the limits achieved by some of the leading dark matter experiment, and those that are projected by current G2 experiments approaching data-taking. Neutrino iso-event contour lines derived for a background-free LXe detector with sub-keV energy threshold from [83] are also presented. The significant reduction in sensitivity observed below 20 GeV/c^2 WIMP masses is due to the dominance of the solar neutrinos NR background from ^{8}B and *hep* neutrinos.

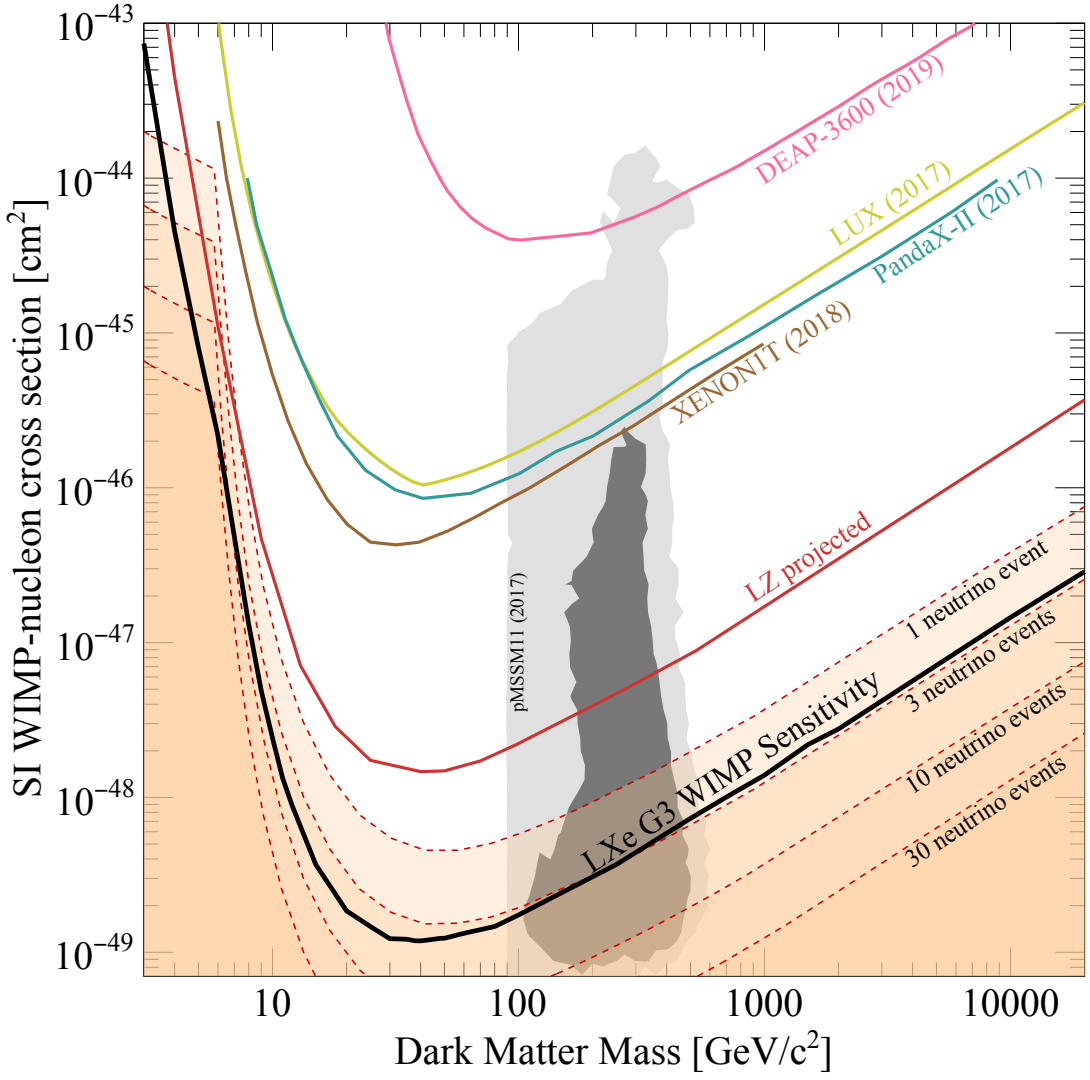

Figure 6.1: Projected sensitivity (90% CL) to SI WIMP-nucleon elastic scattering for a total exposure of 300 tonne-years. A minimum of 1.2×10^{-49} cm^2 is expected at 40 GeV/c^2. Sensitivity projections from the LZ experiment [105] and exclusion limits achieved by XENON1T [73], PandaX-II [74], LUX [181] and the DEAP-3600 [80] collaborations are also provided as a reference. Neutrino isoevent contour lines derived for a background-free LXe detector with sub-keV energy threshold is detailed in [83].

Chapter 7

G3 R&D: Cold Radon Emanation

The use of ultra-radiopure materials is detrimental to the performance of a rare-event search experiment in its capacity to identify, characterise and assign a signal confidence to such rare searches. Furthermore, any hint of a signal in dark matter, neutrinoless double beta decay, or other such rare-searches are modeled against the expected background model, which must be accurately characterised. Radon emanation has emerged to be the most important background limiting the science capability of direct detection G2 experiments such as LZ and XENONnT, despite the screening efforts to date. Future experiments, such as a planned LXe G3 dark matter experiment, will need to control radon backgrounds by a further order of magnitude to achieve a sub-dominant radon level, while opening up avenues for new rare searches. Although screening facilities for radon emanation exist, none of these are capable of assessing radon emanation at cryogenic temperatures, important to experiments such as LZ or future LXe G3, in building reliable and accurate background models. The RAL cold radon emanation facility, detailed in this chapter, is an attempt to study radon emanation from a variety of detector material, to model emanation via recoil and diffusion as a function of temperature.

7.1 Motivation

Emanation of ^{222}Rn from detector material and its subsequent decays, as detailed broadly in chapter 4, is now the leading background contributor to current generation dark matter detectors in search for WIMPs. The concentration of ^{222}Rn in past LXe experiments have been declining as a result of more extensive screening campaigns and scaling, with reported activities of 65 µBq/kg in XENON100 [182], 32 µBq/kg in LUX [183], 22 µBq/kg in PandaX-I [184], 9.8 µBq/kg in XMASS [185], and (3.65 ± 0.37) µBq/kg

Xenon IT ??

in EXO-200 [154]. The projected radon emanation activity for the LZ experiment is given as 1.81 µBq/kg. The improvement in radon activity in LZ over its predecessor, LUX, is associated with the dedicated radon screening campaign [1] and the increase in volume-to-surface ratio of LXe within the detector; despite these improvements, radon emanation is projected to be the largest background contributor in the ER band and in the WIMP ROI, limiting the reach of the experiment.

With second generation dual-phase LXe detectors approaching data taking, there is now an effort to envision the continuation of this technology to probe WIMP-nucleon cross sections to a few 10^{-49} cm, exploring the remaining parameter space down to the *neutrino floor*. However, the radon emanation rates currently achieved, although suppressed to unprecedented levels, are already limiting the science capabilities of G2 experiments. Future G3 experiments, as demonstrated with the toy detector in chapter 6, will have to reduce radon backgrounds by a further order of magnitude, where concentrations of $\sim$0.1 µBq/kg of radon must be achieved in order to probe down to cross sections of $\sim 10^{-49}$ cm [186]. Furthermore, in reducing the radon background to sub-dominant levels in comparison to neutrino backgrounds, new physics capabilities open up within the ER band of such experiments [186]. A precise measurement of the *pp*-neutrino flux will allow for testing the standard solar model (SNO), and can lead to a better understanding of neutrino production and the main energy production mechanism in the Sun [187]. *pp*-neutrino and ^{7}Be neutrinos are estimated to make up more than 98% of the total neutrino flux from the sun. Nevertheless, achieving a low radon level will be the largest background reduction challenge for a G3 experiment, where studies on radon emanation at cryogenic temperatures, novel radon diffusion suppression techniques and online radon removal from LXe will be required to better understand, model and mitigate for radon emanation.

One of the largest sources of uncertainty in modeling the radon emanation concentration within LXe detectors is the lack of data on the properties of radon emanation at operational temperatures (-97.4°C for LZ). The best and worst case estimates of radon emanation in LZ is projected at 11 mBq and 60.8 mBq in total, respectively; driven from room temperature measurements of detector material and cold suppression coefficients based on various other noble gas studies [156]. Facilities that provide high sensitivity radon emanation assays are rare and to-date only perform measurements at room temperatures. With gaseous radon turning into a liquid at -62°C and into a solid state at -70°C, there remains a large uncertainty on how this monatomic gas behaves and diffuses through material when exposed to LXe temperatures. Although the fraction of emanation due to

recoil upon the α-decay of ^{222}Rn is expected to be unaltered, diffusion of ^{222}Rn and gases within solids in general are known to depend on temperature. If the diffusion coefficient substantially changes going from room to LXe temperature, this may give enough time for ^{222}Rn to decay ($\tau_{1/2}$ = 3.82 days) within the material before mixing out into the active LXe, suppressing the background contribution of radon emanation.

The diffusivity, D, of a gas through a solid is dependent on the permeability, K, given as

$$K = Db, \tag{7.1}$$

where b represents the solubility of gas in the material, determining the concentration of gas dissolved in the material at a given partial pressure; whereas diffusivity determines the rate at which gas flows in the material. Experimentation of permeability is often achieved by constructing a thin film of material. A concentration gradient is set up on either side of the sheet; where permeability of a given gas can then be determined through the observation of the time evolution of gas permeation through the film. The dynamics of the flow are determined only by the thickness of the membrane, d, and diffusivity. For such a setup, a breakthrough time is defined as the time taken for a significant amount of gas to permeate through the film, where

$$t_b = \frac{d^2}{6D}. \tag{7.2}$$

Furthermore, permeability and breakthrough time for noble gases through materials are expected to increase with temperature, and assumed to follow the relations [156]

$$K(T) \propto exp\left(\frac{-E_K}{k_B T}\right), \tag{7.3}$$

$$t_b(T) \propto d^2 exp\left(\frac{-E_D}{k_B T}\right), \tag{7.4}$$

where E_K is the energy of permeation, and E_D is the energy of diffusion. However, it's important to note that, although such experimental setup's can further the understanding of permeability and the effect of temperature on diffusivity, radon emanation from material emerge from the constant formation of ^{222}Rn from its parent isotope of ^{226}Ra. Hence, in order to fully understand how emanation changes as a result of temperature, a preliminary understanding of the concentration of ^{226}Ra or ^{238}U and its distribution across the material is also required. Furthermore, although [156] demonstrates experimentally that permeability does indeed follow the relationships given in equations 7.4 with increasing

temperature beyond room temperature, it does not, however, demonstrate this behaviour at much colder temperatures, were liquefaction and solidification takes place.

To focus on developing a further understanding of radon emanation through detector material and its temperature dependence, a cold radon emanation facility (CREF) capable of measuring radon emanation to lower sensitivities than previous achieved by the operational setup detailed in chapter 4 was envisioned. The following sections will outline the design of the facility currently under construction and its operational procedures in becoming a leading laboratory for studying radon in line with the ambitious goals set out for a future G3 LXe observatory. This ambitious project, spanning beyond this thesis, will aim to better understand the recoil and diffusive emanation ofd radon in a temperature range between 77K to room temperature and above; study novel barrier materials and chemical treatments of surfaces to reduce backgrounds from radon emanation and radon plate-out; and eventually study radon filtration techniques, such as low-temperature vacuum swing absorption, as detailed in [188].

7.2 CREF Design

The CREF facility presently under construction is situated at the Rutherford Appleton Laboratory (RAL) within a ISO6 cleanroom. Although it is currently not operational, many parts of the system are under development in tandem. The conceptual design of CREF heavily relies on the UCL system described in chapter 4 with some divergences due to the necessity of cold emanation measurements. The schematic diagram of CREF, demonstrating the piping and the instrumentational layout, designed to maximise operational flexibility is shown in figure 7.1.

The idea behind the system design is to facilitate a high degree of flexibility in operation, with the ability to use different carrier gases, varying sizes of emanation chambers, and the ability to measure radon through a 1-step and a 2-step transfer mechanism. Chambers 1 and 2 are planned to have a volume of $\sim$2.7 L, similar to those operated by the UCL radon system. These will be used for precise radon emanation measurements from smaller samples, where room temperature and cold measurements can be performed. The internal radon emanation background from the chambers is proportional to the surface area, hence smaller surface area will allow for more precise measurements. The small emanation chambers will be cooled using an immersion cooler (Thermo Scientific EK90 LT3291901) with a temperature range of -90°C–40°C. The third chamber (*Chamber-3*) in figure 7.1 is a much larger emanation chamber, with a volume of $\sim$200 L, operating within a 500 L

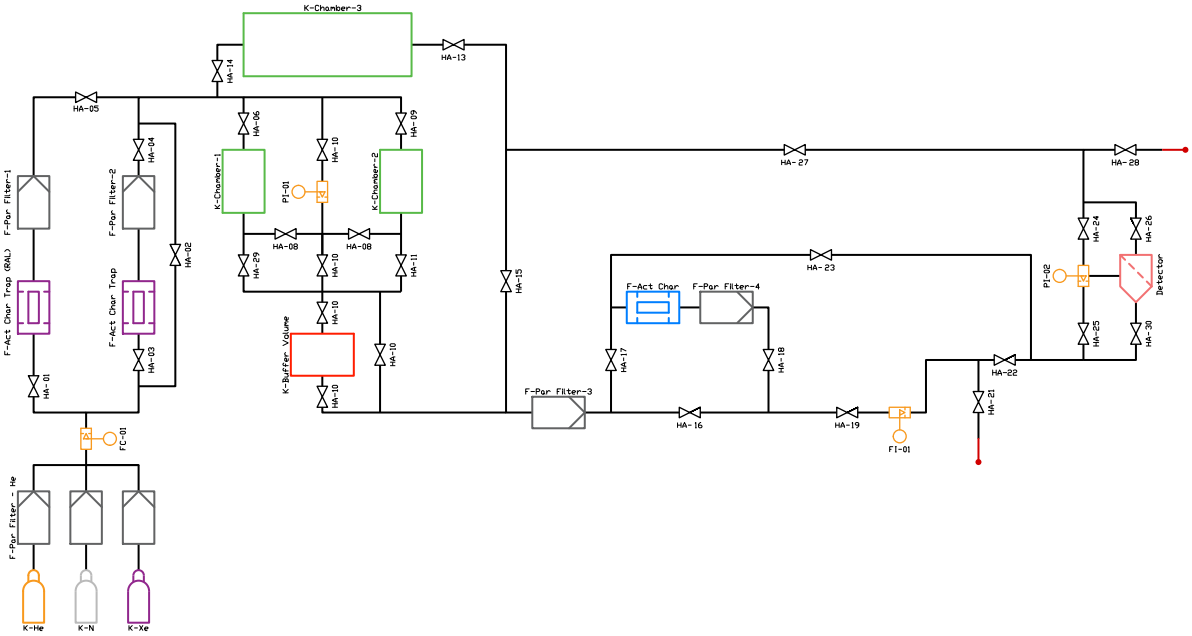

Figure 7.1: Schematic diagram of the CREF gas system flow path.

cryogenic temperature vessel, capable of cooling down to $\sim$77 K. This chamber will be used to hold much larger samples and instrumental systems of a future G3 experiment for more accurate emanation assays. Due to its much large volume, harvesting radon from a volume of this size has to be done through a 2 step transfer mechanism; due to the limitations on volume and pressure of the detection chamber. The emanated radon atoms are first flowed through a radon concentration line, where the radon in the gas is captured by an activated charcoal trapping unit (CarboAct *High-Purity Activated Charcoal*, 0.4–2.0 mm). The radon concentration unit, labeled as *Act Char*, is initially kept at LN temperatures to increase trapping efficiency, and later, heated up so to release the trapped radon, which is transferred into the detection chamber via the carier gas. A pictorial diagram of the large cryogenic chamber setup is shown on figure 7.2.

To achieve lower background levels, it is vital that the carrier gas used within such system is radon-free. As radon is constantly produced in minute quantities, naturally, the carrier gas is contaminated with radon to varying degrees. The CREF gas panel incorporates a radon removal system, constructed from cylinders of activated charcoal and kept inside an ultra-low freezer (Thermo Scientific TLE30086V) operating at -80°C. Labeled as *Char Trap*, the carrier gases will initially go through 0.5 micron particle filters to remove any particulate matter that may otherwise contaminate the gas system and then through the charcoal traps for radon removal. Such a system can be used indefinitely with little or

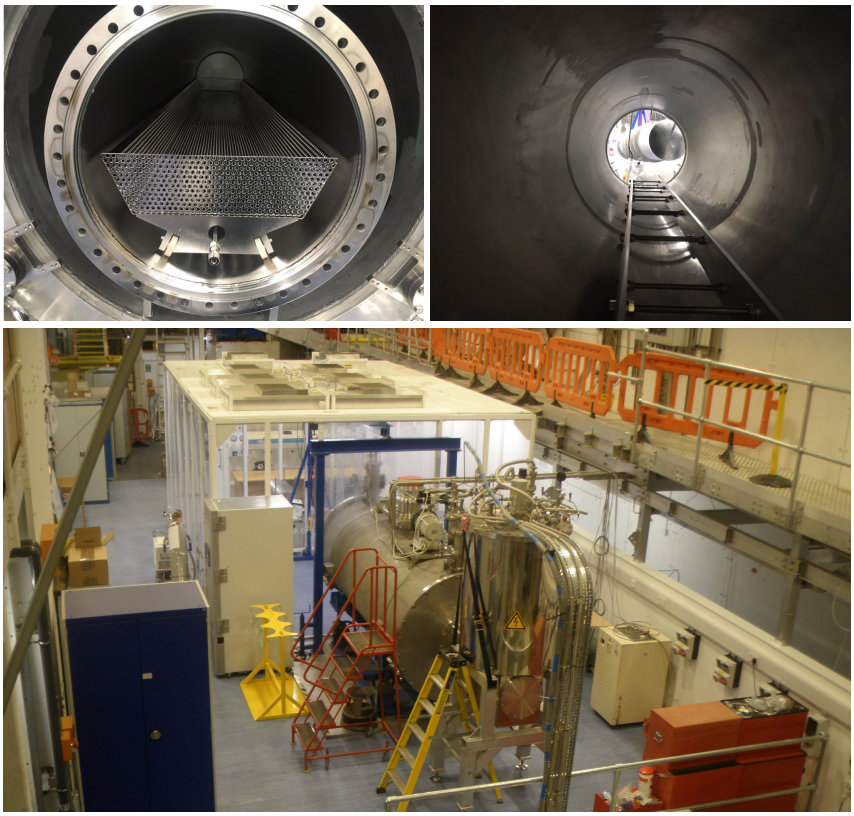

Figure 7.2: Pictorial diagram of the large cryogenic chamber used in CREF. The above two images show the inside of the cryogenic vessel, whereas the image below shows a broader angle of the cryogenic system and its connection to the CREF cleanroom.

no deterioration in performance, as the trapped ^{222}Rn atoms decay away rapidly due to relatively short half-life. Although this setup has been demonstrated to work well with helium and nitrogen, there remains uncertainty on its effectiveness with alternative gas carriers, such as argon or xenon, that require further investigation.

Furthermore, the flow rate of the carrier gas is another variable that is vital in calibrating the system and in assuring repeatability across multiple sample measurements. Often, the detector is calibrated under a set amount of the carrier gas, with the aim to operate under the same pressure for all samples. Moreover, in calibrating the detector, a ^{226}Ra calibration source with known activity is used. The source is initially sealed to allow for ^{222}Rn to build-up, which is then transferred into the detector by using the carrier gas, where the flow time, t_f, determines the activity of ^{222}Rn transferred into the detector. The precision and accuracy of the gas flow directly impacts the precision and accuracy of the detection efficiency. The precise control of the gas flow is achieved through a

multi-gas/range mass flow controller (MFC) (MKS Instruments *P9B*). The MFC is capable of < 750 ms control time and accuracy to within 1% of set point.

The end result of harvesting radon at varying temperatures from the chambers specified above will be to determine the activity of radon that has emanated into these volumes. This will be achieved through the use of an ultra-pure high-sensitivity radon detector. The detector utilised by CREF has been developed by The University of Tokyo (UoT) and operates under the same principles as detailed in section 4.3.2). The electrostatic detector constitutes an 80 L vessel with a PIN-photodiode detection unit, used to capture and detect the α-particles from the decays of ^{218}Po, ^{214}Po and various other isotopes in ^{222}Rn and ^{220}Rn sub-chains. The observed rates of ^{218}Po and ^{214}Po will then be used to reconstruct the radon emanation rate. The background radon levels of the detector is expected to be lower than that operated by UCL, due to the use of knife-edge flanges with metal gaskets to seal the detector, in comparison to the acrylic plate and Viton O-rings that were used in the 70 L radon detector. This modification has led to an improved vacuum level of the vessel, capable of achieving 10^{-4} Pa, as measured by the UoT team on an identical detector to that procured for the CREF project [189]. A pictorial diagram of the 80 L PIN-diode detector is shown in figure 7.3.

Figure 7.3: Pictorial diagram of the 80 L high-sensitivity PIN-diode radon detector.

The detector consists of an 80 L stainless steel vessel, with the inner surface of the vessel electropolished to a roughness of less than 0.8 µm to remove surface contaminants and decrease surface roughness; both of which can contribute to internal radon emanation backgrounds. The PIN-photodiode (HAMAMATSU *S3204-09*) is connected to a ceramic feedthrough, mounted on the top flange of the vessel and offset by 5 cm from the bottom of the flange. The PIN-diode with dimensions 18 mm x 18 mm, has its window removed to reduce energy loss as the α-particles decay towards the photodiode. In operational mode, the p-layer of the PIN-diode is biased at -1.9 kV, while the vessel is held at ground. In addition, the high-voltage feedthrough uses high-purity alumina (Al_2O_3) to reduce internal radon emanation background originating from the detector volume; an improvement on its predecessor detailed in chapter 4. Although an identical radon detector build by the UoT team has been characterised in detail and used by the Super-Kamiokande experiment for radon emanation measurements [189, 190], the CREF detector remains to be characterised and calibrated.

7.3 Operation & Planned Measurements

The eventual aim of the CREF project is to characterise the radon emanation properties of a range of material across a range of temperatures; from metallic substances commonly used for cryogenic vessels in low-background experiments, to a variety of materials and instrumentation of a physicochemical origin. CREF is also aiming to facilitate for radon emanation measurements from a range of sizes by using varying emanation chamber volumes. In order to fully characterise the range of radon emanation properties, a set of initial measurements to determine the detection efficiency, transfer efficiency and component specific intrinsic backgrounds, will be performed.

Detector Efficiency Calibration

The detector efficiency of the radon detector will determine the fractional success of detection of α-particles for a given isotope of interest; resulting in a correction factor to accurately construct the radon emanation rate. In modelling this, a calibration source of known activity of ^{226}Ra is used. The UCL ^{226}Ra calibration source (Pylon Electronics, *RN-1025*) of 1.32($\pm$1%) kBq activity, enables two distinct methods of calibration; *spike* and a *flow-through* calibration.

The *spike* calibration is performed by initially purging the calibration source volume to remove built-up ^{222}Rn. The volume is then sealed for a duration of time until a desired

amount of ^{226}Ra has decayed to ^{222}Rn. The concentration of ^{222}Rn is then transferred into the detector and the activities of ^{218}Po and ^{214}Po are determined. The fractional difference is then calculated for both isotopes and used as an isotope specific correction factor. The uncertainties of the calibration source activity and the uncertainties associated with the level of radon extracted from the sources has to be taken into account.

The *flow-through* method, where gas is continuously moved through the source and detector, is an alternative to the *spike* method, where the uncertainties associated with the level of radon extracted from the source are eliminated, but good knowledge of the flow rate and volume of the detector is required, which may lead to a less accurate correction factor overall.

The CREF system will mostly operate under a high-purity N_2 gas carrier, but other carrier gases may also be considered, i.e., helium or argon. As determined previously, the performance of the electrostatic detector is dependent on the medium of ion transport; hence different gases will have different correction coefficients due to differences in neutralisation affinity. The calibrations discussed above will have to be performed for all carrier gases and differences in pressure that the detector is operated under. As the detector will be operating under room temperature, there is no temperature-specific calibration requirements.

Transfer Efficiency Calibration

O.K. as a 1st step but it is really sample dependent

A second form of correction that has to be taken into account is the transfer efficiency. When using small chambers, the emanated radon is transferred into the detection chamber via the carrier gas flowed through the chamber. A near optimal transfer efficiency is achieved by flowing a gas volume of 10 times the volume of the chamber. Although at room temperature, this is expected to result in $< 99\%$ transfer efficiency, it nevertheless has to be measured. The calibration is performed by initially transferring a known amount of ^{222}Rn into the emanation chamber, followed by a direct transfer from the chamber, into the detector. The transfer will have to follow the usual transfer protocol, using a pre-defined amount of carrier gas volume and a flow rate for consistency.

For the large emanation vessel (*Chamber-3*), the entire 2-step transfer mechanism has to be evaluated. As the emanated radon is initially flowed through the activated charcoal trapping unit, the trapping efficiency has to be determined. This is done by initially flowing a known amount of ^{222}Rn from the calibration source across the *Act Char* unit. Later, the unit is heated up to release the trapped radon and transferred into the detector.

The second part of this calibration is the transfer efficiency from the large chamber to the trapping unit. This is determined by initially injecting a known amount of ^{222}Rn into the large chamber and later, flushing the volume through the trap. The transfer and trapping correction factors are then used to correct for the loss of ^{222}Rn in both processes.

The impact of colder temperature emanation within the small and large chambers on the transfer efficiency has to be taken into account. When a chamber is cooled, it is likely that some of the emanated radon will adhere to the walls of the chamber though intermolecular forces. The degree in which this takes place and its temperature dependence may initially be examined by injecting a known amount of ^{222}Rn into a cooled chamber and determining whether there is a temperature dependence on the measured activity. Although it is too early to postulate a degree of dependence, if such a dependence is measured, transfer efficiencies across pre-set cold temperatures may have to be performed to correct for the loss of ^{222}Rn trapped on the surfaces of the emanation chambers.

Background Measurements

The background expectations from both the detector and the emanation chambers have to be taken into account for an accurate background subtraction from the final measured activity. Although the intrinsic ^{222}Rn background from the small emanation chambers and the piping system is expected to be negligible, these can independently be determined by allowing these volumes to emanate for a period of time and measuring the activity of ^{222}Rn. The large detector however is expected to emanate a non-negligible amount of ^{222}Rn and hence this has to be measured and taken into account for samples emanated within this volume. The intrinsic emanation from the large chamber is expected to vary with temperature, hence, the background expectation has to be determined for each pre-set temperature of operation. Furthermore, a long background measurement on the detector has to be performed to verify the intrinsic amount of ^{222}Rn within the detector. The background from the near-identical radon detector developed for the Super-Kamiokande experiment has been measured over a 156 day period, resulting in 0.33 ± 0.07 mBq/m^3 [190]. A similar background is expected in the CREF detector.

Discussion

One of the few studies conducted on radon emanation at cryogenic temperatures by using gaseous (GAr) and liquid (LAr) argon as an emanation medium concludes with several interesting considerations that may be of importance both for the CREF project

and future dual-phase rare-event noble gas experiments [191]. They examine the radon emanation rates of 100 tungsten welding rods containing (4%) thorium (WTh); evaluating the emanation rates at room temperature under GAr (*case-1*), GAr cooled down to LAr temperatures (*case-2*) and in a LAr medium (*case-3*), emanating directly into the liquid. Although a substantial cold temperature suppression was observed between *case-1* and *case-2*, this was only substantial when the radon transfer took place while the chamber was still at LAr temperatures; when it was let to reach room temperature ($\sim$30 m), the emanation rate was comparable to *case-1*. This was a direct evidence towards emanated radon atoms sticking to the surfaces of the vessel and the rods. Furthermore, the emanation results from *case-3*, a direct emanation into LAr, resulted in a net increase in radon emanation even when compared to the room temperature result.

The conclusion of the study was that while colder temperatures may suppress radon emanation, this is highly dependent on whether the emanation out of the material in hand is due to diffusion or recoiling radon atoms. For material where recoil is the dominant form of emanation, cold temperatures will do little in suppressing radon emanation; as demonstrated with the tungsten welding rods. In such situations, LAr may increase the emanation rate due to the surface roughness of such material. If structural crevasses are dominant on such a surface, the recoiling radon atom may traverse the gap through gaseous media, re-implanting into the opposite side; where in a liquid media, the recoil range is substantially reduced, suppressing re-implantation of recoiling radon atoms, thus increasing the emanation rate, despite cooling.

The effects demonstrated in [191] are critical for the the eventual results of CREF, in both examining the temperature dependence of radon emanation, but also furthering our understanding of other processes that are taking place at these temperatures. Furthermore, it is likely that the medium of emanation, whether gaseous or liquid, can have a non-negligible impact on the measured emanation rate. Furthermore, this difference may indeed impact directly the radon background expectations of dual-phase experiments, such as LZ, where cold suppression coefficients are assumed to construct the projected radon activity. Hence, studying the differences arising from emanation media will be one of the goals of CREF.

still unclear how you suggest to study emanation directly into liquid.

Chapter 8

Conclusive Summary

After nearly a century long development of General Relativity and Quantum Theory, we have arrived at understanding the fabric of the universe through two leading approaches; looking at the universe through the lens of General Relativity—were gravitational influences of large structures are examined, and through Quantum Theory—by examining the sub-atomic microcosm of particles, primarily through the Standard Model. In the standard ΛCDM model of cosmology, the elementary particles of the SM constitute approximately 15% of the matter-density of the universe, with the remaining 85%, although gravitationally present, remains a mystery. There have been many theoretical attempts in proposing new paradigms to explain the nature of dark matter, most prominently through the introduction of new particles beyond the Standard Model. The weakly interacting massive particle (WIMP) hypothesis remains as one of the most promising candidates, where such particles are thermally produced in the early universe with the right relic abundance.

Over the past few decades, a magnitude of approaches has been formulated in searching for this elusive particle; with indirect searches looking for excess radiation in the Galactic Center, through γ-ray observations; the creation of such particles in particle colliders, and through direct detection of WIMP-nucleon scattering. The LUX-ZEPLIN (LZ) experiment at its core is a second-generation dual-phase liquid xenon detector in search for dark matter. Currently in the final stages of construction, with data taking set to begin in late 2020, LZ will utilise on 10 tonnes of LXe, with a 5.6 tonne fiducial volume to search for galactic dark matter; designed to maximize target mass and exposure, while achieving ultra-low radioactivity and active monitoring of residual backgrounds. The detector is equipped with two distinct veto systems; the outer detector scintillation system, designed to veto neutrons and γ-rays originating from radioactive impurities

in material immediately adjacent to the TPC, and the LXe skin system, instrumented with VUV sensitive PMTs to serve as a scintillation-only veto detector, highly effective for γ-rays originating from surrounding material—both of which serve to lower the backgrounds in the WIMP search region of interest. Furthermore, to go beyond the current world-leading limits on WIMP search results and in maximising the discovery potentiality of LZ, the material-makeup of the LZ experiment was held to most stringent radio-purity requirements.

Every single event within a low-background experiment is of critical importance for the search for dark matter. The LZ radioactivity and cleanliness control programs, detailed in [1], were designed to understand the origin and the implications of every known background source that may appear in the WIMP and other search regions of interest. Majority of these background sources are naturally occurring radioactive species, emitting γ-rays, electrons or α-particles. Once detector material is selected and the environment of the detector is set, such backgrounds are *fixed* in nature. Beyond the *fixed contaminants*, *surface contaminants* through dust, material residue and radiogenic plate-out, along with natural *xenon contaminants*, such as ^{85}Kr, combine to constitute all of the material and cleanliness driven backgrounds. LZ has developed and deployed extensive material screening and cleanliness techniques, working in unison, to select some of the most radio-pure material to-date. This was achieved through the use of high-purity germanium spectroscopy, inductively-coupled plasma mass spectrometry, radon emanation screening and surface cleanliness protocols. Furthermore, an experiment was deployed to determine the γ-ray background in the Davis cavern, examining the impact of environmental γ-rays for the WIMP and higher energy searches. The projected background events from *laboratory & cosmogenics* and *detector & surface contaminants* lead to a total of 54 ER and 0.52 NR events within a 1000 live day run for the WIMP selection criteria and energy region of interest.

With rapid improvements across material and cleanliness driven backgrounds, radon emanation, previously sub-dominant in dark matter searches, has emerged to be the most dominant background source in LZ. Background from radon emanation primarily arises from the ground- to ground-state β-emission from the ^{214}Pb progeny of the ^{222}Rn sub-chain, resulting in a uniform ER background within the LXe. The UCL radon emanation system was used extensively along with three other radon facilities, screening for and selecting low-radon emanating materials and components. One of the leading results from the UCL measurements was the higher-than-expected radon emanation from titanium; estimated to contribute 33.6 ± 3.6 mBq to the total warm LZ emanation rate of ~ 60 mBq.

Furthermore, although radon emanation is the most dominant background, almost all measurements are conducted on fractional material pieces and under room temperature; failing to simulate operational conditions. As a result, to construct an accurate projection, both small-scale and large-scale measurements were considered. The comparison between large-scale and bottom-up ICV measurements resulted in a remarkably good agreement, with $46.1^{+4.0}_{-3.8}$ mBq and $48.5^{+5.9}_{-6.0}$ mBq, respectively. Enumerating the outcomes of the sub-system wide measurements result in a total warm emanation rate of 60.4+4.2 mBq. The radon removal system developed for LZ and temperature suppression factors from literature was used to estimate the operational radon emanation rate to within 11.0–21.6 mBq, with the projected activity set to 18.1 mBq for the entire 10 tonnes of LXe.

The LZ detector simulation package, BACCARAT, was used with NEST, to simulate the response of backgrounds in the WIMP region of interest to examine the total number of expected backgrounds. A statistical inference framework, LZSTATS, was further developed and used to study the sensitivity and discovery potential of the experiment to WIMP dark matter for a variety of background scenarios. A cut-and-count analysis was used to estimate the background rates from significant contributors in a 1000 live day run and a 5.6 tonne fiducial mass. The ER and NR counts for a region of interest relevant to a 40 GeV/c^2 WIMP—approximately 1.5–6.5 keV for ERs and 6–30 keV for NRs, revealed that almost 70% of all ER events are as a direct result of radon emanation. An 11-component background model was constructed to evaluate the impact of increased radon emanation levels on the SI WIMP sensitivity and discovery potential. Assuming the best case and worse case scenarios of 11.0 mBq and 60.4 mBq of radon; the 90% CL sensitivity was shown to vary from a cross section 1.34×10^{-48} cm^2 to 1.76×10^{-48} cm^2; although significant, the increase is substantially slow over the range of possible radon scenarios, with the median 90% CL limit staying well below the LZ requirement of 3.0×10^{-48} cm^2. Furthermore, the projected 90% CL sensitivity cross section of a SI WIMP-nucleon, assuming a projected radon activity of 18.1 mBq, was determined to be 1.43×10^{-48} cm^2 for a WIMP mass of 40 GeV/c^2. Moreover, the median 3σ discovery significance was determined to occur at 3.4×10^{-48} cm^2.

Despite the best efforts, G2 dual-phase LXe detectors, soon to go online, are projected to reach SI-WIMP-nucleon sensitivities of $\sim 1.4 \times 10^{-48}$ cm^2 at a 90% CL, leaving a significant amount of the parameter space prior to the cosmic neutrino floor unexplored. To examine the necessary background rates and to explore the potentiality of probing down to the neutrino floor, a G3 toy experiment was envisioned. A 70 tonne LXe detector, similar to LZ, with an active fiducial volume of 60 tonnes was used; assuming the same

spectral background expectation to that of the LZ detector for the WIMP region of interest. With improvements on screening and cleanliness techniques and a much better understanding of radon emanation at operational conditions; a 1/10 reduction factor was assumed on all detector related backgrounds (including **Det.** + **Lab.** + **Cosmo.** + **Surf.**) and radon emanation rates. A PLR analysis was constructed, and the SI WIMP cross section at a 90% confidence level was evaluated for WIMP masses ranging from 5 GeV/c^2 up to 20,000 GeV/c^2. The best projected sensitivity achieved for the toy G3 detector with the assumed background scaling and an exposure of 300 tonne $\times$ years was 1.2×10^{-49} cm^2 for a WIMP mass of 40 GeV/c^2. With this sensitivity, the remaining parameter space that G2 experiments will fail to examine above the coherent scattering of neutrinos from astrophysical sources is comfortably reached.

The advancement in dual-phase LXe technologies in detecting ultra-rare events made possible the search the the most elusive particle known to mankind. With further improvements, it is possible for this technology to transition into a rare event search observatory; looking for dark matter particles at much lower energies, while also becoming competitive in $0\nu\beta\beta$ and the astrophysical neutrino landscape. Although the NR background rates are below one event for the entirety of a planned science run, the ER rates, which impact both the WIMP search and any ER-related physic search, still remain relatively high. The biggest contribution is coming from the material-induced radon emanation. To better understand this background, measure the temperature dependence of radon emanation across different detector materials, and develop techniques to reduce radon diffusion, a cryogenic radon emanation facility has been envisioned and under construction. The CREF facility will be used to model this background more accurately and precisely to achieve the ambitions set for a G3 observatory. A future detector with sub-dominant radon emanation will be able to probe new dark matter models in the ER band of the spectrum, while also expanding the scientific outreach of this technology beyond dark matter.

Bibliography

[1] D. S. Akerib *et al.*, *The LUX-ZEPLIN (LZ) radioactivity and cleanliness control programs*, 2020, 2006.02506.

[2] D. Akerib *et al.*, *Measurement of the gamma ray background in the Davis cavern at the Sanford Underground Research Facility*, Astroparticle Physics **116** (2020).

[3] F. Zwicky, *Die Rotverschiebung von extragalaktischen Nebeln*, Helvetica Physica Acta **6**, 110:127 (1933).

[4] V. M. Slipher, *The radial velocity of the Andromeda Nebula*, Lowell Observatory Bulletin **1**, pp.56 (1913).

[5] A. Friedman, *Über die Krümmung des Raumes*, Zeitschrift für Physik **10** (1922).

[6] E. Hubble, Proceedings of the National Astronomical Society , 15:168 (1929).

[7] Planck, N. Aghanim *et al.*, *Planck 2018 results. VI. Cosmological parameters*, Astron. Astrophys. **641**, A6 (2020), 1807.06209.

[8] J. B. Hartle, *Gravity: An Introduction To Einstein's General Relativity*, Pearson (2003).

[9] S. M. Carroll, *The Cosmological Constant*, Living Rev. Rel. **4** (2001).

[10] S. Dodelson, *Modern Cosmology*, Elsevier (2003).

[11] Particle Data Group, M. Tanabashi *et al.*, *Review of Particle Physics*, Phys. Rev. D **98**, 030001 (2018).

[12] A. A. Penzias and R. W. Wilson, *A Measurement of excess antenna temperature at 4080-Mc/s*, Astrophys. J. **142**, 419 (1965).

[13] J. C. Mather, D. Fixsen, R. Shafer, C. Mosier, and D. Wilkinson, *Calibrator design for the COBE far infrared absolute spectrophotometer (FIRAS)*, Astrophys. J. **512**,

511 (1999), astro-ph/9810373.

[14] Planck, Y. Akrami *et al.*, *Planck 2018 results. IV. Diffuse component separation*, (2018), 1807.06208.

[15] Planck, Y. Akrami *et al.*, *Planck 2018 results. I. Overview and the cosmological legacy of Planck*, Astron. Astrophys. **641**, A1 (2020), 1807.06205.

[16] A. Coc and E. Vangioni, *Primordial nucleosynthesis*, Int. J. Mod. Phys. E **26**, 1741002 (2017), 1707.01004.

[17] R. H. Cyburt, B. D. Fields, K. A. Olive, and T.-H. Yeh, *Big bang nucleosynthesis: Present status*, Rev. Mod. Phys. **88**, 015004 (2016).

[18] B. E. Wood *et al.*, *Two New Low Galactic D/H Measurements from the Far Ultraviolet Spectroscopic Explorer*, The Astrophysical Journal **609**, 838–853 (2004).

[19] B. D. Fields, *The primordial lithium problem*, Ann. Rev. Nucl. Part. Sci. **61**, 47 (2011), 1203.3551.

[20] V. C. Rubin and J. Ford, W.Kent, *Rotation of the Andromeda Nebula from a Spectroscopic Survey of Emission Regions*, Astrophys. J. **159**, 379 (1970).

[21] V. Rubin, N. Thonnard, and J. Ford, W.K., *Rotational properties of 21 SC galaxies with a large range of luminosities and radii, from NGC 4605 /R = 4kpc/ to UGC 2885 /R = 122 kpc/*, Astrophys. J. **238**, 471 (1980).

[22] C. Carignan, L. Chemin, W. K. Huchtmeier, and F. J. Lockman, *Extended hi rotation curve and mass distribution of m31*, Astrophys. J. Lett. **641**, L109 (2006), astro-ph/0603143.

[23] P. Mróz *et al.*, *Rotation Curve of the Milky Way from Classical Cepheids*, The Astrophysical Journal **870**, L10 (2019).

[24] M. Milgrom, *MOND theory*, Can. J. Phys. **93**, 107 (2015), 1404.7661.

[25] J. Moffat, *Scalar-tensor-vector gravity theory*, JCAP **03**, 004 (2006), gr-qc/0506021.

[26] P. Coles and F. Lucchin, *Cosmology: The Origin and evolution of cosmic structure*, Wiley (1995).

[27] R. D. Peccei and H. R. Quinn, CP *Conservation in the Presence of Pseudoparticles*, Phys. Rev. Lett. **38**, 1440 (1977).

[28] T. Schäfer and E. V. Shuryak, *Instantons in QCD*, Rev. Mod. Phys. **70**, 323 (1998), hep-ph/9610451.

[29] J. Callan, Curtis G., R. Dashen, and D. J. Gross, *The Structure of the Gauge Theory Vacuum*, Phys. Lett. B **63**, 334 (1976).

[30] G. 't Hooft, *Symmetry Breaking Through Bell-Jackiw Anomalies*, Phys. Rev. Lett. **37**, 8 (1976).

[31] C. Baker *et al.*, *An Improved experimental limit on the electric dipole moment of the neutron*, Phys. Rev. Lett. **97**, 131801 (2006), hep-ex/0602020.

[32] P. Sikivie, *Experimental Tests of the Invisible Axion*, Phys. Rev. Lett. **51**, 1415 (1983), [Erratum: Phys.Rev.Lett. 52, 695 (1984)].

[33] S. J. Asztalos *et al.*, *SQUID-Based Microwave Cavity Search for Dark-Matter Axions*, Phys. Rev. Lett. **104**, 041301 (2010).

[34] A. Strumia and F. Vissani, *Neutrino masses and mixings and...*, (2006), hep-ph/0606054.

[35] G. Jungman, M. Kamionkowski, and K. Griest, *Supersymmetric dark matter*, Physics Reports **267**, 195–373 (1996).

[36] J. Lesgourgues and S. Pastor, *Neutrino mass from Cosmology*, Adv. High Energy Phys. **2012**, 608515 (2012), 1212.6154.

[37] KATRIN, S. Mertens, *Status of the KATRIN Experiment and Prospects to Search for keV-mass Sterile Neutrinos in Tritium β-decay*, Phys. Procedia **61**, 267 (2015).

[38] M. Aker *et al.*, *Improved Upper Limit on the Neutrino Mass from a Direct Kinematic Method by KATRIN*, Physical Review Letters **123** (2019).

[39] S. F. King, *Neutrino mass models*, Reports on Progress in Physics **67**, 107–157 (2003).

[40] S. Gariazzo, C. Giunti, M. Laveder, Y. F. Li, and E. M. Zavanin, *Light sterile neutrinos*, Journal of Physics G: Nuclear and Particle Physics **43**, 033001 (2015).

[41] A. Aguilar-Arevalo *et al.*, *Significant Excess of Electronlike Events in the MiniBooNE Short-Baseline Neutrino Experiment*, Physical Review Letters **121** (2018).

[42] S. Dodelson and L. M. Widrow, *Sterile neutrinos as dark matter*, Physical Review

Letters **72**, 17–20 (1994).

[43] G. Bertone, D. Hooper, and J. Silk, *Particle dark matter: evidence, candidates and constraints*, Physics Reports **405**, 279–390 (2005).

[44] J. Silk *et al.*, *Particle Dark Matter: Observations, Models and Searches* (Cambridge Univ. Press, Cambridge, 2010).

[45] J. L. Feng, *Dark Matter Candidates from Particle Physics and Methods of Detection*, Annual Review of Astronomy and Astrophysics **48**, 495–545 (2010).

[46] P. Athron *et al.*, *Combined collider constraints on neutralinos and charginos*, The European Physical Journal C **79** (2019).

[47] M. J. Reid, *The Distance to the Center of the Galaxy*, Annual Review of Astronomy and Astrophysics **31**, 345 (1993), https://doi.org/10.1146/annurev.aa.31.090193.002021.

[48] J. I. Read, *The local dark matter density*, Journal of Physics G: Nuclear and Particle Physics **41**, 063101 (2014).

[49] A. G. A. Brown *et al.*, *GaiaData Release 2*, Astronomy Astrophysics **616**, A1 (2018).

[50] S. Sivertsson, H. Silverwood, J. I. Read, G. Bertone, and P. Steger, *The local-dark matter density from SDSS-SEGUE G-dwarfs*, Monthly Notices of the Royal Astronomical Society **478**, 1677–1693 (2018).

[51] J. Bovy *et al.*, *The milky way's circular-velocity curve between 4 and 14 kpc from apogee data*, The Astrophysical Journal **759**, 131 (2012).

[52] F. J. Kerr and D. Lynden-Bell, *Review of galactic constants.*, **221**, 1023 (1986).

[53] M. C. Smith *et al.*, *The RAVE survey: constraining the local Galactic escape speed*, Monthly Notices of the Royal Astronomical Society **379**, 755–772 (2007).

[54] W. Dehnen and J. J. Binney, *Local stellar kinematics from Hipparcos data*, Monthly Notices of the Royal Astronomical Society **298**, 387–394 (1998).

[55] M. W. Goodman and E. Witten, *Detectability of certain dark-matter candidates*, Phys. Rev. D **31**, 3059 (1985).

[56] J. Engel, *Nuclear form-factors for the scattering of weakly interacting massive*

particles, Phys. Lett. B **264**, 114 (1991).

[57] L. Baudis, *Direct dark matter detection: The next decade*, Physics of the Dark Universe **1**, 94–108 (2012).

[58] DAMA, R. Bernabei *et al.*, *First results from DAMA/LIBRA and the combined results with DAMA/NaI*, Eur. Phys. J. **C56**, 333 (2008), 0804.2741.

[59] DAMA, LIBRA, R. Bernabei *et al.*, *New results from DAMA/LIBRA*, Eur. Phys. J. **C67**, 39 (2010), 1002.1028.

[60] COSINE-100, G. Adhikari *et al.*, *Search for a Dark Matter-Induced Annual Modulation Signal in NaI(Tl) with the COSINE-100 Experiment*, Phys. Rev. Lett. **123**, 031302 (2019), 1903.10098.

[61] P. Montini, *Dark matter search with the SABRE experiment*, 2018, 1807.08073.

[62] EDELWEISS, E. Armengaud *et al.*, *Performance of the EDELWEISS-III experiment for direct dark matter searches*, JINST **12**, P08010 (2017), 1706.01070.

[63] N. Mirabolfathi *et al.*, *The Cryogenic Dark Matter Search (CDMS) experiment: Results, status and perspective*, AIP Conf. Proc. **1185**, 623 (2009).

[64] CRESST, J. Schieck, *Direct Dark Matter Search with the CRESST-II Experiment*, p. 445 (2015), 1505.03289.

[65] CRESST, A. H. Abdelhameed *et al.*, *First results from the CRESST-III low-mass dark matter program*, Phys. Rev. **D100**, 102002 (2019), 1904.00498.

[66] G. Alner *et al.*, *First limits on nuclear recoil events from the ZEPLIN I galactic dark matter detector*, Astroparticle Physics **23**, 444 (2005).

[67] XMASS, J. Liu, *The XMASS experiment*, AIP Conf. Proc. **1604**, 397 (2015).

[68] P.-A. Amaudruz *et al.*, *Measurement of the scintillation time spectra and pulse-shape discrimination of low-energy and nuclear recoils in liquid argon with DEAP-1*, Astroparticle Physics **85**, 1–23 (2016).

[69] G. Alner *et al.*, *Status of the ZEPLIN II experiment*, New Astronomy Reviews **49**, 259 (2005), Sources and Detection of Dark Matter and Dark Energy in the Universe.

[70] V. N. Lebedenko *et al.*, *Results from the first science run of the ZEPLIN-III dark*

matter search experiment, Physical Review D **80** (2009).

[71] XENON, E. Aprile *et al.*, *Search for WIMP Inelastic Scattering off Xenon Nuclei with XENON100*, Phys. Rev. **D96**, 022008 (2017), 1705.05830.

[72] H. Zhang *et al.*, *Dark matter direct search sensitivity of the PandaX-4T experiment*, Science China Physics, Mechanics Astronomy **62** (2018).

[73] E. Aprile *et al.*, *Dark Matter Search Results from a One Ton-Year Exposure of XENON1T*, Physical Review Letters **121** (2018).

[74] X. Cui *et al.*, *Dark Matter Results from 54-Ton-Day Exposure of PandaX-II Experiment*, Physical Review Letters **119** (2017).

[75] D. S. Akerib *et al.*, *Extending light WIMP searches to single scintillation photons in LUX*, 2019, 1907.06272.

[76] XENON, E. Aprile *et al.*, *Projected WIMP Sensitivity of the XENONnT Dark Matter Experiment*, (2020), 2007.08796.

[77] SuperCDMS Collaboration, R. Agnese *et al.*, *New Results from the Search for Low-Mass Weakly Interacting Massive Particles with the CDMS Low Ionization Threshold Experiment*, Phys. Rev. Lett. **116**, 071301 (2016).

[78] SuperCDMS Collaboration, R. Agnese *et al.*, *Results from the Super Cryogenic Dark Matter Search Experiment at Soudan*, Phys. Rev. Lett. **120**, 061802 (2018).

[79] DarkSide Collaboration, P. Agnes *et al.*, *Low-Mass Dark Matter Search with the DarkSide-50 Experiment*, Phys. Rev. Lett. **121**, 081307 (2018).

[80] R. Ajaj *et al.*, *Search for dark matter with a 231-day exposure of liquid argon using DEAP-3600 at SNOLAB*, Physical Review D **100** (2019).

[81] DarkSide, P. Agnes *et al.*, *DarkSide-50 532-day Dark Matter Search with Low-Radioactivity Argon*, Phys. Rev. **D98**, 102006 (2018), 1802.07198.

[82] LUX, D. S. Akerib *et al.*, *Results from a search for dark matter in the complete LUX exposure*, Phys. Rev. Lett. **118**, 021303 (2017), 1608.07648.

[83] F. Ruppin, J. Billard, E. Figueroa-Feliciano, and L. Strigari, *Complementarity of dark matter detectors in light of the neutrino background*, Physical Review D **90** (2014).

[84] E. Bagnaschi *et al.*, *Likelihood analysis of the pMSSM11 in light of LHC 13-TeV data*, The European Physical Journal C **78** (2018).

[85] P. Benetti *et al.*, *Detection of energy deposition down to the keV region using liquid xenon scintillation*, Nuclear Instruments and Methods in Physics Research Section A: Accelerators, Spectrometers, Detectors and Associated Equipment **327**, 203 (1993).

[86] E. Aprile and T. Doke, *Liquid xenon detectors for particle physics and astrophysics*, Rev. Mod. Phys. **82**, 2053 (2010).

[87] V. Chepel and H. Araujo, *Liquid noble gas detectors for low energy particle physics*, JINST **8**, R04001 (2013), 1207.2292.

[88] E. Aprile, A. Bolotnikov, D. Chen, and R. Mukherjee, *W value in liquid krypton*, Phys. Rev. A **48**, 1313 (1993).

[89] C. E. Dahl, *The physics of background discrimination in liquid xenon, and first results from Xenon10 in the hunt for WIMP dark matter*, PhD thesis, Princeton U., 2009.

[90] K. Fujii *et al.*, *High-accuracy measurement of the emission spectrum of liquid xenon in the vacuum ultraviolet region*, Nuclear Instruments and Methods in Physics Research Section A: Accelerators, Spectrometers, Detectors and Associated Equipment **795**, 293 (2015).

[91] A. Hitachi *et al.*, *Effect of ionization density on the time dependence of luminescence from liquid argon and xenon*, Phys. Rev. B **27**, 5279 (1983).

[92] L. S. Miller, S. Howe, and W. E. Spear, *Charge Transport in Solid and Liquid Ar, Kr, and Xe*, Phys. Rev. **166**, 871 (1968).

[93] J. Lindhard, M. Scharff, and H. Schioett, *RANGE CONCEPTS AND HEAVY ION RANGES (NOTES ON ATOMIC COLLISIONS, II)*, Kgl. Danske Videnskab. Selskab. Mat. Fys. Medd. .

[94] J. Lindhard and M. Scharff, *Energy Dissipation by Ions in the kev Region*, Phys. Rev. **124**, 128 (1961).

[95] M. Szydagis *et al.*, *NEST: a comprehensive model for scintillation yield in liquid xenon*, Journal of Instrumentation **6**, P10002–P10002 (2011).

[96] J. Mock *et al.*, *Modeling pulse characteristics in Xenon with NEST*, Journal of Instrumentation **9**, T04002–T04002 (2014).

[97] GEANT4, S. Agostinelli *et al.*, *GEANT4: A Simulation toolkit*, Nucl. Instrum. Meth. **A506**, 250 (2003).

[98] J. Brodsky *et al.*, *Noble Element Simulation Technique (Code)*, https://github.com/NESTCollaboration/nest.

[99] D. Akerib *et al.*, *Tritium calibration of the LUX dark matter experiment*, Physical Review D **93** (2016).

[100] LUX, D. S. Akerib *et al.*, *Ultralow energy calibration of LUX detector using* ^{127}Xe *electron capture*, Phys. Rev. **D96**, 112011 (2017), 1709.00800.

[101] E. M. Boulton *et al.*, *Calibration of a two-phase xenon time projection chamber with a* ^{37}Ar *source*, JINST **12**, P08004 (2017), 1705.08958.

[102] I. O. Samblas, *A statistical framework for the characterisation of WIMP dark matter with the LUX-ZEPLIN experiment*, PhD thesis, Imperial College London, 2019.

[103] D. Akerib *et al.*, *Signal yields, energy resolution, and recombination fluctuations in liquid xenon*, Physical Review D **95** (2017).

[104] D. Akerib *et al.*, *The Large Underground Xenon (LUX) experiment*, Nuclear Instruments and Methods in Physics Research Section A: Accelerators, Spectrometers, Detectors and Associated Equipment **704**, 111–126 (2013).

[105] LUX-ZEPLIN, D. Akerib *et al.*, *Projected WIMP sensitivity of the LUX-ZEPLIN dark matter experiment*, Phys. Rev. D **101**, 052002 (2020), 1802.06039.

[106] LZ, D. Akerib *et al.*, *The LUX-ZEPLIN (LZ) Experiment*, Nucl. Instrum. Meth. A **953**, 163047 (2020), 1910.09124.

[107] F. Neves *et al.*, *Measurement of the absolute reflectance of polytetrafluoroethylene (PTFE) immersed in liquid xenon*, Journal of Instrumentation **12**, P01017–P01017 (2017).

[108] D. Akerib *et al.*, *Identification of radiopure titanium for the LZ dark matter experiment and future rare event searches*, Astroparticle Physics **96**, 1–10 (2017).

[109] M. Yeh, A. Garnov, and R. Hahn, *Gadolinium-loaded liquid scintillator for high-*

precision measurements of antineutrino oscillations and the mixing angle, 13, Nuclear Instruments and Methods in Physics Research Section A: Accelerators, Spectrometers, Detectors and Associated Equipment **578**, 329 (2007).

[110] B. J. Mount *et al.*, *LUX-ZEPLIN (LZ) Technical Design Report*, (2017), 1703.09144.

[111] LUX, D. S. Akerib *et al.*, *Low-energy (0.7-74 keV) nuclear recoil calibration of the LUX dark matter experiment using D-D neutron scattering kinematics*, (2016), 1608.05381.

[112] M. Bruemmer, M. Nakib, R. Calkins, J. Cooley, and S. Sekula, *Studies on the reduction of radon plate-out*, (2015).

[113] M. Stein *et al.*, *Radon daughter plate-out measurements at SNOLAB for polyethylene and copper*, Nuclear Instruments and Methods in Physics Research Section A: Accelerators, Spectrometers, Detectors and Associated Equipment **880**, 92–97 (2018).

[114] D. S. Akerib *et al.*, *Radiogenic and Muon-Induced Backgrounds in the LUX Dark Matter Detector*, Astropart. Phys. **62**, 33 (2015), 1403.1299.

[115] F. E. Gray *et al.*, *Cosmic Ray Muon Flux at the Sanford Underground Laboratory at Homestake*, Nucl. Instrum. Meth. **A638**, 63 (2011), 1007.1921.

[116] D. Mei and A. Hime, *Muon-induced background study for underground laboratories*, Phys. Rev. **D73**, 053004 (2006), astro-ph/0512125.

[117] V. Tomasello, M. Robinson, and V. Kudryavtsev, *Radioactive background in a cryogenic dark matter experiment*, Astroparticle Physics **34**, 70 (2010).

[118] P. R. Scovell *et al.*, *Low Background Gamma Spectroscopy at the Boulby Underground Laboratory*, Astropart. Phys. **97**, 160 (2018), 1708.06086.

[119] J. Dobson, C. Ghag, and L. Manenti, *Ultra-low background mass spectrometry for rare-event searches*, Nucl. Instrum. Meth. **A879**, 25 (2018), 1708.08860.

[120] G. Gilmore, *Practical Gamma-ray Spectroscopy* (Wiley, 2011).

[121] R. Noel *et al.*, *Measuring and understanding radon adsorption in microporous materials*, AIP Conf. Proc. **1672**, 070001 (2015).

[122] B. J. Mount *et al.*, *Black Hills State University Underground Campus*, Appl. Radiat. Isot. **126**, 130 (2017).

[123] A. R. Smith *et al.*, *Low Background Counting at LBNL*, Phys. Procedia **61**, 787 (2015).

[124] R. H. M. Tsang *et al.*, *GEANT4 models of HPGe detectors for radioassay*, Nucl. Instrum. Meth. **A935**, 75 (2019), 1902.06847.

[125] D. C. Malling *et al.*, *Dark Matter Search Backgrounds from Primordial Radionuclide Chain Disequilibrium*, (2013), 1305.5183.

[126] Y. Meng *et al.*, *A New Method for Evaluating the Effectiveness of Plastic Packaging Against Radon Penetration*, (2019), 1903.02643.

[127] C. T. Rueden *et al.*, *ImageJ2: ImageJ for the next generation of scientific image data*, CoRR **abs/1701.05940** (2017), 1701.05940.

[128] W. Jacobi, *Activity and Potential Alpha-energy of 222 Radon and 220 Radon-daughters in Different Air Atmospheres*, Health Physics **22**, 441 (1972).

[129] E. O. Knutson, *Modeling indoor concentrations of radon decay products*, Radon and its decay products in indoor air , 161 (1988).

[130] H. Zou *et al.*, *Quantifying the triboelectric series*, Nature Communications **10**, 1427 (2019).

[131] E. S. Morrison *et al.*, *Radon Daughter Plate-out onto Teflon*, AIP Conf. Proc. **1921**, 090002 (2018), 1708.08534.

[132] Molnar Gabor., Belgya Tamas., Revay Zsolt., and International Symposium on Capture Gamma-Ray Spectroscopy and Related Topics (9.) (Budapest) (1996), *Proceedings of the 9. International Symposium on Capture Gamma-Ray Spectroscopy and Related Topics : Budapest, 8-12 October 1996* (Springer, 1997).

[133] J. Heise, *The Sanford Underground Research Facility at Homestake*, Journal of Physics: Conference Series **606**, 012015 (2015).

[134] Daya Bay, F. P. An *et al.*, *Measurement of electron antineutrino oscillation based on 1230 days of operation of the Daya Bay experiment*, Phys. Rev. **D95**, 072006 (2017), 1610.04802.

[135] K. Kim *et al.*, *Tests on NaI(Tl) crystals for WIMP search at the Yangyang Underground Laboratory*, Astropart. Phys. **62**, 249 (2015), 1407.1586.

[136] D. E. Cullen, J. H. Hubbell, and L. Kissel, *EPDL97: the evaluated photo data*

library '97 version.

[137] S. T. Perkins, D. E. Cullen, and S. M. Seltzer, *Tables and graphs of electron-interaction cross sections from 10 eV to 100 GeV derived from the LLNL Evaluated Electron Data Library (EEDL), Z = 1–100.*

[138] D.-M. Mei, C. Zhang, K. Thomas, and F. Gray, *Early results on radioactive background characterization for Sanford Laboratory and DUSEL experiments*, Astroparticle Physics **34**, 33–39 (2010).

[139] D. S. Akerib *et al.*, *Projected sensitivity of the LUX-ZEPLIN experiment to the* $0\nu\beta\beta$ *decay of* ^{136}Xe., Physical Review C **102** (2020).

[140] J. R. Partington, *Discovery of Radon*, Nature **179**, 912 (1957).

[141] P. Scovell, *An Update from the Boulby Underground Laboratory.*

[142] A. Sakoda and Y. Ishimori, *Mechanisms and Modeling Approaches of Radon Emanation for Natural Materials*, Japanese Journal of Health Physics **52**, 296 (2017).

[143] H. M. Araújo *et al.*, *Radioactivity Backgrounds in ZEPLIN-III*, Astropart. Phys. **35**, 495 (2012), 1104.3538.

[144] J. Mott, *Search for double beta decay of* ^{82}Se *with the NEMO-3 detector and development of apparatus for low-level radon measurements for the SuperNEMO experiment*, PhD thesis, University College London, 2013.

[145] X. R. Liu, *Low background techniques for the SuperNEMO experiment*, PhD thesis, University College London, 2017.

[146] E. Choi *et al.*, *Highly sensitive radon monitor and radon emanation rates for detector components*, Nuclear Instruments and Methods in Physics Research Section A: Accelerators, Spectrometers, Detectors and Associated Equipment **459**, 177 (2001).

[147] C. Mitsuda *et al.*, *Development of super-high sensitivity radon detector for the Super-Kamiokande detector*, Nuclear Instruments and Methods in Physics Research Section A: Accelerators, Spectrometers, Detectors and Associated Equipment **497**, 414 (2003).

[148] P. Pagelkopf and J. Porstendörfer, *Neutralisation rate and the fraction of the*

positive ^{218}*Po-clusters in air*, Atmospheric Environment **37**, 1057 (2003).

[149] K. Pushkin *et al.*, *Study of radon reduction in gases for rare event search experiments*, Nucl. Instrum. Meth. **A903**, 267 (2018), 1805.11306.

[150] N. M. Rupp, *On the detection of* ^{222}*Rn with miniaturized proportional counters: background, sensitivity studies and results for XENON1T*, PhD thesis, University of Heidelberg, 2015.

[151] G. Zuzel, *Highly Sensitive Measurements of 222Rn Diffusion and Emanation*, AIP Conference Proceedings **785** (2005).

[152] G. Zuzel and H. Simgen, *High sensitivity radon emanation measurements*, Applied Radiation and Isotopes **67**, 889 (2009), 5th International Conference on Radionuclide Metrology - Low-Level Radioactivity Measurement Techniques ICRM-LLRMT'08.

[153] XENON, E. Aprile *et al.*, ^{222}*Rn emanation measurements for the XENON1T experiment*, (2020), 2009.13981.

[154] J. B. Albert *et al.*, *Investigation of radioactivity-induced backgrounds in EXO-200*, Phys. Rev. **C92**, 015503 (2015), 1503.06241.

[155] E. H. Miller *et al.*, *Constraining radon backgrounds in LZ*, AIP Conf. Proc. **1921**, 050003 (2018), 1708.08533.

[156] S. J. Schowalter, C. B. Connolly, and J. M. Doyle, *Permeability of noble gases through Kapton, butyl, nylon, and "Silver Shield"*, Nuclear Instruments and Methods in Physics Research Section A: Accelerators, Spectrometers, Detectors and Associated Equipment **615**, 267–271 (2010).

[157] D. Akerib *et al.*, *Simulations of Events for the LUX-ZEPLIN (LZ) Dark Matter Experiment*, Astroparticle Physics , 102480 (2020).

[158] D. Akerib *et al.*, *LUXSim: A component-centric approach to low-background simulations*, Nuclear Instruments and Methods in Physics Research Section A: Accelerators, Spectrometers, Detectors and Associated Equipment **675**, 63 (2012).

[159] J. Thomas and D. A. Imel, *Recombination of electron-ion pairs in liquid argon and liquid xenon*, Phys. Rev. A **36**, 614 (1987).

[160] T. Doke *et al.*, *Let dependence of scintillation yields in liquid argon*, Nuclear Instru-

ments and Methods in Physics Research Section A: Accelerators, Spectrometers, Detectors and Associated Equipment **269**, 291 (1988).

[161] J. Haefner *et al.*, *Reflectance dependence of polytetrafluoroethylene on thickness for xenon scintillation light*, Nuclear Instruments and Methods in Physics Research Section A: Accelerators, Spectrometers, Detectors and Associated Equipment **856**, 86–91 (2017).

[162] B. López Paredes *et al.*, *Response of photomultiplier tubes to xenon scintillation light*, Astroparticle Physics **102**, 56–66 (2018).

[163] D. Akerib *et al.*, *Calibration, event reconstruction, data analysis, and limit calculation for the LUX dark matter experiment*, Physical Review D **97** (2018).

[164] V. N. Solovov *et al.*, *Position Reconstruction in a Dual Phase Xenon Scintillation Detector*, IEEE Transactions on Nuclear Science **59**, 3286–3293 (2012).

[165] D. Akerib *et al.*, *Position reconstruction in LUX*, Journal of Instrumentation **13**, P02001–P02001 (2018).

[166] F. Hasert *et al.*, *Observation of neutrino-like interactions without muon or electron in the gargamelle neutrino experiment*, Physics Letters B **46**, 138 (1973).

[167] D. Akimov *et al.*, *Observation of coherent elastic neutrino-nucleus scattering*, Science **357**, 1123–1126 (2017).

[168] J. N. Bahcall and C. Peña-Garay, *Solar models and solar neutrino oscillations*, New Journal of Physics **6**, 63–63 (2004).

[169] Particle Data Group, C. Patrignani *et al.*, *Review of Particle Physics*, Chin. Phys. C **40**, 100001 (2016).

[170] J.-W. Chen, H.-C. Chi, C. P. Liu, and C.-P. Wu, *Low-energy electronic recoil in xenon detectors by solar neutrinos*, Phys. Lett. B **774**, 656 (2017), 1610.04177.

[171] W. A. Rolke, A. M. López, and J. Conrad, *Limits and confidence intervals in the presence of nuisance parameters*, Nuclear Instruments and Methods in Physics Research Section A: Accelerators, Spectrometers, Detectors and Associated Equipment **551**, 493–503 (2005).

[172] L. Moneta *et al.*, *The RooStats Project*, 2010, 1009.1003.

[173] G. Cowan, K. Cranmer, E. Gross, and O. Vitells, *Asymptotic formulae for likelihood-*

based tests of new physics, Eur. Phys. J. C **71**, 1554 (2011), 1007.1727, [Erratum: Eur.Phys.J.C 73, 2501 (2013)].

[174] R. H. Helm, *Inelastic and Elastic Scattering of 187-Mev Electrons from Selected Even-Even Nuclei*, Phys. Rev. **104**, 1466 (1956).

[175] P. Klos, J. Menéndez, D. Gazit, and A. Schwenk, *Large-scale nuclear structure calculations for spin-dependent WIMP scattering with chiral effective field theory currents*, Phys. Rev. D **88**, 083516 (2013).

[176] G. Cowan, K. Cranmer, E. Gross, and O. Vitells, *Power-Constrained Limits*, (2011), 1105.3166.

[177] XENON100, E. Aprile *et al.*, *Online^{222} Rn removal by cryogenic distillation in the XENON100 experiment*, Eur. Phys. J. C **77**, 358 (2017), 1702.06942.

[178] S. Gundacker and A. Heering, *The silicon photomultiplier: fundamentals and applications of a modern solid-state photon detector*, Physics in Medicine & Biology **65**, 17TR01 (2020).

[179] E. Aprile *et al.*, *The XENON1T dark matter experiment*, The European Physical Journal C **77** (2017).

[180] D. Akerib *et al.*, *Improved Limits on Scattering of Weakly Interacting Massive Particles from Reanalysis of 2013 LUX Data*, Physical Review Letters **116** (2016).

[181] LUX, D. Akerib *et al.*, *Limits on spin-dependent WIMP-nucleon cross section obtained from the complete LUX exposure*, Phys. Rev. Lett. **118**, 251302 (2017), 1705.03380.

[182] XENON100, E. Aprile *et al.*, *Dark Matter Results from 225 Live Days of XENON100 Data*, Phys. Rev. Lett. **109**, 181301 (2012), 1207.5988.

[183] LUX, D. Akerib *et al.*, *First results from the LUX dark matter experiment at the Sanford Underground Research Facility*, Phys. Rev. Lett. **112**, 091303 (2014), 1310.8214.

[184] PandaX, M. Xiao *et al.*, *First dark matter search results from the PandaX-I experiment*, Sci. China Phys. Mech. Astron. **57**, 2024 (2014), 1408.5114.

[185] K. Abe *et al.*, *XMASS detector*, Nucl. Instrum. Meth. A **716**, 78 (2013), 1301.2815.

[186] M. Schumann, L. Baudis, L. Bütikofer, A. Kish, and M. Selvi, *Dark matter*

sensitivity of multi-ton liquid xenon detectors, JCAP **10**, 016 (2015), 1506.08309.

[187] DARWIN, J. Aalbers *et al.*, *DARWIN: towards the ultimate dark matter detector*, JCAP **11**, 017 (2016), 1606.07001.

[188] J. Street *et al.*, *Radon Mitigation for the SuperCDMS SNOLAB Dark Matter Experiment*, AIP Conf. Proc. **1921**, 050002 (2018), 1708.08535.

[189] K. Hosokawa *et al.*, *Development of a high-sensitivity 80 L radon detector for purified gases*, PTEP **2015**, 033H01 (2015).

[190] Y. Nakano *et al.*, *Measurement of Radon Concentration in Super-Kamiokande's Buffer Gas*, Nucl. Instrum. Meth. A **867**, 108 (2017), 1704.06886.

[191] H. S. Sebastian Lindemann and G. Zuzel, *Behaviour of 222Rn at cryogenic temperatures*, AIP Conference Proceedings **1338**, 156 (2011), https://aip.scitation.org/doi/pdf/10.1063/1.3579574.